

PRECISION MEASUREMENTS OF DEUTERON  
PHOTODISINTEGRATION USING LINEARLY  
POLARIZED PHOTONS OF 14 AND 16 MEV

by

Matthew Blackston

Department of Physics  
Duke University

Date: \_\_\_\_\_

Approved:

\_\_\_\_\_  
Henry R. Weller, Supervisor

\_\_\_\_\_  
Calvin R. Howell

\_\_\_\_\_  
Mark C. Kruse

\_\_\_\_\_  
Roxanne P. Springer

\_\_\_\_\_  
Ying Wu

Dissertation submitted in partial fulfillment of the  
requirements for the degree of Doctor of Philosophy  
in the Department of Physics  
in the Graduate School of  
Duke University

2007

ABSTRACT

PRECISION MEASUREMENTS OF DEUTERON  
PHOTODISINTEGRATION USING LINEARLY  
POLARIZED PHOTONS OF 14 AND 16 MEV

by

Matthew Blackston

Department of Physics  
Duke University

Date: \_\_\_\_\_

Approved:

\_\_\_\_\_  
Henry R. Weller, Supervisor

\_\_\_\_\_  
Calvin R. Howell

\_\_\_\_\_  
Mark C. Kruse

\_\_\_\_\_  
Roxanne P. Springer

\_\_\_\_\_  
Ying Wu

An abstract of a dissertation submitted in partial fulfillment of the  
requirements for the degree of Doctor of Philosophy  
in the Department of Physics  
in the Graduate School of  
Duke University

2007

Copyright © 2007 by Matthew Blackston  
All rights reserved

# Abstract

A precision measurement of the  $d(\vec{\gamma}, n)p$  reaction was performed at the High Intensity  $\gamma$ -ray Source (HI $\gamma$ S), which is located at the Duke Free Electron Laser Laboratory on the campus of Duke University. The  $\gamma$ -ray beams were nearly 100% linearly polarized, allowing the angular distributions of both the analyzing power and unpolarized cross section to be measured at 14 and 16 MeV. The photons were incident on a heavy water target and the neutrons from the photodisintegration reaction were detected using the Blowfish detector array, which consists of 88 liquid scintillator detectors with large angular coverage.

A transition matrix element (TME) analysis was performed on the data which allowed the amplitudes of the TMEs which contribute to the reaction at these energies to be extracted. This was done by invoking Watson's theorem, which fixes the relative TME phases using the  $n$ - $p$  scattering phase shifts, leaving the TME amplitudes as free parameters in fits to the data. The results indicated very good agreement with a recent potential model calculation for the amplitudes of the three electric dipole ( $E1$ )  $p$ -waves, which account for over 90% of the cross section at these energies.

The extracted TME amplitudes were then used to construct the observable which enters into the Gerasimov-Drell-Hearn (GDH) sum rule integrand. The results are the first experimental indication of a positive value of the GDH integrand in the region near photodisintegration threshold. A positive value at these energies has been shown by theory to be due to relativistic contributions.

## Acknowledgements

As I look back over these last few years of my life, I am keenly aware of how indebted I am to so many people. This list of people to thank is long, but it is worth the effort to express my appreciation.

I could not ask for more from my advisor, Henry Weller. When your door is open you have always been willing to endure me coming in to bombard you with questions or ideas. I have probably learned just as much physics through our conversations together as I have from many textbooks.

I want to thank those who have been part of the Capture group during my time here: Mohammad, Brent, Seth, Sean, Paul, Dick, Mark, Ralph, Moshe, Amanda, and Yannis. You are the ones I have rubbed elbows with in the lab and it is from you that I have learned how to do experimental physics. I also want to thank Matt and Alex for your friendship, both personal and professional, over these years. Your presence at the lab has made coming to work something I look forward to. In addition, I am grateful to the technical staff at TUNL: John, Richard, Chris, Bret, and Patrick. You have always been willing to assist me for just about any reason I've come up with.

This experiment would not have been possible without the help and expertise of the scientists from the University of Saskatchewan and the University of Virginia who are primarily responsible for building and maintaining the Blowfish array here at HI $\gamma$ S: Blaine, Rob, Brad, Ru, Brian, and Ward. The same is true of the scientists and staff at the FEL who were responsible for the great beams used in this experiment: Ying, Stepon, Jingyi, Vern, and Maurice.

I would also like to thank Paolo, through whom I have learned a great deal of physics (not to mention world history) which is very relevant to the work presented

in this dissertation. I have appreciated your friendship just as much as I have appreciated how much you have taught me. Thank you to Michael Schwamb for sharing your theoretical calculations with us and for making yourself available to answer our many questions.

There are many outside of work who have played a role in my life that has been no less valuable to my education here. I want to thank Sam, Matt, Tim, Eric, James, Joe, David, and Michael for always pushing me to follow Christ in every area of my life and for accepting me because of and in spite of all my strengths and weaknesses. A special thanks goes to Todd, who has modeled the love of Christ to me in countless ways. You have taught me how to see life in a way that has allowed me to do my work with greater joy.

I want to thank our church community, which is made up of people who have prayed for and encouraged me and my family through this process as well as the various events of our lives over these years. So many come to mind: the Wardles, Gerbers, Bakers, Carters, Kirks, Fleenors, and Kapurs. In particular, what can I say about how much the friendship of the Jacksons has meant to us? Words don't do justice. All of you have been our "family away from family" and it has been a joy to share life with you.

It would be impossible for me to be writing this if it were not for the love, support, and encouragement of my parents over many years. You have put me in the circumstances that have allowed me to succeed. I'll always be grateful to you and be proud to be called your son. To my sister and brothers, Amy, Andy, and Michael I also say thanks. You too have loved and supported me for many years and have played an important role in shaping who I am today. In addition, I thank my wife's family for the ways in which you have helped and supported us during my education.

And finally, the greatest thank you is reserved for my family. Daniel and Kate,

you have brought more joy into my life than I could have ever imagined. Just a few moments with you reminds me about what life is really about, and in this way, you have both made me a better physicist. Courtney, none of this would be possible without your presence in my life both as a companion and as the one who helps me to persevere. It is amazing to see where we are now compared to where we were when we arrived in Durham. You have been the heart and soul of our family and you have sacrificed much in order for me to reach this goal. You have been a constant in the midst of several years filled with considerable change. It is with deep love and gratitude that I dedicate this dissertation to you.

# Contents

<b>Abstract</b>	<b>iv</b>
<b>Acknowledgements</b>	<b>v</b>
<b>List of Figures</b>	<b>xv</b>
<b>List of Tables</b>	<b>xx</b>
<b>List of Acronyms</b>	<b>xxiii</b>
<b>1 Introduction</b>	<b>1</b>
1.1 Background . . . . .	1
1.2 Goals and Motivation . . . . .	4
1.2.1 The Observables . . . . .	4
1.2.2 Testing Theoretical Calculations . . . . .	6
1.2.3 Transition Matrix Elements . . . . .	7
1.2.4 The GDH sum rule . . . . .	8
1.3 Experimental Tools . . . . .	11
<b>2 Theory</b>	<b>13</b>
2.1 Introduction . . . . .	13
2.2 Kinematics . . . . .	13
2.3 Transition Matrix Elements . . . . .	15
2.4 Potential Model Calculation . . . . .	17
2.4.1 $NN$ Potential . . . . .	17
2.4.2 One-body Currents with Siegert Operators ( $N$ ) . . . . .	18
2.4.3 Meson Exchange Currents (MEC) . . . . .	20

2.4.4	Isobar Configurations (IC) . . . . .	21
2.4.5	Relativistic Currents (RC) . . . . .	22
2.4.6	SAPM Predictions . . . . .	23
2.5	Effective Field Theory . . . . .	23
2.6	The GDH Sum Rule . . . . .	26
2.6.1	Overview of the Derivation . . . . .	27
2.6.2	GDH for the Deuteron . . . . .	28
2.6.3	SAPM Prediction . . . . .	29
<b>3</b>	<b>Description of the Experiment</b>	<b>31</b>
3.1	Introduction . . . . .	31
3.2	The High Intensity $\vec{\gamma}$ -ray Source (HI $\gamma$ S) . . . . .	31
3.2.1	The Duke OK-4 Free Electron Laser (FEL) . . . . .	32
3.2.2	$\gamma$ -ray Production . . . . .	35
3.2.3	Beam Properties . . . . .	37
3.2.4	The Recent HI $\gamma$ S Upgrade . . . . .	42
3.3	HI $\gamma$ S Collimator Hut and Target Room . . . . .	44
3.3.1	Collimator Hut . . . . .	44
3.3.2	Target Room . . . . .	46
3.3.3	Axial Alignment . . . . .	47
3.4	Beam Monitoring . . . . .	48
3.4.1	HPGe: Energy, Energy Spread, and Flux . . . . .	48
3.4.2	Paddle System: Relative Flux Monitor . . . . .	52
3.4.3	Blowfish: Beam Polarization Axis . . . . .	54
3.5	The Blowfish Detector Array . . . . .	55

3.5.1	Array Design . . . . .	55
3.5.2	Blowfish Detectors . . . . .	56
3.5.3	Gain Monitoring System . . . . .	58
3.5.4	Targets . . . . .	60
3.6	Electronics . . . . .	61
3.6.1	Storage Ring Bunch Signal . . . . .	62
3.6.2	Acquisition Windows . . . . .	62
3.6.3	Blowfish or “Neutron” Trigger . . . . .	64
3.6.4	Pedestal Trigger . . . . .	65
3.6.5	HPGe or Flux Trigger . . . . .	66
3.6.6	LED Flasher Trigger . . . . .	67
3.6.7	Flasher Monitor Trigger . . . . .	67
3.6.8	Paddle Trigger . . . . .	68
3.6.9	Miscellaneous Components . . . . .	69
3.7	Data Acquisition System . . . . .	72
<b>4</b>	<b>Data Reduction</b>	<b>73</b>
4.1	Introduction . . . . .	73
4.2	Conversion of Data to the ROOT Framework . . . . .	73
4.3	Pedestal Determination . . . . .	74
4.4	Beam Energy Determination . . . . .	76
4.4.1	HPGe Calibration . . . . .	76
4.4.2	Energy Centroid and Width Determination . . . . .	77
4.5	Gain Determination . . . . .	79
4.5.1	<sup>232</sup> Th Source Runs . . . . .	79

4.5.2	Hardware Pulse Height Threshold Determination . . . . .	82
4.5.3	Flasher Centroid Determination . . . . .	84
4.5.4	Monitor Detector Source Peak Determination . . . . .	86
4.5.5	Gain Determination for Production Runs . . . . .	87
4.6	TDC Calibration . . . . .	90
4.6.1	Scattering from Upstream Materials . . . . .	91
4.6.2	Gamma-flash Alignment . . . . .	93
4.7	Multiplicity Cut . . . . .	95
4.8	Pulse-Shape Discrimination . . . . .	96
4.8.1	PSD Rotation . . . . .	97
4.8.2	PSD Cut Determination . . . . .	99
4.9	Pulse Height Cut . . . . .	100
4.10	Time of Flight Cut . . . . .	102
4.11	Neutron Yields . . . . .	105
4.11.1	Bad Detectors . . . . .	106
4.12	Beam Polarization Axis . . . . .	107
4.13	Raw Observables . . . . .	110
4.13.1	Uncorrected Unpolarized Cross Section . . . . .	113
4.13.2	Uncorrected Analyzing Power . . . . .	113
<b>5</b>	<b>Simulations and Data Correction</b>	<b>116</b>
5.1	Introduction . . . . .	116
5.2	The GEANT4 Toolkit . . . . .	116
5.3	Description of the Simulation . . . . .	117
5.3.1	Geometry and Materials . . . . .	117

5.3.2	Physics Processes Included . . . . .	119
5.3.3	Generating Primary Particles . . . . .	120
5.4	Understanding the Simulation . . . . .	121
5.4.1	Checking Neutron Scattering Cross Sections . . . . .	121
5.4.2	Light Output Response of Blowfish Detectors . . . . .	122
5.4.3	Blowfish Detector Efficiencies . . . . .	125
5.5	Analysis Cuts for Simulated Data . . . . .	127
5.6	Final Comparisons and Summary of Effects . . . . .	129
5.6.1	Comparison to Experimental Spectra . . . . .	129
5.6.2	Summary of Important Effects . . . . .	130
5.7	Correcting the Experimental Data . . . . .	133
5.7.1	Legendre Polynomial Parameterization of the Cross Section . . . . .	133
5.7.2	Fitting Method . . . . .	135
5.7.3	Fit Results . . . . .	138
5.7.4	Corrected Data . . . . .	140
5.8	Estimation of Systematic Errors . . . . .	142
5.8.1	Analysis Cuts . . . . .	143
5.8.2	Geometrical Effects . . . . .	144
5.8.3	Beam Effects . . . . .	145
5.8.4	Miscellaneous Effects . . . . .	146
5.8.5	Table of Systematic Errors . . . . .	147
<b>6</b>	<b>Results and TME Analysis</b>	<b>153</b>
6.1	Introduction . . . . .	153
6.2	Discussion of Results . . . . .	153

6.2.1	Legendre Polynomial Expansion Coefficients . . . . .	155
6.2.2	Unpolarized Cross Section . . . . .	156
6.2.3	Analyzing Power . . . . .	159
6.3	TME Formalism . . . . .	160
6.3.1	Formalism Nomenclature . . . . .	161
6.3.2	Differential Cross Section . . . . .	162
6.3.3	The Choice of TMEs . . . . .	164
6.3.4	Treatment of the TME Phases . . . . .	168
6.4	Fits and TME Results . . . . .	170
6.4.1	Without TME Splittings . . . . .	170
6.4.2	With TME Splittings . . . . .	175
6.5	GDH Sum Rule Integrand . . . . .	182
6.5.1	TME Formalism for $\sigma_P - \sigma_A$ . . . . .	184
6.5.2	GDH Results . . . . .	186
<b>7</b>	<b>Summary and Conclusions</b>	<b>189</b>
7.1	Introduction . . . . .	189
7.2	Summary of the Experiment . . . . .	189
7.3	Summary of the Analysis . . . . .	191
7.3.1	Data Reduction . . . . .	191
7.3.2	Simulations . . . . .	195
7.3.3	Extraction of TME Amplitudes . . . . .	197
7.4	Summary of the Results . . . . .	199
7.4.1	TME Amplitudes . . . . .	199
7.4.2	GDH Integrand . . . . .	203

7.5	Conclusions . . . . .	209
7.6	Future Prospects for $d(\vec{\gamma}, n)p$ at HI $\gamma$ S . . . . .	211
<b>A</b>	<b>TME Formalism Equations</b>	<b>212</b>
A.1	Legendre Coefficients as Functions of TMEs . . . . .	212
A.2	$\sigma_P\text{-}\sigma_A$ in terms of TME Amplitudes . . . . .	216
<b>B</b>	<b>Results in Tabular Form</b>	<b>218</b>
	<b>Bibliography</b>	<b>227</b>
	<b>Biography</b>	<b>231</b>

# List of Figures

1.1	Theoretical observables at 16 MeV. . . . .	5
1.2	$\sigma_P\text{-}\sigma_A$ predictions from Schwamb and Arenhövel. . . . .	9
2.1	Axes and angle definitions for the $d(\vec{\gamma}, n)p$ measurement. . . . .	14
2.2	Neutron kinetic energy as a function of lab angle. . . . .	15
2.3	Some of the diagrams of meson exchange currents included in the SAPM calculation. . . . .	20
2.4	Diagrams of a few of the isobar contributions to the $NN$ interaction and electromagnetic current. . . . .	21
2.5	SAPM predictions for observables of this experiment. . . . .	24
2.6	SAPM predictions for $\sigma_P\text{-}\sigma_A$ for the deuteron photodisintegration channel for variations of the calculation. . . . .	30
3.1	The layout of the DFELL. . . . .	32
3.2	Schematic of the creation of micro-bunches in OK-4. . . . .	35
3.3	$\theta$ definition for the Compton backscattering interaction. . . . .	36
3.4	An example of $\gamma$ -ray energy as a function of scattering angle. . . . .	38
3.5	Beam polarization as a function of photon scattering angle. . . . .	40
3.6	Upgraded HI $\gamma$ S facility. . . . .	43
3.7	HI $\gamma$ S collimator hut schematic. . . . .	45
3.8	HI $\gamma$ S target room overview. . . . .	47
3.9	Sample HPGe spectrum for a HI $\gamma$ S beam. . . . .	49
3.10	The paddle system for relative flux measurements. . . . .	52

3.11	An ADC spectrum from the third scintillator of the paddle system. . . . .	53
3.12	The paddle system counting logic. . . . .	54
3.13	The Blowfish Detector Array. . . . .	56
3.14	A drawing of the cross section of the Blowfish Detector Array. . . . .	57
3.15	Diagram of a single detector from the Blowfish Array. . . . .	58
3.16	Schematic of the gain monitoring system. . . . .	59
3.17	Schematic of acquisition windows for Blowfish electronics. . . . .	63
3.18	Electronics diagram for Blowfish detectors. . . . .	65
3.19	Schematic of the neutron and pedestal triggers. . . . .	66
3.20	Schematic of the flux trigger. . . . .	67
3.21	Schematic of the flasher and monitor triggers. . . . .	68
3.22	Schematic of the paddle trigger. . . . .	69
3.23	Overall schematic of the trigger logic, part 1. . . . .	70
3.24	Overall schematic of the trigger logic, part 2. . . . .	71
4.1	Typical pedestal spectrum from a Blowfish detector ADC. . . . .	75
4.2	Simulated energy spectra for 14 and 16 MeV beams with 0.5" and 1" collimators. . . . .	78
4.3	Compton edge for 2615 keV $\gamma$ -rays from a typical $^{232}\text{Th}$ source spectrum. . . . .	82
4.4	Threshold determination in a Blowfish detector. . . . .	83
4.5	The mean threshold values for all Blowfish detectors for 16 MeV runs. . . . .	84
4.6	Flasher spectrum for a Blowfish detector. . . . .	85

4.7	$^{137}\text{Cs}$ source spectrum in a GSO monitor detector. . . . .	86
4.8	Gain values for two Blowfish detectors as a function of run number. . .	89
4.9	Scatter plot of detector gain versus detector rate. . . . .	90
4.10	Double peaks from a $\gamma$ -flash run for detectors of various $\theta$ . . . . .	92
4.11	Ring yield versus $\theta$ for a run with no target. . . . .	93
4.12	Fits to TDC spectra to determine $\gamma$ -flash TDC channel. . . . .	94
4.13	Typical pulse shapes for a neutron and a $\gamma$ -ray in BC-505 with the long and short ADC gates used for PSD. . . . .	97
4.14	Pulse height versus PSD parameter for a single Blowfish detector be- fore and after rotation. . . . .	98
4.15	TDC versus rotated PSD parameter for a single Blowfish detector summed over all runs. . . . .	100
4.16	Histogram of PSD values for a single Blowfish detector summed over all runs within a wide TDC cut. . . . .	101
4.17	Pulse height spectrum after PSD cut. . . . .	102
4.18	TDC spectra before and after PSD and PH cuts. . . . .	103
4.19	TDC window determination for a single Blowfish detector. . . . .	104
4.20	Raw yields versus detector number for one orientation of the Blowfish Array at $E_\gamma = 14$ MeV. . . . .	106
4.21	Neutron yields for each arm of the array as a function of $\phi$ for all Blowfish orientations at 14 MeV. . . . .	108
4.22	The analyzing power constructed using the $45^\circ$ detectors. . . . .	110
4.23	Schematic of the detector location relative to the polarization plane for a pair of array orientations. . . . .	112

4.24	Uncorrected unpolarized differential cross section for each beam energy.	114
4.25	Uncorrected analyzing power for each beam energy. . . . .	115
5.1	The Blowfish array and target geometry as defined in the GEANT4 simulation. . . . .	118
5.2	Comparison of $^{16}\text{O}(n,n)^{16}\text{O}$ and $d(n,n)d$ cross sections deduced from GEANT4 to evaluated data. . . . .	123
5.3	Light output as a function of proton energy. . . . .	125
5.4	Detector efficiency as a function of neutron energy. . . . .	126
5.5	Comparison of experimental and simulated spectra. . . . .	130
5.6	Comparison of simulated raw observables under various conditions at 16 MeV. . . . .	131
5.7	Simulated neutron yields as a function of detector number using each Legendre polynomial individually as the input cross section. . . . .	137
5.8	Fits to the experimental yields using the simulated yields from the Legendre polynomials. . . . .	139
5.9	Observables before and after corrections for 16 MeV. . . . .	142
6.1	Final experimental observables. . . . .	154
6.2	14 MeV Legendre coefficients. . . . .	155
6.3	16 MeV Legendre coefficients. . . . .	156
6.4	Ratio of the cross section at selected angles to the cross section at $\theta = 90^\circ$ with comparisons to previous measurements. . . . .	158
6.5	Comparison of $\Sigma(\theta_{Lab} = 90^\circ)$ with Previous Measurements. . . . .	160
6.6	Multipole strength as a function of energy for the SAPM calculation.	166
6.7	Spins and parities possible for final states of $M1$ , $E1$ , and $E2$ transitions.	166

6.8	Fits to observables with no splittings. . . . .	173
6.9	Percent multipole contributions with no splittings. . . . .	175
6.10	Absolute multipole contributions with no splittings. . . . .	176
6.11	Fits to observables with splittings. . . . .	178
6.12	Percent of total cross section for each TME amplitude. . . . .	179
6.13	Percent multipole contributions with splittings. . . . .	182
6.14	Absolute multipole contributions with splittings. . . . .	183
6.15	GDH sum rule integrand with no splittings. . . . .	187
6.16	GDH sum rule integrand with splittings. . . . .	188
7.1	PSD spectrum with applied cut displayed. . . . .	192
7.2	TDC spectra before and after PSD and PH cuts with TDC window displayed. . . . .	193
7.3	Schematic of the detector location relative to the polarization plane for a pair of array orientations used to construct the analyzing power. . . . .	194
7.4	Final experimental observables with Legendre fit. . . . .	196
7.5	Fits from the extraction of TME amplitudes. . . . .	200
7.6	Percent of total cross section for each TME amplitude. . . . .	201
7.7	Percent multipole contributions. . . . .	202
7.8	Existing indirect GDH integrand values near threshold. . . . .	207
7.9	GDH sum rule integrand results for this work. . . . .	208

# List of Tables

3.1	Realized Duke FEL operating parameters. . . . .	36
3.2	Expected upgraded HI $\gamma$ S operating parameters. . . . .	44
3.3	Arm and ring numbers for Blowfish detectors. . . . .	58
3.4	Dimensions of the D <sub>2</sub> O target. . . . .	61
4.1	Beam energy centroids and widths from measurements and simulation. . . . .	78
4.2	Adopted values for centroid beam energies for 14 and 16 MeV beams. . . . .	79
4.3	Mean hardware thresholds in the Blowfish detectors. . . . .	84
4.4	Variable definitions for gain determination equation. . . . .	88
4.5	Software PH cuts for each beam energy. . . . .	102
4.6	Extracted deviations of the axis of polarization from the horizontal. . . . .	109
4.7	Fitted analyzing power values using detectors at an angle of 45° from the horizontal plane. . . . .	110
5.1	Light output response function parameters. . . . .	124
5.2	$\chi^2$ values for Legendre polynomial fits. . . . .	139
5.3	Percent systematic errors on 14 MeV cross section points. . . . .	149
5.4	Percent systematic errors on 14 MeV analyzing power points. . . . .	150
5.5	Percent systematic errors on 16 MeV cross section points. . . . .	151
5.6	Percent systematic errors on 16 MeV analyzing power points. . . . .	152
6.1	All possible TMEs for $M1$ , $E1$ , and $E2$ transitions. . . . .	167

6.2	TMEs included in the fits to the data. . . . .	168
6.3	$n$ - $p$ scattering phase shifts for $E_\gamma = 14$ and 16 MeV. . . . .	169
6.4	14 MeV Legendre coefficient ratios. . . . .	172
6.5	16 MeV Legendre coefficient ratios. . . . .	172
6.6	$\chi^2$ values for TME fits with no splittings. . . . .	174
6.7	$\chi^2$ values for TME fits with splittings. . . . .	177
B.1	Raw cross section and analyzing power values for 14 MeV. . . . .	219
B.2	Raw cross section and analyzing power values for 16 MeV. . . . .	219
B.3	Corrected cross section and analyzing power values for 14 MeV. . . .	220
B.4	Corrected cross section and analyzing power values for 16 MeV. . . .	220
B.5	Legendre polynomial coefficients for 14 MeV. . . . .	221
B.6	Legendre polynomial coefficients for 16 MeV. . . . .	221
B.7	TME Amplitudes obtained from fits with no splittings for 14 and 16 MeV. . . . .	222
B.8	14 MeV multipole contributions to the total cross section in percent for fits with no splittings. . . . .	222
B.9	16 MeV multipole contributions to the total cross section in percent for fits with no splittings. . . . .	222
B.10	14 MeV absolute multipole contributions for fits with no splittings. . .	223
B.11	16 MeV absolute multipole contributions for fits with no splittings. . .	223
B.12	14 MeV TME amplitudes obtained from fits with splitting. . . . .	223
B.13	16 MeV TME amplitudes obtained from fits with splitting. . . . .	224

B.14 14 MeV multipole contributions to the total cross section in percent for fits with splittings. . . . .	224
B.15 16 MeV multipole contributions to the total cross section in percent for fits with splittings. . . . .	224
B.16 14 MeV absolute multipole contributions for fits with splittings. . . .	225
B.17 16 MeV absolute multipole contributions for fits with splittings. . . .	225
B.18 $\sigma_P - \sigma_A$ values for all 14 MeV solutions. . . . .	225
B.19 $\sigma_P - \sigma_A$ values for all 16 MeV solutions. . . . .	226

## List of Acronyms

ADC	Analog-to-Digital Converter
BBN	Big Bang Nucleosynthesis
CAMAC	Computer Automated Measurement And Control
CFD	Constant-Fraction Discriminator
CM	Center-of-Mass or Center-of-Momentum
DAQ	Data Acquisition System
DC	Direct Current
DFELL	Duke Free Electron Laser Laboratory
DSR	Duke Storage Ring
EFT	Effective Field Theory
FEL	Free Electron Laser
FWHM	Full-Width-Half-Maximum
GDH	Gerasimov-Drell-Hearn
GG	Gate Generator
GMS	Gain Monitoring System
GSO	Gadolinium-Silicon-Trioxide
HI $\gamma$ S	High Intensity $\gamma$ -ray Source
HOMs	Higher-Order-Modes
HPGe	High Purity Germanium
IC	Isobar Configurations
LED	Light-Emitting Diode
LET	Low Energy Theorem
LINAC	Linear Accelerator
LOR	Light Output Response

MEC Meson Exchange Currents  
NIM Nuclear Instrument Module  
NIST National Institute of Standards and Technology  
OK Optical Klystron  
PH Pulse Height  
PMT Photo-Multiplier Tube  
PSD Pulse-Shape Discrimination  
QCD Quantum Chromodynamics  
RC Relativistic Contributions or Currents  
RF Radio-Frequency  
SAPM Schwamb-Arenhövel Potential Model  
TDC Time-to-Digital Converter  
TMEs Transition Matrix Elements  
TOF Time-of-Flight  
TUNL Triangle Universities Nuclear Laboratory  
VME Versa Module Europa

# Chapter 1

## Introduction

This dissertation describes a precision measurement of deuteron photodisintegration using linearly polarized photons at energies of 14 and 16 MeV. The experiment was performed at the High Intensity  $\gamma$ -ray Source (HI $\gamma$ S) which is located at the Duke Free Electron Laser Laboratory in Durham, NC. This chapter will discuss the background and motivation for the experiment and provide a brief overview of the experimental tools used.

### 1.1 Background

Photonuclear physics got its start when deuteron photodisintegration was first observed experimentally in 1934 by Chadwick and Goldhaber [Cha34], who published a paper with the title “A ‘Nuclear Photo-effect’: Disintegration of the Diplon by  $\gamma$ -rays.” Not long after, Bethe and Peierls published the first theoretical work on the subject in 1935 [Bet35] with the title “Quantum Theory of the Diplon”.

Photonuclear reactions employ  $\gamma$ -rays which interact with nuclear material through the well-understood electromagnetic interaction, making them excellent probes for studying the details of the strong interaction in nuclei. Moreover, deuteron photodisintegration holds a unique place in nuclear physics because the deuteron is the simplest bound nucleus that exists. As Chadwick and Goldhaber observed, the deuteron is “as important to nuclear theory as the hydrogen atom is in atomic theory.”

Since this reaction is so fundamental to our understanding of the  $N$ - $N$  interaction, there is a long history of experimental and theoretical effort devoted to the subject and the time-reversed reaction,  $n$ - $p$  capture. Arenhövel and Sanzone note that nearly every time new experimental techniques or accelerators are developed, or new theoretical concepts are studied regarding the  $N$ - $N$  interaction, the deuteron has served as a “test case” [Are91].

One reason for the early proliferation of work on this reaction is that it is relatively simple to study experimentally. This is in part due to the deuteron’s low binding energy of 2.225 MeV, which allowed experiments to be performed using  $\gamma$ -rays from radioactive sources and low energy nuclear reactions before the advent of higher energy and more sophisticated accelerators.

More recently, photonuclear reactions have been studied using bremsstrahlung photon beams or beams which use Compton scattering of low energy photons from high energy electrons. Both techniques can also be used to produce polarized photons. This, along with the advent of polarized target technologies, has caused considerable effort to be put into the measurement of polarization observables for studying the detailed structure of the  $N$ - $N$  interaction.

On the theoretical side, the first calculation from Bethe and Peierls [Bet35] considered only dipole transitions in the long wave length approximation, with the  $N$ - $N$  force approximated by a zero-range (i.e. delta function) potential. The result was the  $\sin^2\theta$  dependence of the differential cross section which is expected when considering dipole radiation. While the shape of the total cross section agreed well with data, the overall magnitude disagreed significantly. Bethe and Longmire [Bet50] eventually brought agreement by relaxing the zero-range potential assumption, yielding what is called the effective range cross section.

Since then, calculations have included higher multipoles and more elaborate  $N$ - $N$  potentials. Modern calculations go farther, by including meson and isobar (i.e.  $\Delta$ ) degrees of freedom along with relativistic effects, such as the calculation of Schwamb and Arenhövel [Sch01a, Sch01b, Are04] which is reviewed in this dissertation (see Chapter 2). In addition, effective field theory (EFT) calculations are now being performed by starting from a Lagrangian which considers only the relevant degrees of freedom in the problem. In addition, EFT employs power-counting schemes which allow the uncertainty of the calculations to be estimated.

This reaction is also important in the context of Big Bang nucleosynthesis (BBN), since deuteron photodisintegration is related to the  $n$ - $p$  capture reaction through the principle of detailed balance. The  $n + p \rightarrow d + \gamma$  reaction is the first in a chain of reactions which produced the light elements during BBN in the early universe. The reaction rate is therefore crucial in determining the relative abundances of the primordial elements. Moreover, since neutrons are unstable outside the nucleus, this reaction is responsible for “storing” them inside the deuteron, to be used for building even heavier elements in stellar nucleosynthesis. The importance of this reaction has led many to call it the “Baryometer” of the universe.

The fact that there is still so much to learn about this reaction despite the fact that it has been studied since the 1930s is a testament to the special place it assumes in the field of nuclear physics.

## 1.2 Goals and Motivation

### 1.2.1 The Observables

The experiment described in this dissertation used linearly polarized photons incident upon an unpolarized target. Under these conditions, two observables are accessible: the angular distribution of the unpolarized cross section and the analyzing power. The analyzing power is defined as

$$\Sigma(\theta) = \frac{1}{P_\gamma} \frac{\sigma(\theta, \phi = 0^\circ) - \sigma(\theta, \phi = 90^\circ)}{\sigma(\theta, \phi = 0^\circ) + \sigma(\theta, \phi = 90^\circ)}, \quad (1.1)$$

where  $P_\gamma$  represents the linear polarization fraction of the beam and  $\sigma(\theta, \phi)$  is the polarized differential cross section. The polar angle  $\theta$  is measured with respect to the beam axis,  $\phi$  is the azimuthal angle, and the photon is polarized in the  $\phi = 0^\circ$  direction (refer to Figure 2.1). Experimentally, this amounts to measuring the difference in yields for detectors parallel and perpendicular to the beam polarization plane over the sum<sup>1</sup>. One advantage in such a measurement is that the absolute normalization of the cross section drops out in the ratio, making absolute cross section measurements unnecessary.

This experiment was designed to be a precision measurement of both observables at 14 and 16 MeV using a detector array with very large angular coverage. The analyzing power is particularly sensitive to which electromagnetic multipole transitions are present in the interaction. For instance, pure magnetic dipole ( $M1$ ) transitions leading to orbital angular momentum in the outgoing state of  $l=0$  ( $s$ -waves) result in isotropic neutron emission and analyzing power values of zero. On the other hand, for

---

<sup>1</sup>The analyzing power can be expressed in terms of the yields if effects such as multiple scattering and finite geometry are neglected. Otherwise, the yields need to be corrected for such effects.

pure electric dipole ( $E1$ ) transitions most of the neutrons will be emitted parallel to the beam polarization direction and almost none will be emitted in the perpendicular direction, resulting in an analyzing power expectation of about one.

Since electric dipole transitions are known to dominate the reaction at these energies, the reality will be closer to the latter condition. Examples of the two observables from the theoretical calculation of Schwamb and Arenhövel [Sch01a, Sch01b, Are04], which is described in the next chapter, are shown in Figure 1.1.

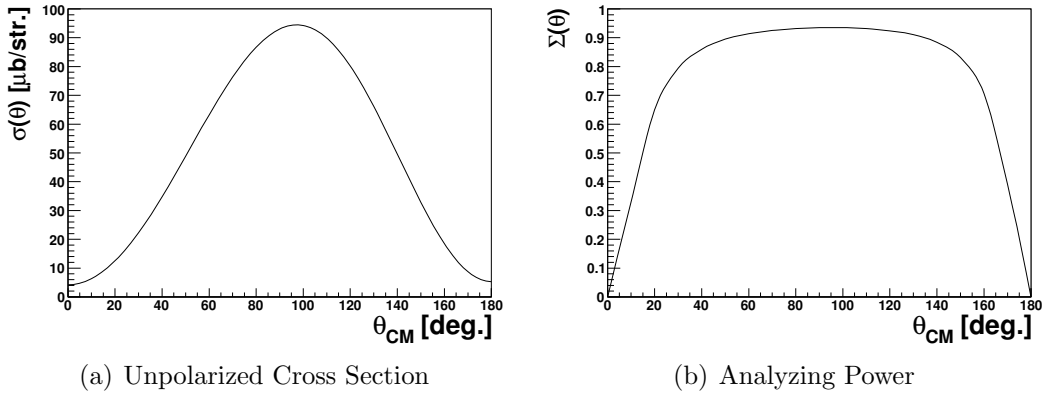


**Figure 1.1:** Theoretical predictions of Schwamb and Arenhövel [Sch01a, Sch01b, Are04] for the cross section and analyzing power at 16 MeV. Both plots are given as a function of the center-of-mass (CM) angle.

Note that the unpolarized cross section is expected to take on a shape similar to  $\sin^2\theta$ , which is expected for a reaction dominated by electric dipole transitions. As mentioned above, the analyzing power values in the central angles are very near one, since these are the primary angles into which neutrons from  $E1$  transitions scatter. However, at the extreme angles, where the  $E1$  cross section dies off, the  $M1$   $s$ -wave contribution causes the analyzing power values to go to zero.

## 1.2.2 Testing Theoretical Calculations

Precision measurements of these observables provide a testing ground for our current understanding of the strong interaction. The angular distributions cover a wide angular range allowing the details of the shapes of the distributions to be compared to modern theoretical calculations.

In particular, questions about the role of meson exchange currents, isobar currents, and relativistic effects can be addressed. A recent potential model calculation from Schwamb and Arenhövel [Sch01a, Sch01b, Are04] addresses these issues. That calculation used a realistic  $N$ - $N$  potential and included the following nuclear currents: non-relativistic one-body currents with Siegert operators, explicit meson exchange currents beyond the Siegert operators, explicit isobar configurations, and relativistic contributions. The Siegert operators are obtained by using Siegert's theorem [Sie37] to write the current density operators in terms of the charge density operators, thus implicitly including the dominant part of the exchange currents [Are91].

While at these energies contributions beyond the one-body currents with Siegert operators have little influence on these observables, an examination of another observable,  $\sigma_P$ - $\sigma_A$  (see Section 1.2.4) reveals the importance of the relativistic effects. A description of how  $\sigma_P$ - $\sigma_A$  can be accessed indirectly in this experiment through the transition matrix elements (TMEs) of the reaction is introduced in Section 1.2.4.

Additionally, while the photodisintegration energies of relevance to Big Bang Nucleosynthesis (BBN) are lower than the energies of this experiment, the dominant reaction mechanisms for BBN, particularly the  $E1$  transitions, are still the most important mechanisms at 14 and 16 MeV. Thus, measurements which help improve our understanding of these interactions at higher energies also give confidence in the ability to perform calculations at energies relevant to BBN.

The  $n$ - $p$  capture reaction has also recently been studied using the techniques of effective field theory (EFT) [Rup00, Che99]. These works perform the calculations for BBN energies using pion-less EFT which begins losing accuracy in the energy region of this experiment. However, several new calculations should be forthcoming which can be compared to these data as a test of EFT [Gri07, Par07].

### 1.2.3 Transition Matrix Elements

The details of the deuteron photodisintegration reaction can be studied by considering it in terms of the contributing transition matrix elements (TMEs). The TMEs describe the basic nuclear physics of an interaction and take the form

$$\langle \psi_f | H_{int} | \psi_i \rangle, \quad (1.2)$$

where  $\psi_f$  is the final state  $n$ - $p$  wave function,  $\psi_i$  is the initial state deuteron wave function, and  $H_{int}$  is the interaction Hamiltonian. In the case of deuteron photodisintegration, it is traditional to perform a multipole expansion on the interaction Hamiltonian so that it is written in terms of the electric and magnetic multipole operators. The probability for a given transition from the ground state to a given final state is proportional to the square of the TME amplitude.

The angular distribution of the observables of this experiment can be written in terms of the most important TMEs which contribute to the reaction at these energies [Wel92]. Each TME can be factored into a term which depends on the radial part of the wave function, called the reduced TME, and a term which depends on the angular part of the wave function. The observables in the formalism used in this work are written in terms of the reduced TMEs. They are labeled using the

notation  $^{2s+1}l_J (pL)$ , where  $s$  is the channel spin,  $l$  is the orbital angular momentum in spectroscopic notation,  $J$  is the total angular momentum, and  $pL$  is the mode and multipolarity of the incoming radiation ( $M1$ ,  $E1$ ,  $E2$ , etc.). The relevant terms at these energies are the  $M1$   $^1s_0$  term, the triplet  $E1$   $p$ -waves ( $^3p_0$ ,  $^3p_1$ , and  $^3p_2$ ), and the triplet  $E2$   $d$ -waves ( $^3d_1$ ,  $^3d_2$ , and  $^3d_3$ ).

Since the TMEs are complex numbers, each can be expressed as an amplitude and a phase, but this leaves too many unknown parameters for a meaningful fit to the data. However, the number of unknowns can be reduced by invoking Watson's theorem [Knu99], which allows the  $n$ - $p$  scattering phase shifts to be used to evaluate the relative phases. In this way the TMEs can be extracted from the data by fitting the polarized differential cross section. The successful extraction of the TME amplitudes thus provides a way to gain a microscopic view of the reaction mechanisms which contribute at this energy. Chapter 6 discusses the extraction of the TME amplitudes from the data of this experiment in detail.

### 1.2.4 The GDH sum rule

Another area of current interest related to deuteron photodisintegration is in the context of the Gerasimov-Drell-Hearn (GDH) sum rule [Ger66, Dre66]. The GDH sum rule takes the form

$$I_{GDH} = \int_{\omega_{th}}^{\infty} \frac{\sigma_P - \sigma_A}{\omega} d\omega = \frac{4\pi^2\alpha}{m^2} \kappa^2 S, \quad (1.3)$$

where  $\sigma_P$  and  $\sigma_A$  are the photo-absorption cross sections for circularly polarized  $\gamma$ -rays incident upon a longitudinally polarized target with beam and target spins parallel and anti-parallel, respectively. The cross section difference is weighted by

the beam energy,  $\omega$ , and the integration goes from photodisintegration threshold,  $\omega_{th}$ , to infinity. On the right hand side,  $\alpha$  is the fine structure constant,  $m$  is the mass of the target particle,  $\kappa$  is the anomalous magnetic moment, and  $S$  is the target spin. The prediction from the calculation of Schwamb and Arenhövel [Are04] for  $\sigma_P - \sigma_A$  as a function of energy for the deuteron photodisintegration channel is shown in Figure 1.2.

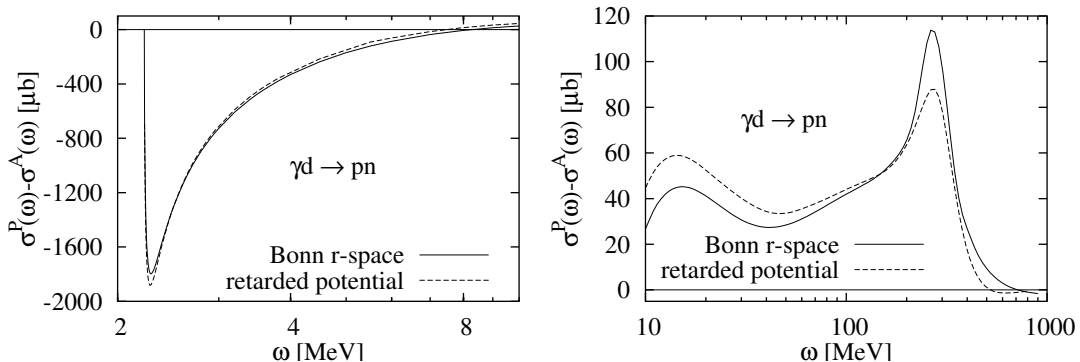


**Figure 1.2:**  $\sigma_P - \sigma_A$  predictions from Schwamb and Arenhövel for the photodisintegration channel. The dashed line is from [Are04] and the solid line is a previous calculation from [Are01]. The biggest difference in the two calculations is the different  $N-N$  potentials which were used (see [Are04] for details). Figure is taken from [Are04].

The GDH sum rule is interesting because it is derived from very fundamental principles and it relates the dynamical spectrum of the deuteron to a magnetic ground state property, its anomalous magnetic moment. A world-wide effort to measure the GDH integrand for the deuteron over a wide range of energies is currently underway. A similar investigation for the proton has been published up to photon energies of 2.9 GeV and an indication of the validity of the GDH sum rule for the proton was obtained [Ahr01].

One of the interesting features of the GDH sum rule for the deuteron is the almost complete cancellation of the contribution to the sum rule above pion threshold by

the contribution below pion threshold. The large negative contribution very near photodisintegration threshold is due to the large  $M1$  transition strength to the  $^1s_0$  state, which is only accessible in the anti-parallel configuration of beam and target spins.

With increasing energy, as the  $M1$  contribution dies away and the  $E1$   $p$ -waves begin to dominate the reaction, the cross section difference changes from negative to positive. The predicted energy at which this change occurs has been found to be dependent upon whether or not relativistic effects are included in the calculation [Are01]. These effects manifest themselves in a difference in the splittings of the reduced  $p$ -wave amplitudes. Schwamb and Arenhövel predict the cross-over point to be just below 8 MeV. Thus a measurement of  $\sigma_P - \sigma_A$  at 14 and 16 MeV is able to either confirm or deny a positive strength, and thus also the importance of relativistic contributions at these energies.

The lack of circularly polarized  $\gamma$ -rays and a polarized target in this experiment is overcome by writing  $\sigma_P - \sigma_A$  in terms of the reduced TME amplitudes using the formalism of [Wel94]:

$$\begin{aligned} \sigma_P - \sigma_A = \frac{1}{2}\pi\lambda^2 & \left[ -|{}^1s_0(M1)|^2 \right. \\ & - |{}^3p_0(E1)|^2 - \frac{3}{2}|{}^3p_1(E1)|^2 + \frac{5}{2}|{}^3p_2(E1)|^2 \\ & \left. - \frac{3}{2}|{}^3d_1(E2)|^2 - \frac{5}{6}|{}^3d_2(E2)|^2 + \frac{7}{3}|{}^3d_3(E2)|^2 \right], \end{aligned} \quad (1.4)$$

where  $\lambda = \lambda/2\pi$  is written in terms of the  $\gamma$ -ray wavelength. Since the  $s$ -wave term is expected to be small at these energies, an extraction of the  $p$ -wave amplitudes is the primary factor in determining the value of the cross section difference at these energies. Writing  $\sigma_P - \sigma_A$  in this form allows the reduced TME amplitudes extracted from these measurements to be used to contribute to the effort of mapping out the

GDH integrand below pion threshold.

### 1.3 Experimental Tools

The ambitious goals for these deuteron photodisintegration measurements can only be achieved if powerful experimental tools are available. Two such tools which allow high precision data to be obtained are the High Intensity  $\gamma$ -ray Source (HI $\gamma$ S) and the Blowfish detector array.

The HI $\gamma$ S facility produces  $\gamma$ -ray beams via the intra-cavity Compton backscattering a free electron laser (FEL) from high energy electrons circulating in a storage ring [Lit97]. HI $\gamma$ S beams are very powerful for performing nuclear physics experiments for several reasons. Among these are the high beam fluxes, narrow and selectable energy spreads, and the high degree of beam polarization.

The high fluxes allow statistically precise measurements to be made in a relatively short amount of running time. The nearly mono-energetic energy profile of the beams means that photon tagging is unnecessary and that the energy of the outgoing neutrons in this reaction are easily obtained by simply observing the angle into which it scatters<sup>2</sup>. Finally, a higher degree of beam polarization causes the polarization asymmetries to be larger, allowing them to be extracted with high precision relatively quickly.

The Blowfish detector array consists of 88 liquid scintillator detectors for neutron detection. They cover a wide angular range, allowing the details of the shapes of the observables to be determined. Overall, it covers about 25% of the full  $4\pi$  solid angle. The scintillators in the array have excellent pulse-shape discrimination properties

---

<sup>2</sup>Neglecting multiple scattering effects. In addition, time-of-flight techniques can also be used for neutron energy determination.

allowing  $\gamma$ -rays to be effectively filtered from the neutron samples. In addition, the pulsed nature of the HI $\gamma$ S beams along with the known path length from the target to the detectors allows time-of-flight techniques to be used to distinguish beam related neutrons from background.

A recent upgrade to the Blowfish array saw the installation of a new gain monitoring system which sends light pulses from a light-emitting diode (LED) to each detector to track their gains during runs [Bew05]. This allows the hardware threshold value to be tracked more accurately, which is very important when considering the effect thresholds play on neutron detector efficiencies. The array is also able to rotate about the beam axis to allow the study and cancellation of systematic effects, which is important for any high precision measurement.

This dissertation will describe how the powerful experimental tools briefly described here were used to pursue the goals mentioned in this chapter. It will discuss how the precision measurements of the accessible observables were used to extract fundamental information about the deuteron photodisintegration reaction in the form of the transition matrix elements of the reaction. Moreover, how those amplitudes were used to access indirect information about the GDH sum rule integrand will also be presented.

# Chapter 2

## Theory

### 2.1 Introduction

The first theoretical treatment of deuteron photodisintegration appeared in 1935 by Bethe and Peierls [Bet35]. Since then there has been a steady stream of theoretical papers devoted to the subject. A good review can be found in [Are91]. This chapter will focus primarily on a recent potential model calculation from Schwamb and Arenhövel [Sch01a, Sch01b, Are04].

The kinematics of the photodisintegration reaction are discussed briefly in Section 2.2 and Section 2.3 introduces the transition matrix elements of the reaction, from which the differential cross section can be constructed. Section 2.4 reviews the calculation of Schwamb and Arenhövel, with each piece of the calculation described in turn. Section 2.5 briefly discusses another approach that can be used for performing these calculations, namely effective field theory, and Section 2.6 provides a discussion of the Gerasimov-Drell-Hearn (GDH) sum rule for the deuteron.

### 2.2 Kinematics

Figure 2.1 shows a diagram of how the axes and angles are defined for the  $d(\vec{\gamma}, n)p$  reaction.  $\vec{p}_n$  is the momentum vector of the outgoing neutron,  $\theta$  is the polar angle measured with respect to the beam axis, and  $\phi$  is the azimuthal angle measured with

respect to the  $x$ - $z$  plane. The beams at HI $\gamma$ S are horizontally polarized along the  $x$  axis.

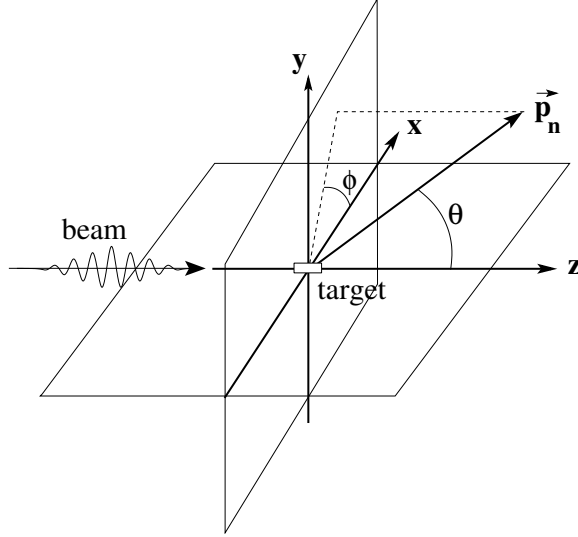


**Figure 2.1:** Axes and angle definitions for the  $d(\vec{\gamma}, n)p$  measurement.  $\vec{p}_n$  is the momentum vector of the outgoing neutron,  $\theta$  is the polar angle measured with respect to the beam axis, and  $\phi$  is the azimuthal angle measured with respect to the  $x$ - $z$  plane. The beams at HI $\gamma$ S are polarized along the  $x$  axis.

Because the reaction leads to a two-body final state, the angle of the outgoing neutron in the lab frame determines its energy. In the center-of-mass (CM) frame the total energy,  $W$ , is given by

$$W = \sqrt{m_d^2 + 2E_\gamma m_d}, \quad (2.1)$$

where  $m_d$  is the mass of the deuteron, and  $E_\gamma$  is the incoming beam energy in the lab frame. This leads to neutron emission in the CM frame at all angles with energy given by

$$T_n^{CM} = \frac{(W - m_n)^2 - m_p^2}{2W}, \quad (2.2)$$

where  $T_n^{CM}$  is the CM neutron kinetic energy, and  $m_n$  and  $m_p$  are the masses of

the neutron and proton, respectively. After boosting to the lab frame, the neutron energy becomes angle dependent with a one-to-one correspondence between energy and angle. Figure 2.2 shows the relation between the lab angle and neutron energy for the two nominal beam energies in this experiment.

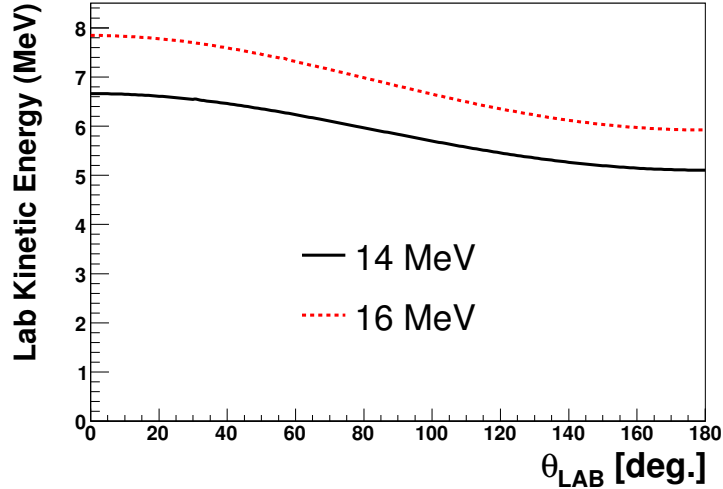


**Figure 2.2:** Neutron kinetic energy as a function of lab angle for 14 MeV (solid black line) and 16 MeV (dashed red line) beams.

## 2.3 Transition Matrix Elements

The differential cross section for deuteron photodisintegration can be described in terms of the Transition Matrix Elements (TMEs) of the reaction. The TMEs represent the probability of a target particle with an initial wave function  $\psi_i$  undergoing a transition to a final state,  $\psi_f$ , under the influence of an interaction Hamiltonian. In the case of deuteron photodisintegration, the interaction Hamiltonian is often written in terms of the electric and magnetic multipole operators originating from the incoming  $\gamma$ -ray beam.

In the CM frame, the differential cross section takes the form [Are91]

$$\frac{d\sigma}{d\Omega} = \frac{(2\pi)^{10}}{(4W)^2} \frac{k}{\omega} |T_{fi}|^2 \quad (2.3)$$

where  $k$  is the CM momentum of the outgoing neutron,  $\omega$  is the CM energy of the incoming photon, and  $T_{fi}$  is the transition matrix element

$$T_{fi} \propto \langle \psi_{np} | \epsilon(\lambda) \cdot \hat{\mathbf{J}}(\omega) | \psi_d \rangle. \quad (2.4)$$

Here  $|\psi_{np}\rangle$  is the wave function of the final state  $n$ - $p$  system and  $|\psi_d\rangle$  is the wave function of the initial state of the deuteron.  $\hat{\mathbf{J}}$  is the nuclear current operator which is ultimately written in terms of the electric and magnetic multipole operators and  $\epsilon(\lambda)$  is the photon polarization vector.

It is important to note that the TMEs are in general complex, so they can be expressed in terms of an amplitude and a phase as

$$T_{fi} = |T_{fi}| e^{i\delta_{fi}}. \quad (2.5)$$

In the case of no angular momentum mixing between the final states, the phases are conveniently given by the  $n$ - $p$  scattering phase shifts, which depend on the quantum numbers of the final state of the scattered wave function. This is a consequence of Watson's theorem [Knu99] and is valid as long as there are no other open reaction channels, which is true for photodisintegration below pion production threshold. The use of Watson's theorem becomes important during the TME analysis performed on the experimental data (see Section 6.3.4).

## 2.4 Potential Model Calculation

The results in this work will be compared to a potential model calculation from Schwamb and Arenhövel [Sch01a, Sch01b, Are04] which will be referred to here as the SAPM (Schwamb-Arenhövel Potential Model) calculation. In addition to all the possible polarization observables, the real and imaginary parts of the TME amplitudes have been calculated for all electric ( $EL$ ) and magnetic ( $ML$ ) multipoles up to  $L=4$ . The full calculation is valid from photodisintegration threshold up to about 500 MeV, though many of the effects included in it are negligible in the energy region of this experiment.

### 2.4.1 $NN$ Potential

In general, the calculation of the electromagnetic multipole TMEs in the non-relativistic framework begins by choosing a realistic  $NN$  potential for use in the non-relativistic two-body interaction Hamiltonian [Are85]. The realistic potential is used to construct the wave function of the deuteron, including both  $s$ - and  $d$ -wave components, and the wave functions of the scattered  $n$ - $p$  final state by solving the Schrödinger equation via numerical integration.

The strong force which the  $NN$  potential describes has several characteristic features, including long-range attraction, short-range repulsion, spin dependence, and the existence of a tensor component, to name a few. While early approaches to  $NN$  potentials were phenomenological, more recent potentials are constructed by modeling the strong force as originating through the exchange of mesons.

One example of an  $NN$  potential constructed from a meson-exchange model is the Bonn potential from [Els86, Els88] which was used in the SAPM calculation. This

potential included one-boson-exchange diagrams involving the  $\pi$ ,  $\eta$ ,  $\sigma$ ,  $\delta$ ,  $\omega$ , and  $\rho$  mesons [Els88]. In addition, the effects of virtual excitations of one or both nucleons into the  $\Delta$  isobar state were added by Schwamb and Arenhövel, as described in Section 2.4.4. It should be noted that the inclusion of isobar configurations in a coupled channel approach requires that the realistic potential be renormalized [Sch01c]. In addition, as opposed to similar previous calculations (e.g. [Are01]) which used static potentials, full retardation effects were included in this calculation.

Once the wave functions have been calculated using the  $NN$  potential, the desired nuclear current operators must be chosen and used to calculate the TMEs between these wave functions. The current operators used in the SAPM calculations can be distinguished as follows: non-relativistic one-body currents with Siegert operators (N), explicit meson exchange currents beyond the Siegert operators (MEC), explicit isobar configurations (IC), and relativistic contributions (RC). Each of these components will be described briefly here and in the following subsections.

## 2.4.2 One-body Currents with Siegert Operators (N)

The current operator,  $\epsilon(\lambda) \cdot \hat{\mathbf{J}}(\omega)$ , from Equation 2.4 is expanded in terms of the electric and magnetic multipoles operators  $\hat{T}_E^L$  and  $\hat{T}_M^L$ , defined as

$$\hat{T}_{E/M}^L = \int d^3x \hat{\mathbf{j}}(\mathbf{x}) \cdot \mathbf{A}_{E/M}^L \quad (2.6)$$

where  $\hat{\mathbf{j}}(\mathbf{x})$  is the current density and  $\mathbf{A}_{E/M}^L$  are the electric ( $E$ ) and magnetic ( $M$ ) multipole fields.  $\mathbf{A}_M^L$  and  $\mathbf{A}_E^L$  are given by

$$\mathbf{A}_M^L = i^L j_L(\omega r) \mathbf{Y}^L \quad (2.7)$$

and

$$\mathbf{A}_E^L = \frac{i}{\omega} \nabla \times \mathbf{A}_M^L, \quad (2.8)$$

where  $j_L(\omega r)$  are the Bessel functions and the  $Y^L$  are the vector spherical harmonics.

Siegert's theorem [Sie37] can then be used to write the current density for the electric multipole operators,  $\hat{T}_E^L$ , in terms of the charge density by invoking current conservation

$$\nabla \cdot \hat{\mathbf{j}}(\mathbf{x}) + i[\hat{H}, \hat{\rho}(\mathbf{x})] = 0, \quad (2.9)$$

where  $\hat{H}$  is the Hamiltonian, and  $\rho(\mathbf{x})$  is the charge density operator. This leaves the so-called Siegert operators which are written in terms of the charge density operators.

At this point, the form of the charge and current density operators are the only ingredients needed for the TME calculations. These are usually separated into the one- and many-body operators as

$$\hat{\rho}(\mathbf{x}) = \hat{\rho}_{(1)}(\mathbf{x}) + \hat{\rho}_{(2)}(\mathbf{x}) + \dots \quad (2.10)$$

$$\hat{\mathbf{j}}(\mathbf{x}) = \hat{\mathbf{j}}_{(1)}(\mathbf{x}) + \hat{\mathbf{j}}_{(2)}(\mathbf{x}) + \dots \quad (2.11)$$

For the part of the calculation described in this subsection, only the one-body currents are considered. One of the advantages of using Siegert operators is that the dominant part of the exchange currents are also implicitly included for the electric terms. They enter into the calculation through the commutator of the potential part of the Hamiltonian with the charge density (see Equation 2.9). Thus, the calculation of the dominant part of the TMEs can proceed without the form of the nuclear current density being explicitly known – only the charge density is necessary [Are91]. However, the explicit form of the current density is required for the magnetic multi-

poles and the parts of the electric multipoles not included in the Siegert operators. The next step in the calculation is the explicit inclusion of exchange currents, which is discussed in the next subsection.

### 2.4.3 Meson Exchange Currents (MEC)

With the inclusion of the one-body currents with Siegert operators, the leading contribution to the full nuclear current of Equation 2.4 has been included [Sch01a]. This is supplemented by including additional interaction currents which are effectively described as the exchange of mesons between the nucleons. The additional currents are necessary in order approximately satisfy current conservation [Are91].

These meson exchange currents (MEC) are included explicitly as effective operators in the SAPM calculation. This includes non-relativistic  $\pi$ ,  $\rho$ ,  $\gamma\pi\rho$  and  $\gamma\pi\omega$  currents, some of the diagrams for which are shown in Figure 2.3.

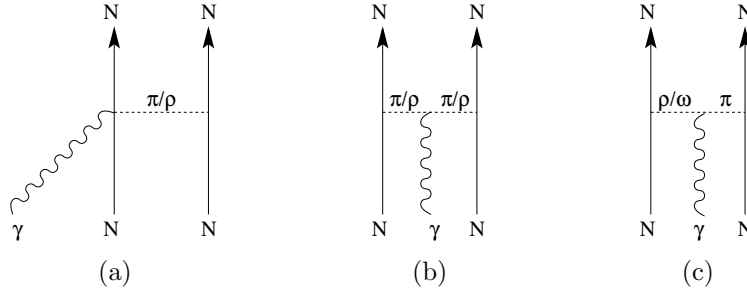


**Figure 2.3:** Some of the diagrams of meson exchange currents included [Sch01b] in the SAPM calculation. Note that these diagrams are shown in the static limit, whereas retardation has been incorporated in all MECs involving pions in the full calculation (see Section 2.4.5).

Because the Siegert operators have already implicitly included a large part of the MEC contribution (see Section 2.4.2), that part of the explicit MEC must be subtracted. This is called the Siegert correction [Fab76, Are91].

### 2.4.4 Isobar Configurations (IC)

Another contribution that is considered in the SAPM calculation is the possibility of the virtual excitation of the nucleons into isobar states (i.e. virtual  $\Delta$  excitations) within the deuteron. This contribution can affect both the  $NN$  interaction and the electromagnetic current and is most important in the region of the  $\Delta$  resonance. Figures 2.4(a) and 2.4(b) show a few of the diagrams which contribute.

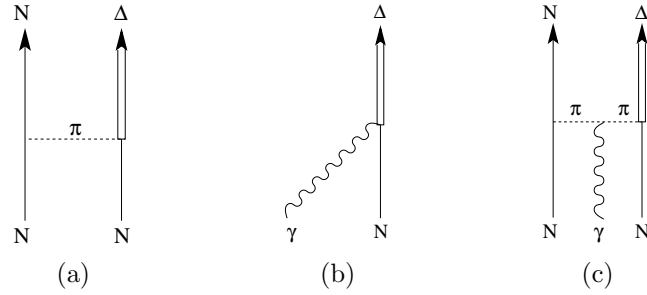


**Figure 2.4:** Diagrams of a few of the isobar contributions to (a) the  $NN$  interaction, (b) the electromagnetic current, and (c) the meson exchange currents.

The isobar contributions are accounted for by introducing isobars explicitly into the nuclear wave functions. The SAPM calculation employs a coupled-channel approach which is non-perturbative with respect to the  $N\Delta$  interaction [Sch07]. This requires the renormalization of the  $NN$  potential.

Isobars also play a role when they are present in the meson exchange current contributions. An examples of such an interaction is shown in Figure 2.4(c). These contributions are referred to as  $\Delta$ -MEC and are also included in the SAPM calculations.

### 2.4.5 Relativistic Currents (RC)

The importance of relativistic effects in deuteron photodisintegration below pion threshold was not realized until [Cam82]. This work showed that the relativistic spin-orbit contribution to the charge density played an important role in the forward (i.e.  $\theta = 0^\circ$ ) cross section, resolving a discrepancy between theory and experiment. More recently, relativistic effects have been shown to have a substantial influence in the GDH sum rule integrand below pion threshold [Are01] (see Section 2.6 for more).

Three classes of relativistic effects are distinguished by [Are91]:

1. relativistic effects in the wave function of an interacting system in its rest frame,
2. the boost of the wave function to a moving frame, which affects spin degrees of freedom and internal structure, and
3. adding terms of relativistic order to the current operator.

However, [Are91] notes that each of these classes are interrelated and require a consistent treatment.

The most dominant relativistic effect by far is the spin-orbit current, which has already been mentioned. This is included in the calculation by adding the appropriate terms to both the charge and current operators, though the spin-orbit effects are seen primarily through the inclusion of the spin orbit terms in the charge density operators which enter into the Siegert operators [Wil88].

Another relativistic effect included in this calculation is retardation in the meson exchange currents. This arises because the theory of relativity requires that the velocity of the propagation of an interaction must be finite rather than instantaneous [Sch01c]. The retarded currents are also required since retardation already appears in the  $NN$  potentials.

The effects resulting from boosting the rest-frame deuteron wave functions, such as Lorentz contraction of the wave function were omitted from the SAPM calculation and are expected to be negligible in the energy region of this experiment [Sch07]. The calculation also includes off-shell effects in the one-body current which arise from the fact that the nucleons involved in photodisintegration are, by virtue of being bound inside the deuteron, off the mass shell. The details about what is meant by off-shell effects can be found in [Sch01a]. These effects play a negligible role in the calculation at these energies.

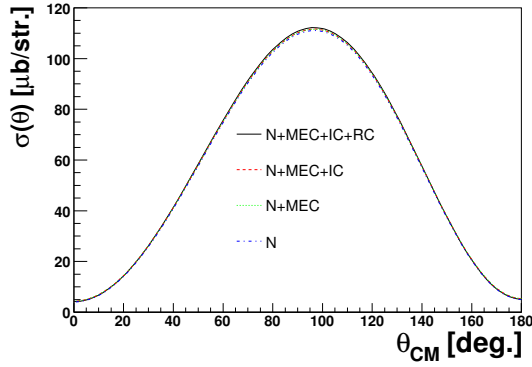
### 2.4.6 SAPM Predictions

Now that all the pieces of the calculations have been summarized, the predictions of the calculation can be presented. Figure 2.5 shows the unpolarized differential cross section and the linear analyzing power for the energies in this experiment.

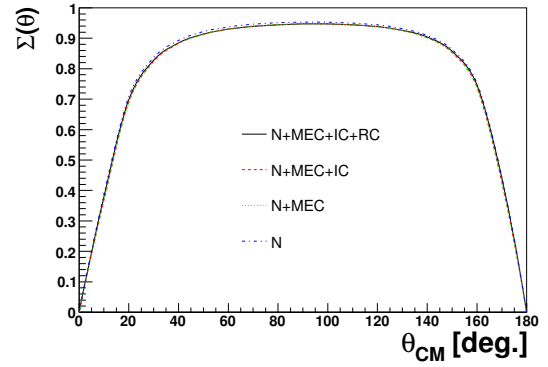
Four curves are shown for each subfigure, corresponding to variations in the calculation just described (see the caption for details). The curves are nearly indistinguishable, indicating that the one-body current with Siegert operators is sufficient to describe these observables at these energies. As is discussed in Section 2.6, this is not the case for the helicity dependent cross section difference which appears in the GDH Sum Rule integrand, where relativistic effects play an important role.

## 2.5 Effective Field Theory

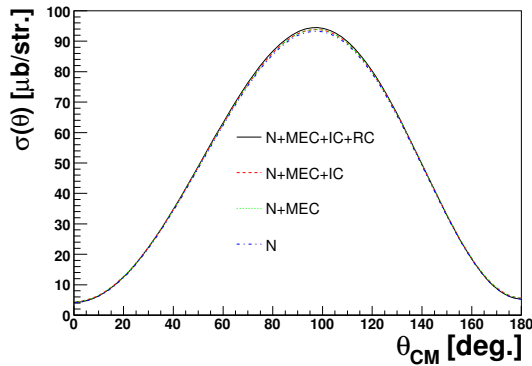
Another approach to calculations for the  $d(\vec{\gamma}, n)p$  reaction is through effective field theory (EFT). Quantum Chromodynamics (QCD) is the theory currently believed to describe interactions involving the strong force. QCD is written in terms of the



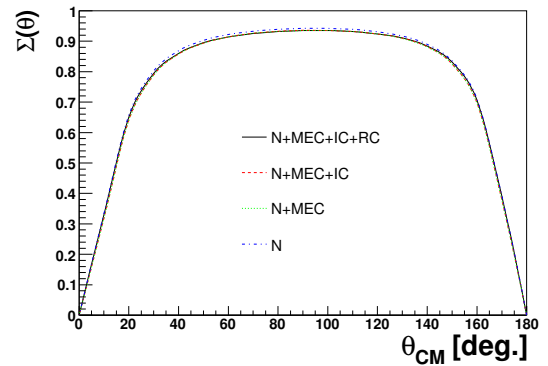
(a) 14 MeV Unpolarized Cross Section.



(b) 14 MeV Analyzing Power.



(c) 16 MeV Unpolarized Cross Section.



(d) 16 MeV Analyzing Power.

**Figure 2.5:** Theoretical predictions of the SAPM calculations for the observables of this experiment. Although nearly indistinguishable, there are four variations of the calculation being shown. The solid black curve is the full calculation (N+MEC+IC+RC), dashed red corresponds to N+MEC+IC, dotted green corresponds to N+MEC, and dash-dotted blue corresponds to N.

quarks which make up hadrons and the gluons which mediate the force between them. Because it is presently too difficult to use the full QCD Lagrangian in calculations in the energy regime relevant to this experiment, EFT techniques can be used to simplify the problem by writing a Lagrangian in terms of the effective degrees of freedom of the interaction.

The effective Lagrangian is constructed by integrating out the quark/gluon and any other higher energy degrees of freedom, leaving the relevant hadronic degrees of

freedom [Hol95]. The effective Lagrangian is also constructed such that the symmetries of the QCD Lagrangian are preserved.

The techniques of EFT can only be applied when there is adequate separation of scales [Rup00]. This is the case in  $n$ - $p$  capture at low energies, since the expansion terms in the calculation, such as the nucleon CM momentum, are much smaller than the mass of the pion [Rup00]. The effects of the particles that are integrated out of the theory are contained in a perturbative expansion of the remaining operators, with an expected expansion parameter that goes as  $Q/m_\pi$  [Rup00]. One advantage of EFT calculations is that uncertainties in the calculations can be estimated by observing the size of the first excluded term in the perturbative expansion.

Two such EFT calculations have been performed for the  $n$ - $p$  capture reaction at energies relevant to Big-bang nucleosynthesis [Che99, Rup00]. They were performed in the context of pion-less EFT, where the pions and other heavier degrees of freedom were integrated out of the theory leaving only nucleons and photons [Che99].

Via the principle of detailed balance, the  $n$ - $p$  capture reaction can be related to the inverse deuteron photodisintegration reaction by [Che99]

$$\sigma(\gamma d \rightarrow np) = \frac{2M_N}{3E_\gamma^2}(E_\gamma - B) \sigma(np \rightarrow d\gamma), \quad (2.12)$$

where  $M_N$  is the isospin averaged value of the nucleon mass,  $B$  is the deuteron binding energy, and  $E_\gamma$  is the energy of the incident  $\gamma$ -ray in the lab. Therefore, the  $n$ - $p$  capture reaction contains the same physical information as the deuteron photodisintegration reaction.

However, the present calculations are most accurate for low  $n$ - $p$  capture center-of-mass energies, and are significantly less accurate at the energies of this experiment.

There is hope that the EFT calculations will soon be expanded to the energy range of this experiment and for the relevant observables [Gri07, Par07]. However, at this point in time, there are no EFT calculations with which to compare the results of this experiment.

## 2.6 The GDH Sum Rule

In general, photo-absorption sum rules relate the static properties of a target particle to its excitation spectrum. In the case of the Gerasimov-Drell-Hearn (GDH) sum rule for the deuteron, the anomalous magnetic moment of the deuteron is related to its helicity dependent photo-absorption cross section difference,  $\sigma_P - \sigma_A$ . The form of the GDH sum rule has already been presented in Equation 1.3.

The anomalous magnetic moment,  $\kappa$  is defined in terms of the total nuclear magnetic moment operator

$$\begin{aligned}\vec{M} &= \mu \vec{S} \\ &= (Z + \kappa) \frac{e}{m} \vec{S},\end{aligned}\tag{2.13}$$

where  $\mu$  is the total nuclear magnetic moment,  $Z$  is the proton number, and  $e$  is the fundamental charge. The anomalous part of the magnetic moment arises from the internal structure of the composite particle.

Like the differential cross section in Equation 2.3,  $\sigma_P - \sigma_A$ , can be expanded in terms of the TME amplitudes of the reaction (see Equation 1.4). Therefore, if the TME amplitudes are extracted from the observables accessible with unpolarized target and linearly polarized beam, then  $\sigma_P - \sigma_A$  can be indirectly accessed through those amplitudes. Section 6.5 describes how that is done.

### 2.6.1 Overview of the Derivation

The GDH sum rule was derived independently in the same year by Gerasimov [Ger66] and then by Drell and Hearn [Dre66] for spin 1/2 particles. It has since been generalized to arbitrary spin (see for example, [Fri77]). The sum rule is derived using fundamental assumptions such as Lorentz invariance, gauge invariance, unitarity, crossing symmetry, and causality of the forward Compton scattering amplitude of the particle.

The two inputs needed to derive the sum rule [Are99] are the low energy theorem (LET), which follows from Lorentz and gauge invariance, and the assumption of an unsubtracted dispersion relation involving the difference in the forward Compton scattering amplitudes for spins of target and photons parallel and anti-parallel, which is a statement of causality [Gia03].

The LET is provided by Low [Low54] and Gell-Mann and Goldberger [Gel54] for spin 1/2 particles, and has been generalized to other spins by, for example, [Fri77]. The LET for the forward Compton scattering amplitude,  $T_\lambda(\omega)$ , for photons of energy  $\omega$  on a target with spin  $S$  parallel or anti-parallel to the direction of the incoming photon is given by [Are99]

$$T_\lambda(\omega) = -\frac{e^2 Z^2}{m} + \lambda \kappa^2 \frac{e^2}{m^2} S \omega + O(\omega^2), \quad (2.14)$$

where  $\lambda$  describes the polarization of the beam which will be 1 or -1 for parallel and anti-parallel configurations. It is worth noting here that the correct form of the second term in the amplitude is only obtained if relativistic contributions are properly included [Are97, Fri77]. The importance of this will be seen in the results of the  $\sigma_P$ - $\sigma_A$  calculation shown below.

The second input is, by invoking causality, the assumption of an unsubtracted dispersion relation involving the difference between the forward Compton amplitudes for spins parallel and anti-parallel

$$\text{Re}f(\omega) = \frac{1}{\pi} P \int_{-\infty}^{\infty} \frac{\text{Im}f(\omega')}{\omega' - \omega} d\omega'. \quad (2.15)$$

$f(\omega)$  in this expression is the difference in the forward Compton amplitudes,  $T_1(\omega) - T_{-1}(\omega)$ . The no-subtraction assumption amounts to assuming that the spin dependence of the cross section decreases with higher  $\gamma$ -ray energies, such that  $\sigma_P - \sigma_A$  converges more quickly than the unpolarized cross section [Are99].

Using the optical theorem, which is a consequence of unitarity, the imaginary part of the amplitude can be written in terms of the photo-absorption cross section. By crossing symmetry<sup>1</sup> and knowing that  $f(\omega)$  is non-zero only above photodisintegration threshold, we are left with

$$T_1(\omega) - T_{-1}(\omega) = \omega \frac{1}{2\pi^2} \int_{\omega_{th}}^{\infty} \frac{\sigma_P(\omega') - \sigma_A(\omega')}{\omega'^2 - \omega^2} \omega' d\omega'. \quad (2.16)$$

The expression becomes the GDH sum rule (Equation 1.3) by taking the derivative with respect to  $\omega$  on both sides and evaluating the remaining expression at  $\omega=0$ .

## 2.6.2 GDH for the Deuteron

The deuteron's anomalous magnetic moment is  $\kappa_d = -0.143$  [Moh00], which gives a total sum rule value of  $I_{GDH}^d = 0.65 \mu\text{b}$ . This  $I_{GDH}$  value is significantly smaller than what is obtained using the anomalous magnetic moments of the proton and neutron individually. Those values are  $I_{GDH}^p = 204.8 \mu\text{b}$  and  $I_{GDH}^n = 233.2 \mu\text{b}$ .

---

<sup>1</sup>Crossing symmetry dictates that  $f(\omega) = f(-\omega)$ .

Above pion threshold, the absorption processes on the deuteron can be reasonably approximated as quasi-free processes involving the nucleons [Are99]. Thus, in the energy region above pion threshold, the GDH contribution can be estimated as the sum of the GDH sum rule values for the proton and neutron, which is  $438 \mu\text{b}$ . If the very small sum rule value for the deuteron is to be realized, the contribution below pion threshold must be roughly of the same magnitude and negative.

Below pion threshold, the only available absorption channel is photodisintegration. The large negative contribution needed to satisfy the sum rule is provided by the magnetic dipole (M1) transition to the  $^1s_0$  outgoing state<sup>2</sup>, which is accessible only in the anti-parallel configuration of the spins and which dominates the reaction near photodisintegration threshold. The triplet  $p$ -wave states resulting from electric dipole (E1) transitions quickly begin to dominate the reaction just above threshold, but their contributions to the GDH sum rule nearly cancel each other at low energies.

### 2.6.3 SAPM Prediction

The SAPM prediction for  $\sigma_P - \sigma_A$  from threshold to about 500 MeV has already been presented in Figure 1.2. A closer look at the cross section difference in the energy region of this experiment shows that the relativistic currents play a large role. Figure 2.6 shows  $\sigma_P - \sigma_A$  for the variations of the calculation discussed in Section 2.4. As noted in [Are97], the size of the effect in this observable due to the inclusion of relativistic currents is not surprising in view of the fact that the term linear in  $\omega$  in the LET (Equation 2.14) is obtained correctly only if the relativistic contributions are properly included. As discussed in Section 2.4.5, the most significant of the relativistic contributions, especially at these energies, is the inclusion of the relativistic spin orbit

---

<sup>2</sup>The notation used here is  $^{2s+1}l_J$ , where  $s$  is the channel spin,  $l$  is the orbital angular momentum, and  $J$  is the total angular momentum. See Section 1.2.3.

current.

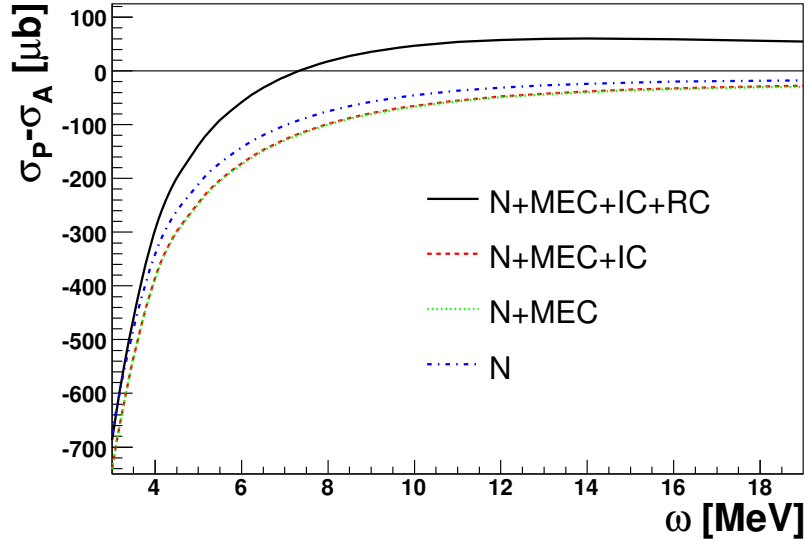


**Figure 2.6:** GDH integrand predictions for SAPM calculations for the deuteron photodisintegration channel for variations of the calculations. The various calculations are labeled in the legend on the figure. The N+MEC and N+MEC+IC are curves are nearly indistinguishable with this scale.

The relativistic effects play an important role in the total sum rule value since they dramatically change the shape of  $\sigma_P - \sigma_A$  at energies less than 100 MeV, making it positive much lower in energy than expected by calculations without the relativistic effects. Also note from Figure 2.6 that the theory predicts the meson exchange currents beyond the Siegert operators to play a very small role, and as expected at these energies the contribution from isobar currents is negligible.

# Chapter 3

## Description of the Experiment

### 3.1 Introduction

A measurement was performed of the differential  $d(\vec{\gamma}, n)p$  cross section using linearly polarized  $\gamma$ -rays incident on a  $D_2O$  target. This chapter outlines each of the components that were necessary to perform the measurement. Section 3.2 describes the production of linearly polarized  $\gamma$ -rays at the High Intensity  $\gamma$ -ray Source (HI $\gamma$ S). Section 3.3 provides an overview of the HI $\gamma$ S collimator hut and target room. The systems in place to monitor the beam are discussed in Section 3.4. The outgoing neutrons were detected using the Blowfish detector array, which is described in Section 3.5. Finally, the electronics (Section 3.6) and data acquisition (Section 3.7) systems are summarized.

### 3.2 The High Intensity $\vec{\gamma}$ -ray Source (HI $\gamma$ S)

The High Intensity  $\vec{\gamma}$ -ray Source is located on the campus of Duke University at the Duke Free Electron Laser Laboratory (DFELL) and operates through a collaboration between the DFELL and the Triangle Universities Nuclear Laboratory (TUNL). The  $\gamma$ -rays are produced via intra-cavity Compton backscattering of a free-electron laser (FEL) with an electron beam circulating in a storage ring [Lit97]. This technique saw its first-ever implementation at the DFELL after being proposed there by

V. N. Litvinenko.

The major accelerator systems of the DFELL that are necessary to produce the nearly 100% linearly polarized and nearly mono-energetic  $\gamma$ -rays are the LINAC injector, the Duke Storage Ring, and the OK-4 Optical Klystron. Recently, an upgrade to the facility saw the installation of a new Booster Injector and the OK-5 Optical Klystron, both of which were not used for this experiment. The upgrade is discussed briefly in Section 3.2.4.

### 3.2.1 The Duke OK-4 Free Electron Laser (FEL)

The FEL's theoretical development began at Stanford University through the studies of J. M. J. Madey [Mad71]. An FEL produces a highly-tunable monochromatic laser beam by means of the coherent radiation of a micro-bunched electron beam in an electromagnetic field.

The description of the Duke OK-4 FEL provided here will give special attention to the operation of the FEL during the time of the  $d(\vec{\gamma}, n)p$  measurement (i.e. before the recent upgrades). The OK-4 FEL is designed to produce ultra-violet and soft X-ray photon beams. An overview schematic of the DFELL can be found in Figure 3.1.

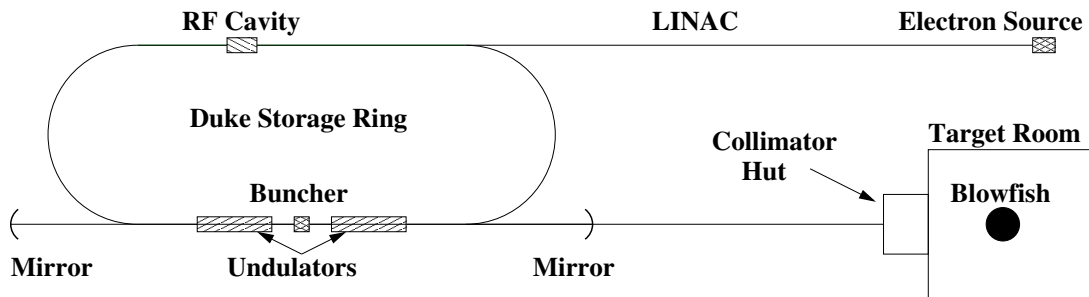


**Figure 3.1:** The layout of the DFELL. The parts of the lab which are relevant to  $\gamma$ -ray production are labeled. Drawing is not to scale.

Electrons were first accelerated to an energy of 270 MeV by means of a linear accelerator (LINAC), and were then injected into the Duke Storage Ring (DSR). The Storage Ring consists of two 34-meter straight sections connected by two arcs of length 19.52 m each, giving a total circumference of 107.46 m. The ring contains 40 dipole magnets (20 on each arc) for beam steering and 64 quadrupole magnets for beam focusing. A radio-frequency (RF) cavity is located on the first straight section and was used to accelerate and sustain the electron beam energy to a maximum of 1.2 GeV. The RF cavity is also used to restore energy to the electrons which is radiated away in the form of synchrotron radiation while the electrons travel through the arc sections. The electrons circulate in the ring with a frequency of 2.79 MHz.

The other straight section houses the components of the Duke OK-4 FEL [Wu 96, Lit96], which was invented by Vinokurov and Skrinky [Vin77]. The optical cavity of the Duke FEL is defined by two highly reflective mirrors located on the axis of the straight section a distance of 53.73 m apart. This distance is chosen so that it is one-half the circumference of the ring, the importance of which is explained below. The OK-4 magnetic system consists of two undulators and a buncher magnet. The undulators use periodically spaced electromagnets to create magnetic fields which alternate, up and down, in the vertical direction. Each undulator has a length of 3.4 meters with a period of 0.10 meters and each can operate with magnetic fields from 0 to 5.36 kG. Between the two undulators is a buncher magnet which consists of one period of an undulator that operates between 0 and 12 kG.

When an electron bunch is injected into the storage ring, it is first “ramped” up to the desired energy<sup>1</sup>. As an electron bunch passes through the undulators, it is forced to “wiggle” in the horizontal direction due to the alternating vertically

---

<sup>1</sup>For  $\gamma$ -ray production, the desired energy is determined by the kinematics of the Compton scattering collision.

oriented magnetic fields. The resulting radiated photons then travel to and reflect off the downstream mirror, pass back through the length of the optical cavity and reflect from the upstream mirror. Because the length of the optical cavity is one-half the circumference of the ring, the relativistic electron bunch reenters the straight section at the same time as the photons which they previously radiated do.

The photons and electrons then co-propagate through the straight section of the ring. The electrons that enter the first undulator are distributed throughout the bunch. These electrons interact with the electromagnetic fields of the photons, and depending on the phase between the electrons within the bunch and the optical field, the electrons gain or lose energy. This happens because the electric field of the photons causes the electrons to be accelerated in the transverse direction. When this transverse motion occurs in the presence of the vertical magnetic field of the undulators the electrons experience a longitudinal force which causes them to lose or gain energy. This effect is called the pondermotive force [Mar85, Sch00]. Thus, a periodic pattern of higher energy and lower energy micro-bunches develops within the full bunch.

After leaving the first undulator, the electrons enter the buncher magnet, whose strong magnetic field alters the path of the electrons. Because the path length of higher energy electrons will be shorter than that of lower energy electrons, the higher energy electrons have a chance to “catch up” to the slower ones in front of them and the lower energy electrons “fall back” to the ones behind them. Thus, a beam with modulation in energy becomes a micro-bunched beam in space with the spacing between micro-bunches being approximately equal to the wavelength of the photons. Figure 3.2 shows an idealized schematic of how these micro-bunches are created. These smaller electron bunches then enter the second OK-4 undulator where they

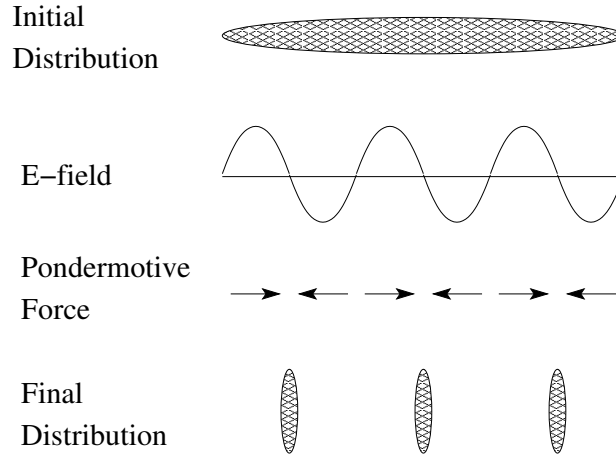


**Figure 3.2:** Idealized schematic of how the pondermotive force experienced by the electrons as they pass through the first undulator and the buncher magnet takes an electron bunch and further bunches it into smaller sub-bunches. This idealized level of sub-bunching does not occur in reality. Figure was adapted from [Sch00].

oscillate in phase with one another, producing coherent light. Table 3.1 summarizes some of the operating parameters for FEL beam production.

### 3.2.2 $\gamma$ -ray Production

$\gamma$ -ray production requires that a second electron bunch be added to the storage ring at a distance exactly half the circumference around the ring from the first bunch. As the second electron bunch passes through the optical cavity,  $\gamma$ -rays are created by a head-on collision between this second bunch and the FEL photons which were radiated and amplified by the first electron bunch. The Compton backscattering collision occurs in a field free region of the optical cavity. Since the electrons are highly relativistic and the FEL photons are relatively low in energy, the resulting  $\gamma$ -rays are produced in a tight cone along the direction of the electron beam.

Through the conservation of momentum and energy, the energy of a Compton

Electrons:	Energy Range	0.23-1.2 GeV
	Energy Resolution ( $\Delta E/E$ )	$\sim 5.8 \times 10^{-4}$ at 1 GeV, zero current limit
	Maximum Current	270 mA, multiple bunches
Photons:	Energy Range	1.5 - 6 eV (800 - 194nm)
	Linewidth ( $\Delta\lambda/\lambda$ )	$10^{-2}$ - $10^{-4}$
	Intra-cavity Power	10-300 W
Storage Ring:	Vacuum	$\sim 10^{-10}$ Torr
	Revolution Frequency	2.79 MHz

**Table 3.1:** Realized Duke FEL operating parameters as of 2007.

scattered photon after a head-on collision is given by

$$E_\gamma = E_\lambda \frac{1 + \beta}{1 + E_\lambda/E_e - (\beta - E_\lambda/E_e) \cos \theta}, \quad (3.1)$$

where  $E_\gamma$  is the scattered  $\gamma$ -ray energy,  $E_e$  and  $E_\lambda$  are the initial energies of the electron and FEL photon respectively,  $\beta$  is the electron velocity in units of the speed of light, and  $\theta$  is the angle between the initial electron momentum and the final  $\gamma$ -ray momentum (see Figure 3.3).

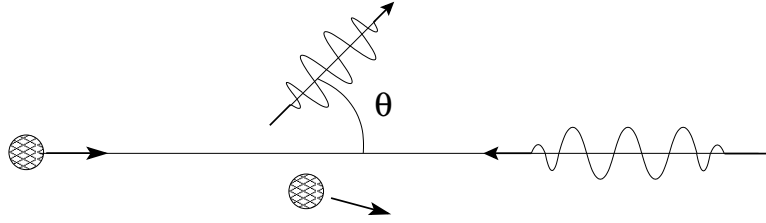


**Figure 3.3:** Compton backscattering of FEL photons by electrons in the Storage Ring.  $\theta$  is the angle between the original electron momentum and the scattered  $\gamma$ -ray momentum.

The  $\gamma$ -ray energy can be further approximated when the relativistic parameter

$\gamma = E_e/m_e c^2 \gg 1$  and when  $\theta$  is small as [Lit97]

$$E_\gamma \cong \frac{4\gamma^2 E_\lambda}{1 + (\gamma\theta)^2 + 4\gamma E_\lambda/m_e c^2}, \quad (3.2)$$

where  $m_e$  is the mass of the electron. These conditions are always true in the Compton backscattering collisions at the DFELL.

The  $\gamma$ -ray energy is peaked at  $0^\circ$  and depends strongly on the angle  $\theta$ . Equation 3.1 was used to generate a plot of the  $\gamma$ -ray energy as a function of scattered  $\gamma$ -ray angle  $\theta$  in Figure 3.4 for 2.79 eV photons scattered from 585.0 MeV electrons. These are conditions similar to the ones used to produce 14 MeV  $\gamma$ -rays in this experiment. For the Duke storage ring, the angular spread and energy spread of the beam is small, allowing the use of a collimator placed a large distance from the collision point to define the energy resolution of the beam.

### 3.2.3 Beam Properties

HI $\gamma$ S beams are extremely useful for nuclear physics experiments because of several features that distinguish them from other  $\gamma$ -ray facilities. Beams at HI $\gamma$ S have high beam intensities, tunable energies, small and selectable beam energy spreads, nearly 100% beam polarization, and a useful time structure.

#### Beam Intensity

Beams produced at bremsstrahlung facilities can have very high intensities. However, the  $\gamma$ -ray energies are produced in a continuum ranging from the electron beam energy down to zero, with the intensity increasing as the energy decreases. The wide range of  $\gamma$ -ray energies requires the use of a tagger which measures the energy of the scattered electron in order to deduce the energy of the associated  $\gamma$ -ray. Taggers are

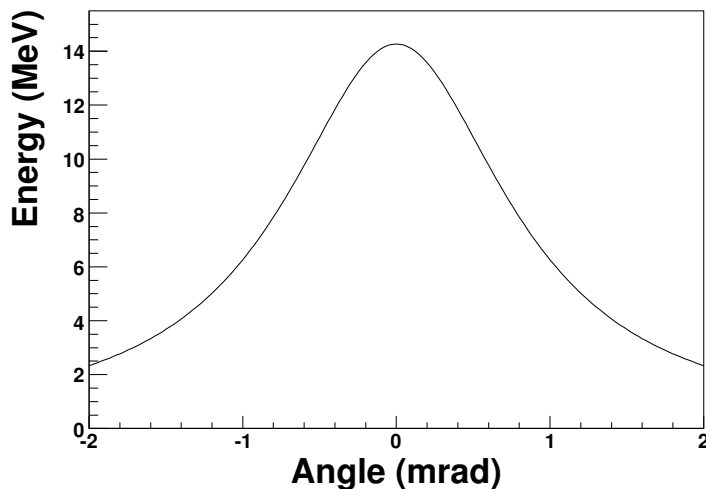


**Figure 3.4:** Energy-angle correlation for  $\gamma$ -rays generated by scattering 445 nm (2.79 eV) FEL photons off 585 MeV electrons, resulting in photons of about 14 MeV. Plot was generated using Equation 3.1. For a 1-inch collimator placed about 60 meters from the collision point, the edges of the collimator would correspond to approximately 0.2 mrad. However, it must be noted that Equation 3.1 does not take into account effects such as the electron energy spread and spatial extent.

count rate limited and thus not all of the  $\gamma$ -rays produced at such facilities can be used. The angular dependence of the energy of HI $\gamma$ S beams makes tagging unnecessary, leaving a larger useable intensity for a given  $\gamma$ -ray energy. In addition, the small energy spread of HI $\gamma$ S beams means that there are no unwanted backgrounds generated by  $\gamma$ -rays of different energies.

Other facilities exist that employ Compton scattering of photons from an external laser by an electron beam. The advantage of the HI $\gamma$ S facility is that intra-cavity Compton scattering is used for  $\gamma$ -ray production. Thus the intensity of the FEL photon beam used in the Compton scattering collision is several orders of magnitude higher than what is achievable by an external laser, resulting in higher  $\gamma$ -ray intensities.

At the time of this experiment, HI $\gamma$ S beams produced total intensities on the

order of  $10^7$ - $10^8$   $\gamma/s$ . After collimation, intensities on the order of  $10^5$ - $10^6$   $\gamma/s$  on target were used during production runs. Beam intensities will be increased once the upgraded facility (Section 3.2.4) becomes fully operational. These high intensities allow experiments which were once limited by reaction count rate to be performed. It also allows reactions with reasonable cross sections to be measured rather quickly. For example, the data in this experiment were obtained in approximately three 14-hour days of running.

### **Beam Energy Spread**

As mentioned in Section 3.2.2, the energy of the  $\gamma$ -rays at HI $\gamma$ S are angle dependent because of the kinematics of the Compton scattering interaction. This allows collimation to be used to select only the beam energies desired and thus defines the energy spread. And, as mentioned above, this also makes the use of a tagger for energy determination unnecessary.

A nearly mono-energetic beam is very useful, especially for experiments that seek to excite states that are located in a densely populated part of an excitation spectrum without exciting nearby states. It is also advantageous for studying reactions with cross sections that change rapidly with energy.

### **Nearly 100% Beam Polarization**

Because the electrons in the Storage Ring are forced to “wobble” in the horizontal direction while interacting with the magnetic field of the OK-4 FEL, the resulting FEL photons are linearly polarized in the horizontal plane. After the photons scatter to become  $\gamma$ -rays, that polarization is almost entirely retained [Lit97].

The polarization-dependent cross section for the scattering reaction in the electron

rest frame is given by [Ber71]

$$\frac{d\sigma}{d\Omega} = \frac{1}{4} r_e^2 \left( \frac{E'}{E} \right)^2 \left( \frac{E'}{E} + \frac{E}{E'} - 2 + 4\cos^2\Theta \right), \quad (3.3)$$

where  $r_e$  is the classical radius of the electron,  $E$  and  $E'$  are the incident and scattered photon energies, and  $\Theta$  is the angle between the incident and scattered photon polarization vectors. The polarization of the beam,  $P_\gamma$ , is defined as

$$P_\gamma = \frac{\sigma(\Theta = 0^\circ) - \sigma(\Theta = 90^\circ)}{\sigma(\Theta = 0^\circ) + \sigma(\Theta = 90^\circ)}. \quad (3.4)$$

Using this expression,  $P_\gamma$  can be expressed as a function of photon scattering angle in the electron rest frame as shown in figure Figure 3.5. Recall that an angle of  $0^\circ$  corresponds to a photon which is completely backscattered in the lab frame.

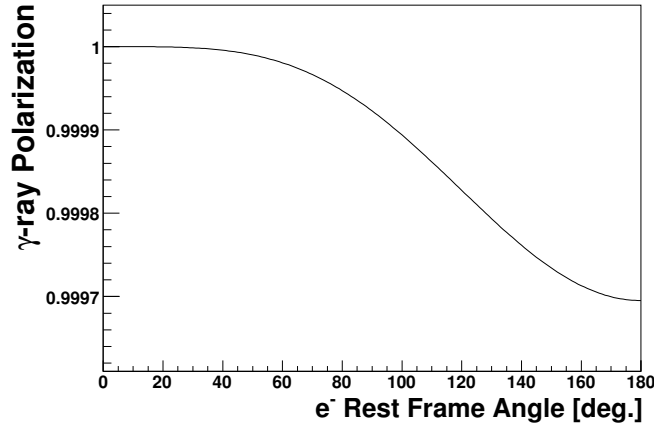


**Figure 3.5:** Beam polarization as a function of photon scattering angle in the electron rest frame. This was produced assuming 445 nm (2.79 eV) FEL photons are scattered off 585 MeV electrons, resulting in photons of about 14 MeV.

Note that the polarization of the  $\gamma$ -rays drops off with increased deviation from the axis defined by the electron beam. Even if the angular acceptance of HI $\gamma$ S beams

covered the full angular range in Figure 3.5, the magnitude of the decrease is no more than about 0.0003 (0.03%), making deviations from 100% polarization negligible for the conditions of this experiment. It should be noted that deviations of the angle of the axis of polarization from the horizontal plane can give the appearance of an effective de-polarization of the beam. Our measurement allows any such deviation to be measured, as described in Section 3.4.3.

A nearly 100% linearly polarized beam is useful for many studies in nuclear physics. Polarized beams grant access to spin dependent observables which are un-accessible with unpolarized beams, allowing for the study of the spin structure of the target which is being probed. For example, the spin dependent observable measured in this experiment is the analyzing power. This observable is a measure of the difference between the cross section for neutrons emitted in the plane of polarization and in the plane perpendicular to the polarization (see Equation 1.1).

### **Time Structure of the Beam**

Because of the nature of  $\gamma$ -ray production at HI $\gamma$ S, the beam has a definite time structure which can be exploited. A burst of  $\gamma$ -rays is produced each time a collision happens in the optical cavity. Because the frequency of the Storage ring is 2.8 MHz per bunch, a collision occurs every 179 ns in the two-bunch mode of operating. This structure allows time-of-flight techniques to be employed to distinguish beam-related events from room background. In addition, particle identification and energy determination (for massive particles) can be performed using the timing information. For example, this experiment used differences in flight times for particles traveling from the target to the detectors to distinguish between  $\gamma$ -rays which were scattered from the target and neutrons which resulted from the photodisintegration reaction.

### 3.2.4 The Recent HI $\gamma$ S Upgrade

The HI $\gamma$ S facility recently underwent an upgrade in order to achieve four goals [Wu07]:

1. significantly increase the  $\gamma$ -ray flux (by more than one order of magnitude) at energies  $\leq 20$  MeV,
2. make high energy  $\gamma$ -ray production possible from 20 MeV to as high as 158 MeV with total intensities on the order of  $10^8$   $\gamma/s$  or greater,
3. allow circularly polarized  $\gamma$ -rays to be produced, and
4. improve beam stability and efficiency, as well as make “flat-top” flux production possible through the continuous electron (“top-off”) injection mode.

The major components of the upgrade needed to achieve these goals were the Booster Injector, a new RF Cavity, and the OK-5 FEL helical undulator system.

#### **Booster Injector**

The Booster Injector is necessary in order to control beam lifetimes at higher beam energies. At energies above 20 MeV, the electrons which participate in the Compton backscattering collision lose so much energy in the recoil that they are unable to be salvaged and recirculated around the Storage Ring. Thus, the electron current in the Storage Ring decreases quickly with time, requiring more frequent stoppages of the beam in order to re-inject electrons into the ring.

In order to overcome this problem, a new Booster synchrotron was developed and installed. It receives electrons from the LINAC and by means of an RF cavity it quickly ramps up the electron beam energy to the operating energy of the Storage Ring. The Booster can accelerate electrons to any energy between 0.23 and 1.2 GeV

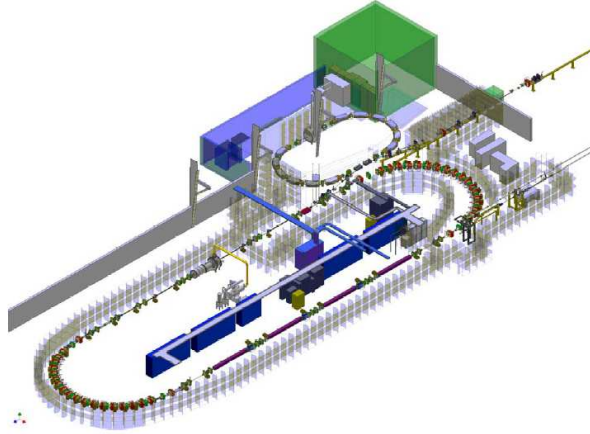


**Figure 3.6:** The layout of the DFELL after the HI $\gamma$ S upgrade.

before injecting into the Storage Ring. This allows electrons to be transferred to the Storage Ring on a relatively continuous basis to replenish lost electrons. Thus the Booster Injector removes the need for frequent beam stoppages.

### **RF Cavity**

Already part of the Storage Ring during this experiment, the new RF Cavity is equipped with higher-order-modes (HOMs) damping. These HOMs create beam instabilities which limit the maximum stored beam current. The new RF Cavity creates a more stable electron beam in the Storage Ring, especially when the Ring is operating with multiple bunches.

## OK-5

Many future HI $\gamma$ S experiments require circularly polarized  $\gamma$ -rays in order to give access to a different set of spin-dependent observables. The current OK-4 optical klystron provides only linearly polarized  $\gamma$ -rays. The newly installed OK-5 system is equipped with electromagnets in a configuration that causes the electrons to “wobble” in a helical pattern, thus radiating circularly polarized FEL photons, which when scattered by a second electron bunch yield circularly polarized  $\gamma$ -rays.

Full operations of the upgraded facility will begin in the Summer of 2007. The operating parameters and performance expectations are found in Table 3.2.

OK-5 Photons:	Energy Range	1.55-9.84 eV
	Linewidth	$10^{-2}$ - $10^{-4}$
	Max Intra-cavity Power	> 300 W
$\gamma$ -rays:	Energy Range	2-158 MeV <sup>(a)</sup>
	Total Flux ( $E_\gamma = 10$ MeV)	> $10^9$ $\gamma$ /s
	Total Flux ( $E_\gamma = 21$ -65 MeV)	> $2 \times 10^8$ $\gamma$ /s <sup>(b)</sup>
	Circular & Linear polarizations	> 90%

**Table 3.2:** A few of the expected upgraded HI $\gamma$ S operating parameters. The total fluxes listed represent examples of expected fluxes at particular energies.

<sup>(a)</sup>Maximum energy limited by availability of appropriate mirrors.

<sup>(b)</sup>Appropriate mirrors are available commercially, but have not been used for  $\gamma$ -ray production at energies above 40 MeV.

## 3.3 HI $\gamma$ S Collimator Hut and Target Room

### 3.3.1 Collimator Hut

For HI $\gamma$ S beams, a collimator is placed in the HI $\gamma$ S collimator hut about 60 meters from the collision point in the optical cavity (see Figure 3.1). Upon entering

the collimator hut, the beam leaves the vacuum beam pipe and from that point travels through air for the remainder of its existence. Figure 3.7 shows a schematic of the Collimator Hut. Inside the collimator hut, the beam first encounters two Cu pre-collimators in order to clean up the beam before encountering the primary collimator. The pre-collimators are 11.4 cm (4.5 in) long with an outer diameter of 10.1 cm (4.0 in). This length of Cu attenuates about 97% of any beam which strikes it at the energies of this experiment. The hole sizes were selected to be 3.8 cm (1.5 in) and 3.1 cm (1.25 in) during this experiment. In general, there are several pre-machined hole sizes from which to choose.

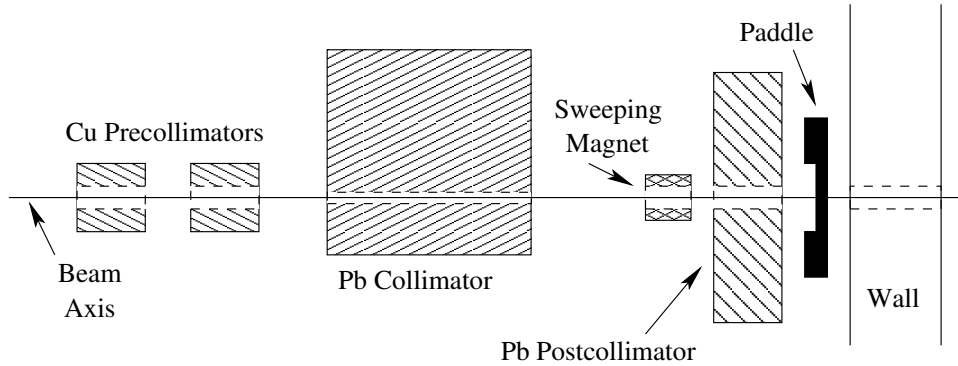


**Figure 3.7:** Schematic of the Collimator Hut at HI $\gamma$ S. Not to scale. See text for dimensions of the collimation systems.

The beam is then collimated to its final size by passing through the primary collimator. The collimator system consists of a 30.5 cm x 30.5 cm x 10.1 cm Pb block with six holes of various sizes drilled through it. The parts of the beam which strike the primary collimator are attenuated by roughly 9 orders of magnitude at these energies. The system is attached to a platform on rails and the platform is now connected to an actuator that is controlled remotely. The actuator system was not in place at the time of this experiment, so the collimator was positioned by hand (see Section 3.3.3). The collimator is selected by placing the desired hole size in the path

of the beam.

A 2.5 cm (1 inch) diameter collimator was used during production runs, which produced an energy spread in the beams of approximately 5% (see Section 4.4.2). A 1.3 cm (0.5 inch) collimator was employed during runs devoted to measuring the centroid energy of the beam. The smaller collimator was used so that the energy spread was small enough for the full-energy peak to be clearly separated from the Compton continuum in the HPGe detector (see Section 3.4.1 for further details on this measurement).

The beam then passed through a  $\sim 0.1$  Tesla sweeping magnet to bend away any electrons created through interactions with upstream materials. This was done to minimize electron background in the flux counting paddle (see Section 3.4.2). Finally, the beam passed through the post-collimator which consists of a large wall of lead with a 5.1 cm (2.0 inch) diameter hole whose purpose is to further clean up any scattered beam before it entered the HI $\gamma$ S target room.

### 3.3.2 Target Room

Once in the target room (Figure 3.8), the beam passed through two more 5.1 cm (2.0 inch) diameter Pb post-collimators. An additional Pb shielding wall which also had a 5.1 cm diameter hole was placed directly before the Blowfish detector array. The Blowfish array is described in Section 3.5. The Pb wall is intended to serve as the final shielding for detectors in the Blowfish array from any  $\gamma$ -rays which have scattered from upstream. A similar Pb shielding wall was placed behind the Blowfish array to shield the detectors from particles scattered from the back of the target room.

The magnitude of the collimation and shielding employed reflects how difficult

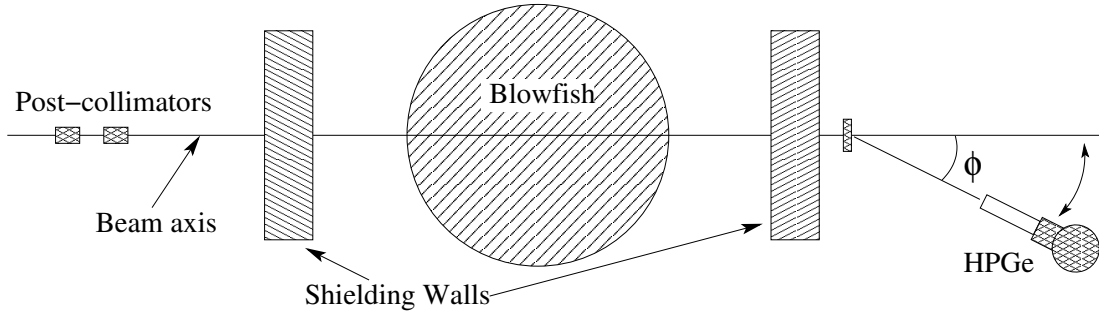


**Figure 3.8:** An overview of the target room at HI $\gamma$ S. Drawing is not to scale.

it is to properly collimate a highly intense  $\gamma$ -ray beam in this energy range. Even with all the shielding described here,  $\gamma$ -rays scattered from upstream were observed in the blowfish detectors whose origin was never accounted for. Fortunately, because the timing of these  $\gamma$ -rays were so different from the neutrons of interest, they were easily distinguished and discarded. However, these  $\gamma$ -rays caused a slight problem when attempting to determine the timing reference point from  $\gamma$ -rays which were scattered from the target into the Blowfish detectors. This is discussed in Section 4.6.1.

Directly after the last shielding wall, a thin Cu target was placed in the path of the beam to serve as a Compton scattering target during production runs. A High-Purity Germanium (HPGe) detector to be used as a flux monitor was placed at a fixed angle from the beam axis in order to measure the Compton scattered  $\gamma$ -rays as described in Section 3.4.1. During runs devoted to determining the beam energy, this detector was placed directly on the beam axis and the Cu target was removed.

### 3.3.3 Axial Alignment

A laser mounted in the collimator hut was employed to ensure the collimators, Blowfish array, and other systems are aligned to the beam axis. The laser strikes a

mirror mounted to the exit beam pipe of the collimator hut which reflects the laser light to a fiducial point at the back of the target room wall. This line then defines the nominal beam axis. The mirror has fine tuning knobs which change the mirror orientation in order to allow the laser to be lined up with the fiducial mark in the event that it becomes misaligned.

Once the line defined by the laser is set, all the experimental apparatuses are aligned to the laser. Since the collimator defines the beam size, the most important aspect is ensuring that the Blowfish array and target are correctly aligned with the collimator. The Blowfish array is mounted on a structure with wheels that easily allow its position to be changed.

## **3.4 Beam Monitoring**

### **3.4.1 HPGe: Energy, Energy Spread, and Flux**

A 123% efficient co-axial High Purity Germanium (HPGe) detector was placed at the back of the target room in order to make measurements of the beam energy, energy spread, and flux. Since the high fluxes of the HI $\gamma$ S beams would cause damage to the HPGE detector, during production runs it was taken off the beam axis. The detector sits on a rail system that allows it be easily re-positioned off axis. Because of this situation, special runs had to be performed by placing the detector on axis with a beam of reduced intensity to limit the flux incident on the detector. Since the process of reducing the beam intensity does not affect any of the beam properties except the flux, the beam energy could be reliably measured during these runs.

When  $\gamma$ -rays strike a HPGe detector, the primary interaction processes are the photoelectric effect, Compton scattering, and electron-positron pair production. The

relative strengths of these three processes depends strongly on  $\gamma$ -ray energy. If the incoming  $\gamma$ -ray is fully absorbed in the detector, via the photoelectric effect, it will contribute to what is termed the full energy peak or photo-peak in the energy spectrum (see Figure 3.9).

However, if an electron-positron pair is produced, the positron will thermalize, annihilate with an electron in the medium, and produce two back-to-back  $\gamma$ -rays<sup>2</sup> of 511 keV (the mass of the electron). If one of these  $\gamma$ -rays leaves the detector, a peak will appear in the spectrum with an energy which is 511 keV lower than the full energy peak. This is called the first escape peak. If both photons from the annihilation leave the detector, a peak will appear with an energy two times the electron mass lower than the full energy, called the second escape peak.

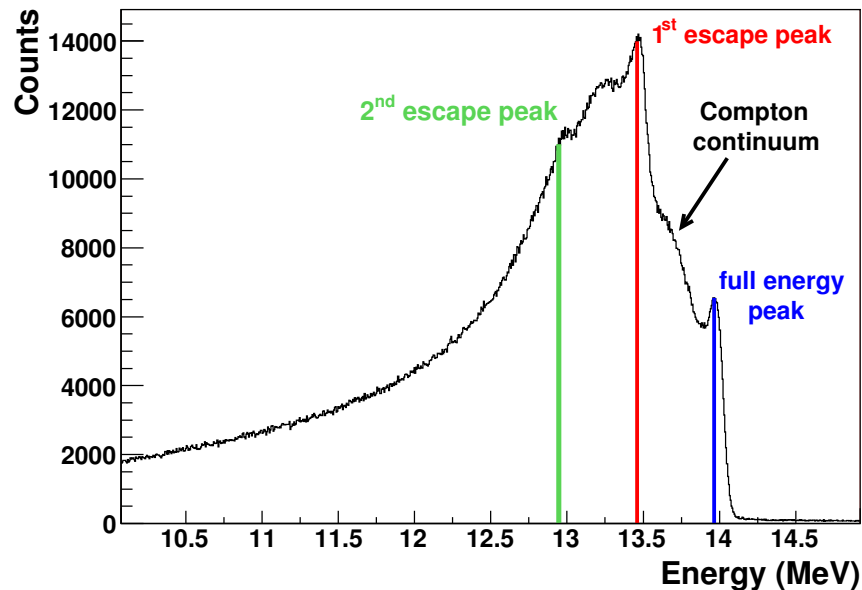


**Figure 3.9:** Sample HPGe Spectrum for a HI $\gamma$ S beam with the prominent features labeled.

---

<sup>2</sup>Two  $\gamma$ -rays are required in order to satisfy conservation of momentum.

In the case of Compton scattering, after scattering from a free electron, the  $\gamma$ -ray can leave the detector without depositing all its energy. Since the energy of the Compton scattered  $\gamma$ -ray can take on a continuum of values, the energy left in the detector will also be on a continuum. The maximum energy of the Compton continuum is referred to as the Compton edge. The value of the Compton edge is given by the incoming energy of the  $\gamma$ -ray minus the minimum energy it can have after Compton scattering. This minimum energy is the energy of a photon which backscatters by  $180^\circ$  from its initial direction.

In reality, the Compton edge does not typically appear as a sharp edge in the spectrum because of finite detector resolution and contributions from multiple Compton scattering events. Thus, depending on the beam spread, the Compton continuum may not be very well separated from the full energy peak. In this case, determining the full beam energy can be more difficult because the centroid of the full energy peak is hard to identify.

For the energies used in this experiment, a 2.5 cm collimator was used during production runs. With a collimator so large, the full energy peak was broad enough that it was not adequately separated from the Compton continuum. Therefore, for beam energy measurements, a 1.3 cm collimator was used, which decreased the beam spread and yielded enough separation in the spectrum so that the full beam energy was easily extracted. The beam energy spread for the 1.3 cm collimator could also be extracted, though this was of limited use in the analysis since all data were taken with a 2.5 cm collimator.

By integrating the counts in the full energy peak and having knowledge of the absolute efficiency of the HPGe detector at measured beam energy, the beam flux at these reduced fluxes can also be obtained. This information can then be combined

with the rate read by the paddle system as a means of calibrating the paddle system for use as a flux monitor in production runs (Section 3.4.2).

During production runs, the HPGe can also be used as a flux monitor. By placing a Cu Compton scattering target upstream of the detector at a precisely measured distance and with the detector at a precisely measured angle with respect to the beam axis, the Klein-Nishina formula for Compton scattering can be used to deduce the incident flux on the Cu target. Figure 3.8 shows the location of the Cu target and the off-axis HPGe. The Klein-Nishina formula for linearly polarized photons scattering from electrons gives a cross section of [Sch00]

$$\frac{d\sigma}{d\Omega} = r_e^2 \left[ \frac{1}{1 + \alpha(1 - \cos \theta)} \right]^2 \left( \cos^2 \theta + \frac{\alpha^2(1 - \cos \theta)^2}{2[1 + \alpha(1 - \cos \theta)]} \right), \quad (3.5)$$

where  $r_e$  is the classical radius of the electron,  $\alpha = \hbar\omega/m_e c^2$ , and  $\theta$  is the angle of the scattered photon in the lab frame.

This technique was employed during this experiment, but the extraction of the incident flux is non-trivial due to several factors. First, the Klein-Nishina cross section drops very rapidly with angle, making a precise knowledge of the geometry mandatory. Second, multiple scattering effects are very difficult to account for and simulations must be employed. Finally, recent tests have revealed that a good deal of electrons are scattered from upstream into the off-axis HPGe detector. Ultimately, it was determined, based upon this last consideration, that the Compton scattering method of flux determination was unreliable without inserting a plastic scintillator in front of the HPGe to veto this large contribution from electrons [Ton07].

For this experiment, only the linear beam asymmetry and the shape of the cross section were needed, making knowledge of the absolute flux unnecessary. Therefore no attempt was made to extract absolute fluxes from either the HPGe in the off axis

position or from the paddle system (discussed in Section 3.4.2).

### 3.4.2 Paddle System: Relative Flux Monitor

A second beam monitoring device was used both as a relative flux monitor and in order to provide a rough absolute measurement of the beam flux. The Paddle system consists of three BC-404 plastic scintillator paddles sandwiched closely together with a thin converter foil between the first and second scintillator paddles (see Figure 3.10). The paddle system is located in the collimator hut as the final obstruction before the beam passes through the wall that divides the hut from the target room.

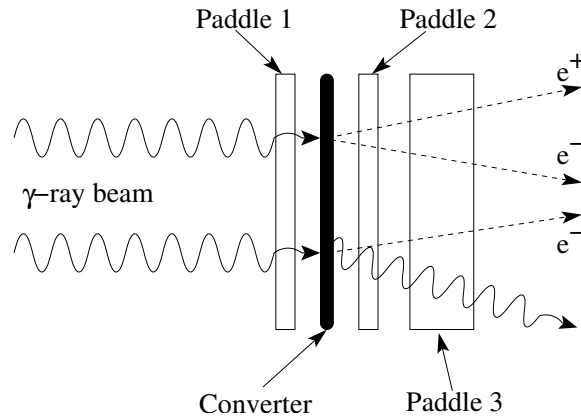


**Figure 3.10:** The configuration of the paddle system used for relative flux measurements.

As the  $\gamma$ -ray beam passes through the converter foil, a small fraction of the  $\gamma$  rays will interact with the foil by Compton scattering or electron-positron pair production. The electrons which are scattered or created will then interact with the subsequent scintillator paddles which are coupled to photomultiplier tubes.

In order to ensure that the signals in the downstream paddles are a result of the beam's interaction with the converter foil and not from electrons that were created from a source upstream of the paddle system, the first scintillator serves as an anti-

coincidence detector for the entire system. If signals are produced in the first and second scintillators, then the event is rejected. The sweeping magnet which was described in Section 3.3.1 serves to reduce the number of false counts due to electrons entering the paddle system from upstream.

The last two scintillators are the counting paddles, with the third paddle being significantly thicker than the first two. Its thickness allows for a slightly better energy resolution so that a Constant-Fraction Discriminator (CFD) threshold for that paddle can be set to accept pairs of electrons which pass through while rejecting single electrons from Compton events. Figure 3.11 shows a sample ADC spectrum for the third paddle. If the threshold were lower, the peak from single electrons would be much larger. With the threshold located as shown in this figure, most of the Compton electrons are rejected.

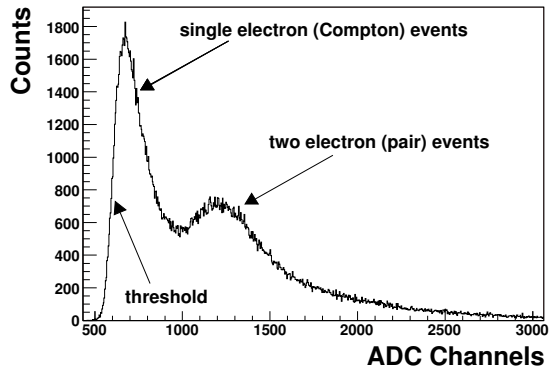


**Figure 3.11:** An ADC spectrum from the third scintillator of the paddle system. The threshold cuts most of the single electrons from Compton events, and accepts electron-positron pairs.

As illustrated in Figure 3.12, the signals are only accepted in the third paddle if there is a coincidence with the second paddle and an anti-coincidence with the first. The logic signal from this coincidence was sent to a scaler which recorded the total counts and a copies of the signal were sent to rate meters which were visible from the

location of the data acquisition computer where the experimenters were located and in the accelerator control room.

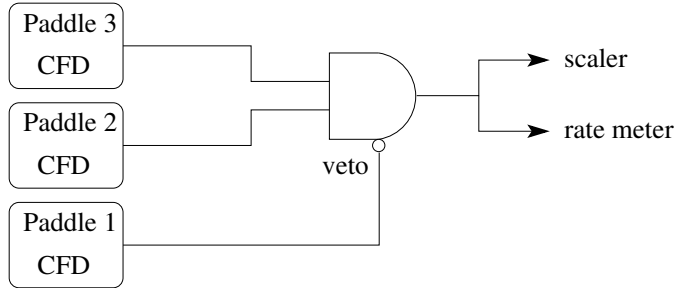


**Figure 3.12:** The paddle system counting logic.

For this experiment, during the runs at reduced beam intensities which were used to check the beam energy, the flux was also obtained from the HPGe detector and used to calibrate the paddle system as a flux monitor. A few points were measured to obtain the trend of the paddle rate versus flux and a linear extrapolation was assumed to be valid to obtain values for beams at higher flux. This provided a rough measure of the absolute beam flux and also served as an indicator of when the beam flux had decreased to the point that a re-injection of electrons was necessary in the Storage Ring. Re-injections were typically requested when the paddle rate dropped to about half its original value.

### 3.4.3 Blowfish: Beam Polarization Axis

During the experiment of [Saw05], it was discovered that the beam polarization axis had rotated with respect to the horizontal plane over the course of the runs. This was attributed to the downstream mirror of the optical cavity becoming optically active and rotating the polarization of the FEL photons.

In order to ensure that a similar problem did not occur during this experiment, the

Blowfish array was used to monitor the beam polarization axis. A beam polarized in the horizontal direction should produce an identical number of counts (within statistics) in the arms which were positioned  $45^\circ$  from the horizontal plane. The results of that analysis determined that the axis of polarization was horizontal to within less than a degree. The details of the analysis can be found in Section 4.12.

## 3.5 The Blowfish Detector Array

### 3.5.1 Array Design

The neutrons from the  $d(\gamma, n)p$  reaction were detected using the Blowfish detector array [Saw05], which consists of 88 BC-505 liquid scintillator detectors positioned at a radial distance of 40.6 cm (16 inches) from the center of the target in a spherical configuration. The detectors are supported by 8 arms spaced uniformly in azimuthal angle  $\phi$ , at intervals of  $45^\circ$  between arms. Each arm contains 11 detectors which are uniformly spaced in polar angle  $\theta$  between  $22.5^\circ$  and  $157.5^\circ$ . The array is designed such that there exists eight detectors of common  $\theta$ , one on each arm, called a ring. Table 3.3 lists the arm and ring number for each detector in the array. The entire array covers a solid angle of about 25% of  $4\pi$  steradians. The convention used for defining these two angles can be found in Figure 2.1. Figure 3.13 shows a picture of the Blowfish array and Figure 3.14 shows a drawing of the cross section of the array.

The entire structure can be rotated as a rigid body about the z axis allowing the absolute  $\phi$ -values of the arms to be determined by the experimenter. This feature was exploited by rotating the array by  $90^\circ$  every few runs in order to cancel systematic effects. A long level was used to ensure that the arms intended to be parallel to the beam polarization were in the horizontal plane.

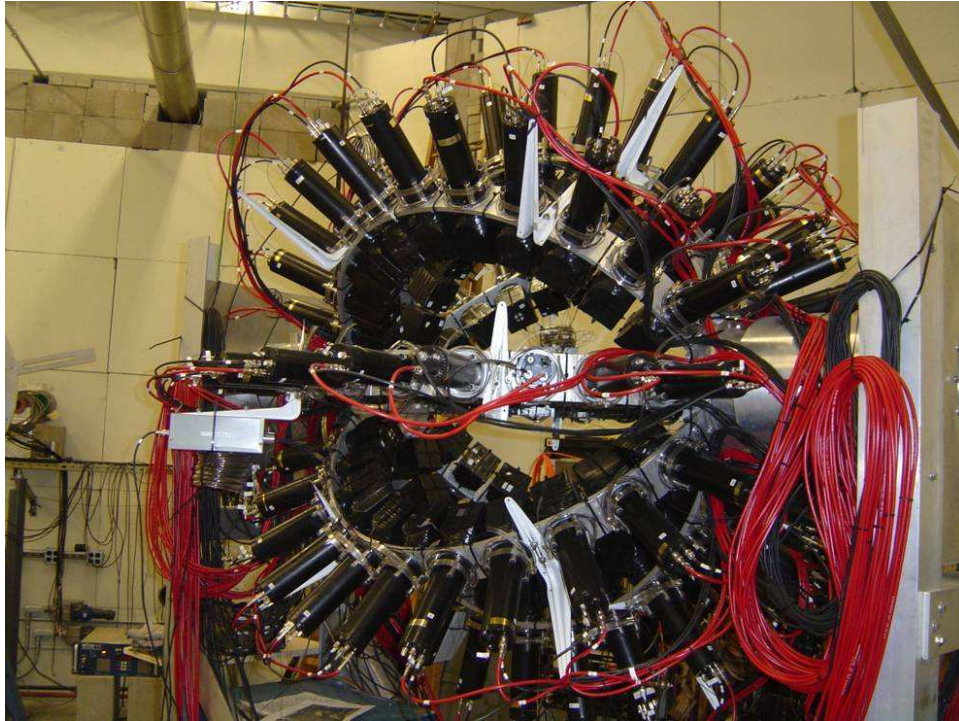


**Figure 3.13:** The Blowfish Detector Array.

### 3.5.2 Blowfish Detectors

Each detector in the array consists of a  $7.6 \times 7.6 \times 6.4 \text{ cm}^3$  volume of BC-505 liquid scintillator contained in a lucite box. Like all liquid scintillators, each detector had a small air bubble which served as an expansion volume. The bubbles in the detectors are estimated to be no more than  $1 \text{ cm}^2$  [Saw07]. A 4.5 cm long light guide couples the active volume to a 2-inch Phillips 2262 photo-multiplier tube. The lucite box is treated with a diffuse high-reflectivity coating, wrapped in an aluminum sheath, and the entire detector is covered with an outer layer of black plastic sheeting [Saw05]. Figure 3.15 shows a diagram of a single detector.

The BC-505<sup>3</sup> scintillator was chosen over NE-213<sup>4</sup> liquid scintillator because its

---

<sup>3</sup>BC-505 is manufactured by Bicon.

<sup>4</sup>NE-213 is manufactured by NE Technology, Ltd.

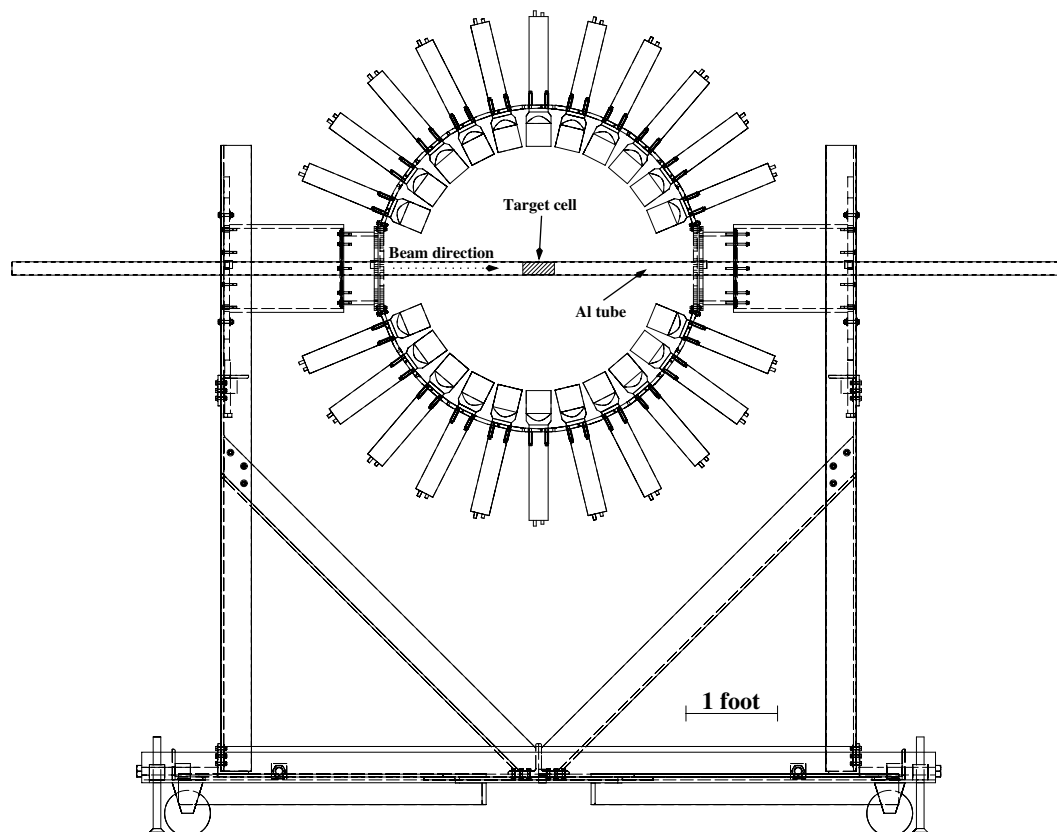


**Figure 3.14:** A drawing of the cross section of the Blowfish detector array. Only two of the eight arms are shown. Picture from [Saw05].

chemical composition is much safer to work with and allows for the use of a lucite box to contain the liquid instead of aluminum or glass [Saw05]. BC-505 has excellent pulse-shape discrimination (PSD) properties (see Section 4.8) allowing the neutrons and  $\gamma$ -rays entering the detectors to be distinguished.

When using liquid scintillators for neutron detection, it is crucial to understand the efficiency of the detector as a function of energy. Considerable work has been done to understand of the Light Output Response (LOR) of the BC-505 material in order to achieve a good understanding the detector response to incident neutrons [Pyw06]. The LOR response curves for BC-505 are discussed briefly in Section 5.4.2. Using the

Ring Number	$\theta$	Arm Number							
		1	2	3	4	5	6	7	8
1	157.5°	1	2	3	4	5	6	7	8
2	144.0°	9	10	11	12	13	14	15	16
3	130.5°	17	18	19	20	21	22	23	24
4	117.0°	25	26	27	28	29	30	31	32
5	103.5°	33	34	35	36	37	38	39	40
6	90.0°	41	42	43	44	45	46	47	48
7	76.5°	49	50	51	52	53	54	55	56
8	63.0°	57	58	59	60	61	62	63	64
9	49.5°	65	66	67	68	69	70	71	72
10	36.0°	73	74	75	76	77	78	79	80
11	22.5°	81	82	83	84	85	86	87	88

**Table 3.3:** Arm and ring numbers for Blowfish detectors. Detectors in a common row comprise a ring and detectors in a common column comprise an arm. Since the array can be rotated about the beam axis, the  $\phi$  value of each arm is not fixed. The spacing between arms is  $\Delta\phi = 45^\circ$ .

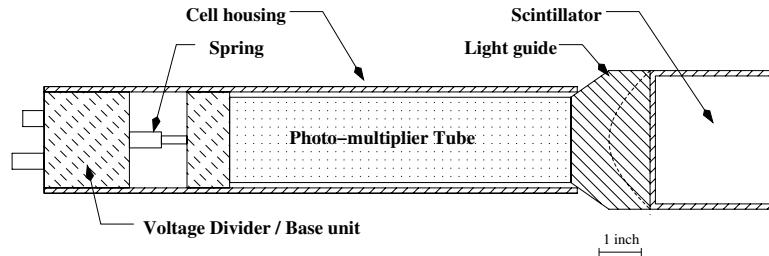


**Figure 3.15:** A diagram of a single Blowfish detector. Picture from [Saw05].

well-determined LOR curves from that work, the Blowfish detector efficiencies were able to be simulated accurately.

### 3.5.3 Gain Monitoring System

This experiment marks the first use of a newly installed gain monitoring system [Bew05] during a physics experiment with the Blowfish array. During previous ex-

periments, a radioactive source<sup>5</sup> was used for the energy calibration of each of the 88 detectors at the beginning and end of each day of running. This method provided no information about the gains of the detectors during the course of day.

However, with the addition of the gain monitoring system, the gains were able to be monitored during production runs on a run-by-run basis by means of light emitting diode (LED) pulses sent through a fiber-optic cable to each detector at periodic times. Therefore if any detector gain change occurred, the LED “flasher” position would shift in the spectrum.

In order to ensure that changes in flasher position were not due to a varying output from the LED, each LED output was also monitored by a Gadolinium-Silicon-Trioxide (GSO) detector which was independent from the Blowfish array. Since there were four LED channels, each producing light signals to 22 Blowfish detectors, four separate monitor detectors were employed.

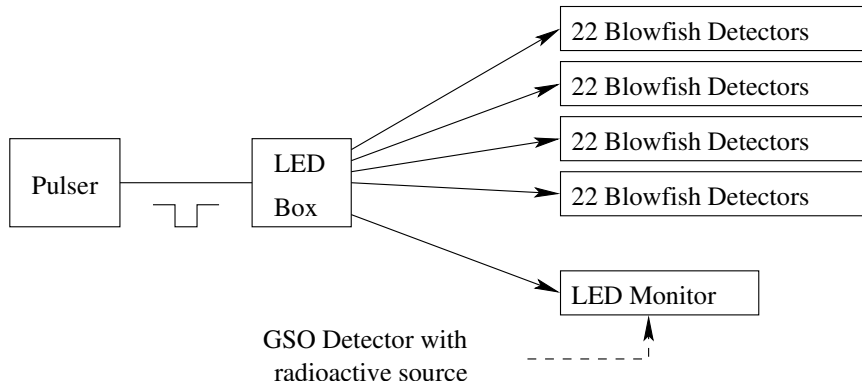


**Figure 3.16:** Schematic of the gain monitoring system. Details can be found in the text.

In addition, a radioactive  $^{137}\text{Cs}$  source was placed in close proximity to the GSO detectors in order to accurately measure the gain of each monitor detector. This served to distinguish shifts in the flasher position in the monitor detector spectrum

<sup>5</sup>The source was typically  $^{137}\text{Cs}$  or  $^{22}\text{Na}$ .

due to gain shifts in the monitor detector from those due to variation in the LED output signal.

In order to calibrate the gain monitoring system, radioactive source runs were performed by placing a  $^{232}\text{Th}$  source in the center of the Blowfish array while simultaneously gathering flasher and monitor detector data. These source runs determined how the flasher position in the pulse height spectrum related to the actual gain as deduced from the  $^{232}\text{Th}$  source edges. This information allowed the gains of each detector to be calculated during production runs using only the flasher on a run-by-run basis. More details about the implementation of this technique can be found in Section 4.5 where the analysis of the data obtained from the gain monitoring system is described.

One additional advantage of the Gain Monitoring System is that the flasher data alerts the experimenter to individual detectors with abnormal behavior over the course of a run. During this experiment, there were two detectors that manifested drastic changes in gain as a single one-hour run progressed. The flasher data was valuable for quickly finding such problematic detectors and discarding them from the analysis.

### 3.5.4 Targets

A heavy water ( $\text{D}_2\text{O}$ ) target was used as the source of deuterons for the  $d(\vec{\gamma}, n)p$  reaction. The heavy water was contained in a thin-walled plastic cylinder with dimensions given in Table 3.4.

An  $\text{H}_2\text{O}$  target, used for background runs, was housed in a nearly identical container. During production runs, a scheme was adopted to record twice as much data with the  $\text{D}_2\text{O}$  target as with the  $\text{H}_2\text{O}$  target.

Length	4.7 cm
Inner Diameter	3.8 cm
Wall thickness	1.2 mm

**Table 3.4:** Dimensions of the D<sub>2</sub>O Target.

Each target was supported in the center of the array by a thin aluminum pipe. The pipe had a diameter not much greater than the outer diameter of the target cell and stretched beyond the total length of the Blowfish array. On the order of 1% of the neutrons leaving the target interact with the Aluminum. This small effect was accounted for in the simulation of the experiment and was found to be negligible. The diameter of the pipe was sufficient to accommodate the 2.5 cm collimated beam without the beam striking it. Figure 3.14 is a drawing that shows how the target was mounted.

## 3.6 Electronics

This section will describe some of the electronics and trigger logic associated with the entire experiment [Iga05]. Triggers were created not only for the Blowfish array, but also for the gain monitoring system, the HPGe detector, and the paddle system. In addition, the Blowfish array and gain monitoring system had to be triggered for multiple types of events. The trigger logic for each system is described below and an overview of the entire trigger logic is provided in Figures 3.23 and 3.24. These figures include some systems which were not used in this experiment, such as an active target.

### 3.6.1 Storage Ring Bunch Signal

This experiment relied heavily on the the exploitation of the timing structure of the HI $\gamma$ S beam in order to distinguish the neutrons created through photo-disintegration from the  $\gamma$ -rays which were Compton scattered from the target (see Section 4.10). Thus a reliable timing signal from the beam was needed.

Such a signal was generated in the storage ring by a capacitive pick-off circuit which created a pulse each time an electron bunch passed through a detector located in the ring. The signal had a frequency of 5.58 MHz, twice the revolution frequency for a single bunch of electrons in the ring. This represents the frequency of  $\gamma$ -ray bursts obtained from the accelerator for the two-bunch mode of operation.

This signal was responsible for the production of many of the gates used in the systems described below and also ultimately served as the TDC start signal for most of the TDCs.

### 3.6.2 Acquisition Windows

The entire trigger logic was governed by acquisition windows, which were created to allow or reject the various triggers based on their timing relative to the beam. Figure 3.17 shows the circuit that creates the windows and their relative timings. Each window is created by manipulating the signal from a bunch in the ring. Note that the windows are actually vetoes, and in that sense only allow gates when no signals are present.

Because  $\gamma$ -rays and relativistic electrons scattered from the target travel at the speed of light before entering the Blowfish array, they arrive at a time before the slower-moving massive neutrons. In describing the arrival of any particles in Blowfish traveling at the speed of light from the target the term “gamma flash” is used. The

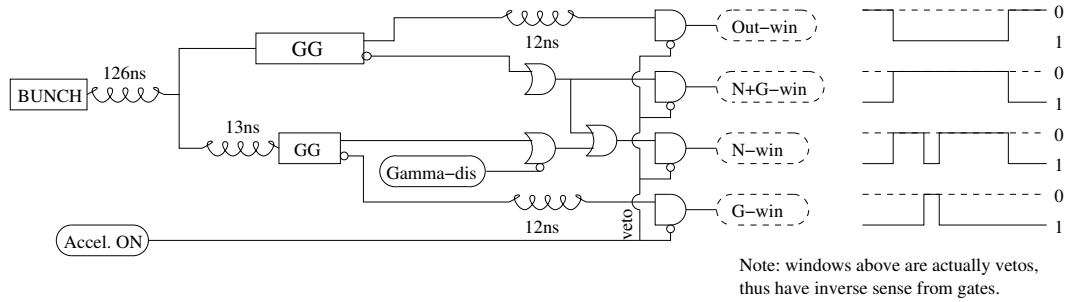


**Figure 3.17:** A schematic of the circuit which creates acquisition windows from the ring bunch signal. Also shown are the relative timings of the gates they create. Details are described in Section 3.6.2. GG stands for gate generator. The other terms are defined in the text.

N+G-win gate from Figure 3.17 is timed to open at a time preceding this gamma flash and stays open long enough to allow neutrons signals to enter as well. The allowance of both neutrons and  $\gamma$ -rays explains the name N+G-win. The Out-win gate is the exact inverse of this window and corresponds to events that are not beam correlated.

Since the count rate for gamma-flash timed events is a great deal larger than that of the photodisintegrated neutrons of interest, many of the gates produced during this time frame are rejected on a prescaled basis. This creates a notch with a width determined by a gate generator (labeled GG in Figure 3.17) in the N+G-win gate called N-win. The location and width of this notch is adjusted until it prescales the appropriate gamma-flash region without cutting into the region corresponding to high energy neutrons. The prescaling is handled by the Data Acquisition System (DAQ) software, which did or did not send a software gate via an output register depending on whether the gamma-flash timing period was accepted or rejected. The output register gate is labeled “Gamma-dis” in Figure 3.17. Note that in contrast to the N-win gate, the gate denoted “G-win” allows only gamma-flash timed events.

For this experiment the prescale factor for the gamma-flash region was 40 for

most production runs. However, short periodic runs were performed with the prescale factor set to 1, in order to obtain the location of the gamma-flash events in the TDC spectra as a reference point in time for each detector. This is discussed in Section 4.6.

Each gate is generated via an AND with another software-controlled gate from the output register, labeled “Accel ON” in the figure. This is set to indicate that the accelerator is running and ring bunch triggers should be expected. The acquisition windows created from bunch signals are used as veto inputs into the electronics of all the systems described below in order to only accept events at the appropriate times relative to the pulsed beam.

### 3.6.3 Blowfish or “Neutron” Trigger

The analog signals from each Blowfish photo-multiplier tube (PMT) were individually discriminated using Ortec CF-8000 constant fraction discriminators (CFDs). The CFDs contained an internal pick-off circuit which allowed the analog signal to be reused. Each analog signal was then delayed, split, and sent to charge-integrating CAEN VME-792 Analog-to-Digital Converters (ADCs). One of the split signals was used to form the “short-gated” signal for pulse-shape discrimination (PSD) and the other was used for the “long-gated” signal. The PSD method employed is described in Section 4.8.

As Figure 3.18 demonstrates, the OR outputs of each 8-channel CFD module were fanned together to form a common OR for all the detectors of the array (called N-OR) to be used to form the trigger for the Blowfish array or “neutron” trigger. A trigger was created from the N-OR only when it fell inside the N-win acquisition window with the resulting trigger termed N-trig. The individual outputs from the

CFDs were delayed and then sent to CAEN VME-775 TDCs as the stop signals. A common start for all the TDC channels was provided by a retimed bunch signal. The individual CFD output were also used to create the long and short gates for PSD.

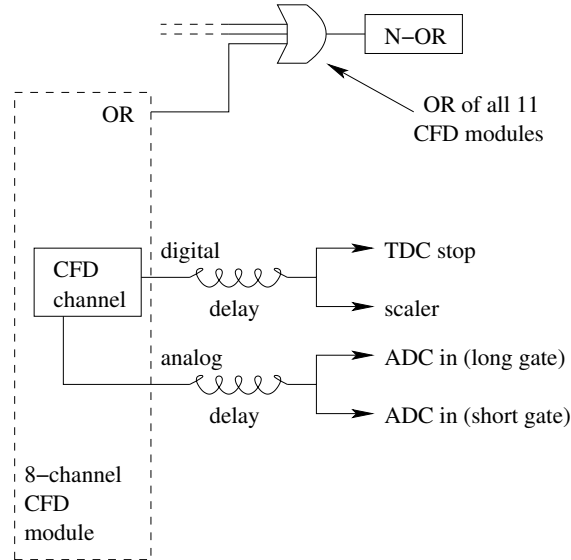


**Figure 3.18:** The electronics diagram for the Blowfish detectors. The N-OR is used to create the neutron trigger (N-trig) as in Figure 3.19.

### 3.6.4 Pedestal Trigger

Charge-integrating ADCs assign a discrete channel number to an incoming signal by integrating the signal over the time period of the gate. Therefore, any DC bias to the signal will result in an offset in ADC channel number being outputted, called the pedestal. The pedestal is easily measured by recording ADC values when no signal is present. During this experiment, the pedestal of each detector was sampled every few seconds during the range of times for the events of interest, thus the N+G-win gate was used.

The pedestal trigger was only created when a software gate called the Paddle

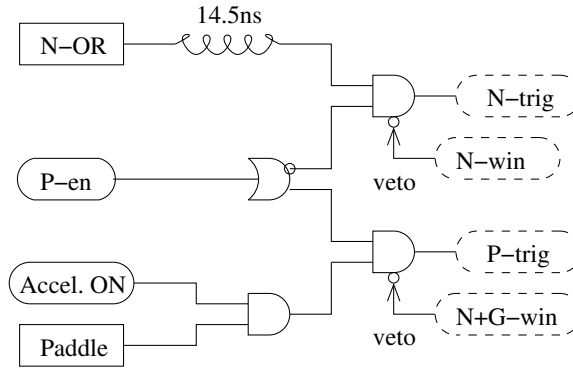


**Figure 3.19:** A schematic of the circuit which creates the neutron and pedestal triggers.

Enable (P-en) was present. This gate was produced periodically in software through the output register. The P-en also effectively served as a veto of the N-trig trigger as shown in Figure 3.19. In addition, the P-en also communicated to the ADC that the VME ADC default mode of zero-suppression should be disabled before receiving the pedestal signals. Ultimately, the pedestal trigger was initiated through an AND between the Accel ON gate, P-en gate, and a discriminated logic signal from the paddle system. The pedestal trigger is called P-trig.

### 3.6.5 HPGe or Flux Trigger

The HPGe was in an off-axis position during production runs and its signals were sampled and made part of the recorded data stream. Like pedestal events, the rate of sampling of flux events was determined by the DAQ software, through the Flux Enable (Flux-en) gate from the output register.

A flux trigger (Flux-trig) was produced when this signal was present along with a discriminated signal from the HPGe CFD (see Figure 3.20). As opposed to the VME-based ADCs used for all other aspects of this experiment, an CAMAC-based

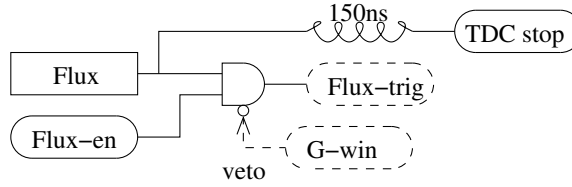


**Figure 3.20:** A schematic of the circuit which creates the flux trigger.

peak-sensing Ortec 413-A ADC was used to read in signals from the HPGe detector.

### 3.6.6 LED Flasher Trigger

The Gain Monitoring System of the Blowfish array monitored the gains of each of the detectors in the array by sending LED pulses to each of the detectors. During runs, a pulser was set to fire periodically from four channels which in turn pulse four LEDs. This was accomplished using the Flash Enable (Flash-en) signal initiated by the DAQ software. Each LED sends light through fiber-optics to 22 of the Blowfish detectors and one GSO monitor detector. A separate output from the pulser gets inverted (to accommodate NIM level modules) and is sent to an ADC to monitor the pulser performance and another copy is sent to a discriminator to create the Flasher Trigger (Flash-trig). The circuit diagram is in the top diagram of Figure 3.21. A flasher event is identified by the DAQ system by the fact that each detector in the Blowfish array fires.

### 3.6.7 Flasher Monitor Trigger

As mentioned in Section 3.5.3, the monitor detectors not only detected and monitored a copy of the LED signals (which are read out following a Flash-trig trigger), but a  $^{137}\text{Cs}$  source was also placed in the box containing the monitor detectors in order to monitor gain shifts in the monitor detectors themselves.

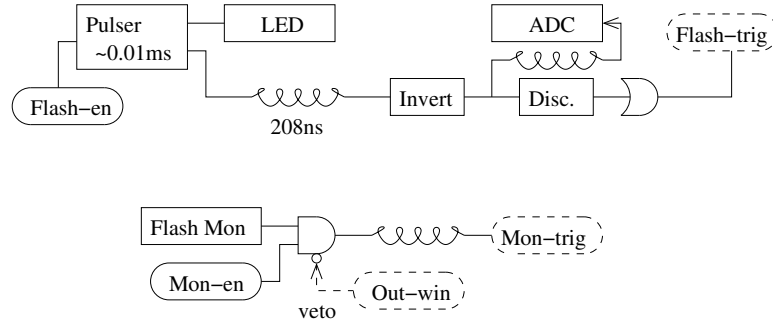


**Figure 3.21:** A schematic of the circuit which creates the flasher (top part of figure) and monitor (bottom part of figure) triggers.

Because the radioactive source would not be synchronized with any beam-related events, it required its own trigger circuit. This was done using the Monitor Enable (Mon-en) gate initiated by the DAQ software periodically (see Figure 3.21). This effectively prescaled the number of source events recorded from the monitor detectors.

### 3.6.8 Paddle Trigger

The most useful information obtained from the paddle system (Section 3.4.2) came from the scaler which reported the total counts in the paddle system over a given time period. However, in order to monitor the gains of the paddle system and determine whether the thresholds were properly accepting electron-positron pairs as opposed to single electrons, copies of signals from the last two paddles were sent to an ADC to sample their pulse-height spectra (see Figure 3.11). The Paddle Enable (Pad-en) periodically allowed these pulse heights to be sampled. In addition, this signal was used as a stop in a TDC with the ring bunch signal as a start in order to monitor variations in the timing signal. The circuit diagram is found in Figure 3.22.

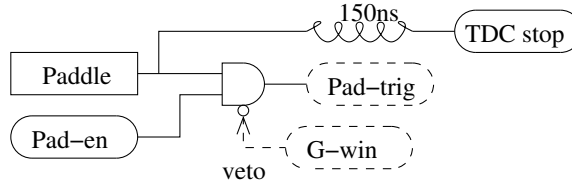


**Figure 3.22:** A schematic of the circuit which creates the paddle trigger.

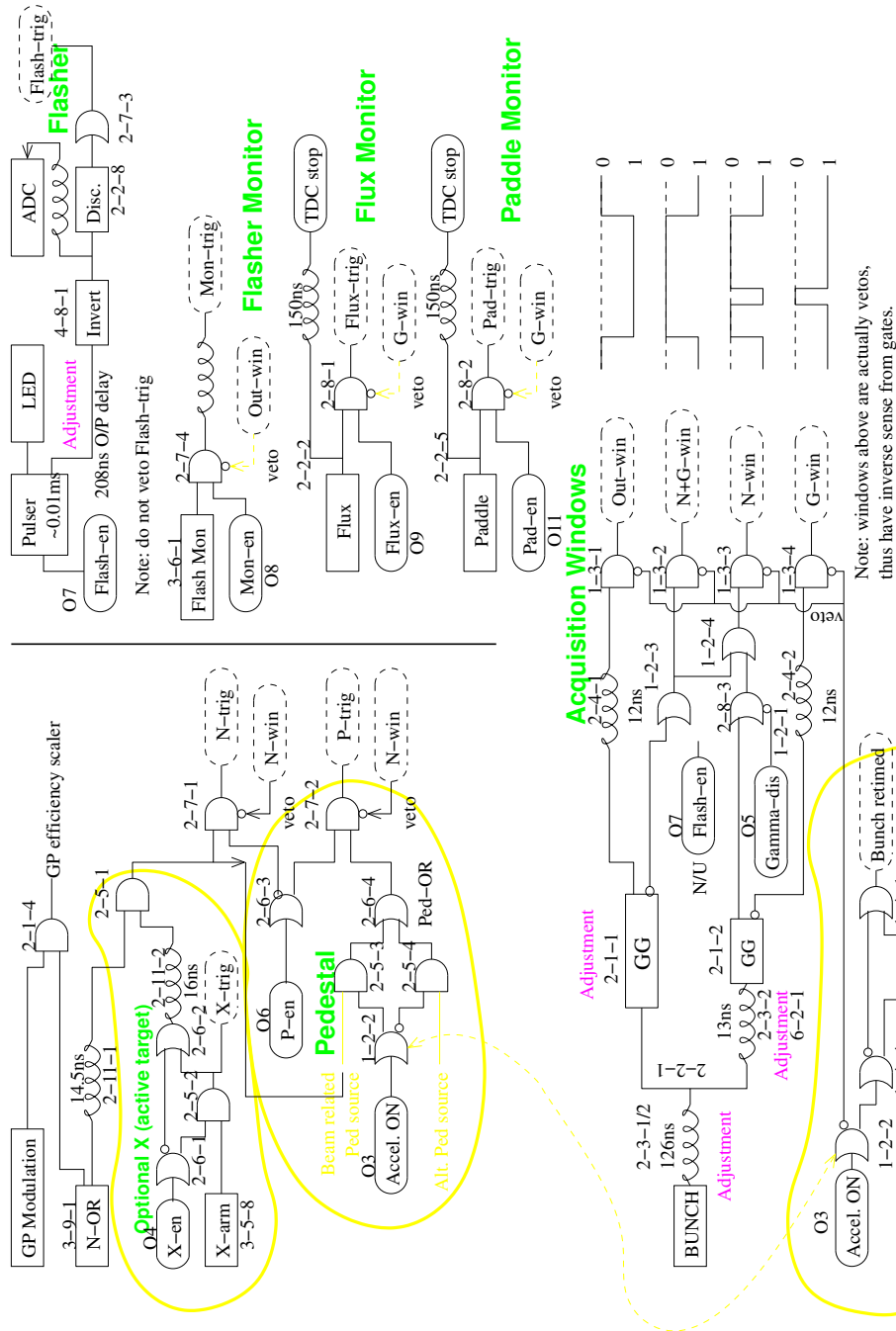
### 3.6.9 Miscellaneous Components

Each of the triggers from the separate systems were ultimately consolidated into a single master trigger. This allowed a single inhibit circuit to be used as opposed to constructing a separate circuit for each system. The master trigger was used to set the inhibit latch and was ORed with a software controlled inhibit while the DAQ was processing events. During this time, no new triggers could be produced by the circuit. The latch was reset by the output register, allowing the next event to be processed. The inhibit circuit can be found in Figure 3.24.

Scalers were employed to record the number of hits in each detector above threshold, paddle counts, the number of times each type of trigger was enabled, and for many other diagnostic checks of the circuit. Almost each signal that went into a scaler recorded both the number of counts obtained continuously and the number of counts obtained only when the DAQ was uninhibited.

A 1 kHz clock was also recorded by a scaler to measure the real-time of a given data run and the inhibited scaler measured the live-time of a given run, by counting only when the DAQ was alive.

A computer-controlled Lecroy 1440 High Voltage mainframe powered the Blowfish detector PMTs and the monitor detector PMTs. The High Voltage settings of each PMT was recorded at the beginning and end of each data run by the DAQ system.



Blowfish Trigger Upgrade, Jan, 2005

Figure 3.23: A global schematic of the trigger logic employed for this experiment, part 1 of 2.

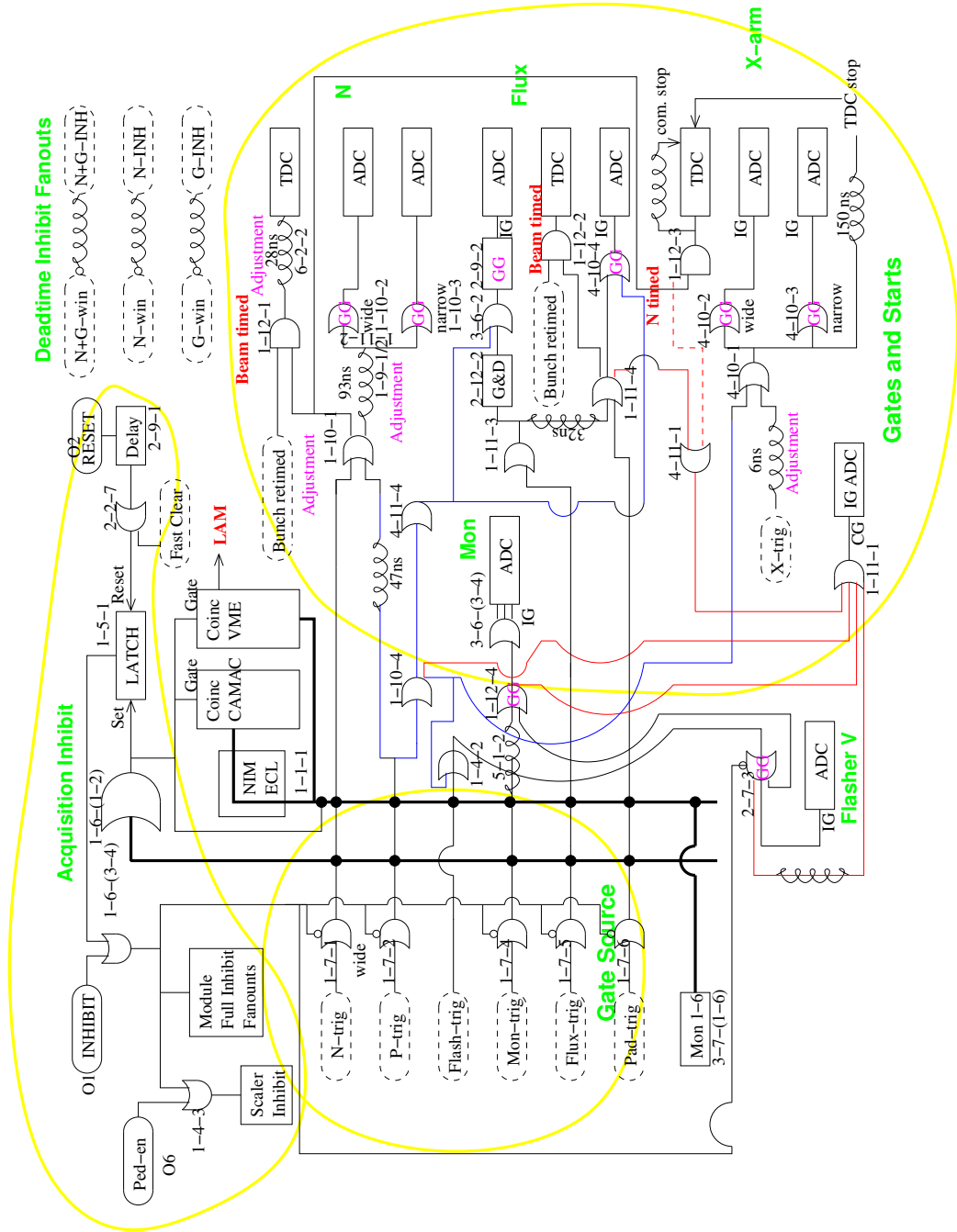


Figure 3.24: A global schematic of the trigger logic employed for this experiment, part 2 of 2.

## 3.7 Data Acquisition System

Data Acquisition was performed with the LUCID DAQ system. LUCID is designed to be able to both acquire and analyze experimental data. The data stream created by LUCID has a reader, a looker, and a writer.

By means of a front-end computer, the reader retrieves data from the data source, such as VME modules in the case of this experiment. It also defines the variables, event types, and trigger conditions of the data stream. The reader makes the data available to the rest of the system and can also perform simple software cuts.

The looker is optional and can be used to perform on-line analysis of the data as it is being retrieved, including a more complex analysis of the data than the reader. While a looker was used as data were being collected during this experiment, it was not ultimately used for data analysis (see Section 4.2).

The writer's sole job is to save the data to disk. Each of these components was run on a Linux workstation. The entire system was typically live on the order of 60% of the time.

# Chapter 4

## Data Reduction

### 4.1 Introduction

This chapter will describe the details of how the data obtained from the experiment described in the previous chapter were analyzed to produce the experimental yields and observables. It begins with a brief description of how the data were converted from the LUCID format to the ROOT framework in Section 4.2. Next, issues related to preparing the data for the analysis cuts are discussed in Sections 4.3-4.6. This includes the determination of the ADC pedestals, the beam energy centroid and width, the Blowfish detector gains, and the TDC calibration. The analysis cuts are then described in Sections 4.7-4.10. The neutron yield extraction is covered in Section 4.11, and Section 4.12 discusses how those yields were used to evaluate the orientation of the beam polarization axis. Finally, the method used for constructing the raw observables from the extracted yields is presented in Section 4.13.

### 4.2 Conversion of Data to the ROOT Framework

The first step in the reduction of the data was the conversion of the raw data from the native LUCID format (see Section 3.7) to the ROOT framework [Bru96]. This was done because of the familiarity of the author with ROOT, eliminating the need to learn entirely new analysis software for reducing the data.

LUCID stored the data on an event-by-event basis with each event tagged based on the trigger that was responsible for the readout of the electronics (Section 3.6). In converting to the ROOT framework, this information was retained, allowing the cuts described in this chapter to be done at the event level.

The data were converted to ROOT trees by modifying a code written by B. A. Perdue [Per05]. A tree is a data structure that ROOT uses to organize data in order to make file sizes small and allow for fast retrieval. Each entry in a tree corresponds to an event in the LUCID file, and the tree is composed of branches that represent the data variables.

Once the data were stored in ROOT trees, the pedestals were determined for each ADC input channel as described in Section 4.3. At that point, the variable arrays which were stored in the ROOT tree had pedestals subtracted (when applicable) and were re-indexed according to detector number in contrast to the original indexing by ADC or TDC module number and input channel location. The result was a tree that contained pedestal subtracted data in an easily accessible form.

The C++ based ROOT analysis program is a powerful tool for data reduction because of the wide variety of built-in classes designed specifically for nuclear and particle physics applications. Having such applications in mind meant the developers created ROOT with the capability of handling large amounts of data in a fast and efficient manner.

## 4.3 Pedestal Determination

As discussed in Section 3.6.4, the offset in ADC channel number resulting from the DC bias of the blowfish PMTs and from any bias in the electronic circuit is

called the pedestal. The pedestal needed to be determined for each individual ADC input channel of the Blowfish detectors so that it could be subtracted from the ADC channel values obtained during neutron events. Thus, the ADC channel value of the pedestal represents the zero of the axis. After the pedestal was subtracted, the axis was then scaled by the gain for each ADC input channel as described in Section 4.5 in order to have an axis calibrated in energy units.

Special triggers were devoted to reading out the the pedestal values when no signals were present in the Blowfish array (Section 3.6.4). On a run-by-run basis, a histogram of each input channel's pedestal value was created and fit with a Gaussian function in order to determine the centroid value. The pedestal values were then subtracted from the raw data, leaving the true ADC channel value. Figure 4.1 shows an example of a typical pedestal spectrum from a Blowfish detector.

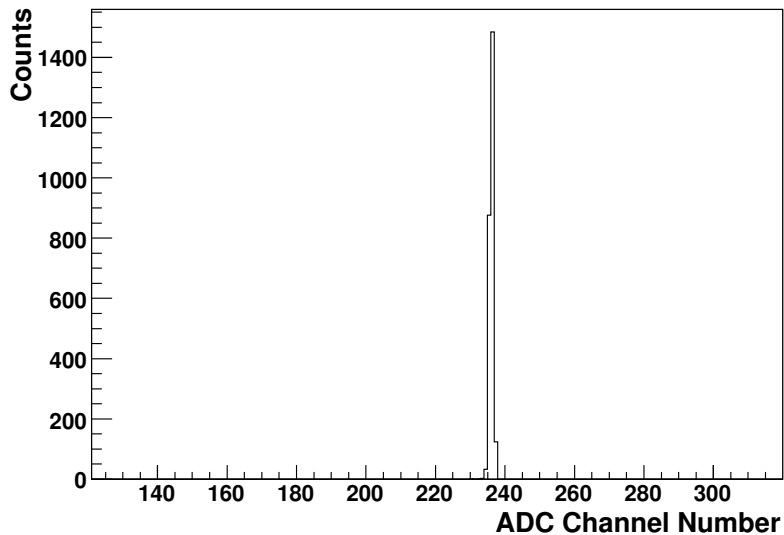


**Figure 4.1:** Typical pedestal spectrum from a single Blowfish detector ADC input channel.

## 4.4 Beam Energy Determination

Runs devoted to beam energy measurements were performed at the beginning of each day and when the beam energy was changed. The accelerator settings used to produce the beams at each energy were stored and reused, making reproducibility of the beam properties very reliable. These runs were performed with a collimator of half the diameter of the one used in production runs, in order to allow the full energy peak in the spectrum to be adequately separated from the Compton continuum (see Section 3.4.1).

### 4.4.1 HPGe Calibration

Before each beam energy measurement, the HPGe detector was moved onto the beam axis as defined by the collimator (see Section 3.3.3) and the target was removed from its position at the center of the Blowfish array. An energy calibration was obtained by allowing the detector to record data obtained from background activity in the room. A 2615 keV room background line from  $^{232}\text{Th}$  and a line from  $^{40}\text{K}$  at 1461 keV were used as two points in a linear fit to calibrate the axis. Enough statistics were typically gathered in 10-15 minutes of counting for the channel positions of these lines to be determined.

The fact that the calibration points were so low in energy relative to the  $\gamma$ -ray beam energy meant that slight errors in the determination of the location of the background lines would result in larger deviations in the calibration at higher energies. The magnitude of the uncertainty in the beam energy centroid value due to this uncertainty was estimated to be about 50 keV.

#### 4.4.2 Energy Centroid and Width Determination

Once the spectra were calibrated, a  $\gamma$ -ray beam with reduced flux ( $< 10^3 \gamma/s$ ) was incident on the detector. About 5 minutes was sufficient to produce a spectrum with enough counts to determine the centroid of the full-energy peak in the spectrum. The centroid of the beam energy was extracted by fitting the high-energy side of the full-energy peak with a Gaussian function. The low-energy side of the peak overlapped with the Compton continuum rendering it unreliable for a good fit. An example of a energy-calibrated spectrum has already been presented in Figure 3.9.

In addition, the width,  $\sigma$ , of the beam is also extracted from the Gaussian fit and converted to a Full-Width-Half-Maximum (FWHM). For the 1.27 cm (0.5") collimator, a FWHM of about 1% was obtained at each beam energy. However, since the energy measurements were done with a collimator of different size than that used during production runs, this FWHM did not correspond to the spread of the beam that was incident on the target during the production runs.

In order to get an estimate of the beam energy spread with the 2.5 cm (1") collimator, simulations were performed by Sun and Wu [Sun07] using operating parameters which matched those of the experiment as closely as possible. The energy distributions obtained from those simulations are shown in Figure 4.2.

Notice that beams with the 1" collimator include a much larger low energy tail than the 0.5" collimated beams. This is not surprising when considering the correlation between energy and angle for the Compton backscattering collision seen in Figure 3.4. Table 4.1 contains a comparison of the width obtained from the measurement with the 0.5" collimator with that which is predicted by the simulation, which reveals reasonable agreement. This result gives us confidence that simulation describes the experiment well enough to take the beam energy width from the simulated 1" results

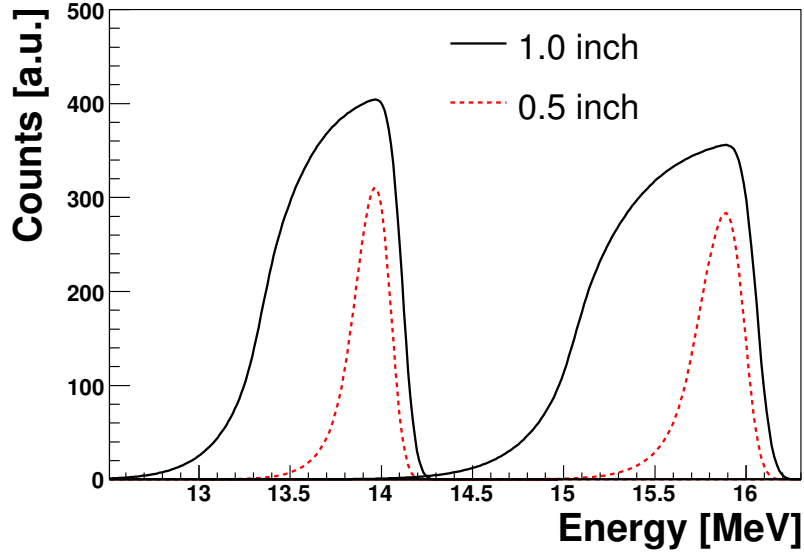


**Figure 4.2:** Simulated energy spectra for 14 and 16 MeV beams with 0.5” and 1” collimators. Simulation from [Sun07].

as a good estimate of the true spread.

Nominal $E_\gamma$	Centroid	Measured $\Delta E/E$	Simulated $\Delta E/E$
0.5” collimator			
14.0 MeV	13.97 MeV	1.1%	1.3%
16.0 MeV	15.89 MeV	1.3%	1.5%
1.0” collimator			
14.0 MeV	13.74 MeV	-	5.4%
16.0 MeV	15.57 MeV	-	6.1%

**Table 4.1:** Beam energy centroids and widths from measurements and simulation.  $\Delta E/E$  is defined as the Full Width at Half Maximum (FWHM) over the centroid energy. The centroid for the 0.5” collimated beam is taken from the measurement, and the centroid from the 1” collimated beam is taken from the simulation as described in the text.

In addition to using the simulation to determine the energy spread of the beam, effective energies were assigned for the 1” collimated beams by taking the energy at which half of the area under each distribution was below the effective energy and half

was above. Those values are also reported in Table 4.1.

The beam energies which were adopted with conservatively estimated uncertainties can be found in Table 4.2. These values along with the widths from Table 4.1 for the 1" collimated beams were used as the parameters for the beam energy profile in the simulation (see Section 5.3.3). These parameters ultimately had a negligible effect on the analysis and results, as seen in Section 5.8. For the rest of this work, the beam energies will be referred to by their nominal values of 14 and 16 MeV.

Nominal $E_\gamma$	Centroid (MeV)
14 MeV	13.7 $\pm$ 0.2
16 MeV	15.6 $\pm$ 0.2

**Table 4.2:** Adopted values for centroid beam energies for 14 and 16 MeV beams.

## 4.5 Gain Determination

The gain of each detector had to be determined in order to calibrate the ADC spectra for the Blowfish detectors. This was done on a run-by-run basis by relating information from the Blowfish gain monitoring system (see Section 3.5.3) to radioactive  $^{232}\text{Th}$  source runs. The installation of the gain monitoring system allows for a marked improvement in gain determination as compared to the previous method of determining gains through source runs performed at the beginning and end of each day of data taking.

### 4.5.1 $^{232}\text{Th}$ Source Runs

The gain monitoring system (GMS) measures only the relative gains for the Blowfish detectors. An independent absolute gain measurement using a radioactive source

provides the GMS with the information needed to extract absolute gains. Thus, as a reference or standard to which the GMS data are compared, the source runs are often referred to as reference runs in the discussion that follows.

Over the course of the experiment, data were recorded each morning and evening and between beam energy changes with a  $^{232}\text{Th}$  source placed at the center of the Blowfish array. A  $^{232}\text{Th}$  source was chosen over a  $^{137}\text{Cs}$  source because the  $\gamma$ -ray of interest from  $^{232}\text{Th}$  is 2.615 MeV as opposed to the 0.660 MeV  $\gamma$ -ray from  $^{137}\text{Cs}$ . The energy deposited by the  $^{232}\text{Th}$   $\gamma$ -ray is much closer to the expected energy deposition by the neutrons of interest from the photodisintegration reaction than that of a  $^{137}\text{Cs}$   $\gamma$ -ray. The  $^{232}\text{Th}$  source emits the desired  $\gamma$ -rays by decaying through its natural decay chain, eventually reaching an excited state of  $^{208}\text{Pb}$ , which subsequently decays by emitting a 2614.533 keV  $\gamma$ -ray.

When the 2615 keV  $\gamma$ -rays enter the BC-505 liquid scintillator detectors, they cause scintillation by Compton scattering with electrons in the detector, which in turn interact with the scintillator material to excite electrons into atomic or molecular states which decay by giving off light. The highest kinetic energy that the recoil electron can possess after Compton scattering with the incident  $\gamma$ -ray is when the  $\gamma$ -ray scatters through an angle of  $180^\circ$ . This electron kinetic energy is termed the Compton edge and is given by the expression

$$E_{CE} = \frac{2E_\gamma^2}{m_e + 2E_\gamma}, \quad (4.1)$$

where  $E_{CE}$  is the Compton edge energy,  $E_\gamma$  is the source  $\gamma$ -ray energy, and  $m_e$  is the mass of the electron.

For the 2615 keV  $\gamma$ -rays from the  $^{232}\text{Th}$  source,  $E_{CE} = 2381 \text{ keV}_{ee}$ . The units, keV electron equivalent, are used in order to normalize all the interactions in the

detector to a consistent scale for the computation of the Light Output Response (LOR) of the detector. The LOR is a measure of the amount of light collected from the interactions of a charged particle with the detector material and is described in more detail in Section 5.4.2. In the  $^{232}\text{Th}$  source interactions, Compton scattered electrons are causing the scintillation in the detector, making  $\text{keV}_{ee}$  the natural units. However, when a neutron interacts with the detector material, the most important interaction is scattering with a proton. If an electron and a proton of the same initial energy travel through the detector, the amount of scintillated light will be different. Thus, the proton energy in the detector must be converted to an electron equivalent energy in order to have a normalized energy scale for considering light output which is independent of particle type.

The Compton edge, which is located at the end of the continuum of energies resulting from Compton scattering, was identified in the pulse height spectrum as the half-maximum point to the right of the most extreme local maximum. The ADC channel number of the Compton edge was determined by smoothing each spectrum, locating the local maximum point at the end of the spectrum, and then stepping down point-by-point on the smoothed spectrum until the half-maximum point was reached. An example of a Compton edge determination from a  $^{232}\text{Th}$  source run is given in Figure 4.3.

Using the known energy of the Compton edge and the corresponding ADC channel value,  $C_{CE}$ , the detector gain,  $G$ , is computed as

$$G = \frac{E_{CE}}{C_{CE}}. \quad (4.2)$$

During the experiment, the gains from source runs were also computed by a routine performed in LUCID. The LUCID determination used a technique which identified

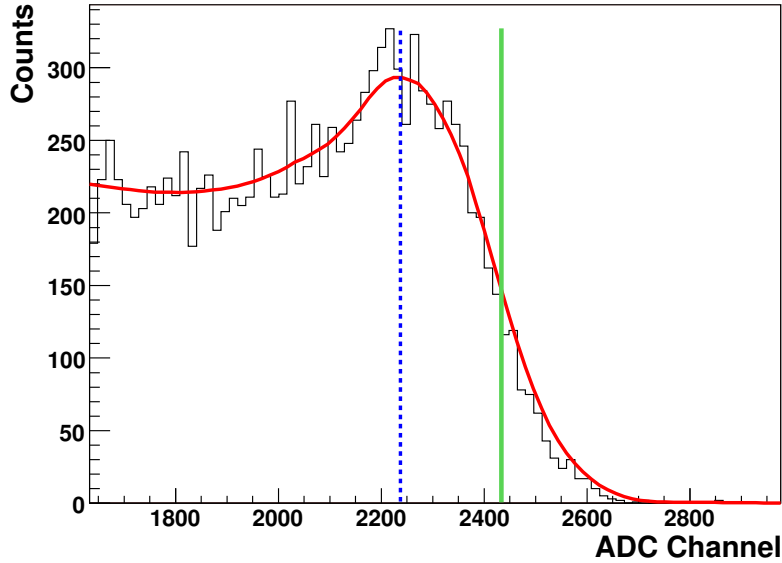


**Figure 4.3:** Compton edge determination in a Blowfish detector from a  $^{232}\text{Th}$  source run. The solid red curve is the smoothed spectrum, the dashed blue line marks the local maximum ADC channel value, and the solid green line marks the half-maximum ADC channel value or Compton edge.

the inflection point<sup>1</sup> of the smoothed spectrum as the Compton edge. The results obtained using the method of gain determination described in this section were checked against the results from the method used by LUCID and agreement was found for the gain values to within half a percent.

#### 4.5.2 Hardware Pulse Height Threshold Determination

The same technique that was used to determine the Compton edges of the  $^{232}\text{Th}$  source spectra was used to determine the hardware thresholds that were set for each Blowfish detector via the CFDs. Figure 4.4 illustrates the threshold determination for a typical spectrum.

---

<sup>1</sup>The inflection point is the point at which the second derivative changes signs.

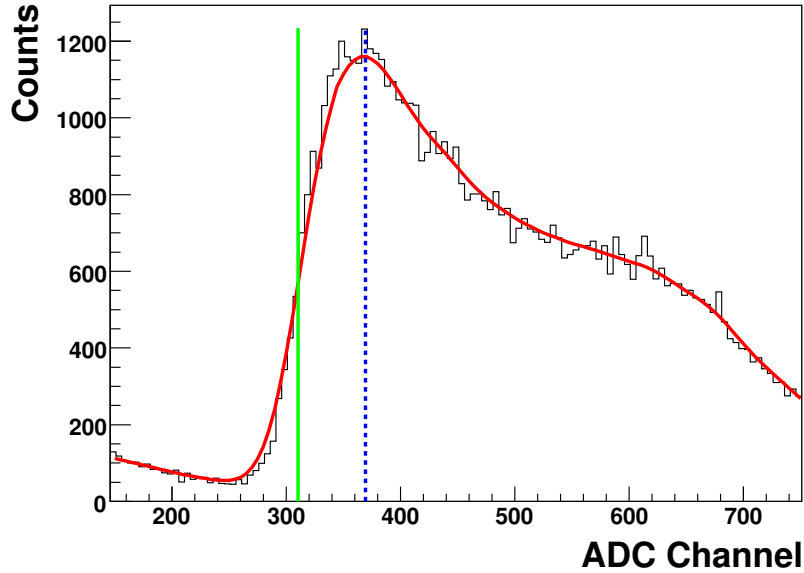


**Figure 4.4:** Threshold determination in a typical spectrum in a Blowfish detector. The red curve is the smoothed spectrum, the dashed blue line marks the local maximum ADC channel value, and the solid green line marks the half-maximum ADC channel value or hardware threshold.

The ADC channel numbers corresponding to the detector thresholds were ultimately converted to  $\text{keV}_{ee}$  using the gain values. The threshold was determined for each source run and each production run. Figure 4.5 shows a histogram of the mean threshold values of each detector. Each entry in this histogram represents the mean threshold for a single detector over all of the 16 MeV runs.

Since neutron detection efficiencies for liquid scintillators depends strongly on detector threshold, a common software pulse height threshold was chosen in order to ensure that each detector shared a common efficiency. This common threshold was set to be larger than the largest hardware threshold. Thus the value of the maximum hardware threshold for any detector in the array as shown in Table 4.3 represents the minimum value that the software pulse height cut can assume. The value of the common pulse height cut was ultimately determined after the PSD cut was applied

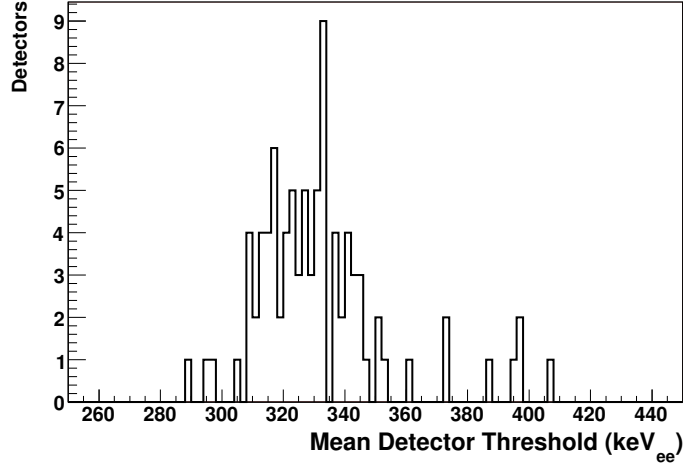


**Figure 4.5:** The mean threshold values for all Blowfish detectors. Each entry corresponds to the mean threshold value for a single detector over all the 16 MeV  $\gamma$ -ray energy runs.

as described in Section 4.9.

$E_\gamma$	Mean HW Thresh.	Std. Dev.	Max. Det. Thresh.
14.0 MeV	329 keV <sub>ee</sub>	27 keV <sub>ee</sub>	409 keV <sub>ee</sub>
16.0 MeV	332 keV <sub>ee</sub>	23 keV <sub>ee</sub>	408 keV <sub>ee</sub>

**Table 4.3:** Mean hardware (HW) thresholds in the Blowfish detectors. The mean represents the average threshold for all the detectors in the array. The maximum detector threshold is the maximum hardware threshold value for a single detector in the array.

### 4.5.3 Flasher Centroid Determination

The GMS works by pulsing a light-emitting diode (LED) periodically, which sends light through fiber optic cables to each Blowfish detector. Because the LED was programmed to emit pulses of constant amplitude, any shift of the LED signal position in the ADC spectrum would indicate a gain change<sup>2</sup>. In the discussion that follows,

<sup>2</sup>This is assuming that the amplitude of the pulses are indeed constant.

the LED pulser is referred to as the "flasher".

The flasher signal was created using four outputs from the LED unit, each with fiber optic cables to 22 Blowfish detectors. In addition, a copy of the LED pulses from each output channel was also sent to a Gadolinium-Silicon-Trioxide (GSO) detector to monitor the amplitude of the LED pulses. This ensured that the amount of light emitted by the LED did not change over time, which would lead to the false impression that the gain had changed.

A typical flasher pulse height spectrum is shown in Figure 4.6. Each spectrum was fit with a Gaussian function to determine the centroid value on a run-by-run basis. A flasher spectrum in the monitor detector looked similar to those of the Blowfish detectors and was also fit using a Gaussian function.

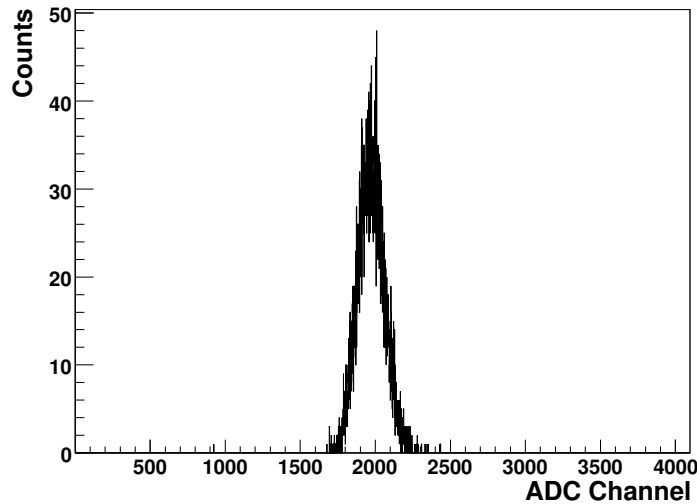


**Figure 4.6:** Typical Flasher spectrum for a Blowfish detector.

#### 4.5.4 Monitor Detector Source Peak Determination

In order to monitor any gain changes in the GSO monitor detectors, a single  $^{137}\text{Cs}$  source was placed near the four monitor detectors. This was to ensure that an apparent shift in the LED pulse amplitude as measured by a monitor detector was not in reality caused by a gain shift in the monitor detector itself. The  $^{137}\text{Cs}$  source spectrum consisted of a full energy peak on top of an exponential background as shown in Figure 4.7. Thus, the spectra were fit with a function consisting of a Gaussian plus an exponential combined with a flat background.

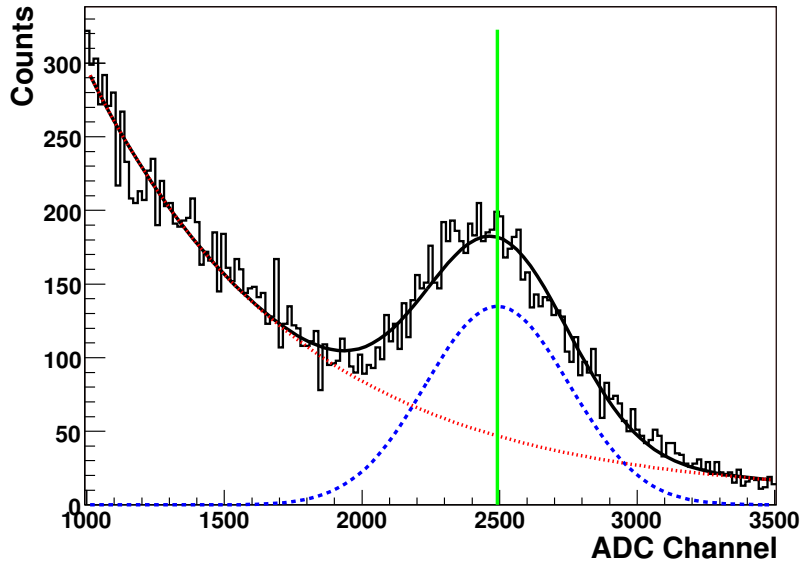


**Figure 4.7:**  $^{137}\text{Cs}$  source spectrum in a GSO monitor detector. The black curve is the fit to the spectrum, the dotted red curve is the sum of the flat background and exponential contribution to the fit, and the dashed blue curve is the Gaussian contribution to the fit. The centroid of the Gaussian is indicated with the solid green line.

### 4.5.5 Gain Determination for Production Runs

After obtaining the full-energy peak positions from the  $^{137}\text{Cs}$  source in the monitor detectors and the flasher centroids for the Blowfish and monitor detectors, this information was used in combination with a reference  $^{232}\text{Th}$  run to calculate the detector gains on a run-by-run basis. In essence, the measurement of the monitor detector gain ensured that the flasher centroid values were obtained correctly in the monitor detectors. The location of the monitor flasher signals then corrected the detector flasher location. The gain changes could then be measured using the relative position of the detector flasher signals.

Thus, the gain for a single detector is given by the expression [Bew05]

$$gain = \frac{E_{\gamma b}}{Source_{b1} \cdot \frac{LED_{b2}}{LED_{b1}} \cdot \frac{LED_{m1}}{LED_{m2}} \cdot \frac{Source_{m2}}{Source_{m1}}}. \quad (4.3)$$

The variables for Equation 4.3 are defined in Table 4.4.

A test of the GMS was performed by comparing the gains obtained for a  $^{232}\text{Th}$  source run directly via the Compton edge method to the gains obtained by using the GMS with an independent  $^{232}\text{Th}$  source run as the reference. This test yielded excellent agreement.

Figure 4.8 displays the gain value as a function of run number for two Blowfish detectors in order to give a sense of the variation in gain over time. Figure 4.8(a) shows the gains of a relatively stable detector as a function of time (run number) and Figure 4.8(b) shows the trend for one which is relatively unstable. The sharp changes in the gain tend to occur when the high voltage applied to the detector PMT is changed, when the detectors sit unused overnight between shifts, or when the array is rotated.

$E_{\gamma b}$	Compton edge energy for the 2615 keV $\gamma$ -rays from the $^{232}\text{Th}$ source
$Source_{b1}$	ADC channel value of the Compton edge in the Blowfish detector from the reference run
$LED_{b1}$	Centroid ADC channel value for LED flasher in the Blowfish detector for the reference run
$LED_{b2}$	Centroid ADC channel value for LED flasher in the Blowfish detector for a production run
$LED_{m1}$	Centroid ADC channel value for LED flasher in the monitor detector for the reference run
$LED_{m2}$	Centroid ADC channel value for LED flasher in the monitor detector for a production run
$Source_{m1}$	ADC channel value of the peak position of the $^{137}\text{Cs}$ source in the monitor detector from the reference run
$Source_{m2}$	ADC channel value of the peak position of the $^{137}\text{Cs}$ source in the monitor detector from a production run

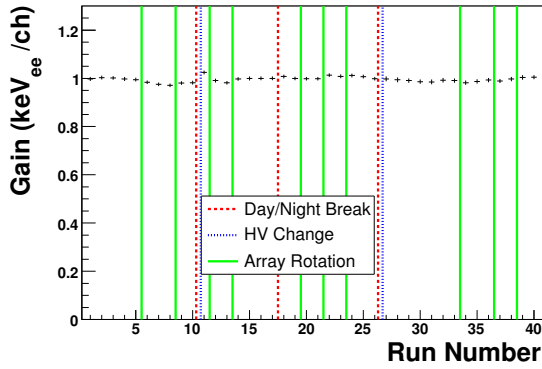
**Table 4.4:** Variable definitions for gain determination equation (Equation 4.3).

In order to ensure that the gain changes resulting from the rotation of the array were real, the pulse-height spectra before and after such a gain change were compared for beam-related events<sup>3</sup>. These spectra manifested scale changes corresponding to the changes in gain computed with the GMS, giving confidence that the gains extracted using the GMS were correct.

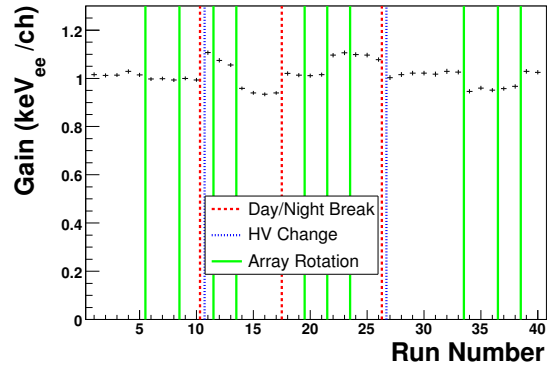
The rotation of the array also changed the  $\phi$  (azimuthal) position of all the detectors in the array. Due to the variation of the polarized cross section as a function of  $\phi$ , the count rate in a given detector depends upon the  $\phi$  angle at which it is located. Therefore, a check was done to determine if the gain changes were dependent upon the rates in the detectors. Figure 4.9 shows a scatter plot of detector gain as a function of detector rate as determined from the scalers. The points include all

---

<sup>3</sup>Here, beam-related events are specified as opposed to gain monitoring system events. Beam-related events are independent of the gain monitoring system and thus serve as a test for problems in the gain monitoring system.



(a) A detector with relatively stable gain.



(b) A detector with relatively unstable gain.

**Figure 4.8:** Gain values for two Blowfish detectors as a function of run number. The dashed red lines indicate times when the detectors were left on but unused for a period of time between the ending of a shift and the beginning of the next shift the subsequent day. Dotted blue lines indicate when a PMT high voltage change was made. Solid green lines indicate when the array was rotated.

the detectors in the array and all runs. From this plot, there appears to be no obvious correlation between detector rate and gain. The scatter plots for each detector individually look very similar.

The reason for the sudden gain changes that occurred after the array was rotated was ultimately never understood. One hypothesis is that the location of the small air bubble in each detector (see Section 3.5.2), which will move to different places in the detector volume depending on the detector  $\phi$  position, might be responsible for altering the light collection efficiency of the detector. Whatever the cause, the use of the GMS was a reliable way to measure these changes, which is a significant improvement over previous experiments with Blowfish that did not have the GMS.

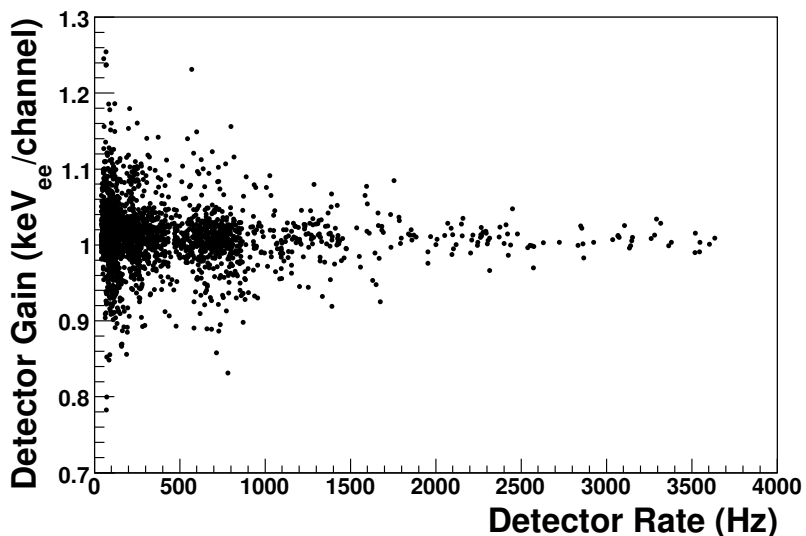


**Figure 4.9:** Scatter plot of detector gain versus detector rate. Rates were determined from the individual detector scalars. The points include all the detectors in the array and all runs with all beam energies.

## 4.6 TDC Calibration

The Blowfish TDCs were calibrated prior to this experiment to 0.1 ns/channel. The full range of values covered 1000 TDC channels or 100 ns. The zeros of the TDC spectra for the Blowfish detectors were each offset from each other by an arbitrary number of TDC channels. This is due to the varying amounts of delays present in the signals between the detector PMTs and the TDC input channels. In order to have each spectrum calibrated relative to a common reference time, they had to be adjusted with independent offsets in the TDC channel number.

This was accomplished by means of lining up the  $\gamma$ -flash for each TDC spectrum to a common TDC channel value. As explained in Section 3.6.2, the  $\gamma$ -flash events come from hits in the detectors that correspond in time to particles scattering from the target and traveling to the detector at the speed of light. These events are

typically Compton scattered photons. For production runs, triggers for these events were pre-scaled in order to avoid swamping the DAQ due to the high count rates in the detectors at forward angles. However, intermittently, runs were taken with the prescale factor set to 1, so that the TDC channel number of the  $\gamma$ -flash could be determined.

### 4.6.1 Scattering from Upstream Materials

In principle, the TDC channel number for the  $\gamma$ -flash can be determined by simply fitting the prominent peak corresponding to the  $\gamma$ -flash with a Gaussian function. However, during the course of the experiment two peaks were observed with timings near what was expected for the  $\gamma$ -flash in the upstream detectors of the array (see Figure 4.10).

The Blowfish detectors are arranged so that one detector from each arm is located at the same  $\theta$  as one detector from each other arm, comprising a ring of eight detectors of common  $\theta$  (see Table 3.3). For the ring of detectors which was closest to the beam axis and at the most extreme back angles ( $\theta = 157.5^\circ$  or Ring 1 from Table 3.3) the separation between the two peaks was greatest. This is seen in Figure 4.10(a). For Ring 2 the peaks were closer (Figure 4.10(b)) in time. The two peaks were observed to move closer as  $\theta$  approached forward angles until they totally overlapped at the forward angles.

The fact that they overlapped at forward angles indicated that the flight path for these upstream scattered  $\gamma$ -rays was not much different than those which scattered off the target. In order to verify which peak corresponded to scattering from the target and which peak was coming from upstream scattering, data were recorded with no target and a single peak was observed. The fact that it occurred earlier in time than

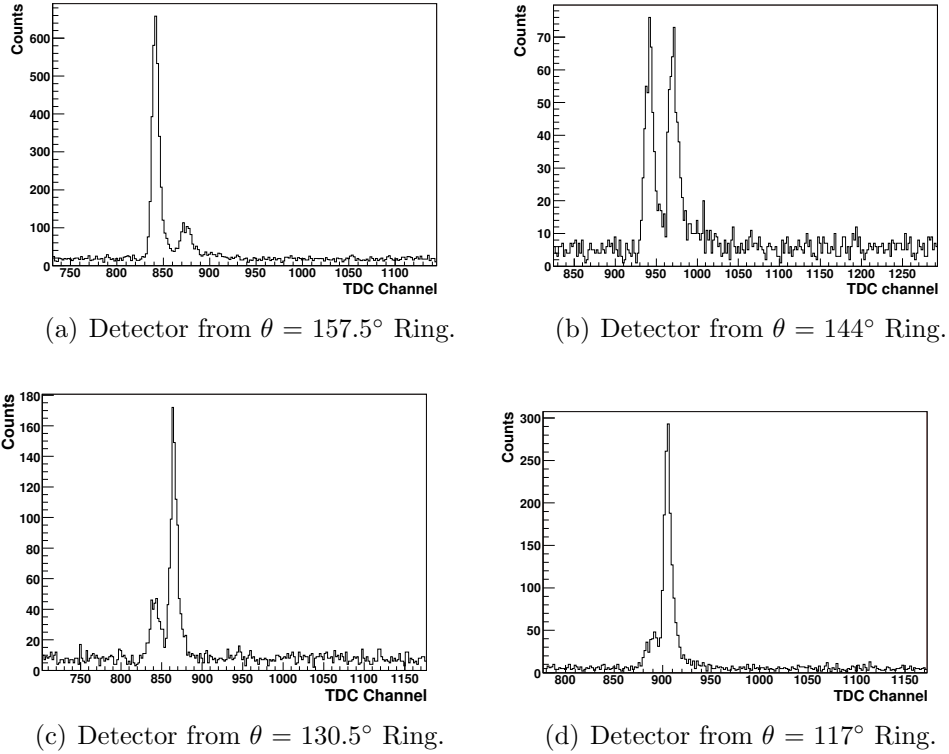


**Figure 4.10:** Double peaks from a  $\gamma$ -flash run for detectors of various  $\theta$ .

the true  $\gamma$ -flash along with the changing spacing between peaks with decreasing  $\theta$  indicates that the origin was from upstream of the target.

Note that the earlier peak has a much larger intensity than the  $\gamma$ -flash peak at  $\theta = 157.5^\circ$ , the two peaks have roughly equal intensities at  $\theta = 144^\circ$ , and the peak from upstream scattering gets steadily smaller as  $\theta$  decreases. The relative intensities as a function of  $\theta$  are shown in Figure 4.11 for a run with no target. The intensity of the early peak finally rises again for the most extreme  $\theta$  value of  $22.5^\circ$ . All of this points to small angle scattering from an upstream source.

The upstream object from which the beam scattered was never identified, but by making use of the no-target run, each extra peak location could be accounted for when performing the Gaussian fit to determine the true  $\gamma$ -flash location.

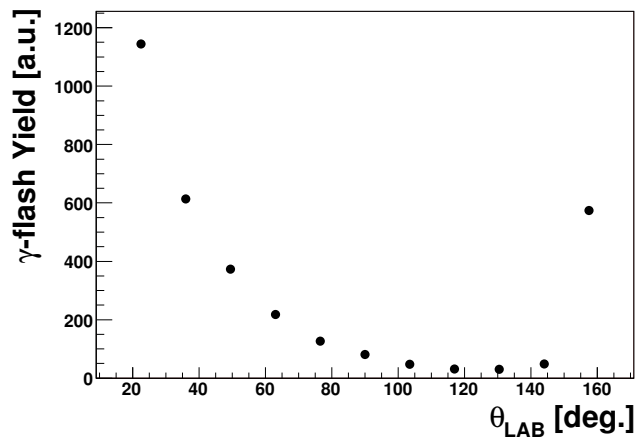


**Figure 4.11:** Ring yield versus  $\theta$  for a run with no target. The yields were determined by summing all yields in a ring of detectors having a common  $\theta$ . Error bars are smaller than the point size.

## 4.6.2 Gamma-flash Alignment

In order to fit the true  $\gamma$ -flash peak, a function consisting of the sum of two Gaussians was used, one for the true peak and one for the extra peak. Because the two peaks began to overlap so quickly as  $\theta$  decreased, a reliable extraction of the centroid and width of the extra peak was impossible for all angles. Thus, these parameters were fixed based on fits done to the spectra obtained from a run with no target. The amplitude of the extra peak was normalized by using a common scale factor for all detectors such that the extra peak amplitudes in the  $\theta = 157.5^\circ$  ring for both runs matched. The  $\theta = 157.5^\circ$  ring was chosen because the extra peaks in these detectors were the most clearly distinguishable of any of the rings (see Figure 4.10).

By fixing the centroid, width, and amplitude of the extra peak, a single Gaussian remained to be fitted to determine the TDC channel number for the  $\gamma$ -flash. An example of such fits at a few  $\theta$  values is shown in Figure 4.12. Once the  $\gamma$ -flash TDC

channel was determined, a simple offset was applied individually to each spectrum to align all  $\gamma$ -flashes to a common TDC channel.

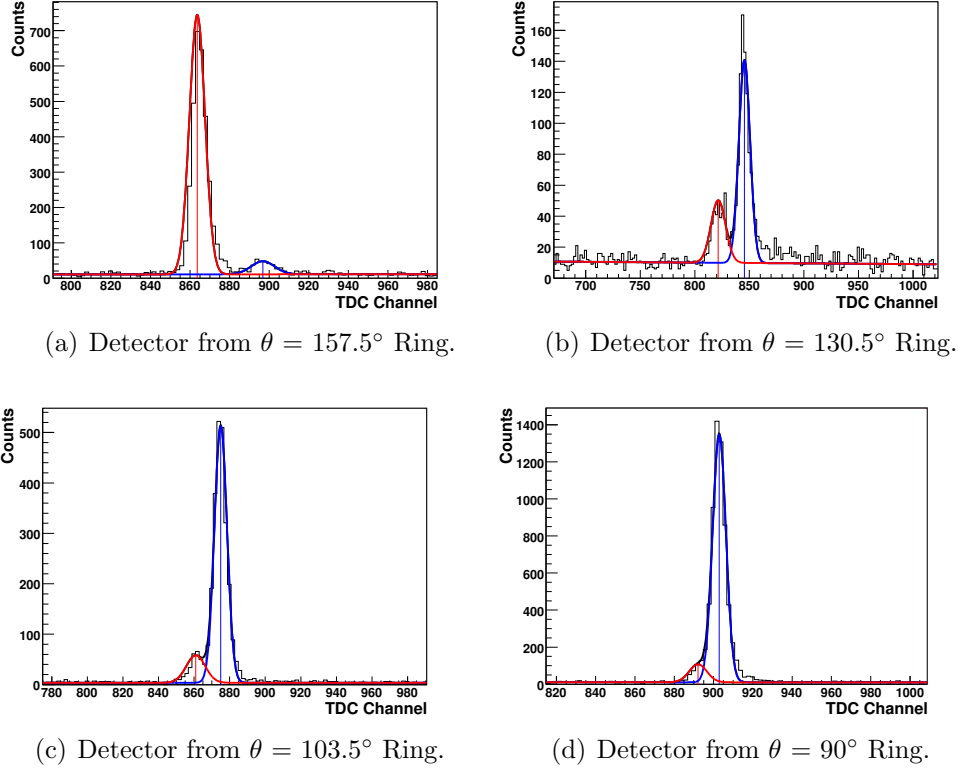


**Figure 4.12:** Fits to TDC spectra to determine  $\gamma$ -flash TDC channel. The red curve (always on the left) is the portion of the fit from upstream scattering, the blue curve (always on the right) is the fit to the  $\gamma$ -flash. Note that the  $\gamma$ -flash channel number is different for different detectors which is why the alignment of the  $\gamma$ -flash is necessary.

The neutrons resulting from the  $d(\vec{\gamma}, n)p$  reaction have energies that are uniquely defined by kinematics. This means that, for a given incident beam energy, the energies of the neutrons entering each detector are determined solely by the angle of the detector into which they scatter<sup>4</sup>. Figure 2.2 shows the relationship between the

<sup>4</sup>This is completely true only if multiple scattering, which will change a neutron's direction and energy after it re-scatters, is ignored. However, the statement is approximately true since the majority of neutrons found in the TDC spectra have a timing corresponding to the initial energy from the photodisintegration reaction.

outgoing neutron energies and the angle through which they scatter. Because of this, the precision of the TDC calibration for this experiment is not required to be exceedingly great. However, as is discussed in Section 4.10, the determination of the time-of-flight (TOF) window required the summing of all the TDC spectra from all the runs for a given beam energy. Therefore, the aligning of the spectra ensured that the spectra were not offset from each other, making the TOF window determination much easier.

## 4.7 Multiplicity Cut

Once all the calibrations were complete, the analysis cuts could be performed on the data sample. The first cut which was performed was the multiplicity cut. The multiplicity is defined as the number of detectors which produce non-zero signals for a given event. All events with multiplicity greater than 1 were cut from the data sample for the following reason.

For an event in which a single detector from Blowfish creates a trigger, the ADCs read all the channels with a common gate which is timed based upon the timing of the signal from the detector responsible for the trigger. If multiple detectors produce signals for a given event, the timing of the ADC gates will all be based on the timing of the signal of the first detector that fired. Since pulse-shape discrimination (PSD) (see Section 4.8) relies upon ADC gates that are precisely timed with respect to the signal, the possibility exists for the PSD determination to be unreliable for detectors that fire subsequent to the first one. The cut was applied when the multiplicity of either the TDC or pulse height was greater than 1.

## 4.8 Pulse-Shape Discrimination

In order to distinguish neutrons from  $\gamma$ -rays entering the Blowfish detectors, pulse-shape discrimination (PSD) was employed. The PSD method relies on the different mechanisms of interaction in the scintillator material by each particle.  $\gamma$ -rays and neutrons, being neutral particles, must first interact with charged particles in the detector in order for scintillation to occur.  $\gamma$ -rays interact primarily with the electrons and neutrons interact primarily with protons in the detector.

As a charged particle moves through the scintillator, it ionizes atoms and molecules and excites atomic and molecular states. Most of the light which comprises a signal is a result of prompt fluorescence which shows up as a large pulse with a fast decay time. However, some of the excited states are longer lived than others. When two molecules in these longer lived excited states interact, one can be left in the ground state and the other can be left in a shorter lived excited state which de-excites at a delayed time relative to the prompt emissions [Kno00].

Because the density of the longer-lived states depends on the rate of energy loss ( $dE/dx$ ), protons and electrons will produce different amounts of light due to delayed emissions. The differing yield from delayed emissions will manifest itself in the decay time of the pulse. In particular, protons, with higher  $dE/dx$ , will have longer “tails” (i.e. decay times) to their pulses than electrons. Figure 4.13 shows the difference in typical pulses from a neutron and a  $\gamma$ -ray in BC-505.

Figure 4.13 also shows examples of the long and short gates which were input to the ADC in order to integrate a copy of the pulse over nearly the entire pulse (long gate) and the pulse excluding the majority of the tail (short gate). The PSD parameter is then defined as the difference between the charge integrated over the long and short gates, giving a measure of the amount of charge in the tail of the

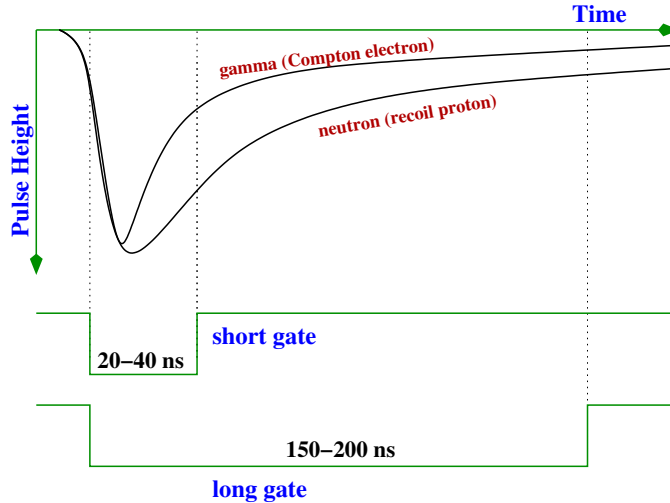


**Figure 4.13:** Typical pulse shapes for a neutron and a  $\gamma$ -ray in BC-505 with the long and short ADC gates used for PSD. The PSD parameter is the difference in the integrated signal using the long and short gates. Figure from [Saw05].

pulse.

When the pulse height<sup>5</sup> (PH) is plotted versus the PSD parameter for many events, two distinct “bands” of events develop in the spectrum, one corresponding to the neutrons and the other to the  $\gamma$ -rays. For this experiment, the long gates ranged from 150-200 ns and the short gate ranged from 20-40 ns. These gates were adjusted before the experiment until the optimum separation between  $\gamma$ -rays and neutrons was achieved. Figure 4.14(a) shows a typical PH versus PSD spectrum for a single detector.

#### 4.8.1 PSD Rotation

In order to make the PSD cut easier to apply, the PH versus PSD spectra were rotated to allow a one-dimensional cut to be applied to the PSD parameter. This was accomplished by shearing the PSD values by an amount that depended upon pulse

<sup>5</sup>Pulse height always refers to the charge integrated over the long gate.

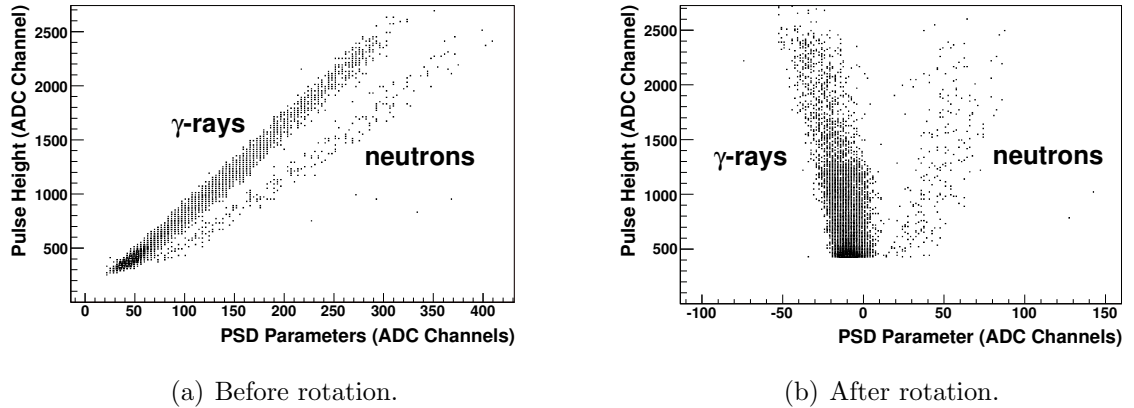


**Figure 4.14:** Pulse height versus PSD parameter for a single Blowfish detector before (a) and after (b) rotation. The neutrons appear in the lower band of the spectrum in (a) and the right-most band of the spectrum in (b). The  $\gamma$ -rays are in the upper and left bands respectively.

height.

The  $\gamma$ -band, which was well-defined for each run,<sup>6</sup> was first fit using a straight line. Then each entire spectrum was sheared by an amount such that the  $\gamma$ -band was placed on a common reference line. For the shear, no change was made to the PH values and the PSD values were simply shifted or offset by an amount that was dependent upon pulse height. The expression for the sheared PSD value ( $PSD_{shear}$ ) is given by

$$PSD_{shear} = PSD + \beta PH \quad (4.4)$$

where  $PSD$  is the original PSD parameter,  $PH$  is the original and unchanged PH value, and  $\beta$  is the pulse height dependent shear factor. An example of a sheared spectrum is given in Figure 4.14(b).

<sup>6</sup>The  $\gamma$ -band is well-defined for each run in contrast to the neutron band, which sometimes sees very little yield depending on a given detector's  $\phi$  location.

## 4.8.2 PSD Cut Determination

The rotated PH versus PSD spectrum allowed a simple cut to be applied to the PSD parameter. Depending on how well the timings of the short and long gates were tuned, there were varying degrees of separation between the neutrons and  $\gamma$ -rays for the Blowfish detectors. Therefore, a common PSD cut location for all detectors could potentially cut away true neutrons depending on where the cut was applied relative to the neutron-band.

In order to apply cuts that ensured that as many true neutrons were accepted for each detector as possible, a distinct cut was applied to each detector. This was done by creating a spectrum for each detector of the TDC value versus rotated PSD parameter. The individual TDC versus PSD spectra for all runs at a given energy were summed together for each detector<sup>7</sup>. An example of such a spectrum for a single detector is shown in Figure 4.15.

A window was then placed around TDC values corresponding to the timing of the photodisintegrated neutrons, as displayed in Figure 4.15. The part of the spectrum that fell within this wide window was then projected onto the PSD axis. The TDC window was utilized in order to maximize the neutron to  $\gamma$ -ray ratio in the projected spectrum. If this was not done, there would be so many  $\gamma$ -rays in the projected spectrum that the neutrons would be difficult to identify. The neutron peak was fit with a Gaussian function.

As a fit to a projected spectrum shows (Figure 4.16), the neutron peak sometimes overlaps with the  $\gamma$ -ray peak. Therefore the right-hand tail of the  $\gamma$ -ray peak was simultaneously fit with a Gaussian function. Finally, events with a PSD value greater

---

<sup>7</sup>In order to be done properly, the PSD value must be corrected by the gain value of each run before the summation.

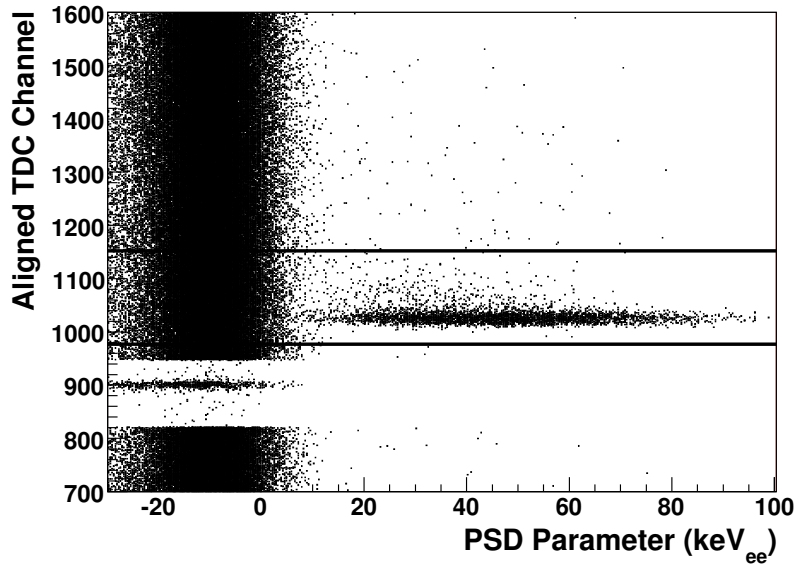


**Figure 4.15:** TDC versus rotated PSD parameter for a single Blowfish detector summed over all runs. The neutrons can be easily identified to the right of the well-populated  $\gamma$ -band on the PSD axis and at an unique time on the TDC axis. Lines indicate where the TDC cut is applied when determining the location of the PSD cut. The final TDC cut is determined as described in Section 4.10

than the point two sigmas to the left of the extracted neutron centroid were kept. Using this method for determining the PSD cut meant that, depending upon the separation between the  $\gamma$ - and neutron-bands, more or less  $\gamma$ -rays will be accepted for a given detector, contributing the background that must eventually be subtracted from the sample. However, in this way the PSD cut was applied in a consistent way for each detector.

## 4.9 Pulse Height Cut

The application of the PSD cut can have the effect of introducing an effective threshold for each detector which may be at value higher than the hardware threshold

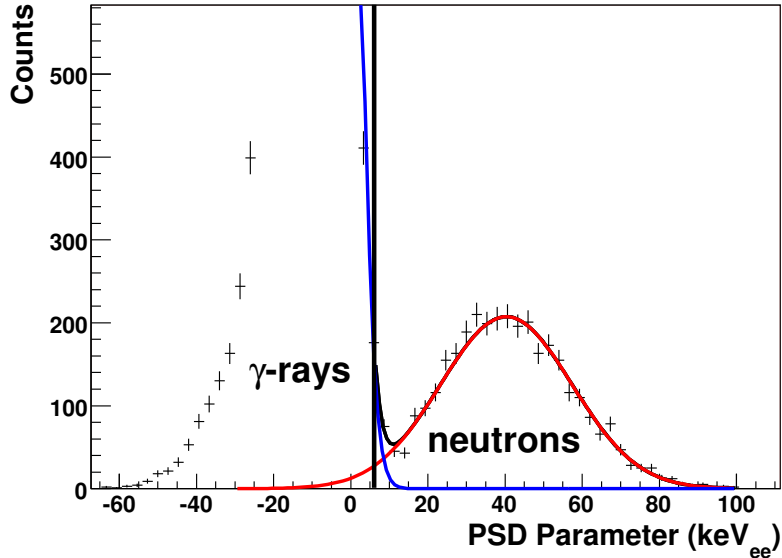


**Figure 4.16:** Histogram of PSD values for a single Blowfish detector summed over all runs within a wide TDC cut. The red curve is the fit to the neutron peak, the blue curve is a fit to the right-hand tail of the  $\gamma$  peak, and the black curve is the sum of the two. The placement of the PSD cut is marked by the vertical black line.

[Saw05]. Since a common PH cut was desired for all the Blowfish detectors in order to have a uniform efficiency as a function of neutron energy, the cut value was determined by extracting the highest single detector effective threshold after the PSD cut and choosing a PH cut value greater than that.

This was done by summing all the calibrated spectra for each detector, smoothing it and determining the edge as described in Section 4.5.2. A pulse height cut was then chosen to be sufficiently above the highest effective threshold. An example from a single detector is shown in Figure 4.17. Table 4.5 gives the values of the PH cut chosen for each energy.

In addition to achieving uniform efficiencies, having a common PH cut made it easier to apply a PH cut to the simulated data which was as close as possible to the

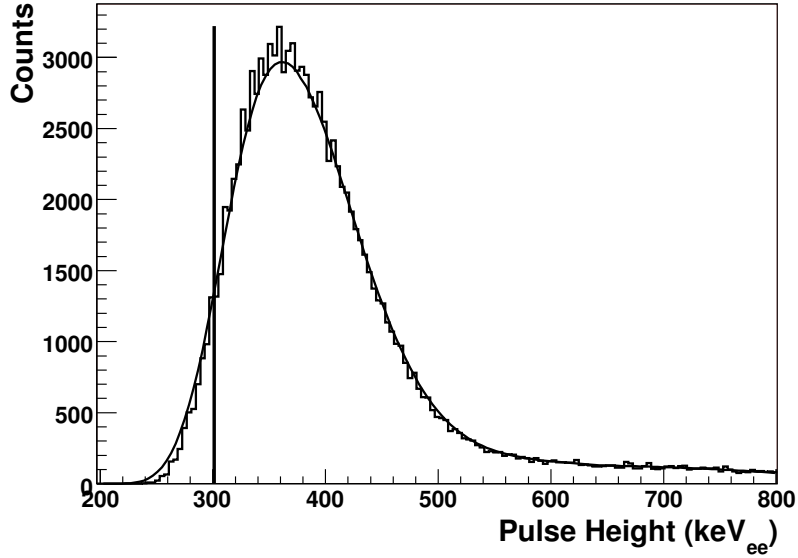


**Figure 4.17:** Pulse height spectrum after PSD cut. The effective threshold is marked by a vertical line.

$E_\gamma$	PH Cut
14.0 MeV	518 keV <sub>ee</sub>
16.0 MeV	595 keV <sub>ee</sub>

**Table 4.5:** Software PH cuts for each beam energy.

cut applied to the data.

## 4.10 Time of Flight Cut

Figure 4.18 shows what TDC spectra for detectors oriented horizontally and vertically look like before and after the PSD and PH cuts are applied. The final cut to the data was applied to the TDC values. A window was chosen that would select events in the TDC spectra with a timing such that they corresponded to the neutrons of the expected energy from kinematics.

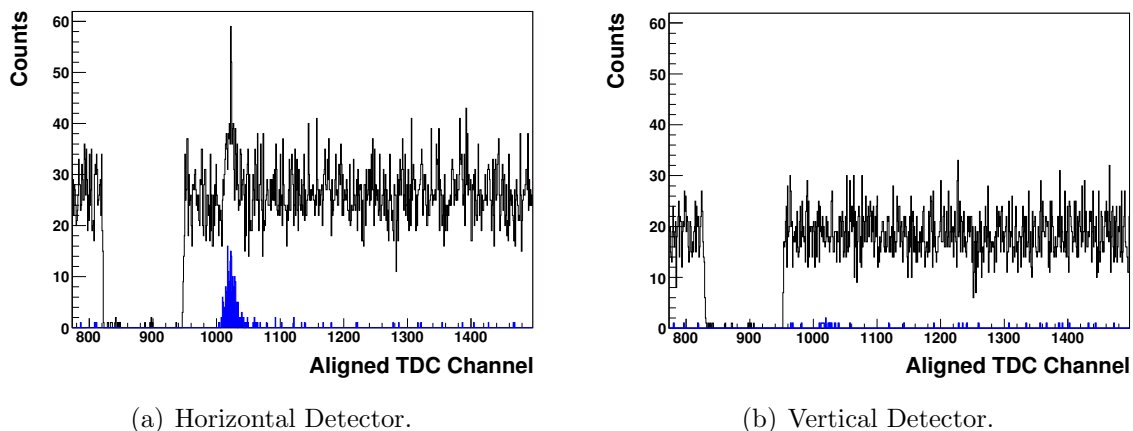


**Figure 4.18:** TDC spectra before and after PSD and PH cuts for detectors oriented (a) horizontally (in the plane of polarization of the  $\gamma$ -ray beam) and (b) vertically (perpendicular to the plane of polarization). The black histogram is the TDC spectrum before PSD and PH cuts are applied and the solid blue histogram (barely visible in (b)) is the spectrum after these cuts are applied. Spectra represent a single run.

Because the photodisintegration reaction we are studying is dominated at these energies by interactions involving electric dipole ( $E1$ ) radiation (see Section 1.2.1), linearly polarized  $\gamma$ -rays incident upon the target will produce neutrons primarily in directions parallel to the plane of polarization. Conversely, very few neutrons will be emitted in directions perpendicular to the plane of polarization. Therefore, the TDC peak for detectors perpendicular to the polarization plane was difficult to locate (see Figure 7.2(b), for example). However, since the Blowfish array was periodically rotated about the beam axis, runs for all the orientations of the array could be summed together in order to give a clear peak when determining the TDC windows. It should also be noted that because the neutrons from the photodisintegration reaction were mono-energetic for a given  $\theta$ , an absolute calibration of the TDC spectra was unnecessary.

The TDC window was determined by fitting the TDC peak with a Gaussian

function on the left side of the peak and extending just past the centroid value (see Figure 4.19). The entire peak was not fit because the right side of the peak possessed a tail due to slower moving neutrons, which result from multiple scattering in the target. From the fit, the centroid value and width of the TDC peak was obtained. The lower TDC limit was then taken to be 3 sigmas below the centroid. The entire window was selected to be 20 ns long, or 200 channels. This wide window was used in order to ensure that all the neutrons, including the slower ones, were included in the sum. This made the analysis less dependent upon the location of the cut and had negligible effect on the errors on the yields after the subtraction of random TDC events, discussed below.

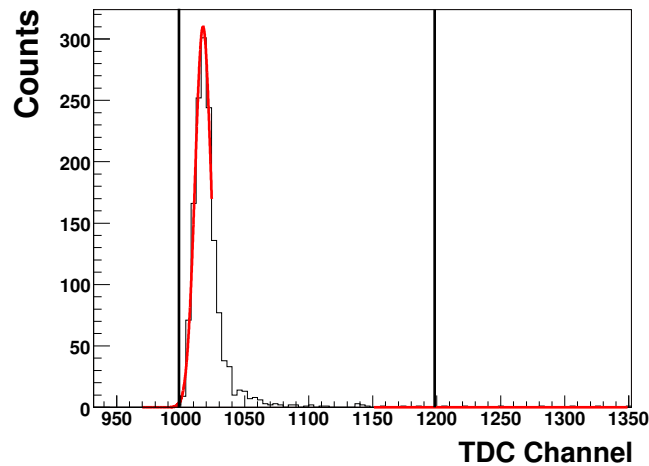


**Figure 4.19:** TDC window determination for a single blowfish detector summed over all runs for a given energy. The red curve is the Gaussian fit to the spectrum and the vertical lines indicate the TDC window used for selecting events.

## 4.11 Neutron Yields

The neutron yield for a given detector was obtained by counting events which passed the multiplicity cut, the PSD cut, the PH cut, and fell within the TDC window. A large window, though not necessarily of equal size, was also selected in the TDC spectra with events that did not correspond in time to the photodisintegrated neutrons. Events in this extra window which passed the same cuts were summed as a sample of the random TDC events. These yields were scaled to match the 20 ns timing window of the “true” neutrons and the difference between the yields in the two windows represented the final neutron yield for a detector. For detectors with good separation of neutrons from  $\gamma$ -rays in the PSD spectra, the random background was small. However, for detectors with poorer PSD separation, the number of random events could be large enough to have a small but perceivable effect on the statistical error of the yields after the subtraction.

In principle, the yields obtained from runs with the H<sub>2</sub>O target should be properly normalized and subtracted from the yields obtained from the D<sub>2</sub>O target runs. However, due to the fact that there was so little background from the H<sub>2</sub>O runs, that procedure had a negligible effect on the yields.

Figure 4.20 shows a plot of raw yields versus detector number for one orientation of the Blowfish array at  $E_\gamma = 14$  MeV. Notice that because of the numbering convention of the detectors in the array (see Table 3.3), three distinct bands exist. The band with lower yields corresponds to detectors oriented vertically, the upper band corresponds to detectors oriented horizontally, and the middle band corresponds to detectors oriented at 45° with respect to the horizontal plane. The middle band is more dense because for any given orientation there are four arms of detectors oriented 45° from the horizontal, whereas the vertical and horizontal directions have only two arms

each.

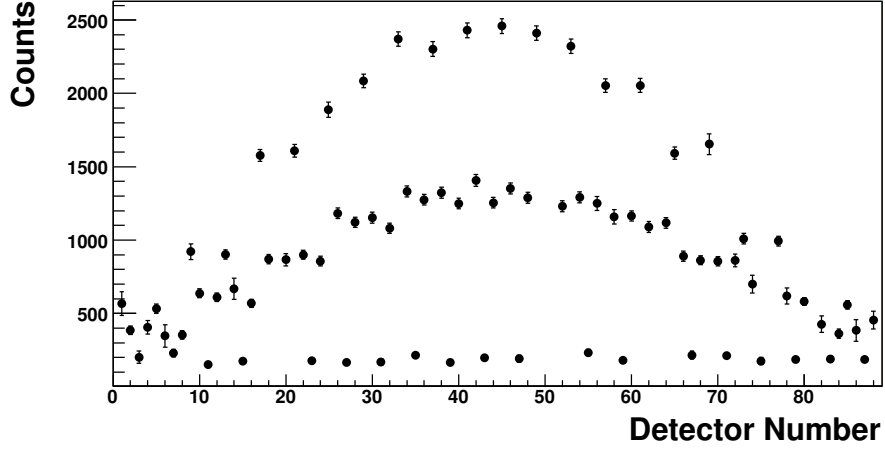


**Figure 4.20:** Raw yields versus detector number for one orientation of the Blowfish Array at  $E_\gamma = 14$  MeV.

#### 4.11.1 Bad Detectors

Several detectors had problems which did not allow them to be used in the analysis. One detector had an extremely poor PH versus PSD spectrum. A few others had drastic gain changes in the midst of single runs as seen in the flasher spectrum from the gain monitoring system. In addition, a few detectors had TDC spectra whose  $\gamma$ -flash position shifted considerably on a run-by-run basis.

For the 16 MeV runs, all the detectors in two rings experienced a common problem and the source was never identified. These detectors, located at  $\theta = 63^\circ$  and  $76.5^\circ$ , exhibited an effective gain shift that lowered the gains on each detector which could not be accounted for using the gain monitoring system. This resulted in a higher effective threshold on the detectors, which lowered their efficiencies. Each of the detectors on these two rings shared a common high voltage power supply module,

so it is possible that a malfunction of this module is the cause of the problem. The effect of having lower efficiencies in these detectors is canceled out in the case of the analyzing powers (see Section 4.13.2) but not in the angular distribution of the unpolarized cross section. Therefore, these detectors were discarded from the analysis of the 16 MeV data.

The yields from all “bad” detectors were deemed unreliable to use in the construction of the observables. Overall, 82 and 69 of the 88 Blowfish detectors were included in the analysis for the 14 MeV and 16 MeV data sets, respectively.

## 4.12 Beam Polarization Axis

A previous measurement using the Blowfish array found a significant deviation of the beam polarization axis from the horizontal plane, which is the plane expected as a result of the design of OK-4 [Saw05]<sup>8</sup>. The polarization plane had rotated by angles as large as 11°. In order to ensure that the polarization plane was horizontal in this experiment, the neutron yields were used to extract the angle of the polarization plane.

The detectors in a single arm of the Blowfish array all share a common  $\phi$  value. If the angle of the polarization axis was inconsistent with 0°, it would be evident in unequal yields in the detectors in the arms oriented at 45° with respect to the horizontal. A plot of the arm yields as a function of  $\phi$  is shown in Figure 4.21 for the 14 MeV data. In this figure, the arm yields for all orientations have been combined by computing the geometric mean in the same way as described in Section 4.13.

Notice that because of the linearly polarized beam and the dominance of electric

---

<sup>8</sup>The reasons for this are mentioned in Section 3.4.3.

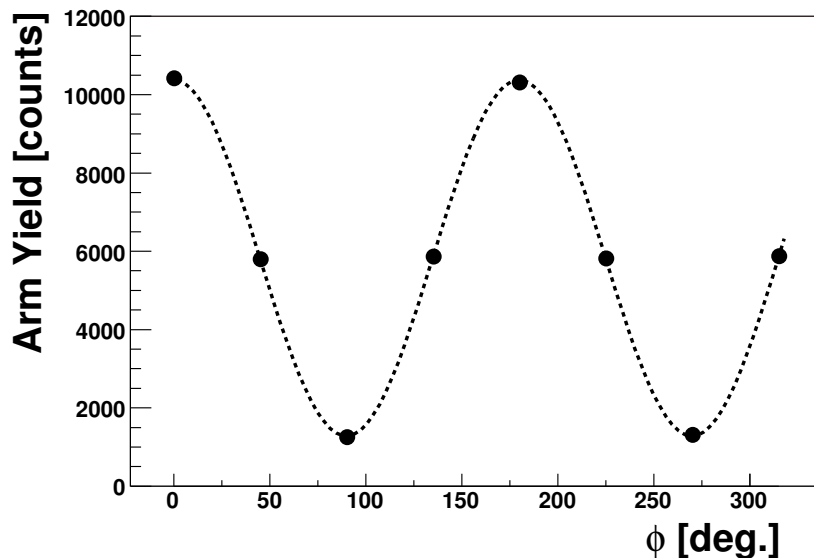


**Figure 4.21:** Neutron yields for each arm of the array as a function of  $\phi$  for all Blowfish orientations at 14 MeV. The dashed line is a fit to the data to determine the angle of the polarization plane with respect to the horizontal. The error bars on the data are smaller than the point size.

dipole ( $E1$ ) transitions in the reaction at these energies, most of the yield appears in the  $\phi = 0^\circ$  and  $180^\circ$  arms, with very little yield in the  $\phi = 90^\circ$  and  $270^\circ$  arms.

By considering only the  $\phi$  dependence of the yields, these data were fit with a function of the form<sup>9</sup>

$$Y(\phi) = A + B \cos [2(\phi - \delta)], \quad (4.5)$$

where  $Y(\phi)$  is the detector yield as a function of  $\phi$ ,  $A$  is the parameter in the fit that gives the overall offset of the data from zero,  $B$  is the parameter in the fit which describes the amplitude of the cosine term, and  $\delta$  is the free parameter which is a measure of the deviation of the angle of polarization from the horizontal.

A fit to the data is shown in Figure 4.21 and the values obtained from the fit for

---

<sup>9</sup>This is the most general form for the  $\phi$ -dependent cross section for the case of linearly polarized photons, as can be seen by taking the associated Legendre polynomial expansion of the cross section found in Equation 5.3 and integrating out the  $\theta$  dependence.

$\delta$  for both energies are summarized in Table 4.6. While they are not in agreement with zero, their values are extremely small, indicating that the axis of polarization does not significantly deviate from the horizontal plane.

Beam Energy	$\delta$
14 MeV	$0.19^\circ \pm 0.16^\circ$
16 MeV	$-0.31^\circ \pm 0.14^\circ$

**Table 4.6:** Extracted deviations of axis of polarization from the horizontal.

An equivalent way of investigating possible deviations is by constructing the linear analyzing power using the detectors  $45^\circ$  from the horizontal plane instead of the vertical and horizontal detectors. The expression for the analyzing power using these detectors is (cf. Equation 1.1)

$$\Sigma_{45^\circ}(\theta) = \frac{1}{P_\gamma} \frac{Y(\theta, \phi = 45^\circ) - Y(\theta, \phi = 135^\circ)}{Y(\theta, \phi = 45^\circ) + Y(\theta, \phi = 135^\circ)} \quad (4.6)$$

where  $Y(\theta, \phi)$  is the yield in a detector located at a given  $\theta$  and  $\phi$  and  $P_\gamma$  is polarization fraction, which is taken to be 1.0 for the HI $\gamma$ S beams. The yields for the various orientations of the Blowfish array were combined as described in Section 4.13.

When constructed using the  $45^\circ$  detectors, the analyzing power values should be consistent with zero if the polarization plane is horizontal. Figure 4.22 shows the  $45^\circ$  analyzing powers for each beam energy. A straight line fit has also been applied to the data to see if the values are consistent with zero. The fit values are presented in Table 4.7.

As with the fits to the yields summed over each arm, the values are not consistent with zero, but are very small. This gives us confidence that the axis of polarization is very nearly horizontal. From this analysis, a conservative estimate of  $\pm 1^\circ$  is adopted

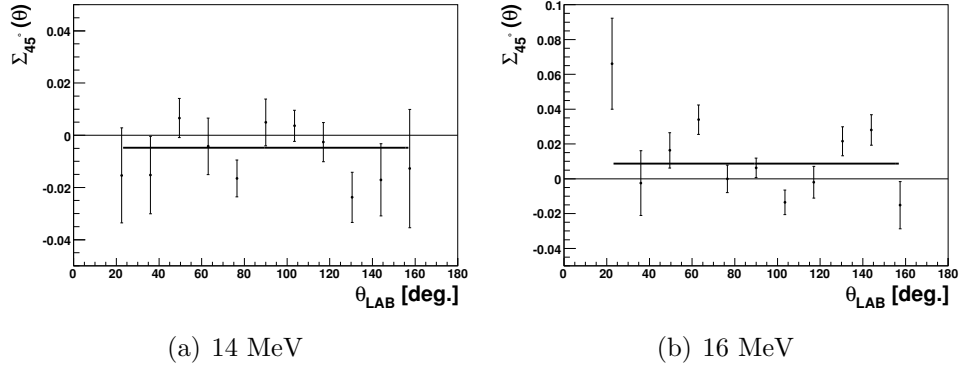


**Figure 4.22:** The analyzing power constructed using the  $45^\circ$  detectors for each beam energy. The expression for  $\Sigma_{45^\circ}$  is given in Equation 4.6. Also shown is a straight line fit to the data.

Beam Energy	Fitted $\Sigma_{45^\circ}$
14 MeV	-0.0048 $\pm$ 0.0028
16 MeV	0.0087 $\pm$ 0.0027

**Table 4.7:** Fitted analyzing power values using detectors at an angle of  $45^\circ$  from the horizontal plane.

for how well the beam polarization axis is known (see Section 5.8).

### 4.13 Raw Observables

The experimental observables are constructed in terms of the raw yields, and are therefore raw in the sense that they have not yet been corrected for finite geometry and multiple scattering effects. The two observables accessible from this experiment are the angular distributions of the unpolarized differential cross section and the linear analyzing power (see Section 1.2.1).

Because of the symmetry of the Blowfish array and the symmetry of the reaction being studied, the number of counts in any two detectors of common  $\theta$  which are  $180^\circ$  from each other in  $\phi$  should see an identical number of counts within statistics.

This expectation has already been confirmed in the studies to determine the beam polarization axis in the previous section.

Therefore, the final yields used in constructing the observables were taken from the weighted mean of such a pair of yields. The weighted mean for the yields from two detectors,  $N_1$  and  $N_2$ , is given by

$$\bar{N} = \frac{N_1/\delta N_1 + N_2/\delta N_2}{1/\delta N_1 + 1/\delta N_2}, \quad (4.7)$$

where  $\delta N$  is the error on the respective detector yield. The error on the mean for two measurements is [Bev92]

$$\delta \bar{N}^2 = \frac{(N_1 - \bar{N})^2(1/\delta N_1^2) + (N_2 - \bar{N})^2(1/\delta N_2^2)}{(1/2)(1/\delta N_1^2 + 1/\delta N_2^2)}. \quad (4.8)$$

For the case of a pair which includes a discarded detector, the mean was simply taken to be the value of the one good detector in the pair with its error.

In addition, for each beam energy there were four orientations of the Blowfish array which were used. For instance, a given arm of the array might assume  $\phi$  values of  $0^\circ$ ,  $45^\circ$ ,  $90^\circ$ , and  $135^\circ$  in successive runs. Therefore, each set of yields at all four orientations had to be combined into single set of yields, which was done by forming the geometric mean.

For example, in the case of two orientations, Figure 4.23 illustrates how the locations of two detectors change. Detector A moves from a horizontal position in Run 1 to a vertical position in Run 2, and detector B does the opposite. In this case, with only two orientations to combine, the geometric mean for the yield in the horizontal direction is written as

$$Y_H = \sqrt{A_1^H B_2^H}, \quad (4.9)$$

where  $A_1^H$  is the yield in detector A for Run 1 when it is horizontal and  $B_2^H$  is the yield in detector B for Run 2 when it is horizontal. The associated error on the mean is

$$\delta Y_H = \frac{Y_H}{2} \sqrt{\left(\frac{\delta A_1^H}{A_1^H}\right)^2 + \left(\frac{\delta B_2^H}{B_2^H}\right)^2}, \quad (4.10)$$

where  $\delta A_1^H$  is the error on  $A_1^H$  and likewise for  $B_2^H$ . A similar combination can be done for the vertical detectors and for those oriented at  $45^\circ$  from the horizontal.

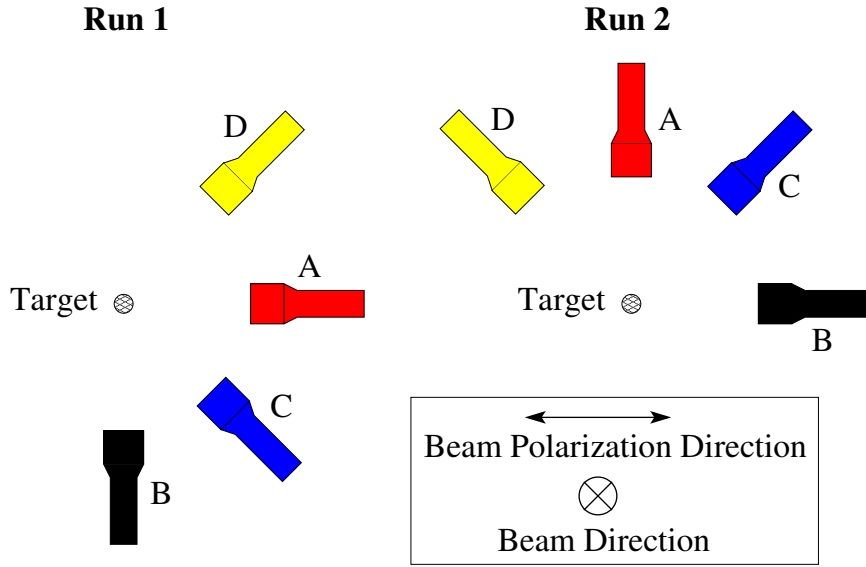


**Figure 4.23:** Schematic of the detector location relative to the polarization plane for a pair of array orientations. From Run 1 to Run 2, the black detector, labeled  $B$ , moves from a vertical position, labeled  $V$ , to a horizontal position, labeled  $H$ . The red detector, labeled  $A$ , moves from a horizontal position to a vertical position. Detectors  $C$  and  $D$  assume horizontal and vertical orientations for Runs 3 and 4.

In the case of combining yields from four orientations, the geometric mean is given in terms of two additional detectors,  $C$  and  $D$ , which assume horizontal positions in Runs 3 and 4, respectively. The geometric mean and associated error in this case is given by

$$Y_H = \sqrt[4]{A_1^H B_2^H C_3^H D_4^H} \quad (4.11)$$

and

$$\delta Y_H = \frac{Y_H}{4} \sqrt{\left(\frac{\delta A_1^H}{A_1^H}\right)^2 + \left(\frac{\delta B_2^H}{B_2^H}\right)^2 + \left(\frac{\delta C_3^H}{C_3^H}\right)^2 + \left(\frac{\delta D_4^H}{D_4^H}\right)^2}, \quad (4.12)$$

and likewise for the vertical and 45° yields.

The yields from all four orientations of the array were combined via the geometric mean for both beam energies. Combining the yields in this way has an additional advantage for analyzing power measurements, which will be discussed in Section 4.13.2.

### 4.13.1 Uncorrected Unpolarized Cross Section

Since the absolute flux on target was not measured for this experiment, the absolute values of the unpolarized differential cross section could not be obtained. However, the shape of the angular distribution was accessible, which is related to the absolute differential cross section by a scale factor.

The shape was obtained by simply summing the yields from all of the detectors having a common  $\theta$ , or in a ring of the Blowfish array. The summation essentially integrates out the effects of having a polarized beam. The uncorrected unpolarized differential cross sections are shown in Figure 4.24 for each beam energy. Note that the overall normalization is arbitrary.

### 4.13.2 Uncorrected Analyzing Power

The analyzing power for the reaction has been defined in Equation 1.1. Neglecting multiple scattering and finite geometry effects, this observable can be constructed in terms of detector yields. These effects are accounted for using a simulation of the experiment as described in Chapter 5. For the HI $\gamma$ S beams, the degree of polarization

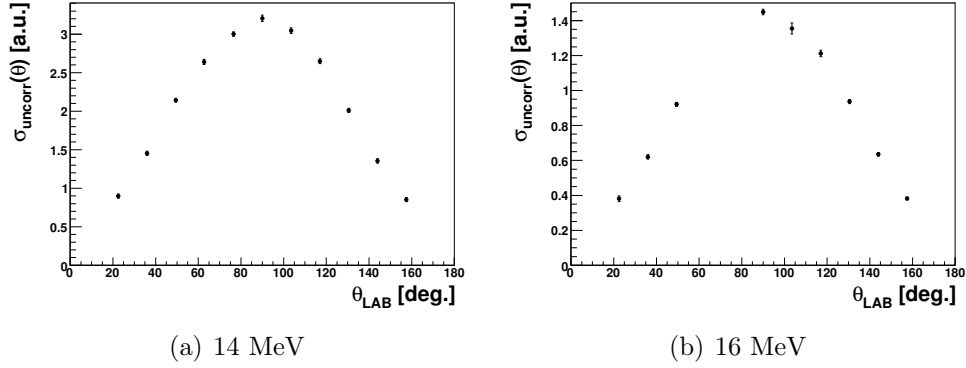


**Figure 4.24:** Uncorrected unpolarized differential cross section for each beam energy.

is nearly 100% and thus  $P_\gamma$  is assumed to be 1.0 (see Section 3.2.3).

The construction of the yields in terms of the geometric mean of several orientations of the array has the advantage that many of the systematic effects can be canceled in the analyzing power. This is done by writing the analyzing power as

$$\Sigma(\theta) = \frac{1 - R(\theta)}{1 + R(\theta)}, \quad (4.13)$$

where

$$R = \sqrt[4]{\frac{A_1^H B_2^H C_3^H D_4^H}{A_2^V B_1^V C_4^V D_3^V}} = \frac{Y_H}{Y_V}. \quad (4.14)$$

The labeling convention is the same as defined for Equation 4.9.  $Y_H$  and  $Y_V$  are the geometric means which are defined as described in Equation 4.11.

Notice in Equation 4.14 that since a given detector appears in both the numerator and denominator of the ratio, the detector efficiency will cancel. Also, since a given orientation of the array appears in both numerator and denominator, the beam flux will also drop out.

The errors on  $R$  and  $\Sigma$  are given by

$$\delta R = R \sqrt{\left(\frac{\delta Y_H}{Y_H}\right)^2 + \left(\frac{\delta Y_V}{Y_V}\right)^2}, \quad (4.15)$$

and

$$\delta \Sigma = \frac{2 \delta R}{(R + 1)^2}, \quad (4.16)$$

where  $\delta Y_H$  and  $\delta Y_V$  are given by Equation 4.12.

This method was used for the computation of the raw analyzing powers for both energies, and the results are shown in Figure 4.25. The correction of both observables for multiple scattering and finite geometry effects will be discussed in the next chapter.

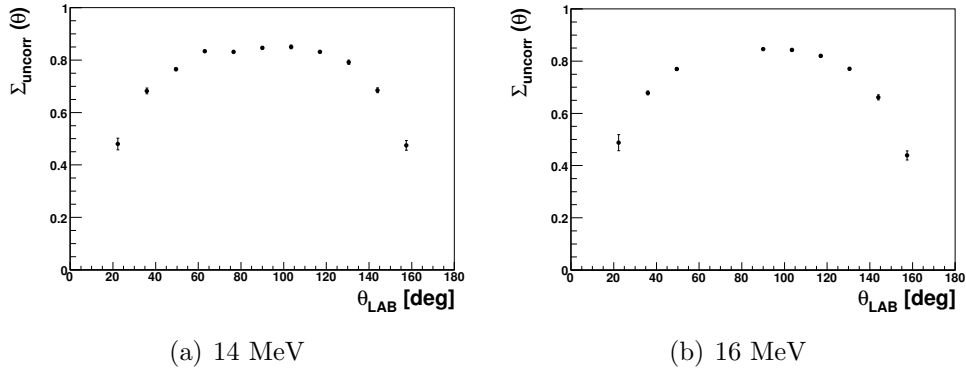


**Figure 4.25:** Uncorrected analyzing power for each beam energy.

# Chapter 5

## Simulations and Data Correction

### 5.1 Introduction

This chapter describes how the raw or uncorrected observables from the previous chapter (see Section 4.13) were corrected for effects such as neutron re-scattering in the target or from other materials and the finite geometry of the experiment. This was accomplished via a simulation of the experiment using the `GEANT4` toolkit which is introduced in Section 5.2. The simulation is described in Section 5.3, and issues related to ensuring that the simulation accurately represents what was observed experimentally are discussed in Section 5.4. The analysis of the simulated data created by `GEANT4` is summarized in Section 5.5 and the method used to correct the data is described in Section 5.7. Finally, a discussion of how systematic errors were estimated is found in Section 5.8.

### 5.2 The `GEANT4` Toolkit

`GEANT4` is a simulation toolkit which was developed for simulating the passage of particles through matter [Ago03]. It includes the following components of importance for the simulation of this experiment:

- the geometry of the target and detectors,

- the materials involved,
- the generation of primary particles, such as neutrons,
- the tracking of particles through materials,
- the physics processes governing particle interactions,
- the response of detectors to interactions, and
- the visualization of the detector and particle trajectories.

The simulation used for this experiment was a modified version of `blowfishX` [Wur06]. `blowfishX` contained all the geometry and materials for the Blowfish array as well as the proper incorporation of responses for the Blowfish detectors. In addition to this, event data from `GEANT4` were recorded in the same format as the experimental data by interfacing the simulation to `LUCID`. Therefore, the `GEANT4` data could be analyzed from start to finish in a way which was identical to the experimental data.<sup>1</sup>

The basic `blowfishX` version was modified to include the target materials and geometry, several primary particle generators, as well as several other additions used to exploit the features of the simulation.

## 5.3 Description of the Simulation

### 5.3.1 Geometry and Materials

The active scintillation volume and lucite light guide for each Blowfish detector was built within `GEANT4` based on the actual dimensions. The detector bases were not

---

<sup>1</sup>As will be discussed in Section 5.5, this statement is true of everything except PSD which was not simulated. Therefore, no PSD cut was applied to the `GEANT4` data.

included in the geometry definition. The composition of the liquid scintillator was taken from the Bicron Data Sheet for BC-505, which gives a Hydrogen to Carbon ratio of 1.331. In addition to the 88 detectors, the entire aluminum frame of the array was defined, along with the steel box which housed the power supplies for the detector PMTs.

D<sub>2</sub>O, H<sub>2</sub>O, and “target-out” configurations were available by simply changing a flag in an input file which is read in each time a simulation runs. The thin plastic walls of the target and the aluminum pipe which supported it were also included. The entire experiment was housed in a large volume of air.

A picture of the defined geometry can be found in Figure 5.1.

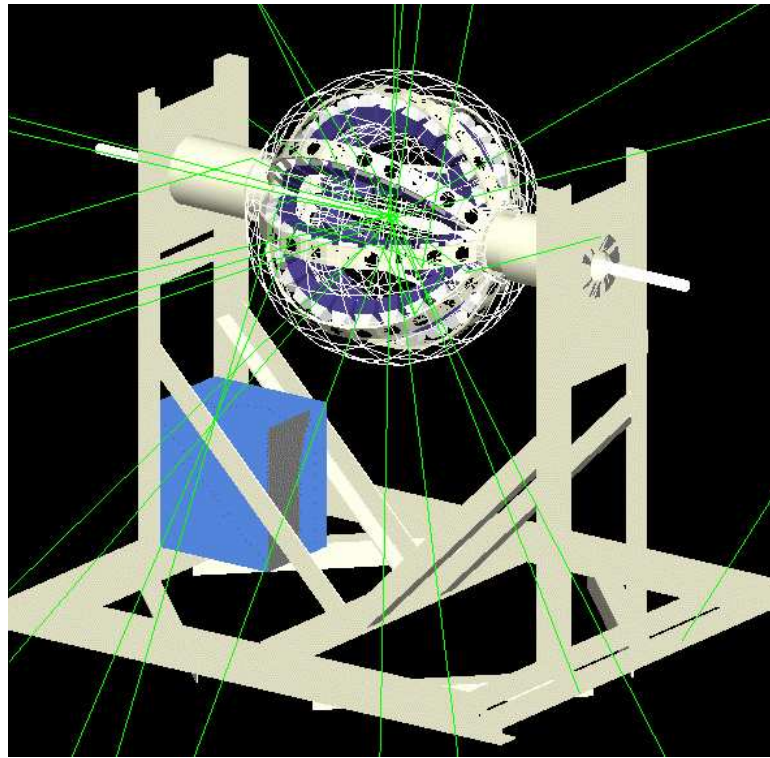


**Figure 5.1:** The Blowfish array and target geometry as defined in the GEANT4 simulation. The lines represent the paths of neutrons generated by the simulation.

### 5.3.2 Physics Processes Included

Electromagnetic and hadronic physics processes involving the following projectiles were included in the simulation. Other processes were included, but are not listed here because of their irrelevance to the present experiment.

- $\gamma$ -rays: photoelectric effect, Compton scattering,  $e^+e^-$  production, photonuclear processes<sup>2</sup>
- electrons/positrons: multiple scattering, ionization, bremsstrahlung,  $e^+e^-$  annihilation, synchrotron radiation, electronuclear processes<sup>3</sup>
- protons and other ions: Rutherford scattering, ionization, and other inelastic reactions such as  $(p, \alpha)$ ,  $(p, n)$ , etc.
- neutrons:  $(n, n)$ ,  $(n, \gamma)$ , and other inelastic reactions such as  $(n, \alpha)$ ,  $(n, n)$ , etc.

All processes were implemented for all nuclei defined in the simulation via the LHEP\_PRECO\_HP physics list which is built-in to GEANT4. The G4NDL3.7 package contains the evaluated data libraries used by LHEP\_PRECO\_HP. These libraries were compiled specifically for applications that required the handling of interactions involving neutrons with high precision. The evaluated data libraries come from the following sources<sup>4</sup>:

---

<sup>2</sup>Photonuclear processes refer to inelastic  $\gamma$ -ray scattering with nuclei.

<sup>3</sup>Electronuclear processes refer to inelastic electron scattering with nuclei.

<sup>4</sup>These libraries can be accessed via the internet. For instance, many are available at the Los Alamos National Laboratory's T2 Nuclear Information Service at <http://t2.lanl.gov/>.

- Brond-2.1
- CENDL2.2
- EFF-3
- ENDF/B-VI.0
- ENDF/B-VI.1
- ENDF/B-VI.5
- FENDL/E2.0
- JEF2.2
- JENDL-FF
- JENDL-3.1
- JENDL-3.2
- MENDL-2

### 5.3.3 Generating Primary Particles

Two approaches could be taken to generating the primary particles in the experiment: a  $\gamma$ -ray beam could be incident upon the target and the cross section for the photodisintegration reaction could be defined by the user in **GEANT4**, or a distribution of neutrons could be generated within the target volume independent of a  $\gamma$ -ray beam according to a chosen distribution which characterizes the reaction cross section. The amount of computing time required to perform the former simulation is significantly greater than the amount required for the later. Therefore, since no significant advantage could be seen to the  $\gamma$ -ray beam method, a distribution of neutrons was generated within the target volume.

A one-inch diameter collimator was used during production runs, so neutrons were generated in the target uniformly within a one-inch diameter circle in the transverse plane (the plane perpendicular to the beam direction). Neutrons were also generated along the length of the target, with a non-uniformity introduced to account for attenuation of the  $\gamma$ -ray beam through the water target. Attenuation factors were obtained from NIST [Nat]. The effect of attenuation meant that there were about

10% less  $\gamma$ -rays in the downstream end of the target as compared to the upstream end. Therefore about 10% less neutrons were generated in the downstream end of the target, though the inclusion of attenuation in the target had a negligible effect on the result (see Section 5.8).

Neutrons were generated with energies determined by the conservation of energy and momentum for a given incoming  $\gamma$ -ray beam energy. The beam energy distribution was approximated by a Gaussian function with centroid and FWHM values matched to the values from Table 4.1.

## 5.4 Understanding the Simulation

Several checks were performed to ensure that the experiment was simulated under the most realistic conditions possible. Because the multiple scattering of neutrons leaving the target was such a significant effect, several neutron scattering cross sections were checked. In addition, the light output response of the detectors needed to be well-known in order to ensure that the detector response was properly modeled.

### 5.4.1 Checking Neutron Scattering Cross Sections

Neutrons which originate in the target having momentum oriented towards a particular detector are sometimes scattered before exiting the target. This changes the momentum direction of the neutron and ultimately affects the measured angular distribution. The same effect can be seen when neutrons scatter from one detector into a second detector. However, this effect is greatly minimized by the multiplicity cut described in Section 4.7.

Because the multiple scattering effects enter into the data corrections so consider-

ably (see Section 5.6.2), the neutron scattering cross sections were checked to ensure that they reproduced known results. These tests were performed by placing a small cylinder<sup>5</sup> of a particular element in the path of a mono-energetic, pencil-sized beam of neutrons. Elastic scattering from  $^{12}\text{C}$ ,  $^{16}\text{O}$ ,  $^{27}\text{Al}$ , protons, and deuterons were tested at neutron energies of 2, 5, and 8 MeV. The 5 and 8 MeV energies correspond roughly to the kinematic range of the outgoing neutrons from the photo-disintegration reaction (see Figure 2.2).

The angular distribution of the cross section for the scattered neutrons was then obtained as a function of scattering angle,  $\theta$ , where  $\theta$  is the angle with respect to the initial neutron beam direction. These angular distributions were then compared with the evaluated data library ENDF/B-VII [Cha06] obtained through the Nuclear and Atomic Data System [McK04]. A few examples of the comparisons are shown in Figure 5.2. Additionally, the total elastic scattering cross section at each energy was compared to the ENDF/B-VII evaluation. Both comparisons revealed good agreement between the simulation and the evaluated data.

## 5.4.2 Light Output Response of Blowfish Detectors

One of the most important aspects of ensuring the accuracy of the simulation is to understand the response of the Blowfish detectors to the incoming neutrons and  $\gamma$ -rays from the experiment. Neutrons and  $\gamma$ -rays collide with protons and electrons, respectively, in the scintillator material and the charged particles deposit energy in the scintillator. The Light Output Response (LOR) describes the amount of light obtained from a given amount of energy deposited in the scintillator.

Scientists from the University of Saskatchewan, who were also responsible for

---

<sup>5</sup>The target was made as small as possible to ensure that multiple scattering in the target did not become significant in the tests.

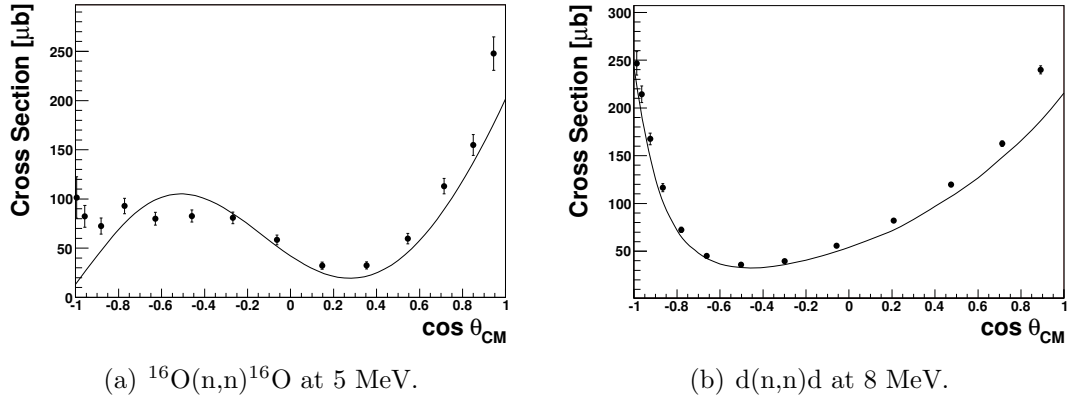


**Figure 5.2:** Comparison of  $^{16}\text{O}(n,n)^{16}\text{O}$  cross section at  $E_n = 5$  MeV and  $d(n,n)d$  cross section at  $E_n = 8$  MeV deduced from GEANT4 to evaluated data. The data points represent the cross section obtained with a pencil-sized beam of 5 MeV and 8 MeV neutrons, respectively, incident upon small  $^{16}\text{O}$  and deuterium cylinders, respectively. The curves are from the ENDF/B-VII evaluation [Cha06].

the construction of the Blowfish array, have measured light output spectra from the Blowfish detectors and have extracted the LOR functions [Pyw06]. The LOR functions were parameterized using the parameterization of Chou [Cho52], given by

$$\frac{dL}{dx} = S \frac{dE}{dx} \left[ 1 + kB \left( \frac{dE}{dx} \right) + C \left( \frac{dE}{dx} \right)^2 \right]^{-1} \quad (5.1)$$

where  $dL/dx$  is the light output per unit path length of the particle traveling through the material,  $S$  is the absolute scintillation efficiency,  $dE/dx$  is the energy loss per unit length, and  $kB$  and  $C$  are constants.

The total light output,  $L(E)$ , for a given incident particle energy,  $E$ , is then given by

$$L(E) = \int_0^R \frac{dL}{dx} dx \quad (5.2)$$

where  $R$  is the range of the particle in the scintillator. Since  $dL/dx$  depends on the absolute scintillation efficiency,  $S$ ,  $L(E)$  can be expressed in terms of equivalent

electron energy,  $L_{ee}$  [Pyw06].  $L_{ee}$  is the energy of an electron which stops in the material which is equivalent to the light output from a particular particle traveling through the scintillator. So in the case of a neutron entering the detector,  $L_{ee}$  is the amount of light produced by a recoil proton in the detector in terms of the energy of an electron which would produce the same amount of light while stopping in the material. Expressing  $L(E)$  in terms of electron equivalent energy allows the absolute scintillation efficiency to be included in the gain determination of the detector [O'R96].

The [Pyw06] work used, among other things, a  $^{252}\text{Cf}$  source in a fission chamber to determine the Chou parameters. It was placed at the center of the Blowfish array and used as a source of low energy neutrons in order to determine the parameters  $kB$  and  $C$  from Equation 5.1. The recoil fission fragments were detected using an ionization chamber and the timing difference between the signal in the chamber and the neutron signal in the detector allowed the energies of the neutrons to be tagged by time of flight. The light output spectra for several neutron energies were then used to determine the light output parameters. The values of these parameters are reported in Table 5.1. Figure 5.3 shows the LOR curves on a log and linear scale compared with data from an equivalent scintillator.

parameter	value
$kB$	$0.0061 \pm 0.0003 \text{ g cm}^{-2} \text{ MeV}^{-1}$
$C$	$(1.0 \pm 0.1) \times 10^{-5} \text{ g}^2 \text{ cm}^{-4} \text{ MeV}^{-2}$

**Table 5.1:** Light Output response function parameters.

These LOR functions were used in the present simulation after being smeared with an empirically determined function as described in [Pyw06]. Pulse height spectra from the simulation were also checked against the experimental data from the [Pyw06]

work to ensure they were implemented correctly in the simulation.

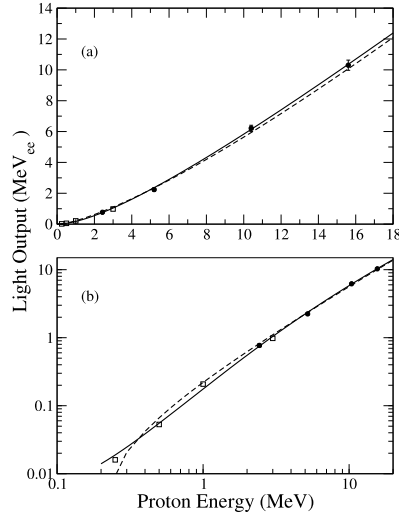


**Figure 5.3:** Light output as a function of proton energy plotted on a linear (a) and log (b) scale. The solid curve is from the Chou parameterization described in the text, and the dashed curve is from the so-called Cecil parameterization (see [Pyw06] for details). The data points are existing data for light output for NE-224, which is equivalent to BC-505. The references for these points can be found in [Pyw06]. Figure is taken from [Pyw06].

### 5.4.3 Blowfish Detector Efficiencies

The proper implementation of the LOR functions in the simulation allowed the uniform software pulse-height cut which was applied to the experimental data to be properly replicated in the simulated data. As was mentioned in Section 4.5.2, the detector efficiency as a function of incoming neutron energy depends strongly on the pulse height cut applied. This is easily understood by considering a neutron which collides with and transfers a small fraction of its energy to a proton. The LOR function determines the amount of light output from such a low energy proton

moving through the scintillator. Depending on the value of the pulse height cut, that low-energy proton may or may not be counted as “detected”. Therefore, the efficiency is higher for lower values of the pulse height cut and the efficiency is lower for higher pulse height cut values.

Figure 5.4 shows the efficiency as a function of neutron energy for various values of the pulse height cut. The simulated data were produced by placing a simulated Blowfish detector in the path of a pencil-size neutron beam with energies from 0 to 10 MeV. Therefore, the efficiencies obtained in this way will be slightly different than the actual efficiencies, which are for neutrons illuminating the entire volume of the detector. The pencil-sized beam was used simply for the purpose of illustrating the effect of the pulse height cut on the efficiency. The data sample was run through all of the cuts described in Section 5.5.

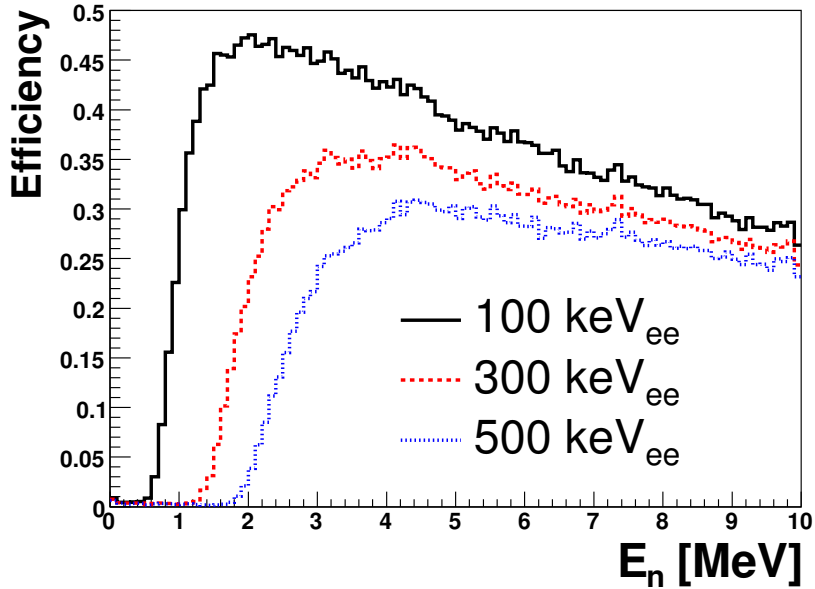


**Figure 5.4:** Detector efficiency as a function of neutron energy. The black histogram corresponds to a PH cut of 100 keV<sub>ee</sub>, the dashed red histogram corresponds to a PH cut of 300 keV<sub>ee</sub>, and the dotted blue histogram corresponds to a PH cut of 500 keV<sub>ee</sub>. See Table 4.5 for the actual values of PH cut selected for each beam energy.

## 5.5 Analysis Cuts for Simulated Data

As mentioned in Section 5.2, the data from the simulation were output in the form of ADC and TDC channel values in LUCID data files. Therefore, since the starting place was the same, the reduction of the simulated data served as a means of checking most of the aspects of the reduction of the experimental data. The data were first converted to ROOT trees and re-indexed from module and channel location to detector number as in Section 4.2.

### Gain Determination

Initially, the gains for the detectors in the simulation were determined by simulating  $\gamma$ -rays from a  $^{232}\text{Th}$  source. The entire gain monitoring system was also included in the simulation, though in the ideal environment of the simulation the gain was arbitrarily set to a value and no gain variation was observed. This would have allowed the gains to be determined in the same way for the simulation as they were for the experiment.

However, this method proved to be unreliable since the simulation integrated all the energy deposited in a detector and converted it to a value for the light output, whereas the experiment integrated the charge in a pulse over the long gate that did not completely extend over the entire pulse (see Figure 4.13). This meant that for  $\gamma$ -rays, whose shorter decay times allowed almost the entire pulse to be integrated over the long gate, the conditions for the simulation and the experiment were very similar and good agreement was found for the detector gains.

But for neutrons entering the detectors, since the long gate cut into the tail of the signal in the experiment but not in the simulation, the gain was overestimated by about 10%. This 10% corresponds roughly to the amount of charge that was not contained in the long gate for the experiment.

Because of this, the gains of the detectors in the simulation had to be determined empirically by matching the end-point of the ADC spectra for the simulation and the experiment for spectra known to consist mostly of neutrons (i.e. after analysis cuts in the data). The correct gain determination for the simulation was important for ensuring that the software pulse height cut was applied to the simulation in the same way it had been to the experimental data.

### **Multiplicity Cut**

As in Section 4.7, any event in which two detectors produced signals was cut from the sample. In the experimental data, this was motivated by the fact that PSD was unreliable for the second signal due to the possible mistiming of the long and short gates. In the simulation, PSD was not performed, but the multiplicity cut was included in order to match the conditions of the experiment as closely as possible.

In the experiment, the DAQ would trigger on the basis of one detector pulse greater than the hardware threshold in the CFD of the particular detector that fired, and the ADCs of each of the Blowfish detectors would then be read out. Therefore, in the simulation, the multiplicity was defined as the total number of detectors which produced signals, as long as at least one was above the average CFD threshold value which was taken from the experimentally determined mean values. Those values can be found in Table 4.3. If no signals were above the hardware threshold, then the multiplicity was zero.

### **Pulse-Shape Discrimination**

No efficient way of replicating PSD in the simulation could be found. Therefore, no PSD cut was included in the simulated data.

### **Pulse Height Cut**

A uniform pulse height (PH) cut was applied to spectra from each detector in

the simulation. The value of the cut was set to the same gain corrected values which were applied to the experiment. Those values are reported in Table 4.5.

### **Time of Flight Cut**

As described in Section 4.10, each TDC spectrum was fit to determine the minimum value of the TDC window and a 20 ns window was integrated from that minimum value, producing the final neutron yields. As in the case of the experimental data, a random window in the TDC spectra was also chosen for subtraction of random events. However, this subtraction clearly had no effect on the yields because the ideal conditions of the simulation contained no such random events.

## **5.6 Final Comparisons and Summary of Effects**

### **5.6.1 Comparison to Experimental Spectra**

The final check of the simulation was to do a direct comparison of various spectra from the simulation to the experimental spectra. Figure 5.5 shows the results of such a comparison.

Note that the width of the TDC spectrum as well as the tail corresponding to slower moving neutrons is well reproduced by the simulation. Properly reproducing these features is important because it indicates that the energy distribution of the outgoing neutrons, which is directly related to the timing information, has been correctly simulated.

The comparison of the ADC spectra also reveal good agreement, especially for the higher channel values. There is some deviation for ADC channel values below about 1000. These are the channel values at which the small background in the data was found to contribute to the ADC spectrum. This background eventually gets

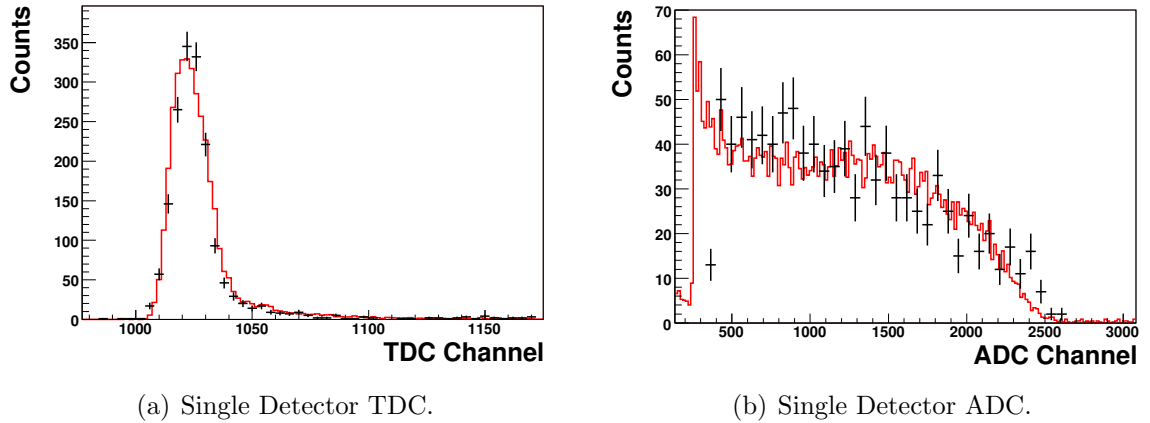


**Figure 5.5:** Comparison of experimental and simulated spectra. The red histograms are the simulated TDC and ADC spectra, and the black data points are from the experiment.

subtracted out when random TDC events are subtracted. Obtaining agreement in the shapes of the ADC spectra is important for ensuring that the pulse height cut has the same effect on the simulation that it does on the data. This final test of the simulation instills confidence that the simulation reliably depicts the experimental conditions.

### 5.6.2 Summary of Important Effects

The purpose of the GEANT4 simulation is to correct for effects such as multiple scattering and finite geometry. In addition, the simulation allows the observables to be easily converted from the lab to the center-of-mass (CM) frame, since the cross section which is input to GEANT4 is always specified in the CM frame, but the output is always in the lab frame.

The most dominant effect corrected for by the simulation is multiple scattering in the target. The magnitude of this effect can be seen by replacing the D<sub>2</sub>O with air

and observing the change in the resulting simulated raw observables. The other effect which was expected to play a significant role in the experiment was finite geometry, especially of the target. The size of this effect can be seen by altering the neutron generator to only generate neutrons from a single point at the center of the target and comparing the resulting observables to a simulation where the neutrons are generated in the full volume of the target<sup>6</sup>.

Figure 5.6 shows the observables obtained from the simulation under these varied conditions. For each of these tests, a cross section similar to what was obtained from the Legendre polynomial fit to the data (see Section 5.7) was used as the input to GEANT4.

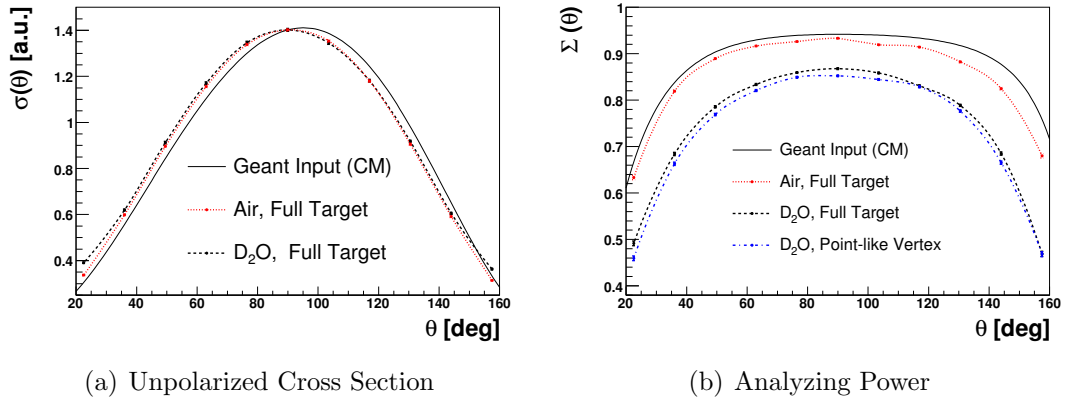


**Figure 5.6:** Comparison of simulated raw observables under various conditions at  $E_\gamma = 16$  MeV. The solid black lines are the observables constructed from the polarized cross section which was input to GEANT4 and are given in terms of center-of-mass angle. All other curves are given in terms of lab angle. “Air” or “D<sub>2</sub>O” indicates what material filled the target space. “Full Target” or “Point-like Vertex” indicates whether neutrons were generated over the entire target volume or at one point at the center of the Blowfish array, respectively. The statistical errors for the points are smaller than the point size. Note that the axes do not start at zero.

The observables constructed from the input cross section are shown in terms of

<sup>6</sup>By full volume, we mean only the volume of the target which is struck by the collimated beam. The term full volume is used in distinction from the point-like vertex mentioned before.

the CM angle and the raw observables are shown as a function of lab angle. From the figure it is easy to see how the boost changes the shapes of the observables. The simulated cross sections in all cases are peaked more toward forward angles in the lab frame than in the CM frame, as expected. In fact, the other effects have very little impact on the results of the differential unpolarized cross section. The analyzing powers exhibit similar behavior under the lab to CM transformation, as seen by the greater deviations from the input analyzing power at back angles than at forward angles, though the effect is much less pronounced.

The effect of multiple scattering is most clearly seen by comparing the analyzing power points (with corresponding curves) denoted “Air, Full Target” to those denoted “D<sub>2</sub>O, Full Target”. As the names indicate, the only difference between the two simulations is that in one case the target was filled with heavy water and in the other it was filled with air. The effect of multiple scattering is to create a distribution of re-scattered neutrons which is isotropic in  $\phi$  that lowers the analyzing power values.

The finite geometry of the target is closely related to the multiple scattering effects. This is seen by a comparison of the analyzing power obtained with the heavy water target with neutrons generated over the full target volume to the analyzing power obtained with neutrons generated from a single point at the center of the target (“Point-like Vertex”). Since the “Full Target” scenario means that some neutrons have a shorter path length to get out of the target, and thus less chance of scattering from the heavy water, the effect of lowering the analyzing power due to multiple scattering is lessened as compared to the “Point-like Vertex” case. This was confirmed by a similar comparison for the case of a target filled with air where a negligible effect due to the finite size of the target was seen. The points corresponding to “Air, Point-like Vertex” which were used in that comparison are not shown because they are

indistinguishable from the “Air, Full Target” points.

It should be noted that the finite geometry of the target had a negligible effect in the unpolarized cross section, so no results are shown for the case of “Point-like Vertex”. In addition, the effects of the attenuation of the beam in the target and of neutrons scattering from the aluminum pipe which held the target were also found to be negligible. An idea of the magnitude of the effect of the finite geometry of the detectors can be seen by comparing the analyzing power values for the simulation with the air target to the analyzing power values constructed from the input **GEANT4** cross section, neglecting the effects of the lab-CM frame boost. The effect is small but not negligible.

## **5.7 Correcting the Experimental Data**

### **5.7.1 Legendre Polynomial Parameterization of the Cross Section**

After understanding the simulation and performing the various checks to ensure its reliability, the raw data were corrected by effectively changing the cross section input to **GEANT4** until the simulated **GEANT4** data gave back what was observed in the experiment. Once the simulated and experimental data match, then the corrected cross section is given by what was ultimately input into **GEANT4**.

In order to implement this method, the cross section was parameterized in terms of an associated Legendre polynomial expansion. Fits to the data indicated that including up to fourth order in the expansion was adequate to fit the data, giving a

polarized cross section of the form

$$\frac{d\sigma}{d\Omega}(\theta, \phi) = A_0 \left[ 1 + \sum_{k=1}^4 a_k P_k(\cos\theta) + \sum_{k=2}^4 e_k P_k^2(\cos\theta) \cos 2\phi \right] \quad (5.3)$$

where the  $a_k$  and  $e_k$  coefficients are parameters which are varied in order to match the experimental data, the  $P_k$  and  $P_k^2$  functions are the associated Legendre polynomials, and  $A_0$  is the scale factor which sets the overall magnitude of the (angle integrated) total cross section, via  $\sigma_T = 4\pi A_0$ . In the case of this experiment, the absolute normalization was not determined, so  $A_0$  became an arbitrary scale factor. The terms in the first summation of the expansion represent the form of the cross section with unpolarized beam. The  $\cos 2\phi$  is present in the second summation because the beam is linearly polarized [Wel92].

Writing Equation 5.3 explicitly in terms of the Legendre polynomials gives

$$\frac{d\sigma}{d\Omega}(\theta, \phi) = A_0 \left( 1 \right. \quad (5.4)$$

$$+ a_1 [\cos\theta] \quad (5.5)$$

$$+ a_2 \left[ \frac{1}{2}(3\cos^2\theta - 1) \right] \quad (5.6)$$

$$+ a_3 \left[ \frac{1}{2}(5\cos^3\theta - 3\cos\theta) \right] \quad (5.7) \quad (5.12)$$

$$+ a_4 \left[ \frac{1}{8}(35\cos^4\theta - 30\cos^2\theta + 3) \right] \quad (5.8)$$

$$+ e_2 [3(1 - \cos^2\theta)] \cos 2\phi \quad (5.9)$$

$$+ e_3 [15\cos\theta(1 - \cos^2\theta)] \cos 2\phi \quad (5.10)$$

$$+ e_4 \left[ \frac{15}{2}(1 - \cos^2\theta)(7\cos^2\theta - 1) \right] \cos 2\phi \Big). \quad (5.11)$$

This parameterization was used to determine the distribution of neutrons which were generated over the entire region of the target illuminated by the  $\gamma$ -ray beam.

Section 5.7.2 describes how the parameters were chosen so that a fit to the data would extract the  $a_k$  and  $e_k$  coefficients.

As was noted in the previous section, this cross section is in the center-of-momentum (CM) frame, so when neutrons were generated according to this cross section, the energies and outgoing angles had to be boosted to the lab frame.

## 5.7.2 Fitting Method

In order to fit the simulated data to the experimental data, the following method was used, following the procedure outlined in [Saw05].

1. Each individual term in the Legendre polynomial expansion of the cross section was taken in turn as the form of the cross section and simulated yields as a function of detector number<sup>7</sup> were obtained for that polynomial. Each Legendre polynomial was singled out by setting a single  $a_k$  or  $e_k$  coefficient to 1.0 and all the rest to zero<sup>8</sup>. After this was done for each Legendre polynomial included in the expansion, the shapes of the simulated yields as a function of detector number for each polynomial were obtained (see Figure 5.7). In the discussion that follows, each simulated yield versus detector number histogram is referred to as  $P_j^G$ , with  $j$  being the index labeling the  $P_k$  and  $P_k^2$  polynomials.
2. These  $P_j^G$  histograms were then substituted into Equation 5.12 in place of the respective Legendre Polynomials. The  $a_k$  and  $e_k$  coefficients were then adjusted using the fitting routine `Minuit`<sup>9</sup> until the linear combination of the  $P_j^G$  histograms matched the experimental yields.

---

<sup>7</sup>Refer to Table 3.3 to see how detector number translates into  $\theta$  and  $\phi$  angles.

<sup>8</sup>See below for a few caveats.

<sup>9</sup>`Minuit` is a function minimization and error analysis routine available in the ROOT analysis package [Jam98]. It was developed as part of the CERN program library.

3. The  $a_k$  and  $e_k$  coefficients extracted from step 2 then represented the corrected cross section for the  $d(\gamma, n)p$  reaction in the CM frame. This allowed the experimental data to be adjusted by means of a correction factor, as described in Section 5.7.4.

It was important to generate the same number of neutrons in **GEANT4** for each  $P_j^G$  in order to ensure that each of the shapes was normalized with respect to each other. In addition, some of the Legendre polynomials when taken alone contained angular regions where the cross section would be negative. For such polynomials, multiples of the  $P_0(\cos\theta) \equiv 1$  term had to be added, giving an input cross section defined as

$$AP_0(\cos\theta) + P_j(\cos\theta) \tag{5.13}$$

where  $j$  is the index of the polynomial under consideration and  $A$  is chosen so that the input cross section is positive over the entire angular region. If the yield versus detector number histogram that resulted from such a cross section is defined as  $S_j^G$ , then the  $P_j^G$  histogram for the polynomial of interest is given by

$$P_j^G = A \times [S_j^G - P_0^G]. \tag{5.14}$$

The  $P_j^G$  histograms obtained after this procedure are found in Figure 5.7. Before being used in the fit as shown in that figure, the symmetries of the experiment and of the forms of the polynomials were used to combine yields in order to reduce the statistical variation. For example, for the regular Legendre polynomials, there is a symmetry about the z-axis that allows all the yields for a given ring to be averaged.

The fits were performed to the yields using the fitting routine **Minuit** [Jam98], which comes as a built-in class in the **ROOT** framework. **Minuit** was used to minimize

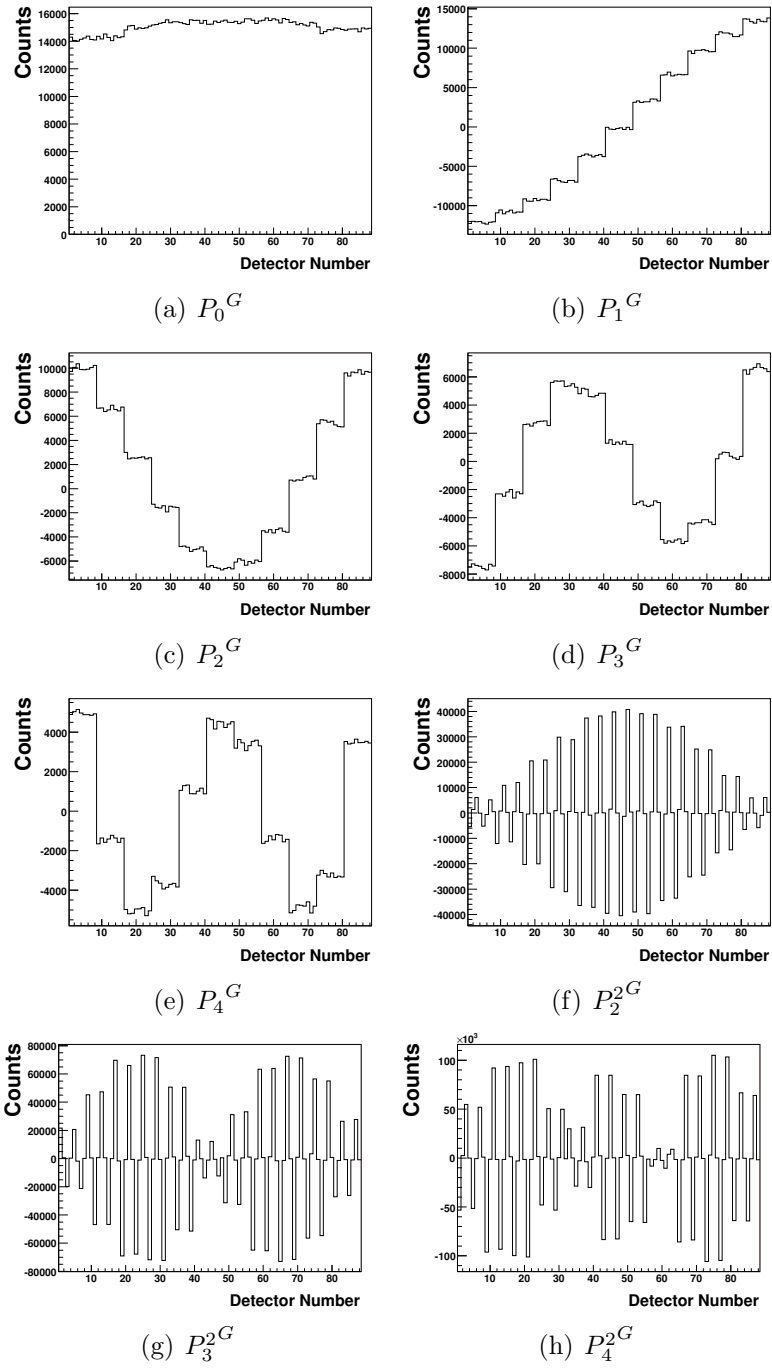


**Figure 5.7:** Simulated neutron yields as a function of detector number using each term in the Legendre polynomial expansion individually as the input cross section. Shown here are the simulated yields for  $E_\gamma = 14$  MeV. Each polynomial was created by generated 30 million neutrons events.

a user-defined  $\chi^2$  function defined as

$$\chi^2 = \sum_{i=1}^{44} \left[ \frac{Y_i - G_i(a, e)}{\delta Y_i} \right]^2 \quad (5.15)$$

where  $i$  sums over the averaged and combined yields for all 44 pairs of detectors<sup>10</sup>,  $Y_i$  is the yield in detector  $i$  with error  $\delta Y_i$ , and  $G_i(a, e)$  is a function of the  $a$  and  $e$  coefficients (the parameters in the fit).  $G_i$  is the fitted yield for a given pair of detectors,  $i$ , given by a generalization of Equation 5.3 in terms of the  $P_k^G$  histograms,

$$G_i = A_0 \left( P_0^G(i) + \sum_{k=1}^4 a_k P_k^G(i) + \sum_{k=2}^4 e_k P_k^{2G}(i) \right), \quad (5.16)$$

where  $A_0$  is the fitting parameter which sets the overall scale of the fit.

In order to estimate the systematic errors on the coefficients, another fit was done to the data by replacing the statistical errors by the systematic errors. The procedure used for estimating the systematic errors on the data can be found in Section 5.8.

### 5.7.3 Fit Results

Fits were performed on both the 14 and 16 MeV yields to extract the Legendre coefficients. `Minuit` also computes the error matrix for the parameters by means of the user-defined  $\chi^2$  function. The errors on the parameters were taken from the diagonal elements of the error matrix. One standard deviation is defined by `Minuit` as the variation on a parameter which increases the  $\chi^2$  value by 1. It should be noted, however, that the errors obtained were larger than what one would obtain from simply moving one parameter until the  $\chi^2$  increased by one with the other parameters were

---

<sup>10</sup>Recall that detector pairs having a common  $\theta$  with a  $\phi$  angle  $180^\circ$  about the beam axis from each other were combined via a weighted mean. After that, the yields from all four orientations were combined via a geometric mean. See Section 4.13 for more details.

held fixed, since the errors from `Minuit` also take correlations between parameters into account [Jam98].

The fits are shown in Figure 5.8. The  $\chi^2$  values and reduced  $\chi^2$  values, defined as the  $\chi^2$  divided by the number of degrees of freedom, for the fits are reported in Table 5.2. Note that for both energies the reduced  $\chi^2$  values, labeled  $\chi_r^2$ , are very close to 1.0, which is expected of a good fit.

$E_\gamma$ (MeV)	$\chi^2$	ndf	$\chi_r^2$
14	35.8	36	0.99
16	27.8	28	0.99

**Table 5.2:**  $\chi^2$ , number of degrees of freedom (ndf), and reduced  $\chi^2$  ( $\chi_r^2$ ) for Legendre polynomial fits to the yields.

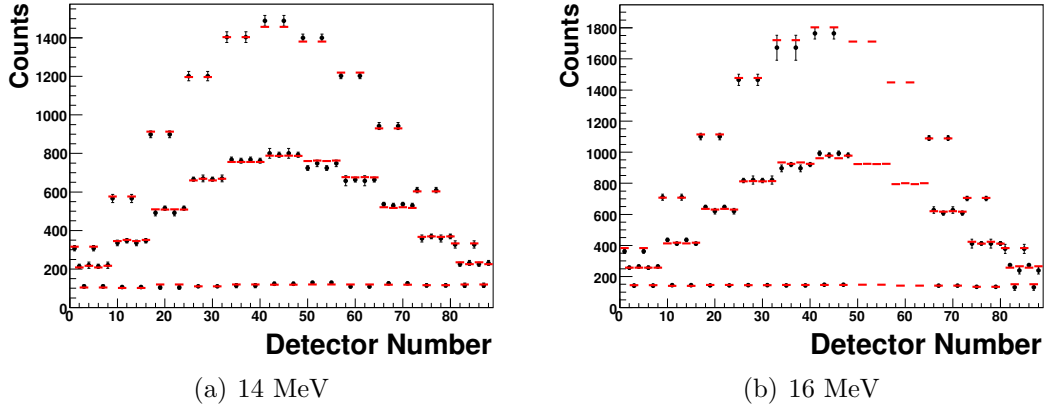


**Figure 5.8:** Fits to the experimental yields using the simulated yields from the Legendre polynomials. The black points are the experimental yields and the red lines are the simulated yields. Note that the yields for the detectors at  $\theta = 63^\circ$  and  $76.5^\circ$  were discarded from the 16 MeV data set (see Section 4.11.1) and are not shown. Also note that the yield obtained from the weighted mean of symmetric pairs of detectors (see Section 4.13) has been put in the place of both detectors which were used to construct the weighted mean. The  $\chi^2$  function was defined to include such mean yield values only once.

The values of the Legendre coefficients extracted from these fits are presented

and discussed in Section 6.2.1. For the purposes of correcting the data, it is sufficient to observe that the fits reproduce the raw observables well, as seen in Figure 5.9 of Section 5.7.4.

### 5.7.4 Corrected Data

After the fits were performed, the functional form of the corrected polarized differential cross section at each energy was known. In terms of the Legendre polynomials, the extracted Legendre coefficients can be used to construct the corrected observables. The unpolarized cross section can be written as

$$\frac{\sigma_{unpol}(\theta)}{A_0} = 1 + \sum_{k=1}^4 a_k P_k(\cos \theta), \quad (5.17)$$

and using the definition of the analyzing power in Equation 1.1 along with Equation 5.3 the analyzing power can be written as

$$\Sigma(\theta) \frac{\sigma_{unpol}(\theta)}{A_0} = \sum_{k=2}^4 e_k P_k^2(\cos \theta). \quad (5.18)$$

In addition, the final values of the simulated yields obtained from the fit via Equation 5.16 are used to construct the simulated raw observables. Thus the raw experimental observables can be corrected by multiplying each point by the ratio of the corrected observables constructed from the extracted Legendre coefficients to the simulated observables. In other words, the correction is performed using the ratio of the GEANT4 input to the GEANT4 output.

Thus, the uncorrected experimental observables are corrected on a point-by-point

basis in the following way

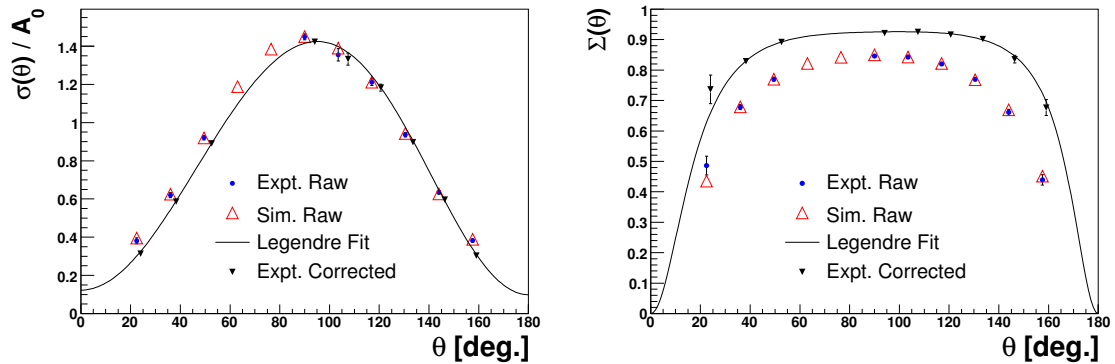
$$\sigma_{corr}^{expt}(\theta) = \sigma_{uncorr}^{expt}(\theta) \frac{\sigma_{corr}^{Leg}(\theta)}{\sigma_{uncorr}^{sim}(\theta)} \quad (5.19)$$

and

$$\Sigma_{corr}^{expt}(\theta) = \Sigma_{uncorr}^{expt}(\theta) \frac{\Sigma_{corr}^{Leg}(\theta)}{\Sigma_{uncorr}^{sim}(\theta)}, \quad (5.20)$$

where the superscripts *exp* and *sim* refer to experimental and simulated data points, respectively, the subscripts *corr* and *uncorr* refer to corrected and uncorrected data, respectively, and the superscript *Leg* refers to the corrected observable constructed in terms of the Legendre expansion using the coefficients from the fit.

As an example, Figure 5.9 shows the observables both before and after corrections along with the fits to the data for the 16 MeV data set. Note that the Legendre fit and the corrected experimental data are plotted as a function of CM angle, whereas the simulated and experimental raw data are plotted as a function of the lab angle. A comparison of the simulated and experimental raw observables shows that the simulated yields determined by the fit reproduce the experimental observables well. In addition, the magnitude of the correction for the analyzing powers was much larger than for for the cross section, as discussed in Section 5.6.2.



(a) 16 MeV Unpolarized Cross Section.

(b) 16 MeV Analyzing Power.

**Figure 5.9:** Observables before and after corrections for 16 MeV. See legend for explanation of symbols and curve. Note that the Legendre fit and corrected experimental data are in terms of CM angle, whereas the experimental and simulated raw data are in terms of lab angle.

## 5.8 Estimation of Systematic Errors

A set of tests was performed to estimate the systematic errors in the experiment. This was done by varying the analysis of the data, using simulations, and performing calculations. In what follows, the methods for determining the systematic error for various potential sources are reviewed.

In all cases where real or simulated data were used to estimate the errors, a Legendre fit was performed on any new data sets which were created in a way identical to what was described in the previous section. In this way, any statistical variation would be smoothed out as much as possible, since we were interested in systematic variations in the data at this point. The deviations of the observables from the original values could then be determined by comparing the Legendre polynomial representation of the observables instead of the statistically varying data points.

The following section will describe how each potential source of systematic error

was handled, and Section 5.8.5 provides a summary table of all the effects with a brief discussion.

### 5.8.1 Analysis Cuts

- **Pulse Height Cut.** The pulse height (PH) cut determined the efficiency with which the Blowfish detectors detected the incoming neutrons. The application of this cut presents a problem only if the pulse height cut applied to the simulation differed from that applied to the experimental data. A mismatch could occur if the gains of the Blowfish detectors were incorrectly determined. In order to estimate the error due to a misplaced PH cut, the PH cut location for the data was varied by  $\pm 3\%$ , which was determined based on a conservative estimate of the error on the gain determination.
- **TOF Cut.** A fit to the leading edge of the TDC spectra determined where the TDC integrating window began. While the leading edge of the window was very straightforward to determine, the trailing edge of the window was not. Ultimately, a large TDC window size of 20 ns (or 200 channels) was chosen as the integrating window. The systematic error associated with this choice was determined by varying the trailing edge of the window by  $\pm 5$  ns.
- **PSD Cut.** The PSD cut location extracted using the methods described in Section 4.8.2 yielded PSD cut value locations very nearly uniform as a function of detector number. A histogram of the cut values for all the detectors gave an approximately Gaussian shaped distribution with a width of about 2.5 ADC channels. Therefore, the systematic error due to the PSD cut was estimated by varying the PSD cut by  $\pm 2.5$  channels.

## 5.8.2 Geometrical Effects

- **Target  $Z$  Location.** The systematic error due to an inaccuracy in our knowledge of the target location was estimated using `GEANT4`. In the experiment, the target was positioned by first centering the aluminum pipe which holds the target within the Blowfish array. A tape measure was then used to push the target a predetermined distance such that it would be located at the center of the array. To estimate the error due to an incorrectly centered target, the  $z$  location was varied by  $\pm \sim 2$  mm, which was the estimated error on how well the  $z$  location of the target was known using this method.
- **Target Transverse Location.** In addition, if the aluminum pipe was not centered in the transverse ( $x$ - $y$ ) direction with respect to the array, then some detectors would be closer to the target than others. The systematic error due to such a misalignment was estimated by varying both the  $x$  and  $y$  placement of the target in the simulation individually by  $\pm 2$  mm.
- **Beam Alignment.** The target was aligned to the beam axis as described in Section 3.3.3. The error due to a misalignment of the array and target with the beam axis was tested by changing the position of the beam axis with respect to the array and target by  $\pm 1$  mm in the simulation.
- **Varying Detector Solid Angles.** Any variations in detector distance from the center of the target would result in a variation of the solid angle of the detectors and shows up as an effective efficiency change in the detectors. Before the experiment, measurements were made of the distance between pairs of detectors which were symmetric about the target location<sup>11</sup>. The measurements

---

<sup>11</sup>What is meant here is that if the target center is defined as  $x=y=z=0$ , symmetric pairs would be

revealed that the average distance between detectors was 32", as expected, with a standard deviation of about 0.25". The variation in the solid angle was computed for deviations of this size and was found to be about 1.6% of the nominal solid angle value. The simulated yields were randomly scaled according to a Gaussian distribution with a standard deviation corresponding this computed variation of the solid angle.

### 5.8.3 Beam Effects

- **Beam Energy Spread.** The systematic errors due to inaccuracies in our knowledge of the beam energy spread were estimated by varying the shape parameters from their nominal values as listed in Table 4.1. The absolute FWHM was varied by  $\pm 10\%$  of its nominal value in the simulation in order to estimate the systematic error.
- **Beam Polarization Rotation.** As described in detail in Section 4.12, a deviation of the angle of the plane of polarization of the beam from the horizontal plane was measured to be less than 1%. Therefore, the beam polarization axis was varied by  $\pm 1\%$  in the simulation in order to determine the systematic error due to any potential rotation of the polarization plane.
- **Beam Intensity Profile.** The beam intensity was assumed to be constant within the entire transverse area of the collimator in the simulation. The dependence of our result on this assumption was estimated by performing a simulation with a Gaussian beam with standard deviation given by half the radius of the collimator.

---

detectors located at  $(x,y,z)$  and  $(-x,-y,-z)$ .

- **Attenuation in Target.** The  $\gamma$ -ray beam attenuation is artificially put into the simulation by varying the amount of neutrons produced along the  $z$ -axis of the target according to the attenuation coefficients from NIST [Nat]. A test was performed to determine the effect of assuming an improper attenuation of the beam by dividing the attenuation coefficient in half in the simulation.
- **Collimator Size.** The effect due to an inaccurate description of the collimator size in the simulation was estimated by changing the collimator radius by  $\pm 1$  mm. Some idea of the way this might effect the results can be gathered from the discussion of the simulation with neutrons generated over the full target volume versus the simulation with neutrons generated from a point-like vertex at the center of the target in Section 5.6.2.
- **Depolarization of  $\gamma$ -rays after Scattering.** Many of the  $\gamma$ -rays which scatter in the target may scatter at small angles, allowing it to interact in the target again. However, as the scattering angle deviates from the initial photon direction, the polarization of the photons will deviate from 1.0 (see Section 3.2.3). A calculation was performed to determine the probability of such  $\gamma$ -rays interacting in the target again after a scatter and this was found to be on the order of a hundredth of a percent of the scattered  $\gamma$ -rays. Thus the error due to this effect is negligible.

#### 5.8.4 Miscellaneous Effects

- **LOR Functions.** The proper execution of the simulations relied on the Light Output Response (LOR) functions for these detectors being known well. These LOR functions were varied from their nominal values by changing the  $kB$  and

$C$  Chou parameters by the magnitude of the errors given in Table 5.1.

- **Statistical Errors in Legendre Polynomial Shapes.** As described in Section 5.7.2, some of the Legendre polynomials when taken alone have angular regions in which they are negative. This problem was handled by adding multiples of the  $P_0$  polynomial until it was positive over the entire range. However, since the cross section could still potentially be very small in those regions, the larger statistical variation on the yields there could affect the correction of the data. The magnitude of this effect was tested by varying the yields in each  $P_j^G$  according to its statistical errors, correcting the data with these new histograms, and observing the effect upon the observables.

### 5.8.5 Table of Systematic Errors

In Table 5.6, the systematic error estimates are shown for each  $\theta$  value and for each observable. The systematic errors are, in general, comparable to the statistical errors. For the most part, the systematic errors for the individual contributions are not particularly large, but the total of the smaller contributions when summed in quadrature result in total systematic errors which are not negligible.

The extreme angles are most sensitive to the effects investigated here, and this is not surprising, since the yields at extreme angles are relatively small, causing even small changes to have larger effects due to the statistical variation that can occur. In this way, the systematic and statistical errors are coupled. This is seen, for instance, in how much effect the TDC and PSD cuts have on the extreme angles. As expected, the systematic errors in the analyzing power values are smaller than those on the cross section values, since there is cancellation of some of these effects due to the way in which the analyzing power is constructed (see Section 4.13.2).

The fact that the  $\chi_r^2$  values from the fits to the data were already consistent with one (see Table 5.2) leads to the expectation that the contribution from systematic effects to the data is small. The estimates presented here bear that out.

14 MeV - Percent systematic Errors on Cross Section Points

	Lab $\theta$										
	22.5°	36.0°	49.5°	63.0°	76.5°	90.0°	103.5°	117.0°	130.5°	144.0°	157.5°
PH Cut	0.2 %	0.2 %	0.2 %	0.4 %	0.4 %	0.4 %	0.2 %	0.1 %	0.2 %	0.8 %	1.7 %
TDC Cut	2.5 %	0.5 %	0.6 %	0.9 %	0.9 %	0.7 %	0.5 %	0.3 %	0.2 %	0.2 %	1.0 %
PSD Cut	3.3 %	0.5 %	1.0 %	0.5 %	0.2 %	0.2 %	0.1 %	0.2 %	0.4 %	0.3 %	4.0 %
Target Z	0.5 %	0.9 %	1.0 %	0.8 %	0.5 %	0.2 %	0.4 %	0.8 %	1.1 %	1.3 %	1.3 %
Target Transverse	0.6 %	0.3 %	0.4 %	0.4 %	0.5 %	0.4 %	0.2 %	0.5 %	0.9 %	1.2 %	1.3 %
Beam Align.	0.1 %	0.4 %	0.3 %	0.2 %	0.1 %	0.2 %	0.2 %	0.2 %	0.3 %	0.4 %	0.7 %
Solid Angle	0.4 %	0.2 %	0.1 %	0.2 %	0.3 %	0.2 %	0.2 %	0.2 %	0.3 %	0.5 %	0.6 %
Beam Width	0.5 %	0.3 %	0.2 %	0.1 %	0.1 %	0.1 %	0.2 %	0.2 %	0.2 %	0.4 %	0.7 %
Beam Pol. Axis	0.2 %	0.1 %	0.1 %	0.1 %	0.2 %	0.2 %	0.1 %	0.1 %	0.2 %	0.5 %	1.0 %
Intensity Dist.	0.4 %	0.3 %	0.2 %	0.2 %	0.2 %	0.1 %	0.1 %	0.1 %	0.2 %	0.7 %	2.0 %
Attenuation	0.2 %	0.1 %	0.1 %	0.1 %	0.1 %	0.1 %	0.1 %	0.1 %	0.1 %	0.2 %	0.4 %
Collimator Size	0.7 %	0.5 %	0.4 %	0.2 %	0.2 %	0.2 %	0.2 %	0.2 %	0.4 %	0.6 %	1.1 %
Light Output	0.5 %	0.6 %	0.5 %	0.4 %	0.2 %	0.2 %	0.3 %	0.5 %	0.6 %	0.6 %	0.7 %
Leg. Poly. Stats	0.4 %	0.5 %	0.7 %	0.3 %	0.4 %	0.5 %	0.4 %	0.3 %	0.8 %	0.5 %	0.6 %
Total	4.4 %	1.6 %	1.9 %	1.5 %	1.4 %	1.2 %	0.9 %	1.2 %	1.9 %	2.5 %	5.7 %
Statistical	3.1 %	2.0 %	1.2 %	1.2 %	1.0 %	1.2 %	1.1 %	1.2 %	1.4 %	2.1 %	3.0 %

**Table 5.3:** Percent systematic errors on 14 MeV cross section points for each lab angle and for each potential contribution. Statistical errors are shown for comparison.

14 MeV - Percent systematic Errors on Analyzing Power Points

	Lab $\theta$										
	22.5°	36.0°	49.5°	63.0°	76.5°	90.0°	103.5°	117.0°	130.5°	144.0°	157.5°
PH Cut	0.3 %	0.1 %	0.1 %	0.1 %	0.1 %	0.1 %	0.1 %	0.1 %	0.2 %	0.5 %	1.1 %
TDC Cut	1.0 %	0.3 %	0.1 %	0.1 %	0.1 %	0.1 %	0.1 %	0.1 %	0.1 %	0.2 %	0.5 %
PSD Cut	1.0 %	0.1 %	0.1 %	0.1 %	0.1 %	0.1 %	0.1 %	0.1 %	0.2 %	0.1 %	0.9 %
Target Z	0.7 %	0.3 %	0.2 %	0.2 %	0.2 %	0.2 %	0.1 %	0.2 %	0.3 %	0.4 %	1.1 %
Target Transverse	1.3 %	0.5 %	0.6 %	0.4 %	0.3 %	0.3 %	0.3 %	0.4 %	0.3 %	0.4 %	1.4 %
Beam Align.	0.1 %	0.4 %	0.4 %	0.2 %	0.1 %	0.2 %	0.2 %	0.2 %	0.2 %	0.3 %	1.0 %
Solid Angle	0.5 %	0.1 %	0.1 %	0.1 %	0.1 %	0.1 %	0.1 %	0.1 %	0.1 %	0.2 %	0.7 %
Beam Width	0.6 %	0.3 %	0.2 %	0.1 %	0.1 %	0.2 %	0.2 %	0.2 %	0.2 %	0.4 %	1.1 %
Beam Pol. Axis	0.4 %	0.1 %	0.1 %	0.1 %	0.1 %	0.1 %	0.1 %	0.1 %	0.1 %	0.5 %	1.4 %
Intensity Dist.	0.6 %	0.2 %	0.1 %	0.2 %	0.1 %	0.1 %	0.1 %	0.2 %	0.1 %	0.6 %	2.9 %
Attenuation	0.4 %	0.2 %	0.1 %	0.1 %	0.1 %	0.1 %	0.1 %	0.1 %	0.1 %	0.1 %	0.5 %
Collimator Size	1.0 %	0.3 %	0.3 %	0.1 %	0.1 %	0.1 %	0.2 %	0.2 %	0.1 %	0.4 %	1.5 %
Light Output	0.8 %	0.4 %	0.3 %	0.3 %	0.2 %	0.2 %	0.2 %	0.2 %	0.3 %	0.5 %	1.2 %
Leg. Poly. Stats	0.7 %	0.5 %	0.4 %	0.4 %	0.2 %	0.2 %	0.2 %	0.3 %	0.3 %	0.8 %	0.9 %
Total	2.8 %	1.1 %	1.0 %	0.7 %	0.6 %	0.6 %	0.6 %	0.7 %	0.8 %	1.6 %	4.8 %
Statistical	4.5 %	1.6 %	0.8 %	0.4 %	0.4 %	0.5 %	0.9 %	0.4 %	1.1 %	1.3 %	3.8 %

**Table 5.4:** Percent systematic errors on 14 MeV analyzing power points for each lab angle and for each potential contribution. Statistical errors are shown for comparison.

16 MeV - Percent systematic Errors on Cross Section Points

	Lab $\theta$										
	22.5°	36.0°	49.5°	63.0°	76.5°	90.0°	103.5°	117.0°	130.5°	144.0°	157.5°
PH Cut	0.2 %	0.1 %	0.1 %	-	-	0.1 %	0.1 %	0.1 %	0.1 %	0.1 %	0.1 %
TDC Cut	4.0 %	0.2 %	0.5 %	-	-	1.6 %	1.0 %	0.4 %	0.3 %	1.2 %	4.0 %
PSD Cut	6.0 %	0.5 %	1.0 %	-	-	0.1 %	0.1 %	0.1 %	0.1 %	0.2 %	2.1 %
Target Z	1.0 %	1.1 %	1.2 %	-	-	0.3 %	0.3 %	0.8 %	1.2 %	1.6 %	1.7 %
Target Transverse	1.3 %	0.3 %	0.3 %	-	-	0.7 %	0.6 %	0.4 %	0.4 %	0.8 %	1.8 %
Beam Align.	0.8 %	0.1 %	0.3 %	-	-	0.3 %	0.2 %	0.2 %	0.2 %	0.5 %	1.1 %
Solid Angle	1.1 %	1.0 %	0.9 %	-	-	0.6 %	0.6 %	1.3 %	1.8 %	1.8 %	0.9 %
Beam Width	0.8 %	0.4 %	0.4 %	-	-	0.4 %	0.3 %	0.2 %	0.4 %	0.7 %	1.3 %
Beam Pol. Axis	0.9 %	0.2 %	0.3 %	-	-	0.4 %	0.3 %	0.3 %	0.2 %	0.2 %	1.2 %
Intensity Dist.	0.8 %	0.3 %	0.6 %	-	-	0.6 %	0.4 %	0.1 %	0.3 %	1.0 %	2.5 %
Attenuation	0.2 %	0.1 %	0.1 %	-	-	0.1 %	0.1 %	0.2 %	0.3 %	0.3 %	0.3 %
Collimator Size	0.7 %	0.3 %	0.4 %	-	-	0.3 %	0.3 %	0.4 %	0.4 %	0.6 %	1.0 %
Light Output	1.0 %	0.7 %	0.7 %	-	-	0.2 %	0.2 %	0.4 %	0.6 %	0.8 %	1.0 %
Leg. Poly. Stats	1.3 %	0.6 %	1.0 %	-	-	0.6 %	0.7 %	1.3 %	2.0 %	2.2 %	2.2 %
Total Percent systematic	18.6 %	2.4 %	3.6 %	-	-	2.2 %	1.7 %	2.2 %	3.2 %	4.0 %	9.0 %
Statistical	4.1 %	2.0 %	1.3 %	-	-	1.1 %	2.3 %	1.5 %	1.2 %	1.5 %	2.0 %

**Table 5.5:** Percent systematic errors on 16 MeV cross section points for each lab angle and for each potential contribution. Statistical errors are shown for comparison.

16 MeV - Percent systematic Errors on Analyzing Power Points

	Lab $\theta$										
	22.5°	36.0°	49.5°	63.0°	76.5°	90.0°	103.5°	117.0°	130.5°	144.0°	157.5°
PH Cut	0.5 %	0.1 %	0.1 %	-	-	0.1 %	0.1 %	0.1 %	0.1 %	0.1 %	0.3 %
TDC Cut	1.2 %	0.2 %	0.1 %	-	-	0.1 %	0.1 %	0.1 %	0.1 %	0.2 %	1.1 %
PSD Cut	2.7 %	0.5 %	0.1 %	-	-	0.1 %	0.1 %	0.1 %	0.1 %	0.1 %	1.4 %
Target Z	0.9 %	0.4 %	0.3 %	-	-	0.1 %	0.2 %	0.3 %	0.6 %	1.0 %	2.0 %
Target Transverse	2.0 %	0.4 %	0.1 %	-	-	0.6 %	0.5 %	0.4 %	0.5 %	0.8 %	2.7 %
Beam Align.	1.3 %	0.1 %	0.1 %	-	-	0.2 %	0.2 %	0.1 %	0.2 %	0.5 %	1.6 %
Solid Angle	1.2 %	0.7 %	0.4 %	-	-	0.7 %	0.3 %	0.3 %	0.8 %	0.8 %	1.3 %
Beam Width	1.2 %	0.4 %	0.2 %	-	-	0.3 %	0.3 %	0.3 %	0.4 %	0.6 %	1.9 %
Beam Pol. Axis	1.5 %	0.1 %	0.1 %	-	-	0.5 %	0.3 %	0.2 %	0.1 %	0.4 %	2.0 %
Intensity Dist.	1.5 %	0.3 %	0.2 %	-	-	0.4 %	0.3 %	0.1 %	0.2 %	0.9 %	3.8 %
Attenuation	0.3 %	0.1 %	0.1 %	-	-	0.1 %	0.1 %	0.1 %	0.1 %	0.1 %	0.6 %
Collimator Size	1.4 %	0.4 %	0.1 %	-	-	0.3 %	0.3 %	0.2 %	0.3 %	0.5 %	1.5 %
Light Output	1.5 %	0.4 %	0.2 %	-	-	0.2 %	0.1 %	0.2 %	0.3 %	0.6 %	1.3 %
Leg. Poly. Stats	1.7 %	0.8 %	0.7 %	-	-	0.8 %	0.4 %	0.3 %	0.9 %	1.4 %	3.7 %
Total Percent systematic	5.4 %	1.5 %	0.9 %	-	-	1.4 %	1.0 %	0.9 %	1.6 %	2.5 %	7.7 %
Statistical	6.4 %	1.2 %	0.8 %	-	-	0.3 %	0.5 %	0.7 %	0.7 %	1.6 %	3.8 %

**Table 5.6:** Percent systematic errors on 16 MeV analyzing power points for each lab angle and for each potential contribution. Statistical errors are shown for comparison.

# Chapter 6

## Results and TME Analysis

### 6.1 Introduction

Chapter 5 described how the data points from the two accessible observables were corrected and put into their final form. This chapter will discuss the results obtained up to this point and describe how these data have been used to extract information about the details of the interaction in terms of the transition matrix elements (TMEs) of the reaction.

The final observables are compared to theory and previous experiments in Section 6.2. Section 6.3 gives an overview of the formalism used to write the observables in terms of the reduced TME amplitudes and phases. This also includes a discussion of the rationale for the choice of TMEs to include in the fits and a description of how the phases of the TMEs were treated. The fits to the data are described in Section 6.4, with and without a simplifying assumption. In Section 6.5, a connection is made between the amplitudes extracted from the fits and the integrand which appears in the Gerasimov-Drell-Hearn (GDH) sum rule. Finally, the results for the GDH integrand from this analysis are presented.

### 6.2 Discussion of Results

The final results for the observables, corrected using the techniques described in the previous chapter, are presented in Figure 6.1. Also shown are the predictions from

the potential model calculation of Schwamb and Arenhövel [Sch01a, Sch01b, Are04], which will be referred to as the SAPM calculation. The experimental unpolarized cross section has been normalized such that the  $A_0$  of the Legendre expansion (Equation 5.3) is 1.0. The same normalization was performed on the theoretical cross section from the SAPM calculation, so that the shapes could be compared directly.

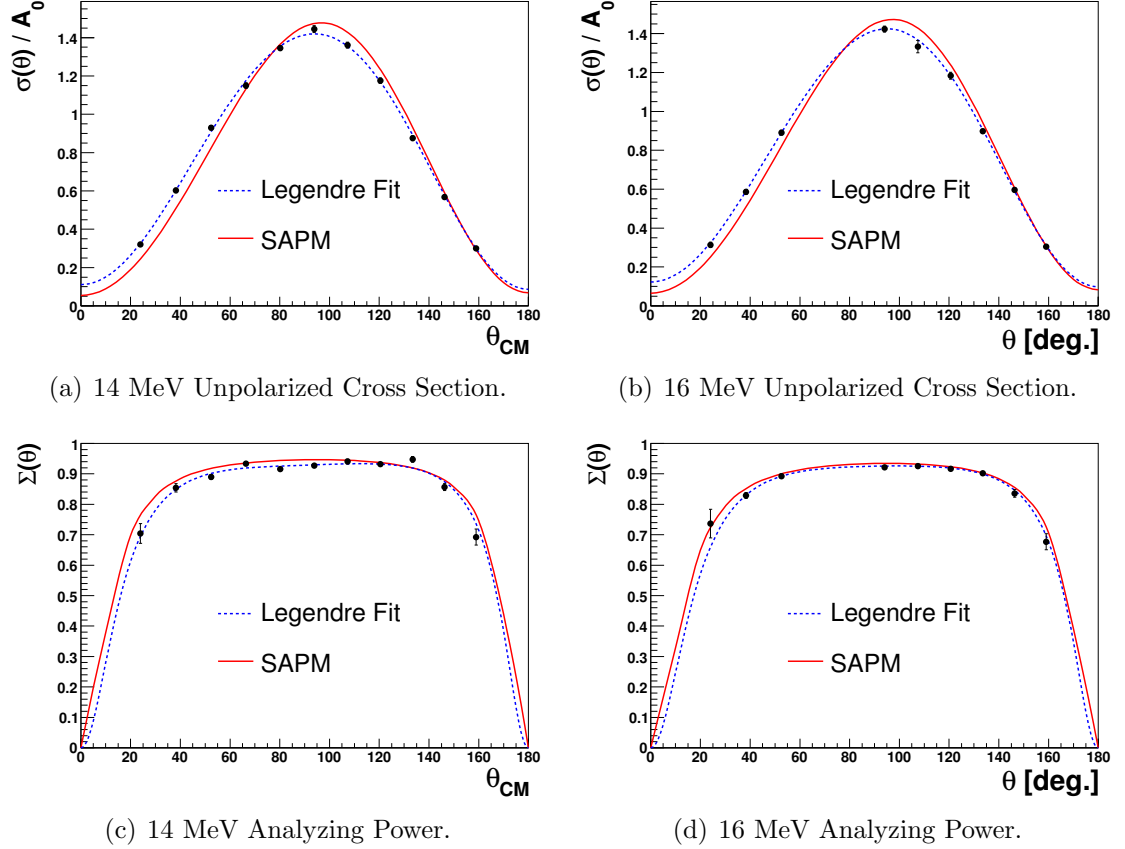


**Figure 6.1:** Final experimental observables. The error bars are statistical only. The blue curve represents the associated Legendre polynomial fit to the yields and the red curve is a potential model calculation from Schwamb and Arenhövel [Sch01a, Sch01b, Are04], referred to here as the SAPM calculation.

## 6.2.1 Legendre Polynomial Expansion Coefficients

The coefficients of an associated Legendre polynomial expansion of the differential cross section (Equation 5.3) were extracted during the process of correcting the data (see Section 5.7). The extracted coefficients are presented in Figures 6.2 and 6.3.

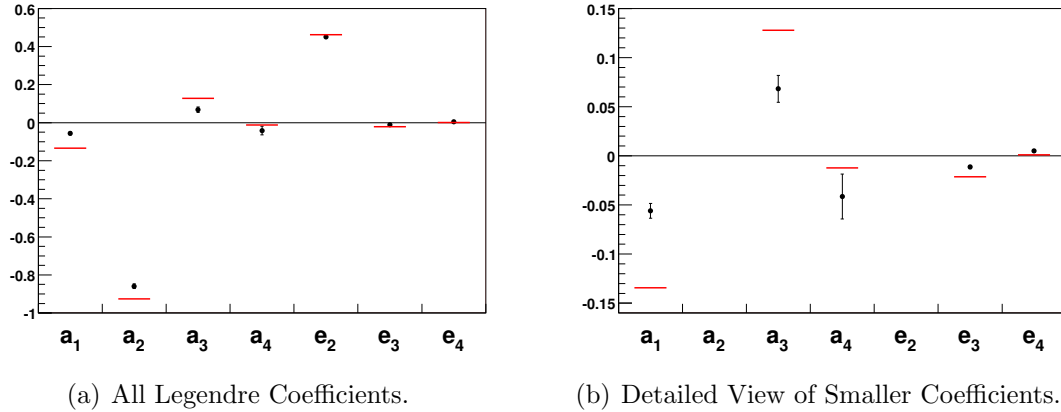


**Figure 6.2:** 14 MeV Legendre coefficients. The red lines represent the Legendre coefficients from the SAPM calculation. Subfigure 6.2(a) displays all the expansion coefficients, and Subfigure 6.2(b) changes the scale on the y-axis in order to see the details of the smaller coefficients. The errors shown are statistical only.

The coefficients follow the same general trend as the theory, but ultimately significant differences exist. Note in particular that the  $a_1$  and  $a_3$  coefficients are smaller than predicted by theory for both energies, giving rise to the difference between theory and data for the fore-aft asymmetry which is observed in the unpolarized cross section of Figure 6.1. The following sections discuss any differences observed in the observables and, when possible, relates them to the results for the Legendre coefficients shown here.

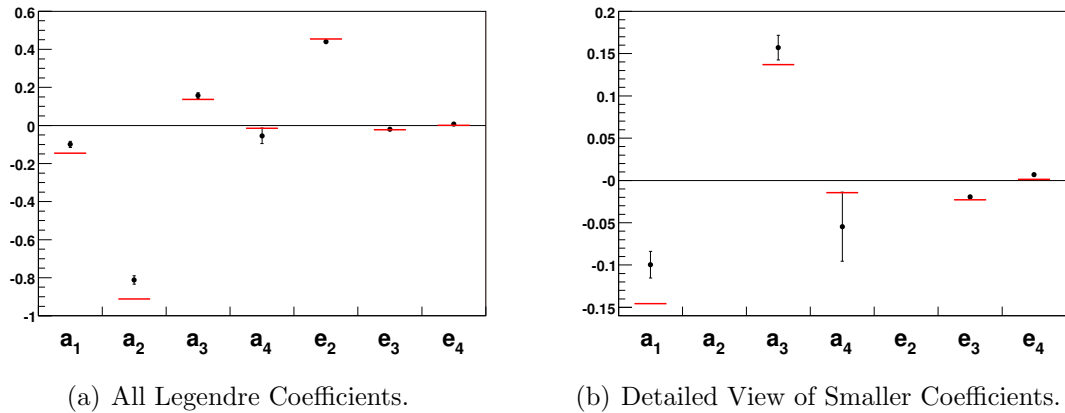


**Figure 6.3:** 16 MeV Legendre coefficients. The red lines represent the Legendre coefficients from the SAPM calculation. Subfigure 6.3(a) displays all the expansion coefficients, and Subfigure 6.3(b) changes the scale on the y-axis in order to see the details of the smaller coefficients. The errors shown are statistical only.

## 6.2.2 Unpolarized Cross Section

In the unpolarized cross section, the values at forward angles for both the 14 and the 16 MeV data sets are slightly larger than predicted from the theory. As discussed in Section 2.4.5, the cross section at  $0^\circ$  has been an area of extensive study on the theoretical side due to disagreements between theory and experiment [Cam82, Fri84, Wil88, Are91]. Those results displayed the importance of relativistic corrections, in particular the need to include the relativistic spin-orbit current in order to correctly predict the cross section at  $0^\circ$ .

Hence, the discrepancy seen between the present data and the theory might be thought to be related to the proper inclusion of the relativistic effects. However, the versions of the SAPM calculation performed with and without the relativistic contributions shown in Figure 2.5 demonstrate that the calculated observables are not greatly influenced by the inclusion of these terms at these energies, leaving uncertainty about the possible cause of the discrepancy. The extraction of the transition matrix

element amplitudes discussed later indicate that the difference in the the electric quadrupole ( $E2$ ) amplitudes leading to  $d$ -waves (orbital angular momentum  $l = 2$ ) in the outgoing state are responsible for the observed differences.

In addition, whereas a slight backward peaking in the theoretical calculation of the unpolarized cross section is seen at both energies, the data are slightly more symmetric about  $90^\circ$ . This feature manifests itself in  $a_1$  and  $a_3$  Legendre expansion coefficients which are smaller than those predicted by the theory (see Figure 6.2 and Figure 6.3). As the TME formalism will show, these coefficients arise primarily from the interference between the electric dipole ( $E1$ ) transitions which lead to  $p$ -waves (orbital angular momentum  $l = 1$ ) in the outgoing channel and the  $E2$   $d$ -waves. Since it will be shown later that good agreement is found for the  $p$ -wave amplitudes (see Figure 6.12), one expects to find smaller  $d$ -wave amplitudes leading to less of a fore-aft asymmetry. In fact, the  $E2$   $d$ -wave contributions are found to differ from the theory, but their contribution to the cross section is larger than predicted by theory. This is related to the way that the  $d$ -waves amplitudes split, which is discussed in more detail in Section 7.4.1.

Another way to observe the differences in the shapes of the unpolarized cross section is to form ratios of the cross section for given angles to the cross section at  $90^\circ$ . The ratios are shown in Figure 6.4 for lab angles of  $45^\circ$ ,  $135^\circ$ , and  $155^\circ$  for these data and for the SAPM calculation. Also shown are data from previous measurements, where the same ratios were constructed.

The comparison to the SAPM calculation displays what was discussed above, namely that the shape of our data agree well with the theory at back angles, but that a significant discrepancy is observed at forward angles. The error bars on the points from this work are statistical only.

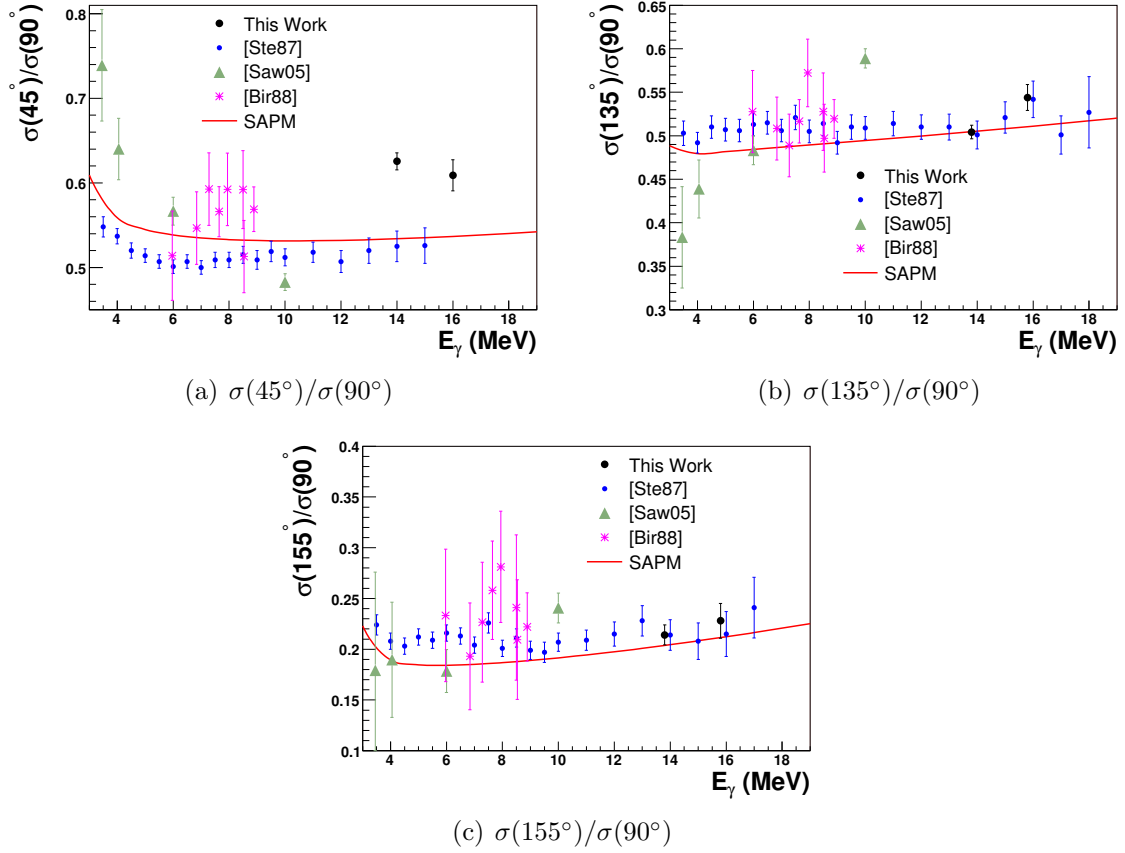


**Figure 6.4:** Ratio of the cross section at selected angles to the cross section at  $\theta = 90^\circ$  with comparisons to previous measurements. The ratios and angles are reported in the lab frame. The references for the previous data are cited on the legend of each plot. The red curve is from the SAPM calculation.

Of the previous experiments shown in Figure 6.4, only the results from Stephenson *et al.* [Ste87] cover the energy range of the present work. That experiment was performed with photons produced via bremsstrahlung at the Argonne high-current electron linac. The photons struck a  $C_2H_2$  target which was chosen to be very thin in order to reduce multiple scattering effects. Plastic scintillators were used to detect the outgoing neutrons and they were placed distances of 10 to 20 meters away from the target allowing time of flight methods to be used for neutron energy determination.

The Stephenson *et al.* experiment was set up specifically to measure the ratios shown in the figure. Since the exact angles needed for a comparison did not exist for the Blowfish array, the Legendre polynomial fit was used to determine the ratios and the errors on the extracted Legendre coefficients were propagated through to produce the error bars seen in the figures. The uncertainties obtained in this way are very similar to the data points at angles near these. Like the comparison with the theory, our results agree very well with [Ste87] at back angles, but poorly at forward angles.

### 6.2.3 Analyzing Power

A comparison between the experiment and the theory for the analyzing power values (Figure 6.1) shows that the shapes of the analyzing powers are very similar. However, the experimental data are slightly lower than the theoretical predictions in the central angle regions. If analyzing power values are systematically lower than theoretical expectations, it is reasonable to expect that it is due to an isotropic component of the reaction which tends to “wash out” the analyzing power. The  $M1$   $s$ -waves ( $l = 0$ ) produce an isotropic distribution of neutrons, but at these energies the  $s$ -waves are too small to produce such an effect<sup>1</sup>. The cause of the lower analyzing power values in this case is due to slight differences between the data and the theory for the splittings of the  $E1$   $p$ -wave amplitudes (see Section 6.4.2).

A comparison is made to previous measurements in Figure 6.5 by plotting the analyzing power at  $\theta_{lab}=90^\circ$  as a function of  $\gamma$ -ray energy for this work and previous works. The error bars for this work are statistical only.

The only result in the energy range of this experiment is from Del Bianco *et al.* [Del81]. That measurement utilized linearly polarized  $\gamma$ -rays obtained from Comp-

---

<sup>1</sup>The  $s$ -waves are too small both from the point of view of the SAPM calculation, and also as obtained from the transition matrix element fits to the data.

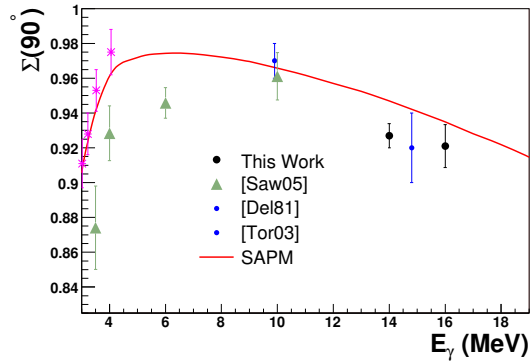


**Figure 6.5:** Comparison of  $\Sigma(\theta_{Lab} = 90^\circ)$  with previous measurements. The analyzing powers are reported for the lab frame. The references for the previous data are cited on the legend of the plot. The red curve is from the SAPM calculation.

ton backscattering an external laser from a high energy electron beam at the Ladon facility in Frascati, Italy. Neutrons were detected using a liquid scintillator and a deuterated scintillator served as both a target and proton detector with PSD capabilities. Time-of-flight was used to obtain the neutron energies. The present results agree well with the point of Del Bianco *et al.* at about 15 MeV. In fact, both results possess the similar feature of obtaining  $90^\circ$  analyzing power values which are less than what the SAPM calculation predicts, although the theory curve is just outside of one standard deviation.

### 6.3 TME Formalism

One of the goals of this measurement was the extraction of the amplitudes of the transition matrix elements (TMEs) which contribute to the reaction at these energies. This is done using the formalism worked out in [Wel92] for linearly polarized  $\gamma$ -rays, which is a special case of the more general formalism from [Wel63]. An overview of the formalism for this reaction is given below.

### 6.3.1 Formalism Nomenclature

The reaction of interest involves particles with the following spin assignments

$$S_d(\vec{L}, S_n)S_p \quad (6.1)$$

where the intrinsic spins of the deuteron, neutron, and proton are given by  $S_d = 1$ ,  $S_n = \frac{1}{2}$ , and  $S_p = \frac{1}{2}$ . Each particle has positive parity:  $\pi_d = \pi_n = \pi_p = +$ .

$L$  is the multipolarity of the incoming linearly polarized  $\gamma$ -ray. The mode of the  $\gamma$ -ray is specified by  $p$ , where  $p=0$  for magnetic multipoles, and  $p=1$  for electric multipoles. For example,  $E1$  radiation is denoted by  $p=1$  and  $L=1$ .

Using these definitions, the following quantum numbers and their relationships can be defined

$$\begin{aligned} \vec{s} &= \vec{S}_n + \vec{S}_p \\ \vec{J} &= \vec{s} + \vec{l} \\ \vec{J} &= \vec{L} + \vec{S}_d \\ \vec{k}' &= \vec{J} + \vec{J}' \end{aligned} \quad (6.2)$$

where  $\vec{s}$  ( $\vec{s}'$ ) is the channel spin, which for two spin- $\frac{1}{2}$  particles can take on values of 0 or 1;  $\vec{l}$  ( $\vec{l}'$ ) is the orbital angular momentum in the outgoing channel;  $\vec{J}$  ( $\vec{J}'$ ) is the total angular momentum of the system; and  $\vec{k}'$  is the index that labels the Legendre polynomial associated with the interference of two TMEs with total spins  $J$  and  $J'$ . The primed variables enter the formalism because two TMEs are allowed to interfere in the expressions that follow, the first being labeled by the unprimed quantum numbers and the second being labeled by the primed ones. The label  $t$  ( $t'$ ) is given to a set of quantum numbers for a given channel ( $p, L, J, l$ , and  $s$ ).

The total parity of the system is denoted by  $\pi$ . The initial parity of the system

is given by the product of the parity of the deuteron and the parity of the incoming radiation field

$$\pi_i = \pi_d \pi_L = (-1)^{p+L+1}. \quad (6.3)$$

The final parity of the system is given by

$$\pi_f = \pi_n \pi_p \pi_l = (-1)^l, \quad (6.4)$$

and since parity is conserved, we can write

$$\pi = \pi_i = \pi_f$$

$$(-1)^{p+L+1} = (-1)^l. \quad (6.5)$$

From this condition, the possible  $l$  values of the outgoing state for a given mode and multipolarity of the incident  $\gamma$ -ray can be determined. For example,  $E1$  radiation leads to  $l=1$  ( $p$ -waves),  $l=3$  ( $f$ -waves), and so on, and  $M1$  radiation leads to  $l=0$  ( $s$ -waves),  $l=2$  ( $d$ -waves), and so on.

### 6.3.2 Differential Cross Section

The differential cross section for polarized beam and unpolarized target can be written as [Wel92]

$$\sigma(\theta, \phi) = \sum_{kq} A_{kq}(\theta) t_{kq}(\phi). \quad (6.6)$$

Here, as the  $\phi$  dependence indicates, information about the beam polarization is carried by the tensor moments,  $t_{kq}$ . In the case of linearly polarized  $\gamma$ -rays, we are restricted to tensor moments with  $k = 0, 2$  and  $q = 0, \pm 2$ . If  $P_{\gamma l}$  is the linear

polarization fraction of the beam, these tensors take the form

$$t_{00} = 1 \quad (6.7)$$

$$t_{20} = \frac{1}{\sqrt{10}} \quad (6.8)$$

$$t_{2\pm 2} = -\frac{P_{\gamma l}}{2} \sqrt{\frac{3}{5}} e^{\pm 2i\phi}. \quad (6.9)$$

From [Wel92] and [Wel63],  $A_{kq}$  can be written as

$$A_{kq}(\theta) = \frac{\lambda^2}{6} \sum_{tt'k'q'} B_{kq}^{k'q'} R_t R_{t'} P_{k'}^{|q'|}(\cos \theta), \quad (6.10)$$

where the  $\gamma$ -ray wavelength is given by  $\lambda = \lambda/2\pi$ , the  $P_{k'}^{|q'|}(\cos \theta)$  functions are the associated Legendre polynomials, and the  $B_{kq}^{k'q'}$  coefficients, which are written in terms of Clebsch-Gordon and Racah coefficients, can be found in [Wel92].

The  $R_t$  terms represent the reduced transition matrix elements (TMEs) of the reaction, denoted by

$$R_t = \langle {}^{2s+1}l_J \pi \parallel R \parallel pL S_d J \pi \rangle. \quad (6.11)$$

The reduced TMEs are the portions of the TMEs which depend only on the radial parts of the wave function, which are obtained after factoring the TMEs into their radial and angular components. The notation that will be used in this work to distinguish the TMEs from each other is  ${}^{2s+1}l_J (pL)$ , where  $l$  is given in spectroscopic notation. For example, two of the TMEs of importance in this reaction are the  ${}^1s_0 (M1)$  and  ${}^3p_2 (E1)$  TMEs.

By considering only the non-zero  $B_{kq}^{k'q'}$  coefficients and using the fact that  $P_{\gamma l}=1.0$

in this experiment, the cross section can be written as

$$\begin{aligned} \sigma(\theta, \phi) = & \frac{\lambda^2}{6} \sum_{tt'k'} \left[ \left( B_{00}^{k'0} + \frac{1}{\sqrt{10}} B_{20}^{k'0} \right) R_t R_{t'} P_{k'}(\cos \theta) \right. \\ & \left. - \sqrt{\frac{3}{5}} B_{22}^{k'2} R_t R_{t'} P_{k'}^2(\cos \theta) \cos(2\phi) \right]. \end{aligned} \quad (6.12)$$

By comparing this expression with Equation 5.3, the  $a_k$  and  $e_k$  coefficients can be written as

$$a_k = \sum_{tt'} R_t R_{t'} \left[ B_{00}^{k'0} + \frac{1}{\sqrt{10}} B_{20}^{k'0} \right], \quad (6.13)$$

and

$$e_k = -\sqrt{\frac{3}{5}} \sum_{tt'} R_t R_{t'} B_{22}^{k'2}, \quad (6.14)$$

with the result that the Legendre expansion coefficients are now obtained as functions of the contributing TMEs. It can be shown [Wel92] that the product  $R_t R_{t'}$  can be replaced by the real part of  $R_t R_{t'}$ . In this way, we write  $Re\{R_t R_{t'}\}$  as the product of two amplitudes and the cosine of the difference between the two TME phases. For example,

$$Re\{R_a R_b'\} = |R_a| |R_b'| \cos(\delta_a - \delta_b') \quad (6.15)$$

where  $\delta_a$  ( $\delta_b$ ) is the phase of  $R_a$  ( $R_b$ ). The  $a_k$  and  $e_k$  equations expressed in terms of the amplitudes and phases of the TMEs considered in this work can be found in Equations A.1-A.8 of Appendix A.

### 6.3.3 The Choice of TMEs

The extraction of the amplitudes of the TMEs of this reaction relies on the assumption that we need only include those amplitudes which contribute significantly

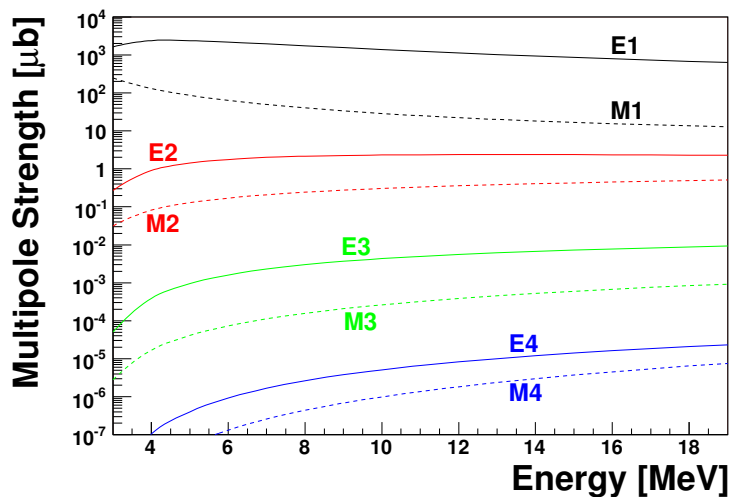
at these energies in our fits to the data. A fit to the data would be impossible if, for instance, all the possible  $M1$ ,  $E1$ , and  $E2$  TMEs were used in the fits. Therefore, the number of TMEs included in the fits was reduced by eliminating TMEs expected to be small. These decisions were made based on selection rules and with guidance from the SAPM calculation.

In determining which  $\gamma$ -ray multipolarities to include in the fits, the fact that the reaction at these energies is known to be dominated by  $E1$  transitions justifies the inclusion of those amplitudes. In addition, the  $M1$  amplitudes are considered because the  $^1s_0$  ( $M1$ ) amplitude is known to be large at photodisintegration threshold from the inverse thermal  $n$ - $p$  capture reaction, and is also expected to play a role in the reaction at these energies.

Including only  $M1$  and  $E1$  radiation limits the sum in the Legendre polynomial expansion to  $k \leq 2$ . Since the Legendre fits to the data have already shown that finite  $a_3$  and  $e_3$  terms exist (see Section 6.2.1), we know that quadrupole terms must also be included. Since these Legendre coefficients result from the interference between amplitudes of opposite parity, this suggests the  $E2$   $d$ -waves should be included. The  $E2$   $d$ -waves, though small in strength at these energies, interfere with the large  $E1$   $p$ -waves which magnifies their importance in the angular distribution of the cross section.

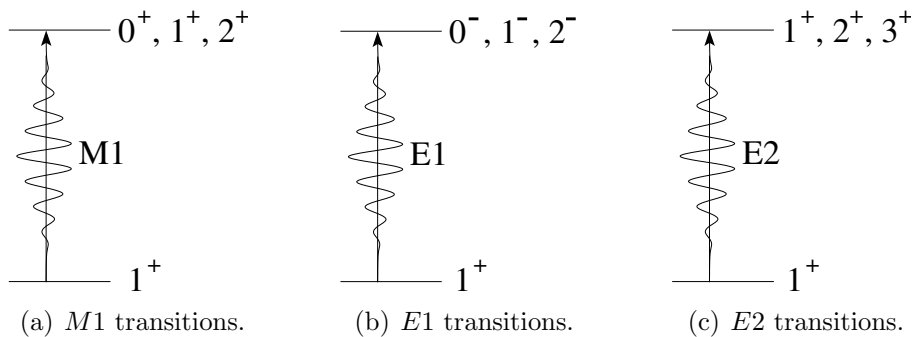
Higher order multipoles should be significantly smaller than these at the energies of this experiment, as seen in the predictions for the multipole strengths to the total cross section for the SAPM calculation up to  $L = 4$  which is shown in Figure 6.6. Using these considerations, we limited ourselves to the inclusion of  $M1$ ,  $E1$ , and  $E2$  multipoles.

Figure 6.7 illustrates the possible  $J^\pi$  values allowed for each multipole transition.



**Figure 6.6:** Multipole strength contributing to the total cross section as a function of energy for the full SAPM calculation up to  $L = 4$ .

The allowed  $J$  and  $\pi$  values are easily determined from the third expression in Equation 6.2 and Equation 6.3. The decision to limit our fits to  $M1$ ,  $E1$ , and  $E2$  radiation leaves the list of possible TMEs found in Table 6.1.



**Figure 6.7:** Spins and parities possible for final states of  $M1$ ,  $E1$ , and  $E2$  transitions in the deuteron. Each spin and parity is labeled as  $J^\pi$ . For example, the deuteron ground state is a  $1^+$  state.

From selection rules we know that several of these TMEs will be small. For example, the  ${}^3s_1(M1)$  term has the same quantum numbers as the ground state of

Transition Matrix Element		Theoretical Cross Section Contribution	
$pL$	$^{2s+1}l_J$	14 MeV	16 MeV
M1	$^1s_0$	17.2 $\mu\text{b}$	14.1 $\mu\text{b}$
	$^3s_1$	$4.11 \times 10^{-3} \mu\text{b}$	$4.54 \times 10^{-3} \mu\text{b}$
	$^1d_2$	1.46 $\mu\text{b}$	1.84 $\mu\text{b}$
	$^3d_1$	$2.38 \times 10^{-2} \mu\text{b}$	$2.77 \times 10^{-2} \mu\text{b}$
	$^3d_2$	$1.46 \times 10^{-2} \mu\text{b}$	$1.84 \times 10^{-2} \mu\text{b}$
E1	$^1p_1$	$1.58 \times 10^{-3} \mu\text{b}$	$2.00 \times 10^{-3} \mu\text{b}$
	$^3p_0$	46.5 $\mu\text{b}$	34.9 $\mu\text{b}$
	$^3p_1$	383 $\mu\text{b}$	330 $\mu\text{b}$
	$^3p_2$	494 $\mu\text{b}$	410 $\mu\text{b}$
	$^3f_2$	10.8 $\mu\text{b}$	12.6 $\mu\text{b}$
E2	$^3s_1$	$5.29 \times 10^{-4} \mu\text{b}$	$5.68 \times 10^{-4} \mu\text{b}$
	$^1d_2$	$2.97 \times 10^{-5} \mu\text{b}$	$3.11 \times 10^{-5} \mu\text{b}$
	$^3d_1$	0.377 $\mu\text{b}$	0.367 $\mu\text{b}$
	$^3d_2$	0.936 $\mu\text{b}$	0.927 $\mu\text{b}$
	$^3d_3$	1.04 $\mu\text{b}$	1.02 $\mu\text{b}$
	$^3g_3$	$2.07 \times 10^{-2} \mu\text{b}$	$2.71 \times 10^{-2} \mu\text{b}$

**Table 6.1:** All possible TMEs for  $M1$ ,  $E1$ , and  $E2$  transitions along with theoretical predictions from the SAPM calculation for the contribution of each to the total cross section.

the deuteron, so it is expected to be negligible because of orthogonality. In addition, the  $^1p_1(E1)$  and  $^1d_2(E2)$  terms are spin-flip ( $\Delta s=1$ ) electric transitions and should also be small.

The  $^3f_2(E1)$  term, while predicted by theory to play a small role at these energies, leads to unstable fits and the generation of unreasonable results. Therefore, it was decided that the  $E1$  contribution to the angular distribution of the observables was reproduced well enough by the much more dominant  $p$ -wave terms and the  $f$ -waves were neglected. It should be noted that the quality of the fits did not suffer due to this choice.

Ultimately, after considering these selection rules and consulting the SAPM cal-

ulation, the TMEs listed in Table 6.2 were included in the fits. Note that we are limiting ourselves to  $M1$ ,  $E1$ , and  $E2$  multipoles and all partial waves higher than  $d$ -waves are being neglected.

M1:	$^1s_0$		
E1:	$^3p_0$	$^3p_1$	$^3p_2$
E2:	$^3d_1$	$^3d_2$	$^3d_3$

**Table 6.2:** TMEs included in the fits to the data.

The validity of these choices will be tested by whether the inclusion of these TMEs is enough to reproduce the data. As a test of whether enough terms had been included, the TME amplitudes and phases listed here were obtained from the SAPM calculation and put into this formalism in order to be compared to the full SAPM calculation of the observables<sup>2</sup>. Good agreement was found. After limiting the TMEs to those listed in Table 6.2, the equations for the  $a$  and  $e$  coefficients appear as shown in Equations A.1-A.8 in Appendix A.

### 6.3.4 Treatment of the TME Phases

As Equations A.1-A.8 demonstrate, there are still a large number of parameters remaining when considering the fact that the amplitudes and phases of each TME must be determined. However, by invoking Watson’s theorem [Knu99], the number of fitting parameters is reduced by almost a factor of two<sup>3</sup>.

Watson’s theorem allows the elastic  $n$ - $p$  scattering phase shifts to be used in determining the phase differences for the photodisintegration TMEs which appear in

<sup>2</sup>Full calculation in the sense that all TMEs up to  $L = 4$  were included.

<sup>3</sup>It would be reduced by exactly a factor of two if the  $^1s_0(M1)$  phase entered into the formalism. However, since terms of different channel spin do not interfere in the cross section, this phase does not appear because there are no other  $s = 0$  terms being included.

the equations in Appendix A. The use of Watson’s theorem in this instance relies on the fact that there are no open reaction channels in the case of  $n$ - $p$  scattering other than radiative capture. In terms of photodisintegration, this condition is met for energies below pion photoproduction threshold.

In addition, the scattering phase shifts can be used only when there is no mixing between angular momentum states<sup>4</sup>, which is the case here. The lack of mixing here is seen by examining the relevant mixing phases at these energies from a phase shift analysis of the  $n$ - $p$  scattering data such as SAID [Cen07] which shows them to be negligible.

Since Watson’s theorem requires the input from the  $n$ - $p$  scattering phase shifts, they were obtained from the SAID phase shift analysis code [Cen07]. The phase shifts used in this analysis at 14 and 16 MeV are listed in Table 6.3. Most of the phase shifts are on the order of a few degrees, except for a few of the  $E1$   $p$ -wave phase shifts which are be slightly larger. Note that the  $^1s_0$  phase does not enter the analysis since terms of different channel spins do not interfere in the cross section.

TME	Phase Shifts	
	14 MeV	16 MeV
$^1s_0$ ( $M1$ )	50.7°	49.0°
$^3p_0$ ( $E1$ )	8.6°	9.3°
$^3p_1$ ( $E1$ )	-4.9°	-5.5°
$^3p_2$ ( $E1$ )	2.9°	3.4°
$^3d_1$ ( $E2$ )	-2.9°	-3.6°
$^3d_2$ ( $E2$ )	4.1°	5.0°
$^3d_3$ ( $E2$ )	0.1°	0.2°

**Table 6.3:**  $n$ - $p$  scattering phase shifts corresponding to  $E_\gamma$  of 14 and 16 MeV from the SAID analysis [Cen07].

---

<sup>4</sup>A more general form of Watson’s theorem can be used in the case of angular momentum mixing, but its application is more complex than described here.

## 6.4 Fits and TME Results

Once the relative phases of the TMEs are fixed, seven TME amplitudes remain as free parameters in a fit to the experimental yields. The same procedure used to fit the yields using Legendre polynomials was used here (see Section 5.7.2). The only difference is that the  $a$  and  $e$  coefficients were no longer the free parameters of the fit. In this case, the coefficients were expressed in terms of the TME amplitudes, which became the free parameters in the fit. As before, the fitting routine `Minuit` [Jam98] was used to determine the fitted values of the amplitudes and their associated errors.

### 6.4.1 Without TME Splittings

The fits to the data followed a two step progression. First, for the TME amplitudes included in the list of Table 6.2, it was assumed that there are no splittings in the reduced  $p$ - and  $d$ -wave amplitudes (i.e.  ${}^3p_0 = {}^3p_1 = {}^3p_2$  and  ${}^3d_1 = {}^3d_2 = {}^3d_3$ ). This assumption has validity at very low energies according to the SAPM calculations, but is not expected to be valid in the energy range of this experiment. Those fits were improved upon by allowing splittings in both the  $p$ - and  $d$ -wave amplitudes, which is discussed in Section 6.4.2.

Under the assumption of no splittings, the equations for the  $a$  and  $e$  coefficients

of the Legendre expansion take on a relatively simple form:

$$\begin{aligned}
A_0 &= 3.75|d|^2 + 2.25|p|^2 + 0.25|s|^2 \equiv 1.0 \\
a_1 &= 7.794|p||d| \cos(\delta_{pd}) \\
a_2 &= -2.25|p|^2 + 2.678|d|^2 \\
a_3 &= -7.794|p||d| \cos(\delta_{pd}) \\
a_4 &= -6.429|d|^2 \\
e_2 &= \frac{1}{2}(2.25|p|^2 + 2.678|d|^2) \\
e_3 &= \frac{1}{6}(7.794|p||d| \cos(\delta_{pd})) \\
e_4 &= \frac{1}{12}(6.429|d|^2),
\end{aligned} \tag{6.16}$$

where  $|s|$  is the  $s$ -wave  $M1$  amplitude ( $|^1s_0|$ ),  $|p|$  is the  $p$ -wave  $E1$  amplitude with  $|^3p_0| = |^3p_1| = |^3p_2| = |p|$ ,  $|d|$  is the  $d$ -wave  $E2$  amplitude with  $|^3d_1| = |^3d_2| = |^3d_3| = |d|$ , and  $\delta_{pd}$  is the relative phase ( $\delta_p - \delta_d$ ) between the  $p$ - and  $d$ -wave amplitudes.

Note from these equations that many of the coefficients have simple relationships between them

$$\begin{aligned}
a_1 &= -a_3 \\
a_3 &= -6 e_3 \\
a_4 &= -12 e_3,
\end{aligned} \tag{6.17}$$

and if  $|p|^2 \gg |d|^2$ , which is true here, we also have

$$a_2 = -2 e_2. \tag{6.18}$$

The experimentally extracted Legendre coefficients can be used to examine how well our data hold up to the assumption of no splitting. The ratios of the coefficients are shown in Tables 6.4 and 6.5 for 14 and 16 MeV, respectively.

	14 MeV Ratios					No splitting Assumption	SAPM Coefficients
	ratio		(stat)		(syst)		
$a_1/a_3$	-0.82	$\pm$	0.16	$\pm$	0.12	-1	-1.05
$a_2/e_2$	-1.91	$\pm$	0.02	$\pm$	0.02	-2	-2.00
$a_3/e_3$	-6.0	$\pm$	1.2	$\pm$	0.9	-6	-6.0
$a_4/e_4$	-8.4	$\pm$	3.3	$\pm$	3.8	-12	-12.4

**Table 6.4:** 14 MeV Legendre coefficient ratios. Both statistical and systematic errors on the ratios are shown. Also shown is the ratio of the same coefficients from the full SAPM calculation.

	16 MeV Ratios					No splitting Assumption	SAPM Coefficients
	ratio		(stat)		(syst)		
$a_1/a_3$	-0.86	$\pm$	0.14	$\pm$	0.32	-1	-1.07
$a_2/e_2$	-1.92	$\pm$	0.02	$\pm$	0.06	-2	-2.00
$a_3/e_3$	-6.4	$\pm$	1.1	$\pm$	3.5	-6	-6.0
$a_4/e_4$	-8.6	$\pm$	4.1	$\pm$	8.4	-12	-12.0

**Table 6.5:** 16 MeV Legendre coefficient ratios. Both statistical and systematic errors on the ratios are shown. Also shown is the ratio of the same coefficients from the full SAPM calculation.

The experimentally determined ratios and the ratios with the no splitting assumption disagree for the first two ratios listed in each table. This is especially seen in the ratio between the largest  $a$  and  $e$  coefficients,  $a_2$  and  $e_2$ , which is significantly lower in the data. This would seem to indicate that the assumption is breaking down at these energies.

However, notice that the ratios from the SAPM calculation still agree with the ratios expected under the no splitting assumption, but the reason for this agreement is not because the splittings are small in the theory at these energies. In fact, if the  $p$ - and  $d$ -wave amplitudes are collapsed in the theory, the ratios listed in Tables 6.4 and 6.5 cannot be reproduced. Therefore, the comparison of these ratios alone is not enough to indicate whether the no splitting assumption is valid here.

Fits to the yields were performed under the assumption of no splittings and Figure 6.8 shows the resulting observables constructed from the fits. Notice that the fits to the data are in fairly good agreement for the unpolarized cross section data, but the fit values are lower than the data at the extreme angles in the case of the analyzing powers.

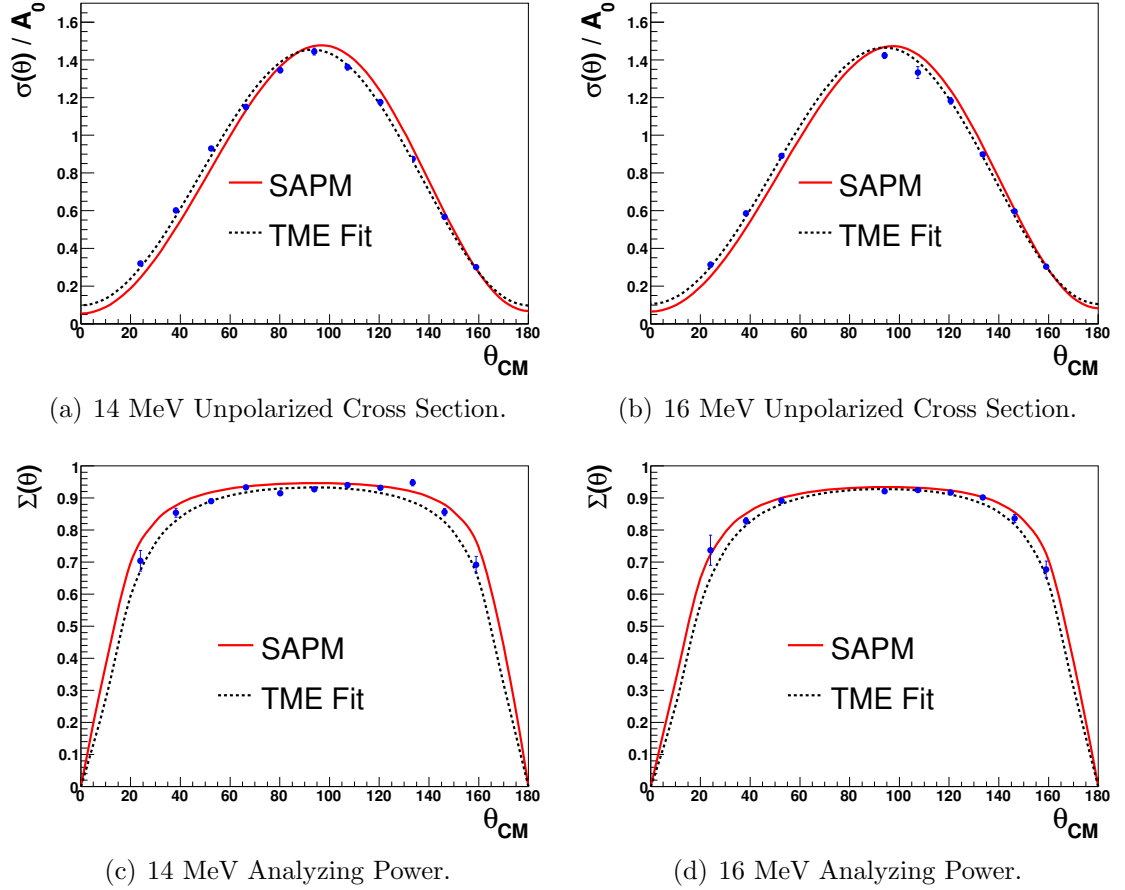


**Figure 6.8:** Fits to the observables with the assumption of no splittings. The error bars on the data are statistical only. The blue curve is the fit and the red curve is from the SAPM calculation.

The systematic errors on the extracted amplitudes were determined by replacing the statistical errors with the systematic errors and fitting the data again. The

extracted reduced amplitudes along with both statistical and systematic errors can be found in tabular form in Appendix B. The  $\chi^2$  values for each fit are shown in Table 6.6.

	$\chi^2$	ndf	$\chi_r^2$
14 MeV	75.7	40	1.9
16 MeV	53.7	32	1.7

**Table 6.6:**  $\chi^2$ , number of degrees of freedom (ndf), and reduced  $\chi^2$  ( $\chi_r^2$ ) for TME fits with no splittings.

It should be noted that the reduced  $\chi^2$  values presented here are larger than those obtained from the Legendre fits to the yields (see Table 5.2). As mentioned above, the only difference in the two fits is the fact that in this case the Legendre coefficients are described in terms of a limited number of TME amplitudes. Thus, the larger  $\chi_r^2$  values indicate that the expressions in Equation 6.16 do not include enough terms to adequately produce the Legendre coefficient values needed to achieve a  $\chi_r^2$  of one.

Figure 6.9 shows the resulting percent contribution to the total cross section from the  $M1$   $s$ -waves,  $E1$   $p$ -waves, and  $E2$   $d$ -waves. The absolute value of each multipole contribution to the cross section can be compared to the theory by multiplying each of the percentages obtained from the fits by the theoretical total cross section. Those comparisons are shown in Figure 6.10.

There is gross disagreement between theory and the extracted multipole contributions for the case of no splittings. The  $s$ -wave  $M1$  contribution is much larger than the theory, and the  $p$ - and  $d$ -wave contributions are significantly smaller. This is not surprising. At these energies, the splittings in the  $p$ -waves are expected to be large enough to be the dominant factor in lowering the experimental analyzing powers below the theory. By not allowing the  $p$ -waves to split, the  $s$ -wave term must

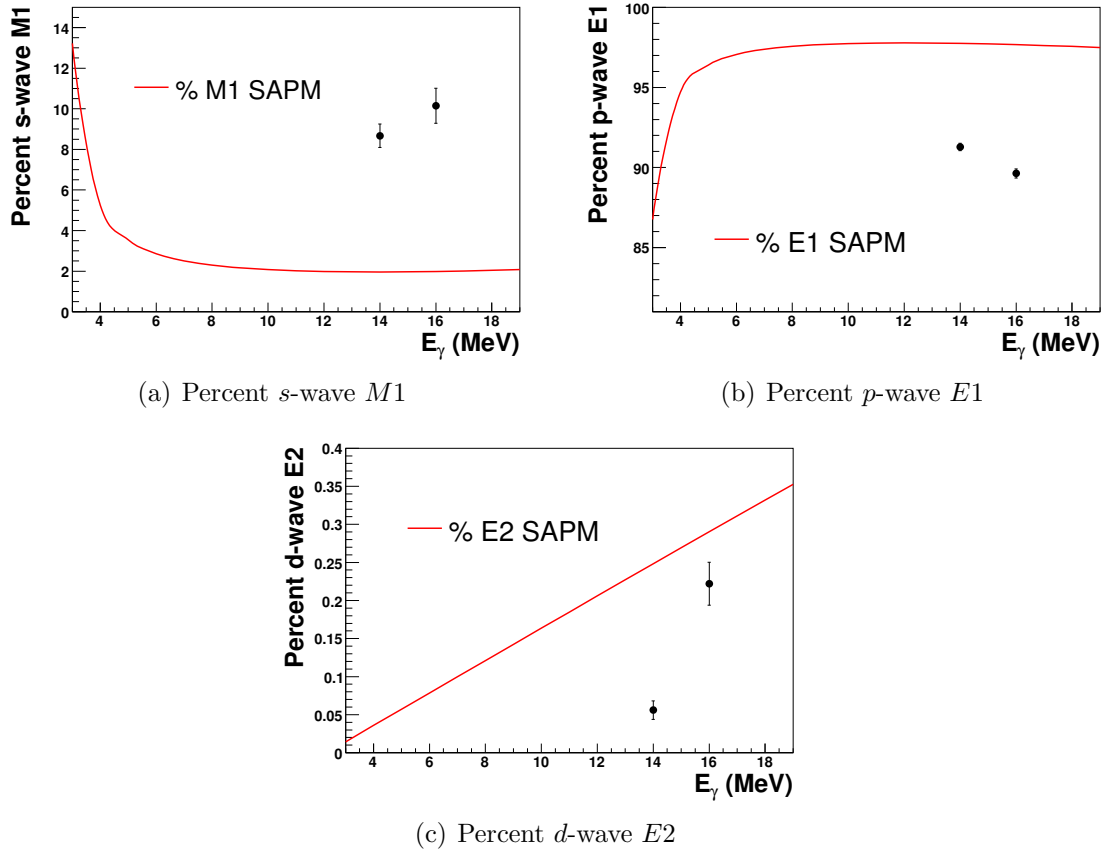
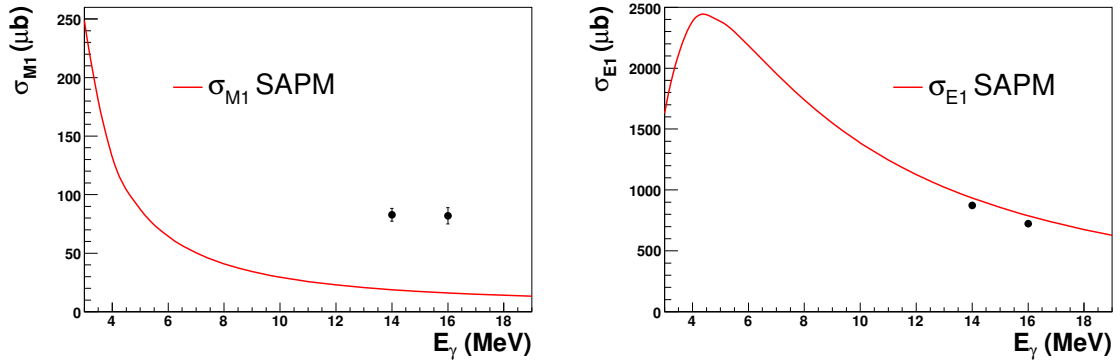


**Figure 6.9:** Percent multipole contributions to the total cross section with the assumption of no splittings. The percent of the cross section is shown for the  $M1$   $s$ -waves,  $E1$   $p$ -waves, and  $E2$   $d$ -waves. The red curve corresponds to the SAPM calculation. The errors shown are statistical only. The errors on the  $p$ -wave data are smaller than the point size.

take on a larger value in order to lower the analyzing power. The fits are improved upon in the next section by lifting the no splitting restriction.

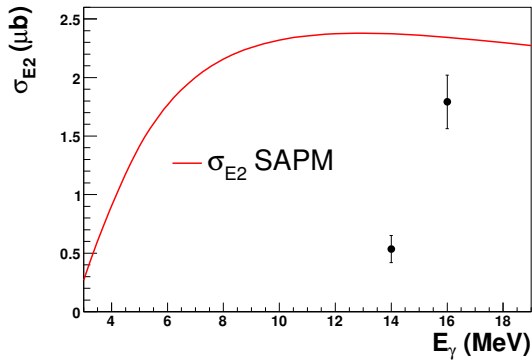
#### 6.4.2 With TME Splittings

The results from the previous section can be improved upon by allowing splittings in the  $p$ - and  $d$ -wave amplitudes. In this case, the equations for the  $a$  and  $e$  coefficients are not as simple as those in Equation 6.16. The complete equations can be found in



(a) Absolute  $s$ -wave  $M1$

(b) Absolute  $p$ -wave  $E1$



(c) Absolute  $d$ -wave  $E2$

**Figure 6.10:** Absolute multipole contributions to the total cross section with the assumption of no splittings. The absolute cross section contribution is shown for the  $M1$   $s$ -waves,  $E1$   $p$ -waves, and  $E2$   $d$ -waves. These values were obtained by multiplying the percentages from Figure 6.9 by the theoretical total cross section. The red curve corresponds to the SAPM calculation. The errors shown are statistical only. The errors on the  $p$ -wave data are smaller than the point size.

## Appendix A.

For the case with splittings allowed, the fits were performed multiple times with the seed values for the amplitudes varied over a wide range because it was found that the results depended on the starting values of the amplitudes. Using this method, both the 14 and 16 MeV fits converged to two distinct sets of solutions. The  $\chi^2$  values of the two solutions were identical, as seen in Table 6.7.

	Solution	$\chi^2$	ndf	$\chi_r^2$
14 MeV	1	68.6	36	1.9
	2	68.6	36	1.9
16 MeV	1	51.0	28	1.8
	2	51.0	28	1.8

**Table 6.7:**  $\chi^2$ , number of degrees of freedom (ndf), and reduced  $\chi^2$  ( $\chi_r^2$ ) for TME fits with splittings.

The systematic errors were determined, as before, by replacing the statistical errors by the systematic errors and performing the fits again. A table of the values extracted from the fits along with the statistical and systematic errors can be found in Appendix B. The observables resulting from the fits for one of the solutions at each energy are shown in Figure 6.11. The fits corresponding to the other solution, if shown, would be indistinguishable from the fits shown there.

The observables obtained from fits to the yields in this case look very similar to the fits without splittings. The largest qualitative difference is the slightly better agreement with the analyzing power values at the extreme back angles for the fits with splittings. While the total  $\chi^2$  values for the fits are reduced with the inclusion of splittings, the reduced  $\chi^2$  values changed very little as compared to the previous fits performed with no splittings. Ultimately, the differences in the  $\chi_r^2$  values between the TME fits and the Legendre fits of Section 5.7.3 is due to the simplifications resulting from the inclusion of a limited number of TME amplitudes in the fits. The quality of the present fits, however, is very good despite the difference in  $\chi_r^2$  values, as can be seen in Figure 6.11.

The biggest difference between the fits with and without splittings is found in the split values of the amplitudes. Here, the amplitudes are in much better agreement with theoretical expectations. The results for the extracted amplitudes are

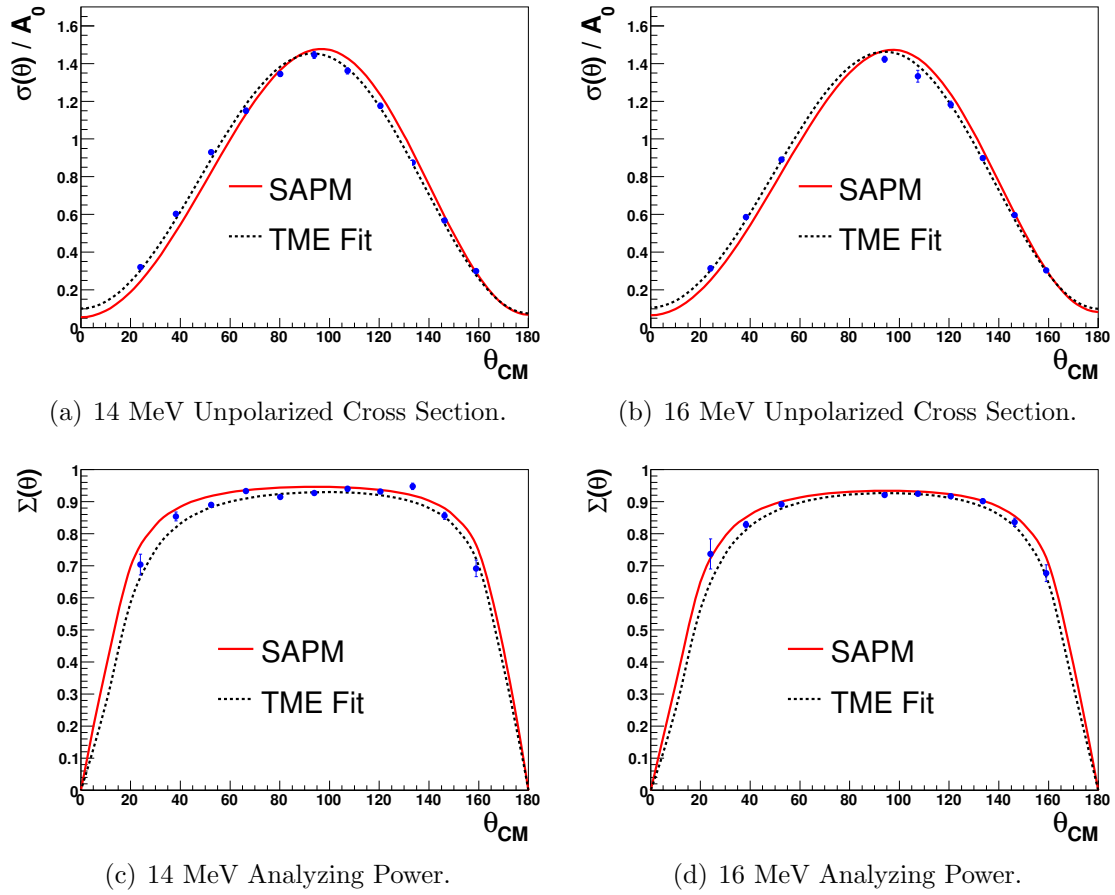


**Figure 6.11:** Fits to the observables with splittings. The error bars are statistical only. The blue curve is the fit and the red curve is from the SAPM calculation.

presented in terms of their percent of the total cross section and compared to the SAPM calculation in Figure 6.12. Also shown are the predictions for the amplitudes for the calculation without the relativistic contributions so that the sensitivity to these effects can be seen.

It should also be noted that often a drastic change in the size of the error bars on the extracted amplitudes is observed from one solution to another. `Minuit` defines a standard deviation for a parameter based on how much it must be changed to cause the  $\chi^2$  function to increase by a value of 1.0. However, in the case of a multi-parameter

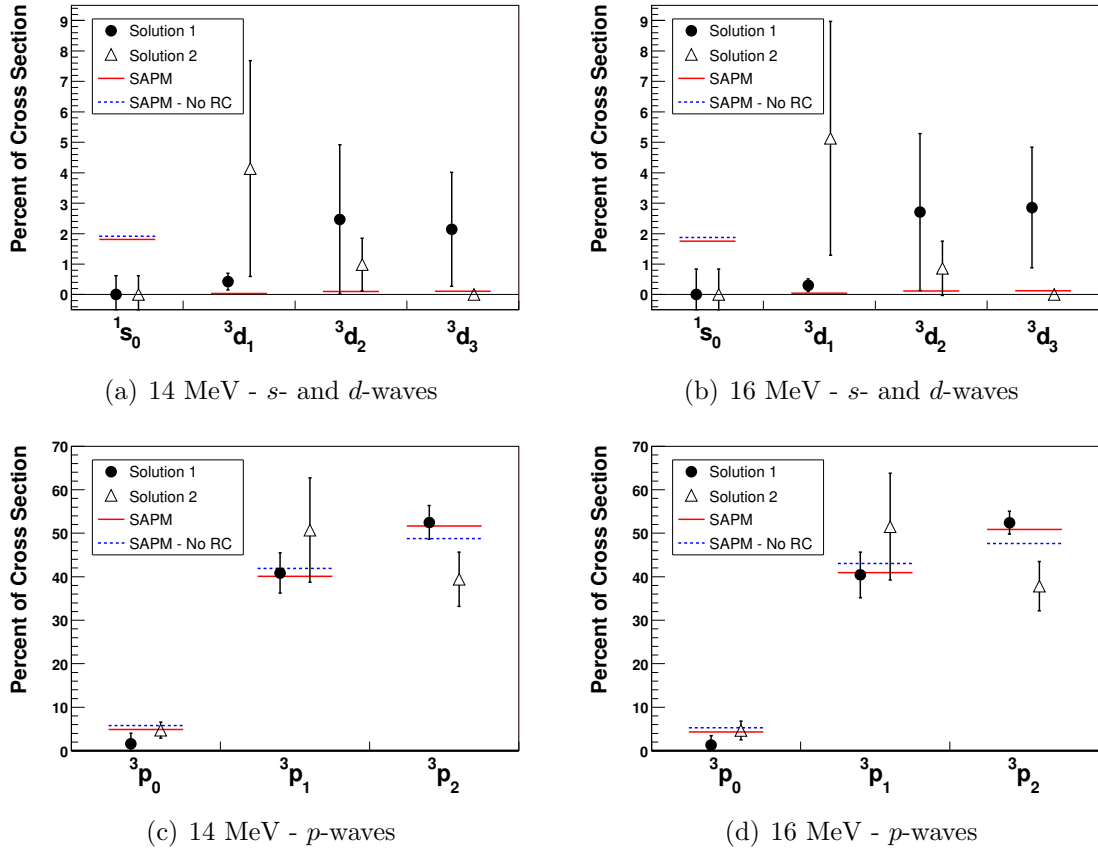


**Figure 6.12:** Percent of total cross section for each TME amplitude. The red lines correspond to the full SAPM calculation and the blue lines correspond to the SAPM calculation without the inclusion of relativistic effects. The two versions of the SAPM calculation for the  $d$ -waves are indistinguishable. The errors shown are statistical only. The errors on the  $^1s_0$  points are smaller than the point size.

fit, the diagonal terms of the error matrix which `Minuit` produces includes the effects of correlations between parameters [Jam98]. The errors on the parameters shown here are taken from the square root of the diagonal terms of the error matrix. Since some of the amplitudes have strong correlations at the  $\chi^2$  minimum of one solution but not at the other, the error bars can differ between solutions. It is thus important to keep in mind that all errors shown here include the effects of correlations.

It should also be noted that for all the fits with splittings allowed, the  $^1s_0$  am-

plitude tended to go to almost exactly zero. This amplitude only comes into the formalism as a squared term in the  $A_0$  coefficient. Thus, it is only constrained by the overall scale factor of the cross section, which has been normalized so that the total cross section is  $\sigma_T = 4\pi A_0 \equiv 4\pi$ , with arbitrary units.

In addition, since it comes in as a squared term, the  $A_0$  equation is an even function with respect to the  $^1s_0$  amplitude. This results from the fact that this amplitude is the only TME included with a channel spin of  $s=0$  and since terms of different channel spin do not interfere in the cross section, it does not interfere with the other TMEs. This makes  $|^1s_0| = 0.0$  a special value from the point of view of fitting routine `Minuit`, since it makes no distinction between positive and negative amplitudes<sup>5</sup>. As the  $^1s_0$  amplitude is being varied, if `Minuit` finds that  $\chi^2$  improves as a result of continuously lowering the amplitude, it will eventually reach zero and become negative, only to have the  $\chi^2$  function begin increasing again. Thus, in such cases the value of the  $^1s_0$  term would settle to almost exactly zero, which is the case in all the fits here. The error was obtained by determining how much it deviated before the  $\chi^2$  was changed by 1.

The fact that the value of the amplitude was so close to zero required that this error be treated slightly differently. Since all the calculations use the square of the  $s$ -wave amplitude, it is the error on the square which is important. But for a value so close to zero, the error on the square always resulted in negligible errors on the  $s$ -wave contribution.

For instance, the final value of the  $^1s_0$  amplitude for Solution 1 at 14 MeV is  $0.0001 \pm 0.1210$ , which is just over two standard deviations away from the theoretical

---

<sup>5</sup>A negative amplitude can be interpreted as a phase change of  $180^\circ$ . There is an ambiguity in the  $n$ - $p$  scattering phases of  $180^\circ$  due to the fact that the scattering matrix contains diagonal terms of the form  $e^{2i\delta}$ , where  $\delta$  is the phase. Thus a change of  $180^\circ$  has no effect on the  $n$ - $p$  scattering cross section, but can play a role in an analysis such as this for TMEs other than  $^1s_0$ .

reduced amplitude value<sup>6</sup> of 0.27. When squaring the amplitude to obtain the percent of the cross section from this term, normal error propagation dictates that the error is  $\delta_{x^2} = |2x\delta_x|$ . Since the amplitude is so near to zero, gives an error on the percent contribution to the cross section of 0.0006 %. The *s*-wave contribution disagrees now by about four orders of magnitude with the theory, when the amplitude itself had been only about two standard deviations away. In order to obtain a more realistic error estimate for the *s*-wave contribution, the error was taken to be the difference between the percent contribution evaluated by squaring the amplitude and the contribution evaluated by squaring the amplitude plus its error.

The percent of the cross section from each multipole, *M1*, *E1*, and *E2*, is shown in Figure 6.13 where it is compared to theory. The percentages were also scaled by the total cross section from the theory in order to compare the absolute values of each multipole contribution. Those results are presented in Figure 6.14.

As is seen from examining the two solutions for a given energy, there is no obvious reason to discount either of the two solutions. Moreover, the total multipole strengths from the two solutions are almost identical apart from the difference in the size of the error bars, despite the fact that such different splittings are obtained in the *p*- and *d*-waves. A detailed discussion of these results is reserved for the next chapter. We simply note here that the *p*-wave splittings are in very good agreement with the theory, which has important consequences for relating our measurements to the GDH sum rule, which is discussed below.

---

<sup>6</sup>Keep in mind that all values quoted for the amplitudes have been normalized such that  $A_0=1$ .

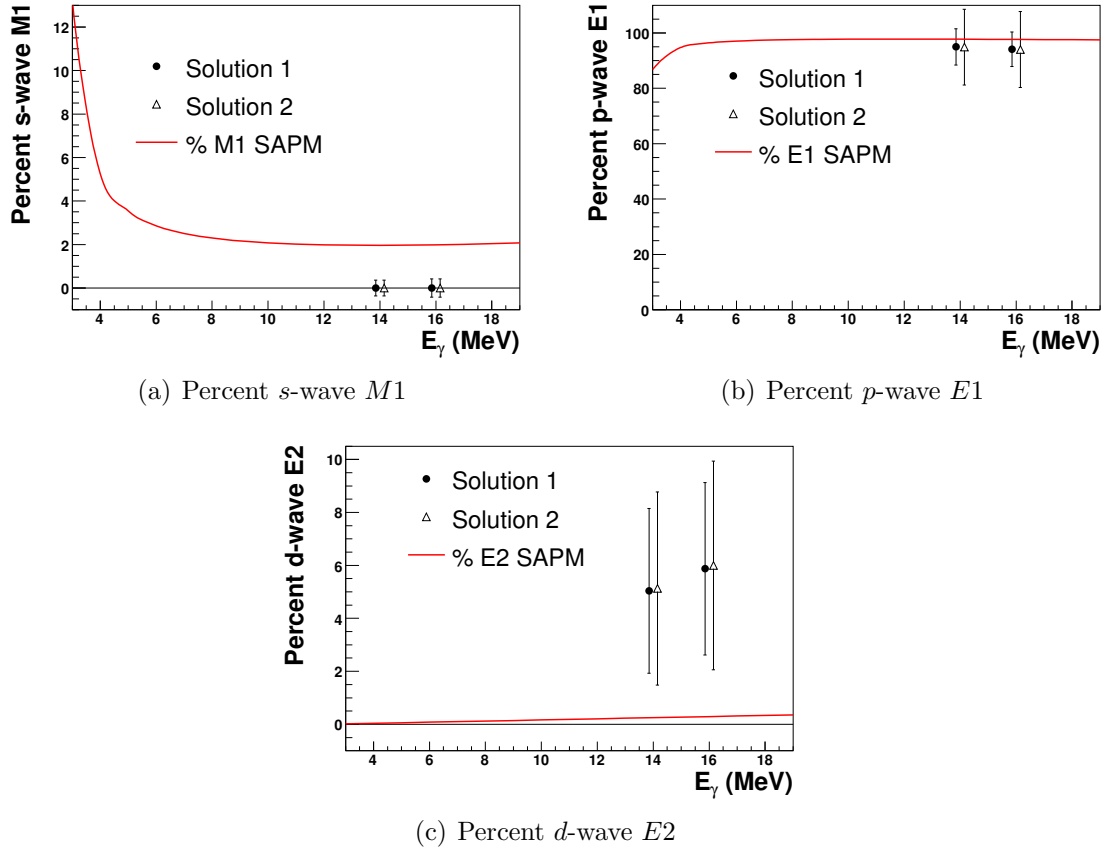
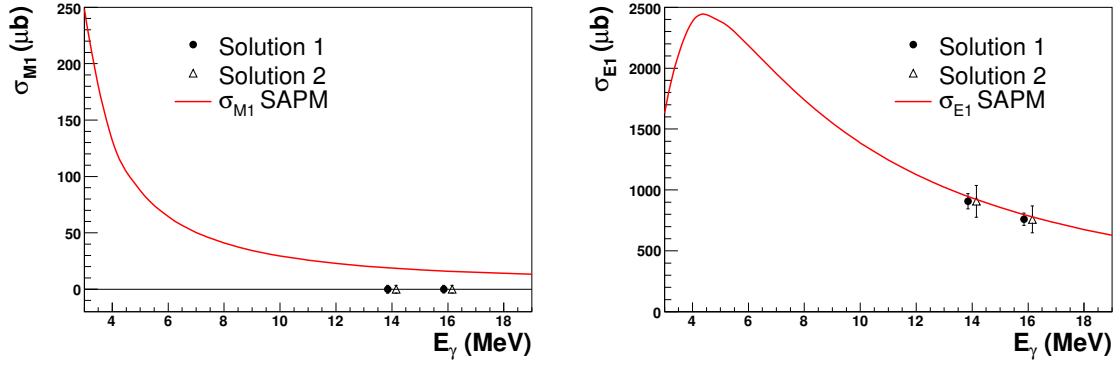


**Figure 6.13:** Percent multipole contributions to the total cross section with splittings. The percent of the cross section is shown for the  $M1$   $s$ -waves,  $E1$   $p$ -waves, and  $E2$   $d$ -waves. The red curve corresponds to the SAPM calculation. The errors shown are statistical only.

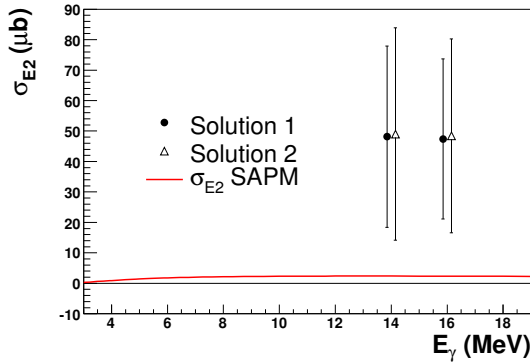
## 6.5 GDH Sum Rule Integrand

In addition to being able to write the cross section and analyzing powers in terms of the contributing transition matrix elements, another observable, the helicity-dependent cross section difference, can also be written in terms of the TME amplitudes. This observable is a measure of the cross section difference for a circularly polarized  $\gamma$ -ray beam incident upon a longitudinally polarized target for spins parallel and anti-parallel.  $\sigma_P - \sigma_A$ , as it is denoted, is of current interest in the field because



(a) Absolute  $s$ -wave  $M1$

(b) Absolute  $p$ -wave  $E1$



(c) Absolute  $d$ -wave  $E2$

**Figure 6.14:** Absolute multipole contributions to the total cross section with splittings. The absolute cross section contribution is shown for the  $M1$   $s$ -waves,  $E1$   $p$ -waves, and  $E2$   $d$ -waves. These values were obtained by multiplying the percentages from Figure 6.13 by the theoretical total cross section. The red curve corresponds to the SAPM calculation. The errors shown are statistical only.

it appears in the integrand of the Gerasimov-Drell-Hearn (GDH) sum rule (see Section 1.2.4). While the present experiment did not have circularly polarized beams or a polarized target, information about  $\sigma_P - \sigma_A$  can be obtained through the TME amplitudes.

### 6.5.1 TME Formalism for $\sigma_P$ - $\sigma_A$

[Wel94] contains the formalism necessary for writing  $\sigma_P$ - $\sigma_A$  in terms of the TME amplitudes. In the case of circularly polarized  $\gamma$ -rays and polarized target, the differential cross section takes the form (cf. Equation 6.6)

$$\sigma(\theta, \phi) = \sum_{kqKQ} A_{kqKQ}(\theta) t_{kq}(\phi) T_{KQ}, \quad (6.19)$$

where the  $T_{KQ}$  terms are the tensor moments describing the target polarization. The equation for the  $A_{kqKQ}$  terms becomes (cf. Equation 6.10)

$$A_{kqKQ}(\theta) = \frac{\lambda^2}{6} \sum_{tt'k'q'} B_{kqKQ}^{k'q'} R_t R_{t'}^* P_{k'}^{|q'|}(\cos \theta). \quad (6.20)$$

where the main difference from Equation 6.10 is that the  $B$  coefficients take on a slightly different form to account for the target polarization. The expression for the  $B_{kqKQ}^{k'q'}$  coefficients is found in [Wel94].

For circularly polarized beams, the tensor moments  $t_{00}$  from Equation 6.7 and  $t_{20}$  from Equation 6.8 are still present, but the  $t_{2\pm 2}$  moment is now zero since  $P_{\gamma t}$  is zero. In addition to these,  $t_{10}$  now enters the formalism and is defined as

$$t_{10} = \frac{P_{\gamma c}}{\sqrt{2}}, \quad (6.21)$$

where  $P_{\gamma c}$  is the fraction of the beam circularly polarized along the direction of propagation, or the fraction of right-handed  $\gamma$ -rays. Pure left-handed  $\gamma$ -rays have  $P_{\gamma c} = -1$ .

The target polarization is described by the  $T_{KQ}$  tensor moments. Here, we have

$$T_{00} = 1 \quad (6.22)$$

$$T_{1Q} = \frac{\langle S_Q \rangle}{\sqrt{S_d(S_d + 1)}}, \quad (6.23)$$

which for longitudinally polarized deuterons with fractional polarization  $P_d$  leaves one non-zero component:

$$T_{10} = \frac{P_d}{\sqrt{2}}. \quad (6.24)$$

By considering the non-zero tensor moments, we find that  $q = q' = Q = 0$ , which in turn leaves us with three non-vanishing  $A_{kqKQ}$  terms:  $A_{0000}$ ,  $A_{1010}$  and  $A_{2000}$ . Equation 6.19 then becomes

$$\sigma(\theta, \phi) = A_{0000} + A_{1010} \frac{P_{\gamma c} P_d}{2} + \frac{A_{2000}}{\sqrt{10}} \quad (6.25)$$

$P_d = 1$  for a 100% polarized target and in the difference,  $\sigma_P - \sigma_A$ ,  $P_{\gamma c}$  changes from 1 to -1. Therefore, in the difference, the terms in Equation 6.25 which do not depend on  $P_{\gamma c}$  drop out. After taking the difference between the two differential cross sections and integrating over the full solid angle, we are left with

$$\sigma_P - \sigma_A = \int A_{1010} d\Omega \quad (6.26)$$

$$= \int \frac{\lambda^2}{6} \sum_{tt'k'} B_{1010}^{k'0} R_t R_{t'}^* P_{k'}(\cos \theta) d\Omega. \quad (6.27)$$

Only the  $k' = 0$  Legendre polynomial survives the integration over solid angle, leaving the  $B_{1010}^{00}$  coefficients, which are non-zero only if  $t = t'$  (i.e. no interference

terms). The final result is then

$$\sigma_P - \sigma_A = \frac{2}{3} \pi \lambda^2 \sum_t B_{1010}^{00}(t) |R_t|^2, \quad (6.28)$$

where the dependence of the  $B$  coefficients on the quantum numbers of the TMEs has been made explicit.

For the TMEs included in our fits to the data (see Section 6.3.3), the expression can be written as shown in Equation 1.4. With the normalization condition  $A_0=1.0$ , Equation 1.4 can be written as a function of the total cross section,  $\sigma_T$ , as

$$\begin{aligned} \sigma_P - \sigma_A = \frac{3}{4} \sigma_T \left[ -|{}^1s_0(M1)|^2 \right. \\ \left. - |{}^3p_0(E1)|^2 - \frac{3}{2}|{}^3p_1(E1)|^2 + \frac{5}{2}|{}^3p_2(E1)|^2 \right. \\ \left. - \frac{3}{2}|{}^3d_1(E2)|^2 - \frac{5}{6}|{}^3d_2(E2)|^2 + \frac{7}{3}|{}^3d_3(E2)|^2 \right]. \end{aligned} \quad (6.29)$$

For the results in this work,  $\sigma_T$  is taken from theory.

## 6.5.2 GDH Results

As this equation shows, if the reduced  $p$ -wave amplitudes are set equal, as is the case in the fits done in Section 6.4.1, then the  $p$ -wave terms exactly cancel. According to the SAPM calculation, this is approximately true near photodisintegration threshold. The same is true of the  $d$ -wave terms, which means that for the case of no splitting,  $\sigma_P - \sigma_A$  can be approximated as

$$\sigma_P - \sigma_A = -\frac{3}{4} \sigma_T |{}^1s_0|^2 \approx -3 \sigma_{M1}, \quad (6.30)$$

where  $\sigma_{M1}$  is the  $M1$  part of the total cross section. In the case of this analysis, this only includes the  $s$ -wave part of the  $M1$  contribution. The  $\sigma_P - \sigma_A$  values obtained under these assumptions are shown in Figure 6.15.

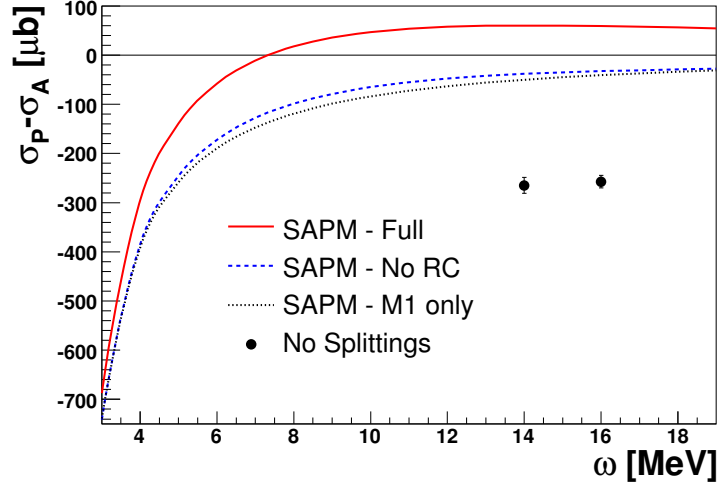


**Figure 6.15:** GDH sum rule integrand with results from this work for the solution with no splittings. The solid red curve is the full SAPM calculation, the dashed blue curve is the full calculation without relativistic currents (RC), and the dotted black curve is  $\sigma_P - \sigma_A$  with only  $s$ -wave  $M1$  contribution considered. The data points represent the value obtained by assuming no splittings, giving the GDH integrand the form  $\sigma_P - \sigma_A \approx -3 \sigma_{M1}$ . The error bars are statistical only.

The GDH values obtained using the no splitting assumption are in gross disagreement with the theory. This is not unexpected since the  $s$ -wave contributions were found to disagree so severely. The splittings are clearly necessary in the energy region of this experiment, so more reliable results are expected using the TME amplitudes with splittings.

As Equation 6.29 shows, the details of the GDH integrand are found primarily in the splittings of the  $p$ -waves. Since the two solutions at each energy had different  $p$ -wave splittings, the  $\sigma_P - \sigma_A$  values obtained using the amplitudes with splittings are also different. Those results are shown in Figure 6.16. It should be noted that the

exclusion of the  $f$ -wave  $E1$  term from our fits has a negligible effect on the GDH integrand values obtained. For instance, the theory predicts a contribution of 15 to 20  $\mu\text{b}$  from the  ${}^3f_2(E1)$  term to  $\sigma_P - \sigma_A$  in this energy region, which is much smaller than the uncertainties obtained on our data points for  $\sigma_P - \sigma_A$ .

The solutions designated Solution 1 are found to be in very good agreement with the theory, whereas the solutions designated Solution 2 disagree significantly. The errors in this result are much larger than those of the no splitting results. The reason for this is because allowing splittings introduces correlations in the parameters, such that the values of the TME amplitudes are less certain. The next chapter discusses the implications of these results.

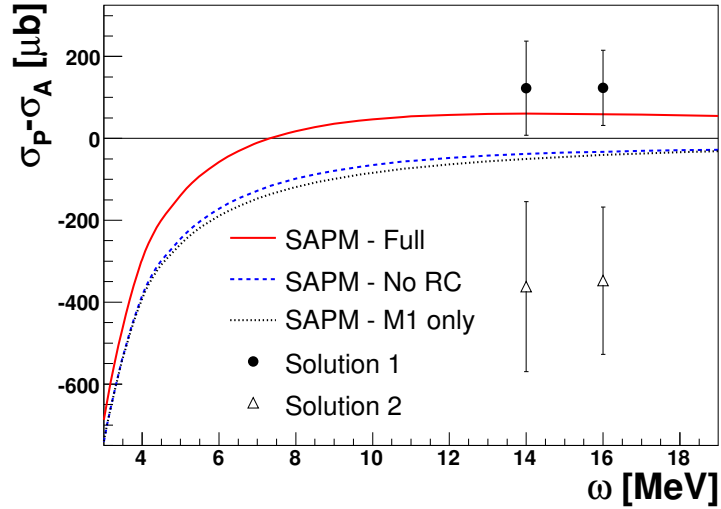


**Figure 6.16:** GDH sum rule integrand with results from this work. The solid red curve is the full SAPM calculation, the dashed blue curve is the full calculation without relativistic currents (RC), and the dotted black curve is  $\sigma_P - \sigma_A$  with only  $s$ -wave M1 interactions included. The circles are solution sets designated Solution 1 for each energy and the open triangles are the solutions which have been designated Solution 2. The error shown are statistical only.

# Chapter 7

## Summary and Conclusions

### 7.1 Introduction

This chapter will summarize the deuteron photodisintegration measurement which has been described in this work. Each aspect of this dissertation will be summarized in turn: the experimental setup in Section 7.2, the analysis of the data in Section 7.3, and the results in Section 7.4. Finally, some concluding remarks are made about the relevance of this work to the field of nuclear physics in Section 7.5 and future prospects for studying this reaction at HI $\gamma$ S are discussed in Section 7.6.

### 7.2 Summary of the Experiment

A precision measurement of the polarized differential cross section for deuteron photodisintegration with linearly polarized  $\gamma$ -rays was performed at beam energies of 14 and 16 MeV. The  $\gamma$ -rays were produced at the relatively new High Intensity  $\gamma$ -ray Source (HI $\gamma$ S), located at the Duke Free Electron Laser Laboratory. HI $\gamma$ S produces  $\gamma$ -rays via the intra-cavity backscattering of a free electron laser (FEL) by electrons circulating in the Duke Storage Ring.

For this measurement, the HI $\gamma$ S beams were incident upon a heavy water ( $D_2O$ ) target located at the center of the Blowfish neutron detector Array. The target was 4.7 cm in length with a diameter of 3.8 cm. An identical target filled with  $H_2O$  was

used to determine the background contribution from the Oxygen, which was found to be negligible for this experiment.

The Blowfish detector array consists of 88 BC-505 liquid scintillator neutron detectors with angular coverage from  $22.5^\circ$  to  $157.5^\circ$  in polar angle  $\theta$ , measured with respect to the beam axis. The detectors are supported by 8 arms, each containing 11 detectors and with a spacing between arms of  $45^\circ$  in azimuthal angle,  $\phi$ . The entire array can rotate about the beam axis allowing for the cancellation of systematic effects.

The Blowfish detectors have excellent pulse-shape discrimination (PSD) properties, allowing neutrons which enter the detector to be distinguished from  $\gamma$ -rays. It is also equipped with a gain monitoring system to monitor the gains of each detector on a run-by-run basis. Each detector receives a pulse of light of constant amplitude from an LED, allowing gains to be determined by measuring the relative position of the centroid of the LED spectrum in production runs. The absolute gain is then determined by relating the centroid positions obtained in production runs to those obtained during a run with a  $^{232}\text{Th}$  source placed at the center of the array, where the gains are directly measured.

The experiment was performed over the course of four days with beam-on-target fluxes on the order of  $5 \times 10^5$   $\gamma$ /s for beams collimated to 1 inch in diameter. The polarized differential cross section was used to construct the angular distribution of the unpolarized cross section and linear analyzing power. The analyzing power is defined in terms of the polarized differential cross section as

$$\Sigma(\theta) = \frac{1}{P_\gamma} \frac{\sigma(\theta, \phi = 0^\circ) - \sigma(\theta, \phi = 90^\circ)}{\sigma(\theta, \phi = 0^\circ) + \sigma(\theta, \phi = 90^\circ)}, \quad (7.1)$$

where  $P_\gamma$  is the linear polarization fraction of the beam. Experimentally this amounts

to measuring the difference in yields for detectors parallel and perpendicular to the beam axis over the sum. Both accessible observables were measured at 14 and 16 MeV.

## 7.3 Summary of the Analysis

### 7.3.1 Data Reduction

Before any analysis cuts were placed on the data set, the information from the gain monitoring system was used to determine the detector gains for each run to properly calibrate the ADC spectra. In addition, since the TDC spectra for each detector were offset in time from each other by arbitrary amounts, they were aligned to a common reference time. This was done by extracting and aligning the centroid of the  $\gamma$ -ray flash in the TDC spectra, which is a peak corresponding to the time it takes for  $\gamma$ -rays which were Compton scattered from the target to reach the detectors.

The first cut that was performed on the data was a multiplicity cut. The multiplicity of an event is defined as the number of detectors that produce a signal for that event. Because of the way in which pulse-shape discrimination (PSD) was performed, the PSD information was only reliable for events with multiplicity of 1 (see Section 4.7). Therefore, all other events were discarded.

The PSD cut was then applied to discard signals which did not have the signal features expected of neutrons entering the detectors. The PSD properties of these detectors produced very good separation between the neutrons and  $\gamma$ -rays, as displayed in Figure 7.1.

After the PSD cut was applied, a common pulse height cut was applied to each detector which served as a common software threshold. This was done to ensure that

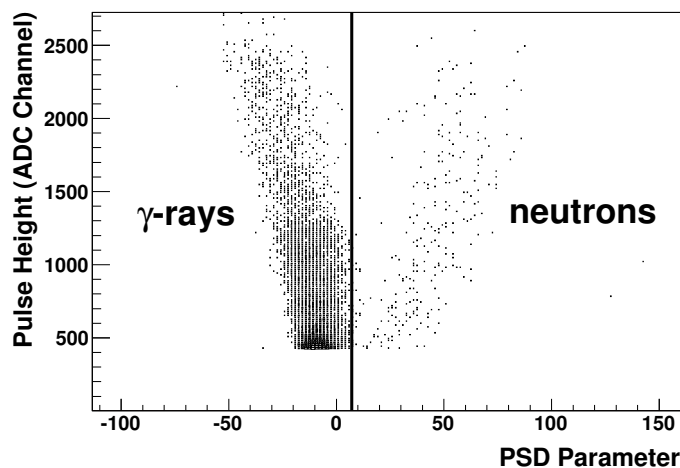


**Figure 7.1:** An example PSD spectrum with applied cut indicated by the vertical line. These data are taken from a single detector over the course of a single production run.

the detection efficiency, which depends on detector threshold, was the same for all detectors. The cut location was determined by taking a value greater than the largest hardware threshold of any detector in the array.

After each of these cuts, the TDC spectra show very clear neutron peaks. Figure 7.2 shows the TDC spectra for detectors parallel and perpendicular to the beam polarization axis both before and after the PSD cut. Since the reaction is dominated at these energies by electric dipole ( $E1$ ) transitions, a greater number of the neutrons should be emitted in the horizontal direction, parallel to the polarization axis, compared to the vertical direction.

The neutron yields were extracted by summing the counts in the spectra within the TDC window also indicated in Figure 7.2. The large size of the TDC window is to ensure that the window does not cut into the tail of the neutron peak, corresponding to lower energy (slower moving) neutrons. The presence of slower moving neutrons is due primarily to multiple scattering in the target.

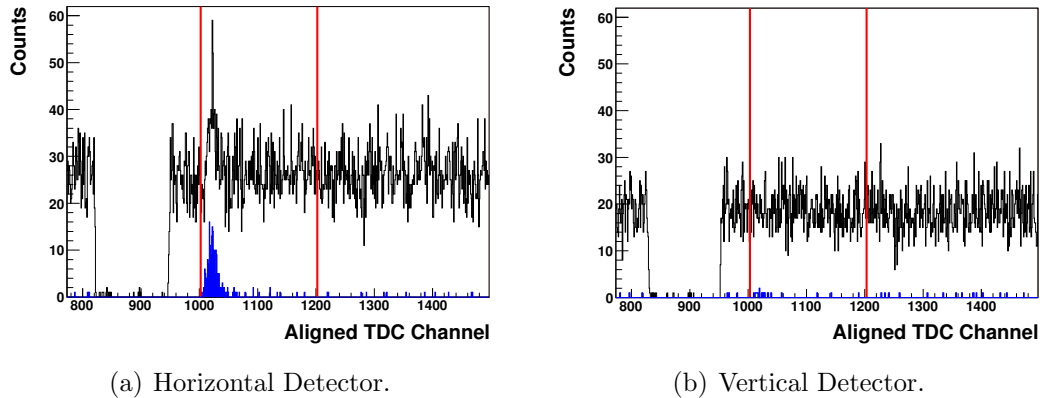


**Figure 7.2:** TDC spectra before and after PSD and PH cuts for detectors at  $\theta=90^\circ$  oriented (a) horizontally – in the plane of polarization of the  $\gamma$ -ray beam and (b) vertically – perpendicular to the plane of polarization. The black histograms are the TDC spectra before PSD and PH cuts are applied and the blue solid histograms (barely visible in (b)) are the spectra after these cuts are applied. The red lines mark the TDC window which was used to accept neutron events. This window was applied to the PSD and PH filtered spectra in blue. These spectra are from single detectors at  $\theta=90^\circ$  and from a single run.

Once the yields were extracted, the two observables were constructed. The angular distribution of the unpolarized cross section was determined by summing the yields in the detectors for all  $\phi$  angles for a common  $\theta$ , thus integrating out the beam polarization dependence. Absolute flux values were not obtained, so the unpolarized cross section remains unnormalized.

Because the Blowfish detector array rotated about the beam axis, the analyzing power can be constructed in terms of detector yields in a way that cancels many of the systematic effects. For example, for a set of four orientations of the Blowfish array with detectors  $A$ ,  $B$ ,  $C$ , and  $D$  located in the horizontal plane for Runs 1, 2, 3, and 4, respectively (see Figure 7.3 for examples for Runs 1 and 2), the analyzing

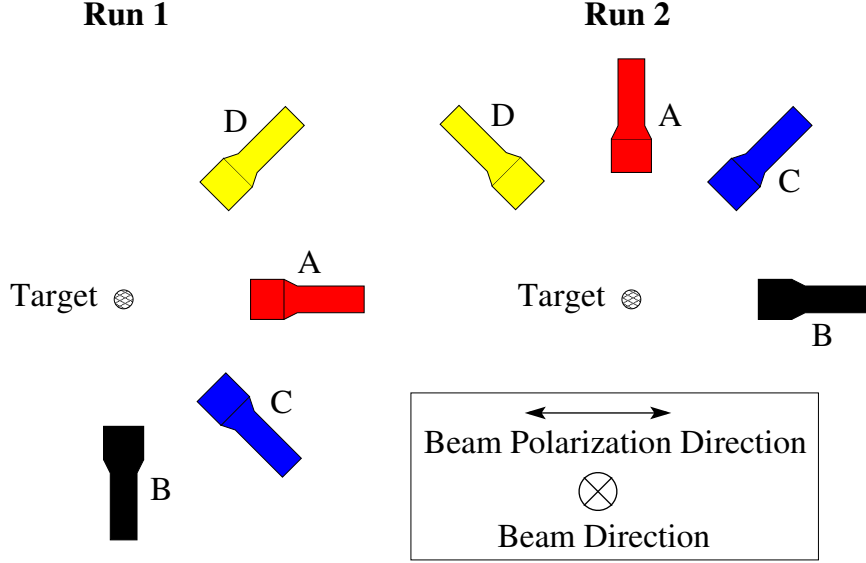


**Figure 7.3:** Schematic of the detector location relative to the polarization plane for a pair of array orientations used to construct the analyzing power. From Run 1 to Run 2, the black detector, labeled  $B$ , moves from a vertical position, labeled  $V$ , to a horizontal position, labeled  $H$ . The red detector, labeled  $A$ , moves from a horizontal position to a vertical position. Detectors  $C$  and  $D$  are placed in the horizontal plane for Runs 3 and 4, respectively.

power can be written in terms of the geometric mean as

$$\Sigma(\theta) = \frac{1 - R(\theta)}{1 + R(\theta)} \quad (7.2)$$

with

$$R = \sqrt[4]{\frac{A_1^H B_2^H C_3^H D_4^H}{A_2^V B_1^V C_4^V D_3^V}} \quad (7.3)$$

All the quantities in this expression are defined as in Equation 4.14.

Note that because the yields from a given detector appear in both the numerator and the denominator, any systematic effects such as detector efficiency will drop out when the analyzing power is constructed in terms of this ratio.

### 7.3.2 Simulations

The experimental observables extracted from the raw yields were corrected for multiple scattering and finite geometry effects using a **GEANT4** simulation of the experiment. The full geometry of the Blowfish array was constructed in the software, including the aluminum support structure. The **LHEP\_PRECO\_HP** physics list, which was developed to handle interactions involving neutrons with high precision, was used to describe the physical interactions.

The data were corrected by effectively changing the cross section which describes the distribution of the outgoing neutrons until the yields which were output from **GEANT4** matched the experimental yields (see Section 5.7 for details). This involved a fit to the experimental yields which was performed using the fitting routine **Minuit** [Jam98]. The angular distribution was parameterized by an associated Legendre polynomial expansion of the cross section in the CM frame, given by

$$\frac{d\sigma}{d\Omega}(\theta, \phi) = A_0 \left[ 1 + \sum_{k=1}^4 a_k P_k(\cos\theta) + \sum_{k=2}^4 e_k P_k^2(\cos\theta) \cos 2\phi \right] \quad (7.4)$$

where the  $a_k$  and  $e_k$  coefficients are the parameters which are varied in order to match the experimental yields, and  $A_0$  is the scale factor which sets the overall magnitude of the (angle integrated) total cross section, via  $\sigma_T = 4\pi A_0$ . In the case of this experiment, the overall scale was not determined, so  $A_0$  became an arbitrary scale factor in the fits to the yields<sup>1</sup>.

Once the  $a_k$  and  $e_k$  coefficients were obtained from the fits to the raw yields, the corrected analytic form of the cross section was obtained. The raw observables were then corrected with a correction factor defined as the ratio of the analytic form of

---

<sup>1</sup> $A_0$  is later set to 1.0 for the TME analysis.

the corrected observables to the simulated observables constructed from the GEANT4 output. The final results are shown in Figure 7.4 along with the observables constructed using the extracted Legendre coefficients and a comparison to a theoretical potential model calculation from Schwamb and Arenhövel [Sch01a, Sch01b, Are04], which will be referred to here as the SAPM calculation. Note that detectors at  $\theta = 63^\circ$  and  $76.5^\circ$  experienced problems during the 16 MeV runs that did not allow them to be used in the analysis (see Section 4.11.1).

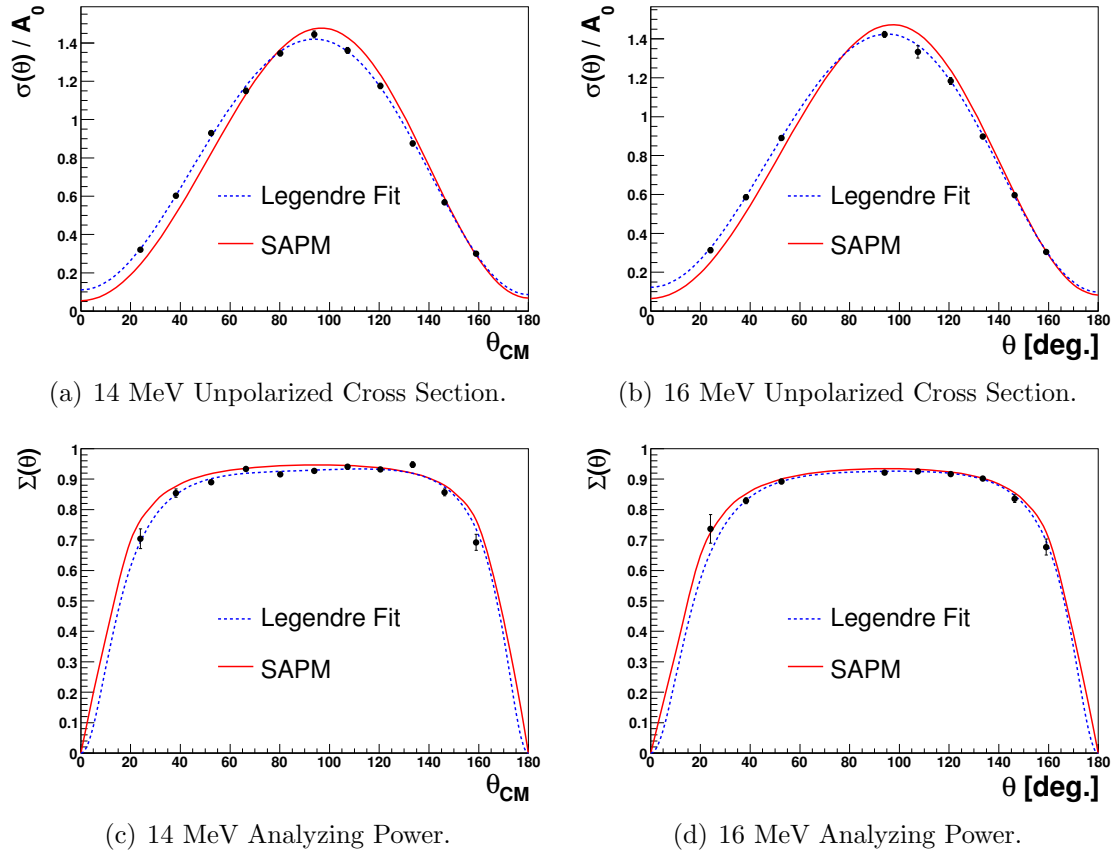


**Figure 7.4:** Final experimental observables. The error bars are statistical only. The blue dashed curve corresponds to a Legendre fit to the yields, and the solid red curve is a theoretical calculation from Schwamb and Arenhövel [Sch01a, Sch01b, Are04].

### 7.3.3 Extraction of TME Amplitudes

The polarized differential cross section can be written in terms of the amplitudes and phases of the transition matrix elements (TMEs) which contribute to the reaction. The TMEs take the form

$$\langle \psi_{np} | O_{pL} | \psi_d \rangle, \quad (7.5)$$

where  $\psi_{np}$  is the wave function of the outgoing  $n$ - $p$  system,  $\psi_d$  is the wave function of the ground state of the deuteron, and  $O_{pL}$  are the electric ( $p=1$ ) and magnetic ( $p=0$ ) multipole operators with multipolarity  $L$ .

In this analysis, we write the observables in terms of the reduced TMEs. The reduced TMEs represent the part of the TME involving only the radial part of the wave functions, with the angular part factored out. We will refer to the reduced TMEs in terms of the relevant quantum numbers only, using the notation  $^{2s+1}l_J$  ( $pL$ ) where  $^{2s+1}l_J$  labels the quantum numbers of the outgoing  $n$ - $p$  system. The channel spin is denoted by  $s$ , which for two spin 1/2 particles can take on values of 0 or 1,  $l$  is the orbital angular momentum in spectroscopic notation ( $s$ -waves are  $l=0$ ,  $p$ -waves are  $l=1$ ,  $d$ -waves are  $l=2$ , etc.), and  $J$  is the total spin,  $\vec{l} + \vec{s}$ .

The polarized differential cross section is written in terms of the TMEs by expressing the  $a$  and  $e$  coefficients of Equation 7.4 in terms of the reduced TME amplitude and phases using the formalism of [Wel92] (see Section 6.3 for an overview). After considering selection rules and with guidance from the SAPM calculation, the

following TMEs are included in the fits (see Section 6.3.3):

$$\begin{aligned}
& {}^1s_0(M1) \\
& {}^3p_0(E1) \quad {}^3p_1(E1) \quad {}^3p_2(E1) \\
& {}^3d_1(E2) \quad {}^3d_2(E2) \quad {}^3d_3(E2).
\end{aligned} \tag{7.6}$$

Note that we are limiting ourselves to  $M1$ ,  $E1$ , and  $E2$  multipoles and all partial waves higher than  $d$ -waves are being neglected.

The isospin of the outgoing states is known by observing that the Pauli principle for nucleon-nucleon systems requires that  $l + s + T$  be odd, where  $T$  is the isospin of the system [McC68]. Since the deuteron has an isospin of 0, the isospin nature of each transition is thus determined: the  ${}^1s_0(M1)$  state is reached through an isovector transition, as are the triplet  $p$ -wave ( $E1$ ) states, while the triplet  $d$ -wave ( $E2$ ) states are reached through isoscalar transitions.

The remaining TMEs are complex numbers, each consisting of an amplitude and a phase. However, through Watson's Theorem, the relative phases can be fixed using the  $n$ - $p$  scattering phase shifts [Knu99]. The application of Watson's theorem in our case relies on the fact that there are no open channels other than photodisintegration and that the mixing between angular momentum states is small. The small mixing phases from the SAID analysis [Cen07] confirm that this condition holds for the energies of this experiment<sup>2</sup>. The use of Watson's theorem allows the number of fitting parameters to be reduced by almost a factor of two.

Once the TMEs were selected, the experimental yields were fit using the `Minuit`

---

<sup>2</sup>The most significant coupling for the TMEs included in this analysis is between the  $E1$   ${}^3p_2$  and  ${}^3f_2$  terms. However, in addition to the mixing being small at these energies, the  ${}^3f_2$  term has not been included in this analysis.

fitting routine [Jam98], which varied the amplitudes to match the distribution of the yields at each energy. The results of those fits are summarized in the following sections.

## 7.4 Summary of the Results

### 7.4.1 TME Amplitudes

Since the set of amplitudes obtained from the fits depended upon the initial values given to `Minuit` for the seed amplitudes, the starting values of each amplitude were varied and many fits were done to each data set. This method yielded two distinct sets of amplitudes with  $\chi^2$  values which were indistinguishable. A fit corresponding to one of the solutions for each energy is shown in Figure 7.5. The fit from the other solution, if shown, would be indistinguishable from the fits in this figure.

The individual amplitudes were converted to percentages of the total cross section and compared to the SAPM predictions in Figure 7.6. The drastic change in error bars sometimes observed between the two solutions arises because the uncertainties produced by `Minuit` take into account correlations between the parameters [Jam98]. The degree of correlation between parameters is different for the two solutions, resulting in differing sizes for the error bars.

Using the TME amplitudes extracted from the fits, the percent of the total cross section from the  $M1$ ,  $E1$ , and  $E2$  multipoles can be compared to theory, as shown in Figure 7.7.

As is seen from examining the two solutions for a given energy, there is no obvious reason to discount either of the two solutions on physical grounds. Moreover, the total multipole strengths from the two solutions are almost identical apart from the

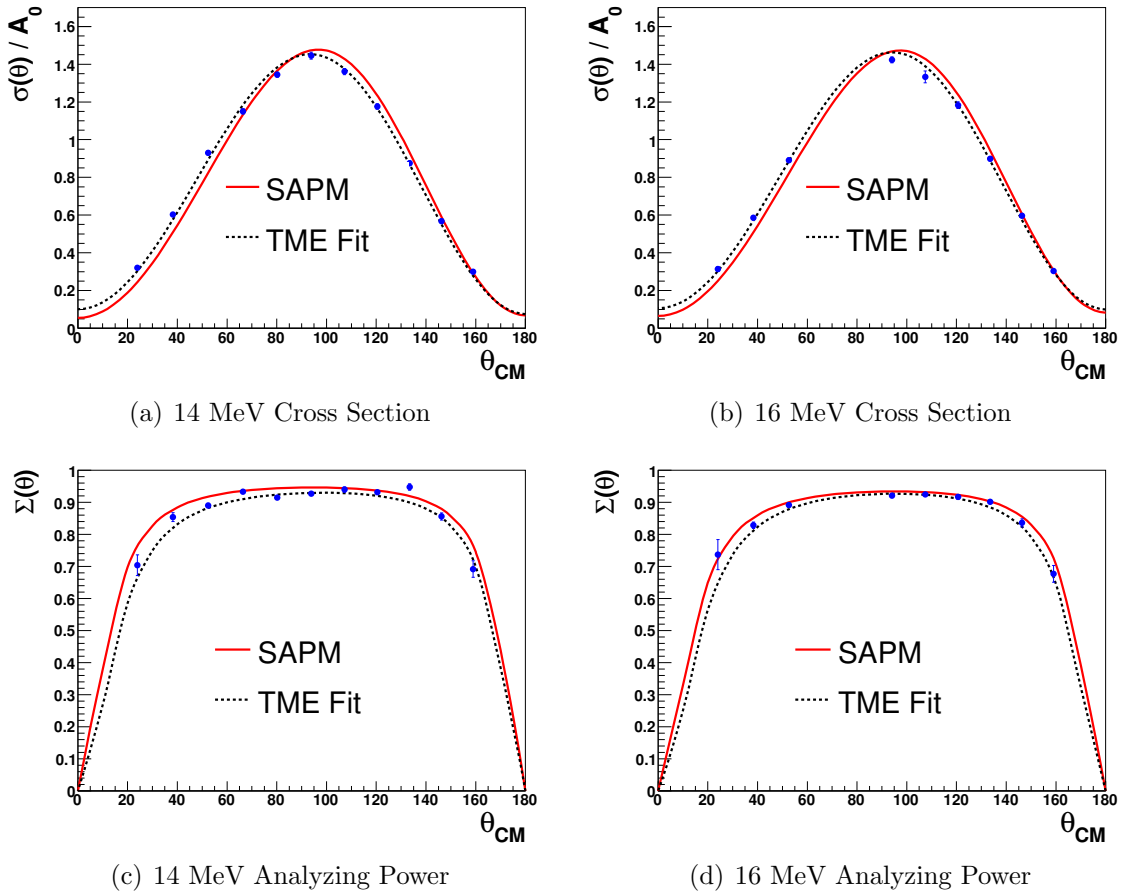


**Figure 7.5:** Fits from the extraction of TME amplitudes. The solid red curve is the SAPM calculation and the dotted black curve is the fit. The errors on the data points are statistical only.

difference in the size of the error bars, despite the fact that different splittings are obtained in the  $p$ - and  $d$ -waves.

In all fits, the  $^1s_0$  amplitude had a value consistent with zero, whereas the theory predicted a contribution of a few percent. Ultimately, since the  $s$ -wave term plays such a small role in the cross section at these energies ( $< 2\%$  of the total cross section according to theory), the  $s$ -wave term has little influence in the fits and on the other results.

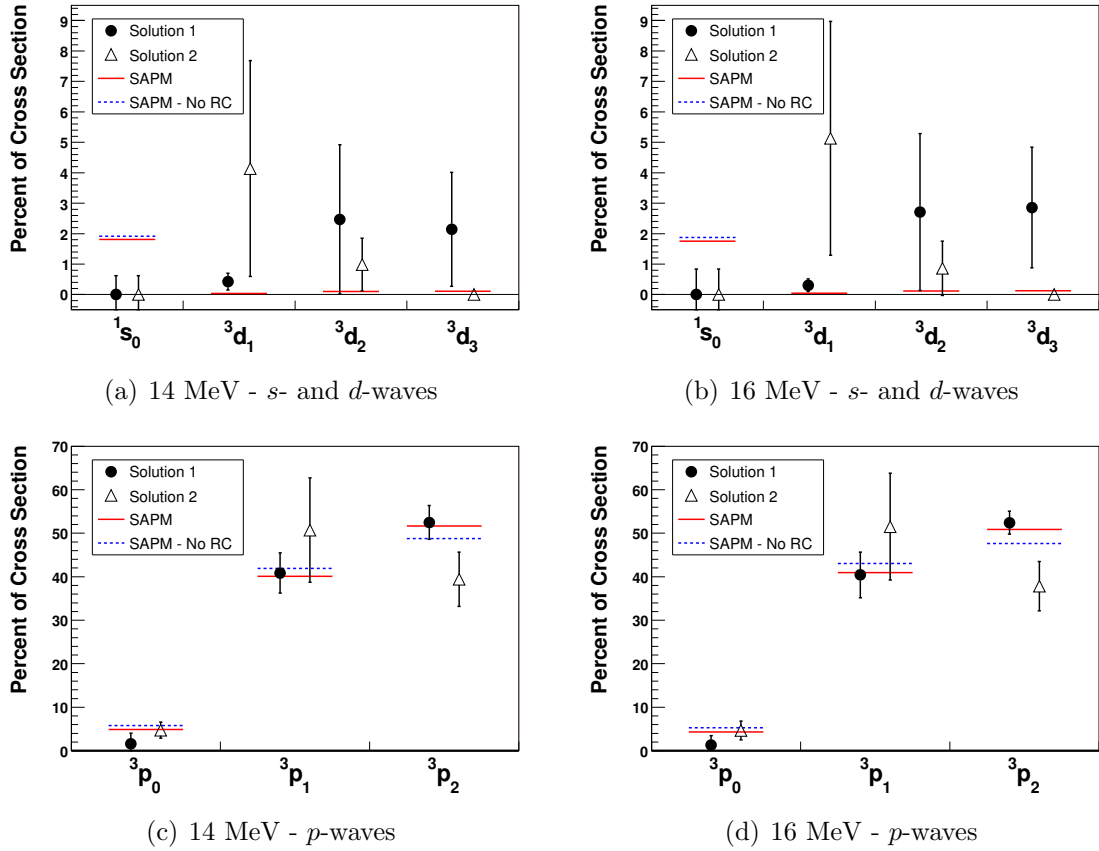


**Figure 7.6:** Percent of total cross section for each TME amplitude. The solid red lines correspond to the full SAPM calculation and the dashed blue lines correspond to the SAPM calculation without the inclusion of relativistic effects. These two versions of the SAPM calculation for the  $d$ -waves are indistinguishable at this scale. The errors on the data points are statistical only.

Typically, the lower analyzing powers in the data as compared to the theory are due to a component in the cross section which is isotropic in  $\phi$  that tends to wash out the analyzing power values. Since the  $^1s_0$  term results in such a distribution of neutron yields, it is a natural candidate for explaining such an effect. However, as the  $s$ -wave result shows, it cannot be responsible for the discrepancy in the analyzing power since it goes to zero in all the fits. The effect in this case is due primarily to the  $p$ -wave splittings.

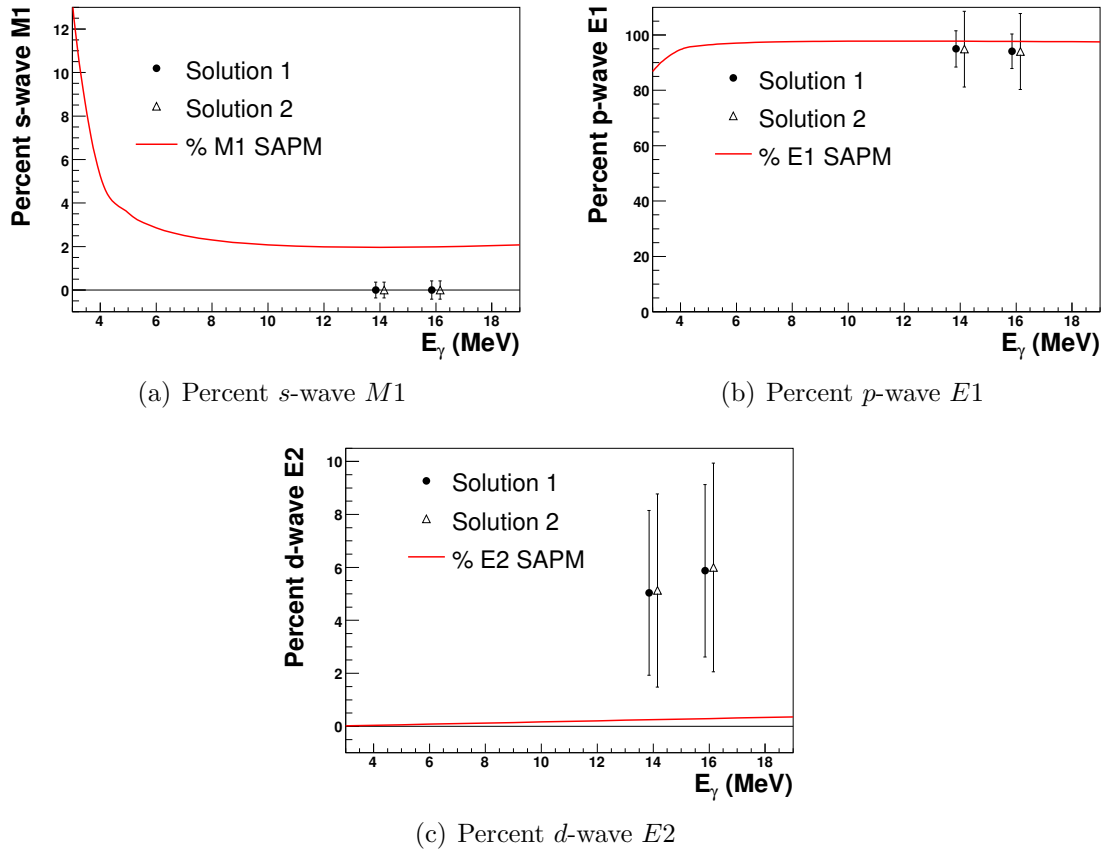


**Figure 7.7:** Percent multipole contributions to the total cross section from TME fits. The percent of the cross section is shown for the  $M1$   $s$ -waves,  $E1$   $p$ -waves, and  $E2$   $d$ -waves. The red curve corresponds to the predicted percentages from the SAPM calculation. The errors on the data points are statistical only.

Unlike the  $s$ -wave results, the  $p$ -waves are found to be in excellent agreement with the theory. Here, the solutions designated solution 1 for each energy are in very good agreement with the SAPM calculation, especially with respect to the relative strengths of the  $^3p_1$  and  $^3p_2$  amplitudes. Since these two amplitudes account for over 90% of the total cross section, this is a significant result in terms of the overall agreement with the theory. The second solution does not agree as well for for the  $^3p_2$  amplitude, although it does for the other two  $p$ -waves. In addition, the relative sizes

of the  ${}^3p_1$  and  ${}^3p_2$  amplitudes are opposite of what is observed for solution 1.

As seen in Figure 7.7(c), the  $d$ -wave results are larger than predicted by theory. Since the  $d$ -waves are still a small percentage of the total cross section, they affect the angular distribution of the unpolarized cross section primarily through interference with the dominant  $p$ -waves in the  $a_1$  and  $a_3$  coefficients (see Equations A.2 and A.4 in Appendix A). The  $P_1$  and  $P_3$  Legendre polynomials which these terms multiply are what account for any asymmetry about  $\theta = 90^\circ$  in the unpolarized cross section. The nearly symmetric distributions of the unpolarized cross sections leads to the expectation that the  $d$ -wave component will be smaller than predicted by the theory. However, a larger total  $d$ -wave contribution was found at both energies. This result is possible if the  $d$ -waves split in such a way that their contributions tend to cancel each other in the  $a_1$  and  $a_3$  expressions.

Therefore, the  $d$ -wave contributions are responsible for the difference in the forward asymmetry in the cross section and thus also for the differences observed between the data and the theory for the forward angle yields. While the  $d$ -wave amplitude values obtained here disagree with the theory, due to the large uncertainty in those amplitudes, the total contributions only disagree by approximately one and a half standard deviations.

### 7.4.2 GDH Integrand

The Gerasimov-Drell-Hearn (GDH) sum rule [Ger66, Dre66] has been introduced earlier (see Sections 1.2.4 and 2.6). It takes the form

$$I_{GDH} = \int_{\omega_{th}}^{\infty} \frac{\sigma_P - \sigma_A}{\omega} d\omega = \frac{4\pi^2\alpha}{m^2} \kappa^2 S. \quad (7.7)$$

where  $\sigma_P$  and  $\sigma_A$  are the photo-absorption cross sections for circularly polarized  $\gamma$ -rays incident upon a longitudinally polarized target with beam and target spins parallel and anti-parallel, respectively. The cross section difference is weighted by the beam energy,  $\omega$ , and the integration goes from photodisintegration threshold,  $\omega_{th}$ , to infinity. On the right hand side,  $\alpha$  is the fine structure constant,  $m$  is the mass of the target particle,  $\kappa$  is the anomalous magnetic moment, and  $S$  is the target spin.

Because of the deuteron's small anomalous magnetic moment of  $\kappa_d = -0.143$  [Moh00], the total sum rule value for the deuteron is  $I_{GDH}^d = 0.65 \mu\text{b}$ . This is significantly smaller than is obtained from the nucleons individually, which have values of  $I_{GDH}^p = 204.8 \mu\text{b}$  and  $I_{GDH}^n = 233.2 \mu\text{b}$  for the proton and neutron, respectively. Above pion threshold, the interactions of photons with the deuteron consist primarily of photo-pion production and can be thought of as occurring with a neutron or proton which is nearly free (i.e. the quasi-free approximation) [Are99]. Thus, above pion threshold, a sum rule contribution of approximately  $I_{GDH}^p + I_{GDH}^n = 438 \mu\text{b}$  is expected, making an equally large negative contribution below pion threshold necessary to achieve the small deuteron value.

Below pion threshold, only the photodisintegration channel is open. Almost all of the negative contribution is predicted to come in the region very near photodisintegration threshold, where the magnetic dipole transition to the  $^1s_0$  state is large and only accessible in the anti-parallel configuration of target and photon spins. The  $E1$   $p$ -wave terms, which begin to dominate just above threshold, almost completely cancel each other in  $\sigma_P - \sigma_A$  in the low energy region.

The degree of the cancellation of the  $p$ -wave terms depends on the detailed splittings between the three amplitudes. An important consequence of this is the location

of the zero crossing of  $\sigma_P - \sigma_A$ , which occurs as the  $M1$   $s$ -wave term dies off and as the  $p$ -waves cancel each other less, making  $\sigma_P - \sigma_A$  positive. The crossing point is predicted by the SAPM calculation to be just below 8 MeV, but this has not been verified experimentally.

As seen in the variations of the SAPM calculation in Figure 7.9, the relativistic contributions are expected to play a significant role at these energies in determining the zero crossing. In fact, the inclusion of the relativistic currents causes the sum rule value for integration from photodisintegration threshold up to about 100 MeV to be less negative by more than 30% [Are01]. Without these currents in the calculation, the magnitude of the negative contribution below pion threshold is much larger than the positive contribution above pion threshold, making the cancelation required to achieve the small sum rule value impossible. The major relativistic contribution is from the relativistic spin-orbit current. It has been noted that the large effect from relativistic contributions is not surprising in light of the fact that the proper form of the Compton scattering amplitude used in the derivation of the GDH sum rule is not obtained unless relativistic contributions are considered [Are97].

Even without the capabilities to produce circularly polarized photons or longitudinally polarized targets<sup>3</sup>,  $\sigma_P - \sigma_A$  can be extracted from the present data by writing it in terms of the reduced TME amplitudes of the reaction using the formalism of [Wel94]. In terms of the TME amplitudes included in the fits to the data,  $\sigma_P - \sigma_A$  can

---

<sup>3</sup>The HI $\gamma$ S facility presently has the capability to produce circularly polarized photons and a polarized target is under construction. However, at the time of this experiment, neither were available.

be written as

$$\begin{aligned} \sigma_P - \sigma_A = \frac{3}{4} \sigma_T & \left[ -|s_0(M1)|^2 \right. \\ & - |^3p_0(E1)|^2 - \frac{3}{2}|^3p_1(E1)|^2 + \frac{5}{2}|^3p_2(E1)|^2 \\ & \left. - \frac{3}{2}|^3d_1(E2)|^2 - \frac{5}{6}|^3d_2(E2)|^2 + \frac{7}{3}|^3d_3(E2)|^2 \right]. \end{aligned} \quad (7.8)$$

This particular form of the expression, written in terms of the total cross section,  $\sigma_T$ , is valid only when the normalization condition  $A_0=1.0$  is enforced<sup>4</sup>. For this analysis, the theoretical  $\sigma_T$  is used to determine the value of  $\sigma_P-\sigma_A$ .

As this equation shows, if the reduced  $p$ -wave amplitudes are set equal, then there is no contribution from the  $p$ -wave terms. According to the SAPM calculation, this is approximately true near photodisintegration threshold. The same is true of the  $d$ -wave terms, which means that for the case of no splitting,  $\sigma_P-\sigma_A$  can be approximated as

$$\sigma_P - \sigma_A = -\frac{3}{4}\sigma_T|s_0|^2 \approx -3 \sigma_{M1}, \quad (7.9)$$

where  $\sigma_{M1}$  is the  $M1$  part of the total cross section. A comparison of the curves for the full calculation and the  $M1$ -only calculation in Figure 7.9, shows that the deviations from this approximation are predicted to start to become significant above 4 MeV.

While there are currently no direct experimental data for the GDH integrand on the deuteron below pion threshold, several indirect measurements similar to the one described in this work have recently been performed to extract  $\sigma_P-\sigma_A$  below 10 MeV [Ahm07]. Those results used the simplification of Equation 7.9 to obtain the results shown in Figure 7.8.

Three of the results shown were obtained using the analyzing power at one angle

---

<sup>4</sup>The more general form in terms of the absolute normalization of the cross section is given in Equation A.9 in Section A.2 of Appendix A. More details concerning the normalization of the  $\sigma_P-\sigma_A$  expression can also be found there.

from [Tor03, Sch00, Del81] and the assumption that only  $s$ - and  $p$ -waves (without splitting) are present. The [Hol83] experiment was a photodisintegration measurement with unpolarized photons, with the outgoing neutron polarization being measured. Other values are taken from  $n$ - $p$  capture experiments [Sod87, Dro76] with polarized neutron beams, again using the assumption of  $s$ - and  $p$ -waves only. The angular distribution of the polarized cross section for data taken with the Blowfish array were used to extract the cross section difference below 10 MeV in a way similar to what is described below [Saw05]. All of the results neglected the splittings in the  $p$ -waves and, when included,  $d$ -waves. For details on how these data were converted to  $\sigma_P - \sigma_A$  values, see [Ahm07].

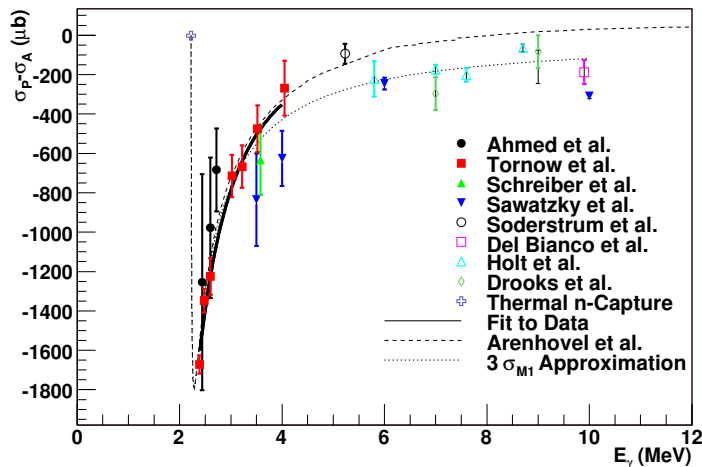


**Figure 7.8:** Existing GDH sum rule integrand values. The full calculation from Arenhövel [Are01] as well as the prediction for considering only the  $M1$  component are shown, as is a fit to the data below 4 MeV. See [Ahm07] for details.

A fit was performed to the data below 4 MeV and the resulting curve was integrated from threshold to 4 MeV to get the GDH contribution near threshold. A value of  $-414^{+88}_{-99} \mu\text{b}$  was obtained, compared to values of  $-424 \mu\text{b}$  and  $-431 \mu\text{b}$  obtained from doing the same integration for the full calculation and the  $M1$ -only contribution,

respectively, from Arenhövel [Are01].

It should be noted that none of the methods used to obtain these GDH values were able to observe positive values because of the assumption of no splitting in the  $p$ - and  $d$ -wave amplitudes. Under this assumption, only the  $s$ -wave  $M1$  term contributes to the integrand, which can only generate negative GDH values since transitions to the  $^1s_0$  state occurs only in the anti-parallel configuration of beam and target spins.

Therefore, in the energy range of this experiment, it is primarily the details of the  $p$ -wave splittings which determine  $\sigma_P - \sigma_A$ , since the  $s$ - and  $d$ -wave contributions to the cross section difference are small. Despite the fact that the  $p$ -wave splittings for the two solutions are not dramatically different (see Figure 7.6), the two solutions at each energy result in very different  $\sigma_P - \sigma_A$  results. The results are shown in Figure 7.9.

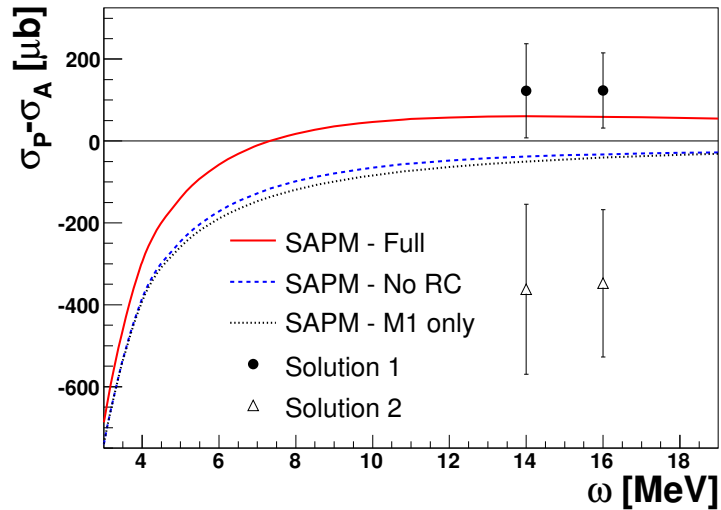


**Figure 7.9:** GDH sum rule integrand with results from this work. The red curve is the full SAPM calculation, the dashed blue curve is the full calculation without relativistic currents (RC), and the dotted black curve is  $\sigma_P - \sigma_A$  with only  $M1$  terms included. The circles are solution sets designated Solution 1 for each energy and the open triangles are the sets designated Solution 2. The error bars are statistical only.

The solutions designated Solution 2 for each energy, which from the point of view of the fits to the data cannot be excluded, are in disagreement with the theory. However, it is extremely unlikely that these are the physical solutions, since these large negative values would result in a negative contribution to the total sum rule that would be so large that it could not be canceled by the contribution above pion threshold to achieve the small total deuteron Sum Rule value.

On the other hand, the solutions designated Solution 1 for both energies agree well with the SAPM predictions. Considering these to be the preferred solutions based on the arguments stated above, they give the first experimental indication of a positive  $\sigma_P - \sigma_A$  value in the region below 20 MeV. This is related to the importance of relativistic effects in the calculations at these energies since, as already mentioned, the theory indicates that the positive strength is due to the addition of these effects.

## 7.5 Conclusions

The successful measurements of the angular distributions of the unpolarized cross section and analyzing powers for the photodisintegration reaction are the most precise to date in this energy region. In addition, there are very few deuteron photodisintegration experiments in this energy region which have been able to extract the distributions with such a large angular coverage. The precision of the data coupled with the nearly 100% linearly polarized beam have allowed the contributing reduced TME amplitudes to be extracted, something which has not been possible previously.

The virtue in these achievements is that they provide new ways of testing our understanding of this fundamental photonuclear reaction. This measurement can be used to compare to theoretical calculations based on potential models and effective

field theory. In addition, the details of the various electric and magnetic multipole transitions which contribute to the reaction help us to better understand this reaction whose inverse is so important to Big-Bang nucleosynthesis (BBN) at lower energies.

The extraction of the contributing TMEs of the reaction also allows the reaction to be viewed on the microscopic level. It gives insight into the details of the mechanisms which work together to produce the final observables. In particular, the splittings of the  $p$ -wave amplitudes have never been observed experimentally and are in good agreement with theoretical calculations from Schwamb and Arenhövel [Sch01a, Sch01b, Are04]. Such confirmation of the underlying details of the theory ensures that any agreement found between the theoretical and experimental observables is not simply fortuitous.

In the study of the fundamental strong interaction, spin observables have become very important in nuclear physics, especially since technologies now exist for producing polarized targets. Not only do the analyzing power measurements from this experiment test our understanding of the spin dependent parts of the strong interaction, but the Gerasimov-Drell-Hearn sum rule integrand constructed from these measurements also provides insight into this area. By virtue of being a difference in cross sections,  $\sigma_P - \sigma_A$  necessarily highlights the spin dependency of the interaction, since all non-spin dependent parts drop out of the difference.

Therefore, the results for  $\sigma_P - \sigma_A$  deduced from this experiment make an important contribution to this vibrant area of research. The sets of TME amplitudes at each energy which yielded positive GDH integrand values are the first experimental indication of positive GDH strength in the energy region near photodisintegration threshold. It can also be considered a verification of the importance of relativistic effects in the interaction at these energies, since the theory predicts the positive

strength to be due to these effects.

Moreover, in writing the GDH integrand in terms of the reduced TMEs, the dependence of  $\sigma_P - \sigma_A$  on the detailed splittings of the  $p$ -wave amplitudes is manifest. This provides a microscopic view of the GDH integrand at these energies which is not accessible from a direct GDH measurement.

## 7.6 Future Prospects for $d(\vec{\gamma}, n)p$ at HI $\gamma$ S

The study of deuteron photodisintegration at HI $\gamma$ S is far from complete. There are plans to make several more measurements over a large energy range in the coming years. These plans are briefly described below.

In the work of [Saw05], an unexpectedly large asymmetry between forward and backward angles was discovered at 3.5 and 4 MeV (see Figure 6.4). That experiment used the Blowfish array and was in many other ways very similar to the experiment described here. More studies are planned to verify those results and gain a better understanding of the reaction in that energy region, which is of interest in the BBN calculations mentioned above.

In addition, plans are underway to perform a direct measurement of the GDH integrand at energies below pion threshold at HI $\gamma$ S. A polarized deuterated butanol target is under construction and the HI $\gamma$ S facility is already capable of producing circularly polarized  $\gamma$ -rays. The experiment will employ the Blowfish array and is planned for mid-2008. The ultimate goal is to measure the GDH integrand for the deuteron up to pion threshold, thereby connecting to world GDH data for the deuteron which already exist above pion threshold.

# Appendix A

## TME Formalism Equations

Section A.1 of this appendix provides the equations necessary to write the differential cross section in terms of the reduced transition matrix element (TME) amplitudes and phases. Section A.2 provides the equation for the helicity dependent cross section difference,  $\sigma_P - \sigma_A$ , in terms of the reduced TME amplitudes. The formalisms used can be found in [Wel92] and [Wel94].

### A.1 Legendre Coefficients as Functions of TMEs

The differential  $d(\gamma, n)p$  cross section for the case of linearly polarized  $\gamma$ -rays can be written in terms of an associated Legendre polynomial expansion as shown in Equation 5.12. Using the formalism described in Section 6.3, the  $a$  and  $e$  coefficients from Equation 5.12 can be written as functions of the amplitudes and phases of the TMEs. The equations presented below include all TMEs which have been included in the analysis of the present experiment (see Section 6.3.3). Terms of the form  $|^{2s+1}l_J(pL)|$  denote the amplitude of the TME and the variables  $\delta_{2s+1}l_J$  indicate the phase of the TME. It is important to note that for the analysis described in this dissertation, the TME amplitudes were normalized such that  $A_0=1.0$ . Also note that the equations below can be used along with Equation 5.12 only if the beam is 100% linearly polarized. If it is not, each of the  $e$  coefficients must be scaled by  $P_\gamma$ , which is the linear polarization fraction of the beam.

$$\begin{aligned}
A_0 &= 0.25 |^1s_0(M1)|^2 + 0.25 |^3p_0(E1)|^2 + 0.75 |^3p_1(E1)|^2 & (A.1) \\
&+ 1.25 |^3p_2(E1)|^2 + 0.75 |^3d_1(E2)|^2 + 1.25 |^3d_2(E2)|^2 \\
&+ 1.75 |^3d_3(E2)|^2
\end{aligned}$$

$$\begin{aligned}
a_1 &= 0.866 |^3p_0(E1)| |^3d_1(E2)| \cos(\delta_{3p_0} - \delta_{3d_1}) & (A.2) \\
&+ 0.649 |^3p_1(E1)| |^3d_1(E2)| \cos(\delta_{3p_1} - \delta_{3d_1}) \\
&+ 1.949 |^3p_1(E1)| |^3d_2(E2)| \cos(\delta_{3p_1} - \delta_{3d_2}) \\
&+ 0.043 |^3p_2(E1)| |^3d_1(E2)| \cos(\delta_{3p_2} - \delta_{3d_1}) \\
&+ 0.649 |^3d_2(E2)| |^3p_2(E1)| \cos(\delta_{3d_2} - \delta_{3p_2}) \\
&+ 3.637 |^3p_2(E1)| |^3d_3(E2)| \cos(\delta_{3p_2} - \delta_{3d_3})
\end{aligned}$$

$$\begin{aligned}
a_2 &= -0.187 |^3p_1(E1)|^2 & (A.3) \\
&- 0.438 |^3p_2(E1)|^2 + 0.187 |^3d_1(E2)|^2 \\
&+ 0.223 |^3d_2(E2)|^2 + 0.857 |^3d_3(E2)|^2 \\
&- 0.500 |^3p_0(E1)| |^3p_2(E1)| \cos(\delta_{3p_0} - \delta_{3p_2}) \\
&- 1.125 |^3p_1(E1)| |^3p_2(E1)| \cos(\delta_{3p_1} - \delta_{3p_2}) \\
&+ 0.625 |^3d_1(E2)| |^3d_2(E2)| \cos(\delta_{3d_1} - \delta_{3d_2}) \\
&+ 0.071 |^3d_1(E2)| |^3d_3(E2)| \cos(\delta_{3d_1} - \delta_{3d_3}) \\
&+ 0.714 |^3d_2(E2)| |^3d_3(E2)| \cos(\delta_{3d_2} - \delta_{3d_3})
\end{aligned}$$

$$\begin{aligned}
a_3 &= -0.866 |^3p_0(E1)| |^3d_3(E2)| \cos(\delta_{3p_0} - \delta_{3d_3}) \\
&+ -1.732 |^3p_1(E1)| |^3d_3(E2)| \cos(\delta_{3p_1} - \delta_{3d_3}) \\
&+ -1.732 |^3p_2(E1)| |^3d_2(E2)| \cos(\delta_{3p_2} - \delta_{3d_2}) \\
&+ -1.559 |^3p_2(E1)| |^3d_1(E2)| \cos(\delta_{3p_2} - \delta_{3d_1}) \\
&+ -1.039 |^3p_2(E1)| |^3d_3(E2)| \cos(\delta_{3p_2} - \delta_{3d_3}) \\
&+ -0.866 |^3d_2(E2)| |^3p_1(E1)| \cos(\delta_{3d_2} - \delta_{3p_1})
\end{aligned} \tag{A.4}$$

$$\begin{aligned}
a_4 &= -0.952 |^3d_2(E2)|^2 - 0.524 |^3d_3(E2)|^2 \\
&+ -2.571 |^3d_3(E2)| |^3d_1(E2)| \cos(\delta_{3d_3} - \delta_{3d_1}) \\
&+ -2.381 |^3d_2(E2)| |^3d_3(E2)| \cos(\delta_{3d_2} - \delta_{3d_3})
\end{aligned} \tag{A.5}$$

$$\begin{aligned}
e_2 &= 0.094 |^3p_1(E1)|^2 \\
&+ 0.219 |^3p_2(E1)|^2 + 0.094 |^3d_1(E2)|^2 \\
&+ 0.112 |^3d_2(E2)|^2 + 0.429 |^3d_3(E2)|^2 \\
&+ 0.250 |^3p_2(E1)| |^3p_0(E1)| \cos(\delta_{3p_2} - \delta_{3p_0}) \\
&+ 0.563 |^3p_1(E1)| |^3p_2(E1)| \cos(\delta_{3p_1} - \delta_{3p_2}) \\
&+ 0.312 |^3d_1(E2)| |^3d_2(E2)| \cos(\delta_{3d_1} - \delta_{3d_2}) \\
&+ 0.036 |^3d_1(E2)| |^3d_3(E2)| \cos(\delta_{3d_1} - \delta_{3d_3}) \\
&+ 0.357 |^3d_2(E2)| |^3d_3(E2)| \cos(\delta_{3d_2} - \delta_{3d_3})
\end{aligned} \tag{A.6}$$

$$\begin{aligned}
e_3 = & 0.144 |{}^3p_0(E1)| |{}^3d_3(E2)| \cos(\delta_{3p_0} - \delta_{3d_3}) & (A.7) \\
& + 0.144 |{}^3p_1(E1)| |{}^3d_2(E2)| \cos(\delta_{3p_1} - \delta_{3d_2}) \\
& + 0.289 |{}^3p_1(E1)| |{}^3d_3(E2)| \cos(\delta_{3p_1} - \delta_{3d_3}) \\
& + 0.260 |{}^3p_2(E1)| |{}^3d_1(E2)| \cos(\delta_{3p_2} - \delta_{3d_1}) \\
& + 0.289 |{}^3p_2(E1)| |{}^3d_2(E2)| \cos(\delta_{3p_2} - \delta_{3d_2}) \\
& + 0.173 |{}^3p_2(E1)| |{}^3d_3(E2)| \cos(\delta_{3p_2} - \delta_{3d_3})
\end{aligned}$$

$$\begin{aligned}
e_4 = & 0.079 |{}^3d_2(E2)|^2 + 0.044 |{}^3d_3(E2)|^2 & (A.8) \\
& + 0.214 |{}^3d_3(E2)| |{}^3d_1(E2)| \cos(\delta_{3d_3} - \delta_{3d_1}) \\
& + 0.198 |{}^3d_2(E2)| |{}^3d_3(E2)| \cos(\delta_{3d_2} - \delta_{3d_3})
\end{aligned}$$

## A.2 $\sigma_P - \sigma_A$ in terms of TME Amplitudes

The TME amplitudes can also be used to construct  $\sigma_P - \sigma_A$ , which appears in the integrand of the GDH sum rule. Every possible  $M1$ ,  $E1$ , and  $E2$  amplitude is included in the expression that follows. This formalism is worked out in [Wel94].

$$\begin{aligned}
 \sigma_P - \sigma_A = \frac{\pi\lambda^2}{2} [ & - 1.000|{}^1s_0(M1)|^2 + 2.500|{}^1d_2(M1)|^2 & (A.9) \\
 & - 1.500|{}^3s_1(M1)|^2 - 1.500|{}^3d_1(M1)|^2 \\
 & + 2.500|{}^3d_2(M1)|^2 - 1.500|{}^1p_1(E1)|^2 \\
 & - 1.000|{}^3p_0(E1)|^2 - 1.500|{}^3p_1(E1)|^2 \\
 & + 2.500|{}^3p_2(E1)|^2 + 2.500|{}^3f_2(E1)|^2 \\
 & - 1.500|{}^1p_1(M2)|^2 + 2.333|{}^1f_3(M2)|^2 \\
 & - 1.500|{}^3p_1(M2)|^2 - 0.833|{}^3p_2(M2)|^2 \\
 & - 0.833|{}^3f_2(M2)|^2 + 2.333|{}^3f_3(M2)|^2 \\
 & - 0.833|{}^1d_2(E2)|^2 - 1.500|{}^3s_1(E2)|^2 \\
 & - 1.500|{}^3d_1(E2)|^2 - 0.833|{}^3d_2(E2)|^2 \\
 & + 2.333|{}^3d_3(E2)|^2 + 2.333|{}^3g_3(E2)|^2 ]
 \end{aligned}$$

The total cross section can be written as [Wel92]

$$\sigma_T = \frac{2\pi\lambda^2}{3} A_0, \tag{A.10}$$

where  $A_0$  is given by Equation A.1. For our analysis, we enforce the normalization condition  $A_0=1.0$ . Therefore, we can write  $\sigma_P - \sigma_A$  in terms of the total cross section

by setting  $A_0$  in Equation A.10 to 1.0, solving for  $\lambda^2$  and substituting it into Equation A.9. This amounts to the following substitution in Equation A.9:

$$\frac{\pi\lambda^2}{2} \rightarrow \frac{3}{4}\sigma_{TOT}. \quad (\text{A.11})$$

# Appendix B

## Results in Tabular Form

This appendix provides tables of data for all the major results of this thesis. See the caption for each table for any explanations. The following is a list of the tables in this appendix.

- Raw observables: Tables B.1 and B.2
- Corrected observables: Tables B.3 and B.4
- Legendre polynomial coefficients: Tables B.5 and B.6
- Results from fits with no splittings
  - TME Amplitudes: Table B.7
  - Multipole contributions in percent: Tables B.8 and B.9
  - Absolute multipole contributions: Tables B.10 and B.11
- Results from fits with splittings
  - TME Amplitudes: Tables B.12 and B.13
  - Multipole contributions in percent: Tables B.14 and B.15
  - Absolute multipole contributions: Tables B.16 and B.17
- $\sigma_P$ - $\sigma_A$  results: Tables B.18 and B.19

**14 MeV Raw Observables**

$\theta_{lab}$	$\sigma/A_0$	$\Sigma$
22.5°	0.416 ± 0.013	0.479 ± 0.022
36.0°	0.672 ± 0.013	0.682 ± 0.011
49.5°	0.988 ± 0.012	0.765 ± 0.006
63.0°	1.219 ± 0.015	0.834 ± 0.004
76.5°	1.389 ± 0.013	0.831 ± 0.004
90.0°	1.484 ± 0.019	0.847 ± 0.005
103.5°	1.410 ± 0.016	0.850 ± 0.007
117.0°	1.226 ± 0.015	0.831 ± 0.004
130.5°	0.931 ± 0.013	0.792 ± 0.008
144.0°	0.627 ± 0.013	0.685 ± 0.009
157.5°	0.395 ± 0.012	0.475 ± 0.018

**Table B.1:** Raw cross section and analyzing power values for 14 MeV. All values are given in the lab frame. Errors are statistical only.**16 MeV Raw Observables**

$\theta_{lab}$	$\sigma/A_0$	$\Sigma$
22.5°	0.381 ± 0.016	0.486 ± 0.031
36.0°	0.620 ± 0.013	0.678 ± 0.008
49.5°	0.921 ± 0.012	0.770 ± 0.006
90.0°	1.449 ± 0.016	0.846 ± 0.003
103.5°	1.355 ± 0.032	0.843 ± 0.005
117.0°	1.212 ± 0.018	0.820 ± 0.005
130.5°	0.936 ± 0.011	0.770 ± 0.005
144.0°	0.635 ± 0.010	0.661 ± 0.010
157.5°	0.382 ± 0.008	0.439 ± 0.017

**Table B.2:** Raw cross section and analyzing power values for 16 MeV. All values are given in the lab frame. Errors are statistical only.

**14 MeV Corrected Observables**

$\theta_{CM}$	$\sigma/A_0$	stat.	syst.	$\Sigma$	stat.	syst.
24.0°	0.321	± 0.010	± 0.014	0.704	± 0.032	± 0.019
38.2°	0.602	± 0.012	± 0.010	0.854	± 0.014	± 0.010
52.4°	0.930	± 0.011	± 0.018	0.890	± 0.007	± 0.009
66.4°	1.150	± 0.014	± 0.018	0.933	± 0.004	± 0.007
80.2°	1.345	± 0.013	± 0.019	0.915	± 0.004	± 0.005
93.8°	1.444	± 0.018	± 0.018	0.927	± 0.005	± 0.005
107.2°	1.361	± 0.015	± 0.013	0.940	± 0.008	± 0.006
120.4°	1.176	± 0.014	± 0.014	0.933	± 0.004	± 0.007
133.4°	0.875	± 0.012	± 0.017	0.948	± 0.010	± 0.007
146.2°	0.568	± 0.012	± 0.014	0.856	± 0.011	± 0.014
159.0°	0.301	± 0.009	± 0.017	0.692	± 0.026	± 0.033

**Table B.3:** Corrected cross section and analyzing power values for 14 MeV. All values are given in the CM frame.**16 MeV Corrected Observables**

$\theta_{CM}$	$\sigma/A_0$	stat.	syst.	$\Sigma$	stat.	syst.
24.1°	0.314	± 0.013	± 0.025	0.737	± 0.047	± 0.040
38.4°	0.586	± 0.012	± 0.011	0.829	± 0.010	± 0.012
52.6°	0.891	± 0.012	± 0.026	0.892	± 0.007	± 0.008
94.0°	1.423	± 0.016	± 0.031	0.921	± 0.003	± 0.013
107.4°	1.333	± 0.031	± 0.023	0.925	± 0.005	± 0.009
120.6°	1.183	± 0.018	± 0.026	0.917	± 0.006	± 0.008
133.6°	0.898	± 0.011	± 0.029	0.902	± 0.006	± 0.015
146.4°	0.596	± 0.009	± 0.023	0.836	± 0.013	± 0.021
159.0°	0.304	± 0.006	± 0.020	0.677	± 0.026	± 0.052

**Table B.4:** Corrected cross section and analyzing power values for 16 MeV. All values are given in the CM frame.

### 14 MeV Legendre Polynomial Coefficients

	stat.		syst.		SAPM
$A_0$	1.000	$\pm$ -	$\pm$ -	-	1.000
$a_1$	-0.056	$\pm$ 0.006	$\pm$ 0.005		-0.134
$a_2$	-0.860	$\pm$ 0.009	$\pm$ 0.008		-0.926
$a_3$	0.068	$\pm$ 0.011	$\pm$ 0.008		0.128
$a_4$	-0.041	$\pm$ 0.014	$\pm$ 0.018		-0.012
$e_2$	0.450	$\pm$ 0.002	$\pm$ 0.002		0.463
$e_3$	-0.011	$\pm$ 0.001	$\pm$ 0.001		-0.021
$e_4$	0.005	$\pm$ 0.001	$\pm$ 0.001		0.001

**Table B.5:** Legendre polynomial coefficients for 14 MeV. SAPM stands for the Schwamb Arenhövel Potential Model calculation [Sch01a, Sch01b, Are04]. Note that the  $A_0$  coefficient is 1.0 by definition.

### 16 MeV Legendre Polynomial Coefficients

	stat.		syst.		SAPM
$A_0$	1.000	$\pm$ -	$\pm$ -	-	1.000
$a_1$	-0.077	$\pm$ 0.006	$\pm$ 0.012		-0.146
$a_2$	-0.855	$\pm$ 0.009	$\pm$ 0.026		-0.912
$a_3$	0.089	$\pm$ 0.013	$\pm$ 0.044		0.137
$a_4$	-0.034	$\pm$ 0.014	$\pm$ 0.030		-0.014
$e_2$	0.446	$\pm$ 0.002	$\pm$ 0.004		0.455
$e_3$	-0.014	$\pm$ 0.001	$\pm$ 0.003		-0.023
$e_4$	0.004	$\pm$ 0.001	$\pm$ 0.002		0.001

**Table B.6:** Legendre polynomial coefficients for 16 MeV. SAPM stands for the Schwamb Arenhövel Potential Model calculation [Sch01a, Sch01b, Are04]. Note that the  $A_0$  coefficient is 1.0 by definition.

TME Amplitudes - No Splitting									
TME	14 MeV					16 MeV			
	stat.		syst.			stat.		syst.	
$ s $ ( $M1$ )	0.608	$\pm$ 0.018	$\pm$ 0.015			0.652	$\pm$ 0.016	$\pm$ 0.021	
$ p $ ( $E1$ )	0.635	$\pm$ 0.001	$\pm$ 0.001			0.633	$\pm$ 0.001	$\pm$ 0.001	
$ d $ ( $E2$ )	0.012	$\pm$ 0.001	$\pm$ 0.001			0.016	$\pm$ 0.001	$\pm$ 0.002	

**Table B.7:** TME Amplitudes obtained from fits with no splittings in the  $p$ - and  $d$ -waves for 14 and 16 MeV. All TME amplitudes are normalized such that  $A_0=1.0$ .

14 MeV Multipole Contributions in Percent - No Splitting						
	(%)	stat.		syst.		SAPM
Percent $M1$	9.2	$\pm$ 0.6	$\pm$ 0.5			1.8 %
Percent $E1$	90.7	$\pm$ 0.4	$\pm$ 0.3			96.6 %
Percent $E2$	0.06	$\pm$ 0.01	$\pm$ 0.01			0.25 %

**Table B.8:** 14 MeV multipole contributions to the total cross section in percent for fits with no splittings in the  $p$ - and  $d$ -waves. SAPM stands for the Schwamb Arenhövel Potential Model calculation [Sch01a, Sch01b, Are04].

16 MeV Multipole Contributions in Percent - No Splitting						
	(%)	stat.		syst.		SAPM
Percent $M1$	10.5	$\pm$ 0.5	$\pm$ 0.7			1.8 %
Percent $E1$	89.4	$\pm$ 0.4	$\pm$ 0.4			96.1 %
Percent $E2$	0.09	$\pm$ 0.01	$\pm$ 0.02			0.29 %

**Table B.9:** 16 MeV multipole contributions to the total cross section in percent for fits with no splittings in the  $p$ - and  $d$ -waves. SAPM stands for the Schwamb Arenhövel Potential Model calculation [Sch01a, Sch01b, Are04].

**14 MeV Absolute Multipole  
Contributions - No Splitting**

	stat.		syst.		SAPM
$\sigma_{M1} (\mu\text{b})$	88.3	$\pm 5.4$	$\pm 4.4$		17.3
$\sigma_{E1} (\mu\text{b})$	867.0	$\pm 3.7$	$\pm 2.9$		923.4
$\sigma_{E2} (\mu\text{b})$	0.53	$\pm 0.10$	$\pm 0.07$		2.35

**Table B.10:** 14 MeV absolute multipole contributions for fits with no splittings in the  $p$ - and  $d$ -waves. Values were obtained by scaling the percent contributions by the total cross section from theory. SAPM stands for the Schwamb Arenhövel Potential Model calculation [Sch01a, Sch01b, Are04].

**16 MeV Absolute Multipole  
Contributions - No Splitting**

	stat.		syst.		SAPM
$\sigma_{M1} (\mu\text{b})$	85.1	$\pm 4.3$	$\pm 5.5$		14.1
$\sigma_{E1} (\mu\text{b})$	721.4	$\pm 3.1$	$\pm 3.4$		775.9
$\sigma_{E2} (\mu\text{b})$	0.73	$\pm 0.10$	$\pm 0.15$		2.32

**Table B.11:** 16 MeV absolute multipole contributions for fits with no splittings in the  $p$ - and  $d$ -waves. Values were obtained by scaling the percent contributions by the total cross section from theory. SAPM stands for the Schwamb Arenhövel Potential Model calculation [Sch01a, Sch01b, Are04].

**14 MeV TME Amplitudes - With Splitting**

TME	Solution 1			Solution 2			SAPM
	stat.	syst.		stat.	syst.		
$^1s_0 (M1)$	0.000	$\pm 0.121$	$\pm 0.101$	0.000	$\pm 0.121$	$\pm 0.101$	0.269
$^3p_0 (E1)$	0.255	$\pm 0.193$	$\pm 0.115$	0.436	$\pm 0.085$	$\pm 0.050$	0.441
$^3p_1 (E1)$	0.738	$\pm 0.042$	$\pm 0.026$	0.823	$\pm 0.097$	$\pm 0.069$	0.731
$^3p_2 (E1)$	0.648	$\pm 0.024$	$\pm 0.027$	0.562	$\pm 0.045$	$\pm 0.037$	0.643
$^3d_1 (E2)$	0.075	$\pm 0.024$	$\pm 0.017$	0.235	$\pm 0.101$	$\pm 0.072$	0.023
$^3d_2 (E2)$	0.141	$\pm 0.070$	$\pm 0.043$	0.089	$\pm 0.039$	$\pm 0.020$	0.028
$^3d_3 (E2)$	0.111	$\pm 0.049$	$\pm 0.037$	0.006	$\pm 0.021$	$\pm 0.005$	0.025

**Table B.12:** 14 MeV TME amplitudes obtained from fits with splitting allowed in the  $p$ - and  $d$ -waves. SAPM stands for the Schwamb Arenhövel Potential Model calculation [Sch01a, Sch01b, Are04]. Note that all amplitudes are normalized such that  $A_0=1.0$ .

### 16 MeV TME Amplitudes - With Splitting

TME	Solution 1			Solution 2			SAPM
	stat.	syst.		stat.	syst.		
$^1s_0 (M1)$	0.000 ± 0.129	± 0.131		0.000 ± 0.129	± 0.131		0.265
$^3p_0 (E1)$	0.228 ± 0.193	± 0.235		0.434 ± 0.100	± 0.109		0.416
$^3p_1 (E1)$	0.737 ± 0.048	± 0.062		0.832 ± 0.099	± 0.143		0.739
$^3p_2 (E1)$	0.650 ± 0.016	± 0.033		0.552 ± 0.041	± 0.063		0.638
$^3d_1 (E2)$	0.064 ± 0.022	± 0.035		0.263 ± 0.098	± 0.148		0.025
$^3d_2 (E2)$	0.148 ± 0.070	± 0.104		0.083 ± 0.043	± 0.060		0.030
$^3d_3 (E2)$	0.128 ± 0.045	± 0.070		0.002 ± 0.017	± 0.025		0.027

**Table B.13:** 16 MeV TME amplitudes obtained from fits with splitting allowed in the  $p$ - and  $d$ -waves. SAPM stands for the Schwamb Arenhövel Potential Model calculation [Sch01a, Sch01b, Are04]. Note that all amplitudes are normalized such that  $A_0=1.0$ .

### 14 MeV Multipole Contributions in Percent - With Splitting

	Solution 1			Solution 2			SAPM
	(%)	stat.	syst.	(%)	stat.	syst.	
Percent $M1$	0.0 ± 0.4	± 0.3		0.0 ± 0.4	± 0.3		1.8 %
Percent $E1$	95.0 ± 6.5	± 5.6		94.9 ± 13.6	± 9.9		96.6 %
Percent $E2$	5.0 ± 3.1	± 1.9		5.1 ± 3.6	± 2.4		0.23 %

**Table B.14:** 14 MeV multipole contributions to the total cross section in percent for fits with splittings in the  $p$ - and  $d$ -waves. SAPM stands for the Schwamb Arenhövel Potential Model calculation [Sch01a, Sch01b, Are04].

### 16 MeV Multipole Contributions in Percent - With Splitting

	Solution 1			Solution 2			SAPM
	(%)	stat.	syst.	(%)	stat.	syst.	
Percent $M1$	0.0 ± 0.4	± 0.4		0.0 ± 0.4	± 0.4		1.8 %
Percent $E1$	94.1 ± 6.3	± 9.2		94.0 ± 13.7	± 19.4		96.1 %
Percent $E2$	5.9 ± 3.3	± 5.0		6.0 ± 3.9	± 5.8		0.3 %

**Table B.15:** 16 MeV multipole contributions to the total cross section in percent for fits with splittings in the  $p$ - and  $d$ -waves. SAPM stands for the Schwamb Arenhövel Potential Model calculation [Sch01a, Sch01b, Are04].

**14 MeV Absolute Multipole  
Contributions - With Splitting**

	Solution 1				Solution 2				SAPM		
	stat.		syst.		stat.		syst.				
$\sigma_{M1}$ ( $\mu\text{b}$ )	0.0	$\pm$	3.5	$\pm$	2.4	0.0	$\pm$	3.5	$\pm$	2.4	17.3
$\sigma_{E1}$ ( $\mu\text{b}$ )	907.6	$\pm$	62.5	$\pm$	53.3	906.7	$\pm$	130.4	$\pm$	94.6	923.4
$\sigma_{E2}$ ( $\mu\text{b}$ )	48.2	$\pm$	29.7	$\pm$	18.6	49.0	$\pm$	34.9	$\pm$	23.2	2.4

**Table B.16:** 14 MeV absolute multipole contributions for fits with splittings in the  $p$ - and  $d$ -waves. Values were obtained by scaling the percent contributions by the total cross section from theory. SAPM stands for the Schwamb Arenhövel Potential Model calculation [Sch01a, Sch01b, Are04].

**16 MeV Absolute Multipole  
Contributions - With Splitting**

	Solution 1				Solution 2				SAPM		
	stat.		syst.		stat.		syst.				
$\sigma_{M1}$ ( $\mu\text{b}$ )	0.0	$\pm$	3.4	$\pm$	3.5	0.0	$\pm$	3.4	$\pm$	3.5	14.1
$\sigma_{E1}$ ( $\mu\text{b}$ )	759.9	$\pm$	50.5	$\pm$	74.2	47.4	$\pm$	26.3	$\pm$	40.1	775.9
$\sigma_{E2}$ ( $\mu\text{b}$ )	758.8	$\pm$	110.6	$\pm$	156.8	48.4	$\pm$	31.8	$\pm$	47.1	2.3

**Table B.17:** 16 MeV absolute multipole contributions for fits with splittings in the  $p$ - and  $d$ -waves. Values were obtained by scaling the percent contributions by the total cross section from theory. SAPM stands for the Schwamb Arenhövel Potential Model calculation [Sch01a, Sch01b, Are04].

**14 MeV  $\sigma_P$ - $\sigma_A$  Values**

	stat.		syst.		SAPM	
No splittings	-265	$\pm$	16	$\pm$	13	-50 ( $M1$ )
With Splittings (1)	123	$\pm$	115	$\pm$	86	60 (Full)
With Splittings (2)	-362	$\pm$	208	$\pm$	157	60 (Full)

**Table B.18:**  $\sigma_P$ - $\sigma_A$  values for all 14 MeV solutions. The (1) denotes Solution 1 for the case of allowing splittings in the  $p$ - and  $d$ -waves and (2) denotes Solution 2. SAPM stands for the Schwamb Arenhövel Potential Model calculation [Sch01a, Sch01b, Are04]. The values shown for the SAPM calculation correspond to using only the  $M1$  part of the cross section to construct  $\sigma_P$ - $\sigma_A$  ( $M1$ ) and using the full calculation (Full). Experimental values were obtained using the total cross section from the SAPM calculation to obtain the correct normalization (see Section A.2 for details).

**16 MeV  $\sigma_P$ - $\sigma_A$  Values**

	stat.		syst.		SAPM
No splittings	-257	$\pm 13$	$\pm 17$		-41 ( <i>M1</i> )
With Splittings (1)	124	$\pm 92$	$\pm 102$		59 (Full)
With Splittings (2)	-348	$\pm 180$	$\pm 255$		59 (Full)

**Table B.19:**  $\sigma_P$ - $\sigma_A$  values for all 16 MeV solutions. The (1) denotes Solution 1 for the case of allowing splittings in the  $p$ - and  $d$ -waves and (2) denotes Solution 2. SAPM stands for the Schwamb Arenhövel Potential Model calculation [Sch01a, Sch01b, Are04]. The values shown for the SAPM calculation correspond to using only the  $M1$  part of the cross section to construct  $\sigma_P$ - $\sigma_A$  ( $M1$ ) and using the full calculation (Full). Experimental values were obtained using the total cross section from the SAPM calculation to obtain the correct normalization (see Section A.2 for details).

## Bibliography

- [Ago03] S. Agostinelli *et al.* *GEANT4: A simulation toolkit*. Nucl. Instrum. Meth., **A506**(2003) 250–303.
- [Ahm07] M.A. Ahmed *et al.*, 2007. Private Communication. Publication forthcoming.
- [Ahr01] J. Ahrens *et al.* Phys. Rev. Lett. **87**(2001) 022003.
- [Ang05] C.T. Angell. TUNL Progress Report, **XLIV**(2005) 208.
- [Are85] H. Arenhövel. Lecture Notes in Physics, **234**(1985) 276.
- [Are91] H. Arenhövel and M. Sanzone. Few-Body Syst., Suppl., **3**(1991) 1.
- [Are97] H. Arenhövel *et al.* Phys. Lett., **B407**(1997) 1.
- [Are99] H. Arenhövel. Few-Body Syst., **26**(1999) 43.
- [Are01] H. Arenhövel. In D. Drechsel and L. Tiator, editors, *Proc. Symposium on the GDH Sum Rule, Mainz, 2000*, page 67. World Scientific, Singapore, 2001.
- [Are04] H. Arenhövel, A. Fix, and M. Schwamb. Phys. Rev. Lett., **93**(2004) 202301.
- [Ber71] V. B. Berestetskii *et al.* *Relativistic Quantum Theory*, volume 4 of *Course of Theoretical Physics*. Pergamon Press, 1971.
- [Bet35] H.A. Bethe *et al.* Proc. Roy. Soc., **A148**(1935) 146.
- [Bet50] H.A. Bethe *et al.* Phys. Rev., **77**(1950) 647.
- [Bev92] P.R. Bevington. *Data Reduction and Error Analysis for the Physical Sciences*. WCB/McGraw-Hill, 2nd edition, 1992.
- [Bew05] B.E. Bewer. *Development of a Gain Monitoring System for a Neutron Detector Array*. Master’s thesis, University of Saskatchewan, 2005.
- [Bir88] Y. Birenbaum *et al.* Phys. Rev. Lett., **61**(1988) 810.
- [Bru96] R. Brun and F. Rademakers, 1996. ROOT - *An Object Oriented Data Analysis Framework*, Proceedings AIHENP’96 Workshop, Lausanne, Sep. 1996, Nucl. Inst. & Meth. in Phys. Res. A 389 (1997) 81-86. See also <http://root.cern.ch/>.
- [Cam82] A. Cambi *et al.* Phys. Rev. Lett., **48**(1982) 462.

- [Cen07] Center for Nuclear Studies, The George Washington University, 2007. SAID analysis: [http://gwdac.phys.gwu.edu/analysis/nn\\_analysis.html](http://gwdac.phys.gwu.edu/analysis/nn_analysis.html).
- [Cha34] J. Chadwick *et al.* *Nature*, **134**(1934) 237.
- [Cha06] M.B. Chadwick, P. Obložinský, M. Herman, et al. *ENDF/B-VII.0: Next Generation Evaluated Nuclear Data Library for Nuclear Science and Technology*. Nuclear Data Sheets, **107**(2006) 2931–3118.
- [Che99] J.-W. Chen *et al.* *Phys. Rev.*, **C60**(1999) 065205.
- [Cho52] C.N. Chou. *Phys. Rev.*, **87**(1952) 904.
- [Cro01] B.T. Crowley. *Development of a Compton-scattering-based Beam-intensity Monitor at the HIGS Facility*. Master's thesis, Duke University, 2001.
- [Del81] W. Del Bianco *et al.* *Phys. Rev. Lett.*, **47**(1981) 1118.
- [Dre66] S. D. Drell, A. C. Hearn. *Phys. Rev. Lett.*, **16**(1966) 908.
- [Dro76] J. Drooks. Ph.D. thesis, Department of Physics, Yale University, 1976.
- [Els86] Ch. Elster. Ph.D. thesis, Bonn, 1986.
- [Els88] Ch. Elster *et al.* *Phys. Rev. C*, **38**(1988) 1828.
- [Fab76] W. Fabian and H. Arenhövel. *Nucl. Phys. A*, **258**(1976) 461.
- [Fri77] J.L. Friar. *Phys. Rev.*, **C16**(1977) 1504.
- [Fri84] J.L. Friar *et al.* *Phys. Rev. C*, **30**(1984) 441.
- [Gel54] M. Gell-Mann and M.L. Goldberger. *Phys. Rev.*, **96**(1954) 1433.
- [Ger66] S. B. Gerasimov. *Sov. J. Nucl. Phys.*, **2**(1966) 430.
- [Gia03] M.M. Giannini. In M. Battaglieri M. Anghinolfi and R. De Vita, editors, *GDH 2002: Proceedings of the Second International Symposium on the Gerasimov-Drell-Hearn Sum Rule and the Spin Structure of the Nucleon, Genova, Italy, 2002*, page 1. World Scientific, Singapore, 2003.
- [Gri07] H.W. Griesshammer, 2007. Private Communication.
- [Hol83] R.J. Holt *et al.* *Phys. Rev. Lett.*, **50**(1983) 577.
- [Hol95] B.R. Holstein. *Chiral Perturbation Theory: a Primer*, 1995.
- [Iga05] R. Igarashi, 2005. Private Communication. Material in this section is taken mainly from the *Blowfish Trigger Manual*, dated August 22, 2005.

- [Jam98] F. James, 1998. CERN Program Library Long Writeup D506, Version 94.1, CERN Geneva, Switzerland.
- [Kno00] G. F. Knoll. *Radiation Detection and Measurement*. John Wiley and Sons, Inc., 3rd edition, 2000.
- [Knu99] L.D. Knutson. Phys. Rev. C, **59**(1999) 2152.
- [Lit96] V.N. Litvinenko *et al.* Nucl. Instrum. Methods Phys. Res., Sect. A, **375**(1996) 46.
- [Lit97] V.N. Litvinenko *et al.* Phys. Rev. Lett., **78**(1997) 4569.
- [Low54] F.E. Low. Phys. Rev., **96**(1954) 1428.
- [Mad71] J.M.J. Madey. J. Appl. Phys., **42**(1971) 1906.
- [Mar85] T. C. Marshal. *Free-electron Lasers*. Macmillan, Inc., 1985.
- [McC68] I.E. McCarthy. *Introduction to Nuclear Theory*. John Wiley & Sons, 1968.
- [McK04] M.S. McKinley, B. Beck, and D.P. McNabb. Lawrence Livermore National Laboratory Report No. UCRL-WEB-152626-REV-1, (2004). (unpublished).
- [Moh00] P. Mohr *et al.* Rev. Mod. Phys., **72**(2000) 351.
- [Nat] National Institute of Standards and Technology (NIST).
- [O'R96] G.V. O'Rielly, *et al.* Nucl. Instrum. Meth., **A368**(1996) 745–749.
- [Par07] T.-S. Park, 2007. Private Communication.
- [Per05] B.A. Perdue, 2005. Private Communication.
- [Pyw06] R.E. Pywell, *et al.* Nucl. Instrum. Meth., **A565**(2006) 725–730.
- [Rup00] G. Rupak. Nucl. Phys., **A678**(2000) 405.
- [San83] A.M. Sandorfi *et al.* IEEE Trans. Nucl. Sci., **NS-30**(1983) 3083.
- [Saw05] B. D. Sawatzky. *A Measurement of the Neutron Asymmetry in  $d(\vec{\gamma}, n)p$  Near Threshold*. Ph.D. thesis, University of Virginia, 2005.
- [Saw07] B. D. Sawatzky, 2007. Private Communication.
- [Sch00] E. C. Schreiber. *Measurement of a High-Intensity Gamma-Ray Beam and the Analyzing Power for  ${}^2H(\vec{\gamma}, n)p$  Near Threshold*. Ph.D. thesis, Duke University, 2000.

- [Sch01a] M. Schwamb and H. Arenhövel. Nucl. Phys. A, **696**(2001) 556.
- [Sch01b] M. Schwamb and H. Arenhövel. Nucl. Phys. A, **690**(2001) 682.
- [Sch01c] M. Schwamb and H. Arenhövel. Nucl. Phys. A, **690**(2001) 647.
- [Sch07] M. Schwamb, 2007. Private Communication.
- [Sie37] A.J.F. Siegert. Phys. Rev., **52**(1937) 787.
- [Sod87] J.P. Soderstrum *et al.* Phys. Rev., **C35**(1987) 1246.
- [Ste87] K.E. Stephenson *et al.* Phys. Rev., **C35**(1987) 2023.
- [Sun07] C. Sun and Y. Wu, 2007. Private Communication.
- [Ton07] A.P. Tonchev, 2007. Private Communication.
- [Tor03] W. Tornow *et al.* Phys. Lett., **B574**(2003) 8.
- [Vin77] N.A. Vinokurov and A.N. Skrinsky. Report No. INP, **77-59**(1977).
- [Wel63] T.A. Welton. *Fast Neutron Physics*, volume II, page 1317. Interscience, 1963.
- [Wel92] H.R. Weller *et al.* Atomic Data and Nuclear Data Tables, **50**(1992) 29.
- [Wel94] H.R. Weller *et al.* Atomic Data and Nuclear Data Tables, **58**(1994) 219.
- [Wel03] H.R. Weller and M.W. Ahmed. Mod. Phys. Lett., **A18**(2003) 1569.
- [Wil88] P. Wilhelm *et al.* Few-Body Syst., **3**(1988) 111.
- [Wu 96] Y. Wu *et al.* Nucl. Instrum. Methods Phys. Res., Sect. A, **375**(1996) 74.
- [Wu07] Y. Wu, 2007. Private Communication.
- [Wur06] W.A. Wurtz, 2006. Private Communication.

# Biography

## Matthew Allen Blackston

### Personal

- Born in Columbia, TN on March 6, 1978

### Education

- B.S. Applied Physics, Tennessee Technological University, Cookeville, TN, 2000
- Graduate Studies, Reformed Theological Seminary, Orlando, FL, 2001-2002
- A.M. Physics, Duke University, Durham, North Carolina, 2005

### Publications

*The  ${}^7\text{Li}(d,n_0){}^8\text{Be}$  and  ${}^7\text{Li}(d,n_1){}^8\text{Be}$  reactions below 160 keV*, A. Sabourov, M.W. Ahmed, M.A. Blackston, *et al.*, Phys. Rev. C **74**, 064611 (2006).

*In Beam Tests of Implanted Helium Targets*, J.E. McDonald, R.H. France III, R.A. Jarvis, M.W. Ahmed, M.A. Blackston, *et al.*, Journal of Instrumentation, **1** P09003 (2006).

*Astrophysical S factor for the  ${}^{11}\text{B}(d,n){}^{12}\text{C}$  reaction below 135 keV*, Y. Parpottas, M.W. Ahmed, M.A. Blackston, *et al.*, Phys. Rev. C **74**, 015804 (2006).

*First evidence for spin-flip M1 strength in  ${}^{40}\text{Ar}$* , T.C. Li, N. Pietralla, A.P. Tonchev, M.W. Ahmed, T. Ahn, C. Angell, M.A. Blackston, *et al.*, Phys. Rev. C **73**, 054306 (2006).

*Astrophysical S factor for the  ${}^7\text{Li}(d,n_0){}^8\text{Be}$  and  ${}^7\text{Li}(d,n_1){}^8\text{Be}$  reactions*, A. Sabourov, M.W. Ahmed, M.A. Blackston, *et al.*, Phys. Rev. C **73**, 015801 (2006).

*Effects of Isospin Mixing on Statistical Properties of  ${}^{26}\text{Al}$  and  ${}^{30}\text{P}$* , J.F. Shriner, Jr., M.A. Blackston, C.A. Grossmann, K.T. Mahar, and G.E. Mitchell, Capture Gamma-Ray Spectroscopy and Related Topics, ed. Stephen Wender, AIP Press (New York), 2000, p.497.